Synthesis and Derivatisation of Hetero-Atomic Zintl Anions and Multi-Metallic Clusters of the Tetrel and Pentel Elements

Synthese und Derivatisierung hetero-atomarer Zintl-Anionen sowie multi-metallischer Cluster der Tetrele und Pentele

Kumulative Inauguraldissertation zur Erlangung des akademischen Grades eines Doktors der Naturwissenschaften, dem Fachbereich Chemie an der Philipps-Universität Marburg vorgelegt von

Diplom-Chemiker
Stefan Martin Jürgen Mitzinger
aus Karlsruhe

Prof. Dr. Stefanie Dehnen,
Philipps-Universität Marburg, Erstgutachtertin

Prof. Dr. John Corrigan,
The University *of* Western Ontario, Zweitgutachter

Einreichungsdatum: 19.12.2017
Prüfungsdatum: 05.02.2018

Philipps-Universität Marburg, 2018
Hochschulkennziffer 1180

Diese Arbeit wurde in der Zeit von April 2013 bis Dezember 2017 unter der Leitung von Frau Prof. Dr. Stefanie Dehnen (Fachbereich Chemie der Philipps-Universität Marburg) und Herrn Prof. Dr. John Corrigan (Department of Chemistry of *The* University *of* Western Ontario) angefertigt.

Acknowledgements

For the strong and lasting support during my thesis I would like to thank the following institutions and funding agencies:

Philipps-Universität Marburg and *The* University *of* Western Ontario for financial support and laboratory infrastructure. The Deutsche Forschungsgemeinschaft (DFG) and the National Sciences and Engineering Research Council of Canada (NSERC) for their financial support for consumable material. The Friedrich-Ebert Stiftung and the German Federal Ministry for Education and Research for a generous scholarship during my studies in Germany and Canada. The Gesellschaft Deutscher Chemiker (GDCh), the Marburg University Research Academy (MARA) and the German Academic Exchange Service (DAAD) for several travel grants over the last years.

Furthermore I would like to thank my cooperation partners Prof. Scott McIndoe and his group at the University of Victoria, British Columbia, Canada and Dr. Florian Weigend and his group at the Karlsruhe Institute of Technology.

I thank my co-workers and colleagues in the Dehnen and Corrigan Group as well as in the analytical Service Departments at the Departments of Chemistry at Philipps-Universität Marburg and *The* University *of* Western Ontario. Especially I would like to thank Prof. Stefanie Dehnen for her kindness, wisdom and motivation during my studies. Also, I would like to thank Prof. John Corrigan for his advice, support and motivation during the last seven years.

For the support of my family and the friends I made and lost over the years I am very grateful.

Eidestattliche Versicherung

Ich erkläre, dass meine Promotion noch an keiner anderen Hochschule als der Philipps-Universität Marburg, Fachbereich Chemie, versucht wurde.
Ich versichere, dass ich die Dissertation „Synthesis and Derivatisation of Hetero-Atomic Zintl Anions and Multi-Metallic Clusters of the Tetrel and Pentel Elements“ selbst und ohne fremde Hilfe verfasst, nicht andere als die in ihr angegebenen Quellen oder Hilfsmittel benutzt, alle vollständig oder sinngemäß übernommenen Zitate als solche gekennzeichnet sowie die Dissertation in der vorliegenden oder einer ähnlichen Form noch bei keiner anderen in- oder ausländischen Hochschule anlässlich eines Promotionsgesuchs oder zu anderen Prüfungszwecken eingereicht habe.

Marburg, den 19.12.2017 Stefan Mitzinger

Contents

List of Figures

List of Tables

1 Introduction

1.1 A Utopian Dream: What we want from Hetero-Atomic Clusters

Multi-metallic clusters and core-shell nanoparticles have been discussed for application in catalysis, especially since catalytically active metal centers have been incorporated into the cluster core and shell. [1,2,3,4] As intermediates between single atoms and particles they can, in theory, combine the benefits of both worlds: uniformity and activity combined in a structured topology with the potential to form extended networks. Single metal atoms cannot exist under catalytic conditions without the support of ligands and nano particles from a top-down approach come an inherent size dispersity. However, multi-metallic clusters, that have been shown to be synthesised without ligands in solid, solution and the gas phase, combine key advantages of single metal atoms and nano particles and enable the synthesis of uniform clusters without ligands. These clusters may bear catalytic active metals, or even shown their own form of catalytic activity due to cooperative effects of different metals combined in the framework of binary, ternary or multinary clusters. The utilisation of multi-metallic clusters, so far, is limited to small or medium scale feasibility studies due to their sensitivity to various environments in which chemical processes are meant to run. In particular, charged clusters are prone to many kinds of charge neutralisation reactions, be it oxidation of negatively charged clusters or reduction of positively charged clusters, as even the most convenient cluster charge accompanied by an electronic closed-shell configuration, may be overcome by thermodynamics in the end. Protecting thermodynamically unstable clusters with sterically demanding ligands has been proven a viable way to delay decomposition. However, this can result in sacrificing reactivity since the catalytic activity is related to access to the active site and therefor necessitates an approachable metal centre.

In this light, the synthesis of ligand-free cluster frameworks is an important step to attain the desired catalytic reactivity. The first steps in this direction have been already done in the

synthesis of ligand-free multi-metallic clusters: the successful synthesis of binary Zintl anions. For the heavier main group elements, several Zintl anions have been obtained and described in detail. However, in terms of their flexibility none has come close to the chemistry that evolved around homo-atomic polyanions of germanium.[5,6] Attaching several organic and metal-organic ligands,[7,8,9] linking clusters directly or with organic linkers,[10] incorporating metal atoms into the cluster core[11] or attaching them on the outside of the cluster framework,[12] the variety of Zintl anions of germanium has shown is unmatched, so far.

The employment of germanium, a metalloid element, might be seen as an extension of the chemistry resulting from its metallic character, but it may also be that the metalloid behavior is the key difference, as the clever and fairly straight-forward derivatisations for Ge have not been reported for the heavier main group elements so far. A logical step from this point of view would be to explore the chemistry of lighter binary Zintl anions. Moving away from the metallic character in the heavy main group elements can have certain advantages: Oxidation states for non-metallic elements in compounds are much more stable then the ones of metals, therefore they can tolerate various environments in chemical processes more easily; the solubility is much improved. Moreover, if one considers the derivatisation of a cluster with an organic group, the energetic differences between the atomic orbitals, that are to be combined, are much smaller for third or forth period elements with carbon than for fifth and sixth period elements. Hence, moving from multi-metallic clusters to hetero-atomic clusters is just a logical step if one is to make more robust clusters.

Following this general idea, this work aims to lay a foundation for the chemistry of the lighter Zintl anions and will present the first results in this direction. The following sections will focus on the basics behind this chemistry. The results will be discussed in the subsequent chapters.

1.2 Polyanions of the Main Group Elements

Among the main group elements, the elements of group 13 to 17 are known to form polyanionic species. An enormous variety of polyanions is known, exhibiting structural motifs from oligomeric chains to complex networks. [13] Despite their rich and beautiful chemistry, poly- and interhalogenide species, polysilicates, polyphosphates, polysulfates, polymetallates and other binary or ternary polyanions will not be discussed in this section. Homo-atomic polyanions of group 16 will only be mentioned briefly. Instead this section will focus on homo-atomic polyanions of group 13 to group 15 elements, as they are most relevant foundations for the chemistry of this work. Also, this section aims to inform the reader about the variety of compounds accessible to date. The chemistry of these species will be discussed in Section 1.5 on page 29 along with selected examples.

1.2.1 Polyanions of Group 13

The heavier E^{13} elements Ga, In and Tl form polyanions, which are considered classical Zintl anions. For B no stable polyanions have been isolated in the solid state. Al along with Ga can form polyanions like E_3^- and E_4^{8-} (see Figure 1.1 on the next page(a)) in phases with Sr (e.g. Sr_8Al_7 and Ba_8Ga_7).
Ga, In and Tl form tetrahedral polyanions that are isoelectronic to Ge_4^{4-} (see also Section 1.2.2 on page 5) and P_4 in A_2E (A = Li, Na), whereas in AE phases (A = Ca, Ba; E=Ga, In) the E^- units are isoelectronic to E^{14} elements and form (distorted) diamond structures. In KTl and CsTl a diamond structure cannot be achieved due to the large size of the cation. [14] In these phases clinched Tl_6^{6-} [15] octahedra are formed. As shown in Figure 1.1 on the next page all polyanions of E^{13} show a very large number of negative charges, which need to be compensated if the compound is to be isolated in any form. Coulomb interactions and covalent interactions between anions and cations must be carefully considered. Due to its lowest electronegativity in the group polyanions of Tl are more easily polarised and can therefore be accessed in a manifold variety, followed by polyanions of In. Tl_5^{7-}, [16] Ga_6^{8-} [17] and Tl_6^{8-} [18] comply with Wade-Mingos rules and form *closo*-clusters (see 1.1 on the following page (d-e)). In_4^{8-}, Tl_4^{8-} [16] and In_5^{9-} [19] form *nido*-clusters. However, there are clusters that do not comply with Wade-Mingos rules, because their electron count is lower than expected for *closo*-clusters (for E^{13} elements: $(E_n)^{(n+2)-}$). Tl_7^{7-} realises a structure that shows a Jahn-Teller distortion (here axial compression). In the case of Tl_7^{7-} the compression leads to a Tl–Tl bond between the apical atoms. Figure 1.1 on the next page illustrates other known structure motifs for E^{13} elements. In phases with alkaline earth metals isolated anions like Ga^{5-}, dimers like Ga_2^{8-} and linear trimers like Tl_3^{7-} have been found. [14,16,20]

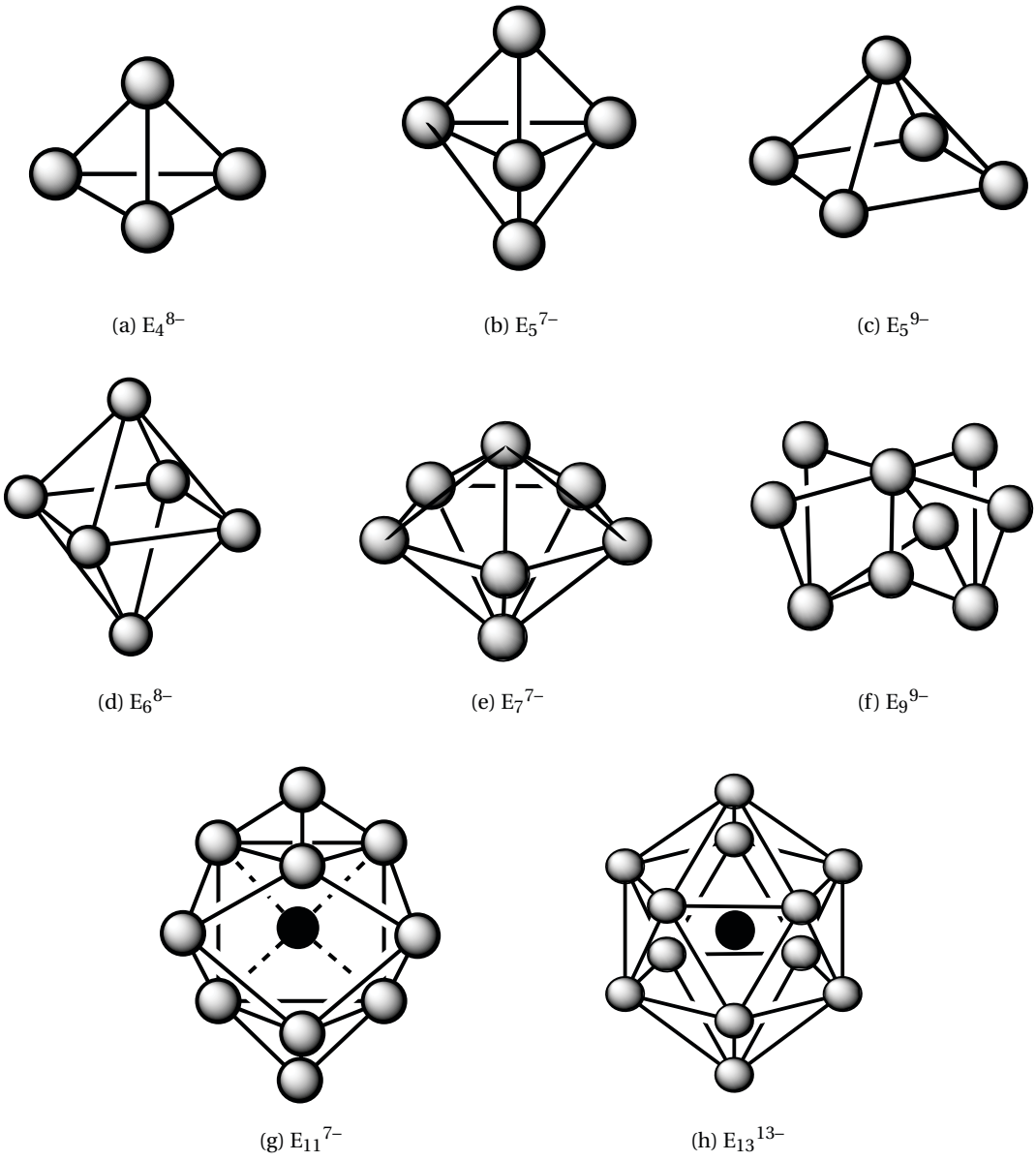

(a) E_4^{8-} (b) E_5^{7-} (c) E_5^{9-}

(d) E_6^{8-} (e) E_7^{7-} (f) E_9^{9-}

(g) E_{11}^{7-} (h) E_{13}^{13-}

Figure 1.1: Structures of selected E^{13} polyanions

Cluster	$\mathbf{E^{13}}$	**valence e$^-$**	**skeletal e$^-$**	**Wade type**	**VEC**
E_4^{8-}	Tl	20	12	*nido*	5
E_5^{7-}	Tl	22	12	*closo*	4.44
E_5^{9-}	Tl	24	14	*nido*	4.80
E_6^{8-}	Ga	26	14	*closo*	4.33

Table 1.1: Overview of selected E^{13} polyanions

1.2.2 Polyanions of Group 14

Electron-deficient E^{14} polyanions comply with Wade-Mingos rules (see also Section 1.4.3 on page 23) easily as E^{14} atoms are isoelectronic with $(E^{13})^-$ and isolobal with B–H. *Closo*-clusters of E^{14} should possess the general formula of $(E^{14}{}_n)^{2-}$.

Like for group 13 elements, isolated polyanions and dimers have been reported for group 14 elements as well. Si^{4-} [21], Ge^{4-} [22], Sn^{4-} [23] and Pb^{4-} [24] have been isolated from ternary phases of alkali metals and alkaline earth metals with the respective E^{14} element. $(E^{14}{}_2)^{6-}$ dimers have been isolated for Si, Ge and Sn, but not for Pb so far.[25,26,27] The only trimer reported to date is $Sn_3{}^{7-}$ which was found in the phase of Li_7Sn_3.[28] Another most interesting polyanion, that was exclusively found in the Zintl phase KLi_2Sn_8 is $Sn_8{}^{6-}$,[29] which features a very uncommon square anti-prismatic structure (see Figure 1.3 on the next page(d)).

The so far mentioned polyanions of group 14 elements have all been identified from Zintl phases (see also Section 1.3.1 on page 13 for a definition). More relevant to this work are the polyanions that have been isolated from solution. Table 1.2 on page 7 summarises E^{14} polyanions that have been isolated from solution or that have been reported to be present in Zintl phases exclusively. Although the polyanions exclusively present in the solid state are equally important for understanding the relationship between structure and electronic situation, they do not play an important role in the active chemistry of this field due to their high negative charge and the resulting limited solubility. To date no polyanion with a charge higher than 4– has been isolated from solution at ambient temperature. This is due to the almost impossible task to arrange more than four sequestered cations around one rather small polyanion. However, considering only steric reasons, this might be achievable in liquid ammonia without the help of sequestering agents.

Among the polyanions of group 14 one can also find cyclic polyanions, which exhibit π-aromaticity: $Si_6{}^{10-}$ [30] and $Si_5{}^{6-}$ [21] form quasi-planar rings, but could only be isolated in the solid state from the phases $Ba_2Mg_3Si_4$ and Li_8MgSi_6, respectively.

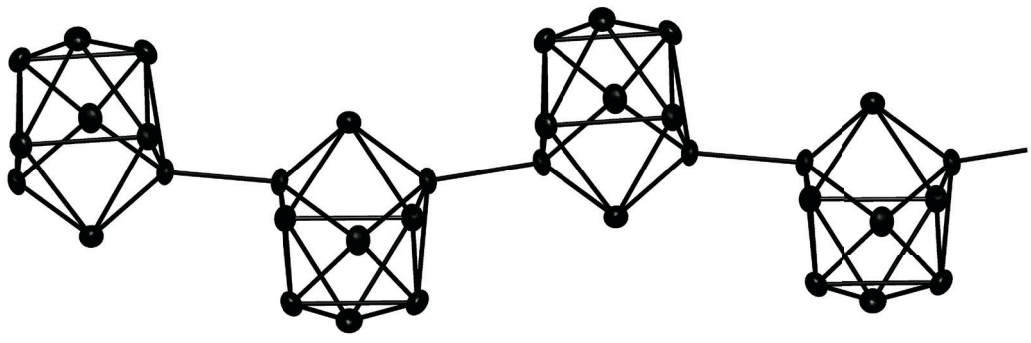

Figure 1.2: Visualisation of the $^1_\infty[Ge_9]^{2-}$ chain

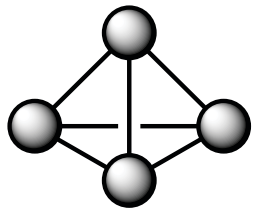

(a) E_4^{4-}

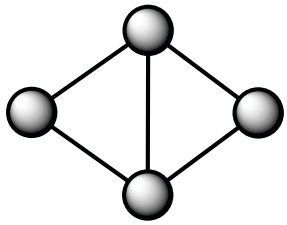

(b) E_4^{6-}

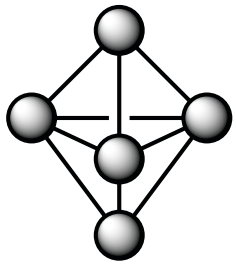

(c) E_5^{2-}

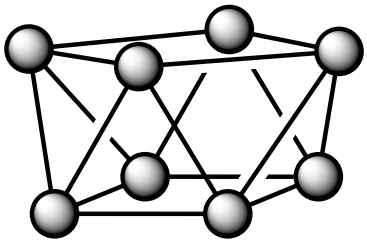

(d) E_8^{6-}

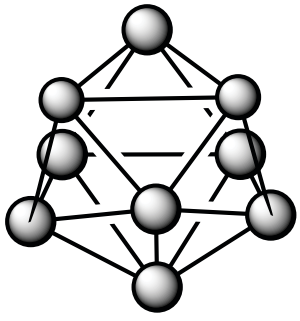

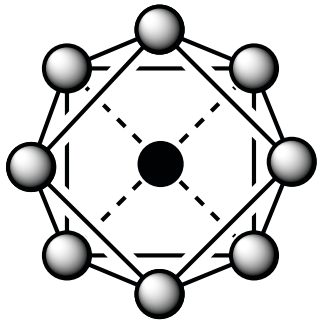

(e) E_9^{x-} (x=2,3,4) in two views

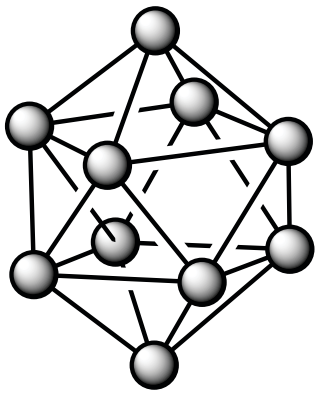

(f) E_{10}^{2-}

Figure 1.3: Structures of selected E^{14} polyanions

Polyanions crystallised from solution have been isolated with bare or sequestered cations from liquid ammonia at low temperature or with (semi)sequestered cations at ambient temperature. As the cations are alkali metal cations, crown ethers like 18-c-6 or cryptands like crypt-222 are ideal sequestering agents. In the case of the polyanions E_4^{4-} and E_9^{4-}, they are extracted directly from the stoichiometrically corresponding Zintl phases AE or A_4E_9, respectively. E_5^{2-}, E_9^{2-} and E_9^{3-} are accessible from non-stoichiometric phases in lower yields but can also be

Cluster	in solution	in solid	valence e⁻	skeletal e⁻	Wade type	VEC
E_4^{4-}	Sn, Pb	Si, Ge, Sn, Pb	20	12	*nido*	5
E_4^{6-}		Si	22	14	*arachno*	5.50
E_5^{2-}	Si, Ge, Sn, Pb		22	12	*closo*	4.44
E_8^{6-}		Sn	38	22	*arachno*	4.75
E_9^{2-}	Si, Ge		38	20	*closo*	4.22
E_9^{3-}	Si, Ge		39	21	–	4.33
E_9^{4-}	Si, Ge, Sn, Pb	Si, Ge, Sn, Pb	40	22	*nido*	4.44
E_{10}^{2-}	Ge, Pb		42	22	*closo*	4.66

Table 1.2: Overview of selected E^{14} polyanions

isolated upon extraction of A_4E_9 phases after oxidation.
In addition to the polyanions already discussed, oligomeric and polymeric assemblies of polyanions have also been reported. So far they are limited to Ge_9 clusters that are directly linked to (an)other Ge_9 cluster(s). A dimeric motif was reported by Fässler *et al.* in 2011,[31] here the two Ge_9 clusters link via a 2c2e bond, resulting in a $(Ge_9–Ge_9)^{6-}$ unit. Sevov *et al.* published the first trimeric assembly of Ge_9 clusters in 2002.[32] Here the outer Ge_9 units connect to the central unit via two 2c2e bonds, resulting in a $(Ge_9–Ge_9–Ge_9)^{6-}$ trimer, in which the central Ge_9 unit does not bear any formal charge. Furthermore, a linear tetrameric structure of Ge_9 was reported by Sevov *et al.* in 2003.[33] Guloy *et al.* reported a $^1_\infty[Ge_9]^{2-}$ polymer upon a $2e^-$ oxidation of Ge_9^{4-} (see Figure 1.2 on page 5).[34] A linkage of these units can also be achieved with (metal-)organic linkers and is discussed in Section 1.6.3 on page 35.

1.2.3 Polyanions of Group 15

For group 15 elements the larger valence electron number allows for an easier formation of electron precise clusters (in which all bonds represent 2c2e bonds), the polyanions in this group are, hence, not electron deficient by nature.[14] The application of Wade-Mingos rules (see also Section 1.4.3 on page 23) is therefore not helpful. For E^{15} elements a large number of polyanions were identified in the solid state and in solution reaching from E_2^{2-} dimers of Bi to high-nuclearity E_{26}^{4-} polyphosphides (see Figure 1.4 on page 10 for a structural overview). A list of E^{15} polyanions can be found in Table 1.3 on page 9. This section will focus on anions accessible via solution-based methods.
The smallest group 15 polyanion is Bi_2^{2-}. In the solid state it is present in the Zintl phase Cs_3Bi_2.[35] It exhibits metallic conductivity and Pauli-paramagnetism. The dimeric Bi_2^{2-} is iso-valence-electronic to singlet oxygen and its bond length of 267.6(4) pm is the shortest observed Bi–Bi distance in the solid state.[14] Hence, a higher bond order is suggested for

this polyanion. In contrast, Bi_2^{2-} obtained from solution has a significantly longer bond length of 283.7 pm, which is consistent with a Bi–Bi double bond. [36] The cyclic polyanions E_4^{2-} have been successfully isolated in solution for all group 15 elements (see Figure 1.4 on page 10(e)). Whereas Bi_4^{2-} is isolated from the extraction of the phases K_5Bi_4 and K_3Bi_4 [37], the light analogue P_4^{2-} is synthesised without the necessity of a Zintl phase by the reduction of diphosphane with elemental Cs in liquid ammonia. [38] All cyclic E_4^{2-} are planar and possess six π-electrons and are considered aromatic molecules, exhibiting D_{4h} symmetry. Bi_4^{2-} can also be reduced further in solution, yielding a zigzag chain of Bi_4^{6-} (see Figure 1.4 on page 10(b)). [39] The most renown polyanions in this group are the nortricyclane-type polyanions of E_7^{3-}. They are accessible for all group 15 elements via reduction with alkali metals in liquid ammonia or from phases with alkali metals in the ratio A_3E_7. A solvated P_7^{3-} was first synthesised by von Schnering and Schmidpeter in 1984 [40]. The polyanion is made up a basal three membered ring, in which each atom is connected to a bridging P atom. The three bridging P atoms connect to one apical P atom. The polyanion has an idealised C_{3v} symmetry. The ^{31}P-NMR spectrum at 50 °C features a sharp singlet at –119 ppm. If cooled down to –60 °C the ^{31}P-NMR spectrum shows three multiplets at –57, –103 and –162 ppm in a ratio of 1:3:3. [41] A similar behavior was also recorded in the solid-state NMR spectrum of Li_3P_7. [42] Another notable polyanion is Sb_8^{8-}. [43] It features a double crown structure like S_8 and illustrates the application of the pseudo-element concept as each Sb^- anion acts like sulfur (see Figure 1.4 on page 10(h)). To date this double crown structure is limited to Sb. Ufosane-type structures with the formula E_{11}^{3-} are known for P [44], As [45], Sb [45] and Bi [46], with Bi_{11}^{3-} being the youngest member of this family, discovered by Dehnen *et al.* in 2014. The larger polyanions E_{14}^{4-}, E_{16}^{2-}, E_{19}^{3-}, E_{21}^{3-}, E_{22}^{4-} and E_{24}^{4-} play only a minor role as their synthesis is limited to P so far (with the exception of E_{14}^{4-}, which has also been synthesised with As). [14]

1.2.4 Polyanions of Group 16

For oxygen only the polyanions O^{2-}, O_2^-, O_2^{2-} and O_3^- are known, [13,14] here the term polyanion does not exclusively indicate a multiple negatively charged species, but also a polyatomic nature of the anion. O^{2-} is the most common anion of group 16. It is present in metal oxides, silica glass and in melts of element oxoacids. The hyperoxide O_2^- is present in alkali and alkali earth metal salts like NaO_2 and $Ca(O_2)_2$. They disproportionate to oxygen, peroxides and hydroxide anions in aqueous solution. Peroxides O_2^{2-} can be synthesised by the reaction of alkali metals with oxygen at normal pressure or by oxidation of alkaline earth oxides at higher temperature and pressure. The red ozonide species O_3^- is present in the salts AO_3 (A= Na, K, Rb, Cs, NMe_4). They can be synthesised from hyperoxides with ozone. They react vigorously with water under formation of oxygen and hydroxide anions, whereas under heat

Cluster	in solution	in solid
E_2^{2-}	Bi	Bi
E_4^{2-}	P, As, Sb, Bi	
E_4^{6-}	Bi	
E_5^{-}	P	
E_5^{5-}	Sb	
E_6^{4-}	As	As
E_7^{3-}	P, As, Sb, Bi	P, As, Sb
E_8^{8-}	Sb	
E_{11}^{3-}	P, As, Sb, Bi	P, As
E_{14}^{4-}	P, As	
E_{16}^{2-}	P	
E_{19}^{3-}	P	
E_{21}^{3-}	P	
E_{22}^{4-}	P	
E_{24}^{2-}	P	

Table 1.3: Overview of selected E^{15} polyanions

they decompose to oxygen and hyperoxides. As these polyanions differ from the topic of this work, they will not be discussed in greater detail.
Polysulfides can be synthesised from the reaction of sulfur with alkali or alkaline earth metals in liquid ammonia.[47] They form sulfide, disulfide, trisulfide and even larger polyanions (S_n^{2-}, n =1 – 7). Single charged polysulfides (S_n^{-}, n= 1 – 4, 6) are known to be the reason for the exceptional colour of minerals like ultramarine. The heavier group 16 elements Se and Te form polyanions that exhibit chain, ring and layered structures. For Po no polyanions have been synthesised so far.

1.2.5 Zintl Anions

In general Zintl anions possess a framework of covalently bonded homo- or hetero-atomic atoms from the metallic or meta-metallic group 13–15 elements, in which all or some atoms possess a negative charge. They can bear (metal-)organic groups and can incorporate one or more atoms within their structure (see also Section 1.5 on page 29). Originally, the term was limited to polyanions extracted from distinct Zintl phases (see also Section 1.3.1 on page 13) but it was shown that similar anions can also form directly in solution. They obey the Zintl-Klemm formalism (see Section 1.3.3 on page 14). They have been named in honor of Eduard Zintl, who laid the ground-breaking foundations to this style of chemistry in 1931,[48,49] after investigating reports by Joannis that solutions of sodium in liquid ammonia could dissolve antimony and lead.[50]

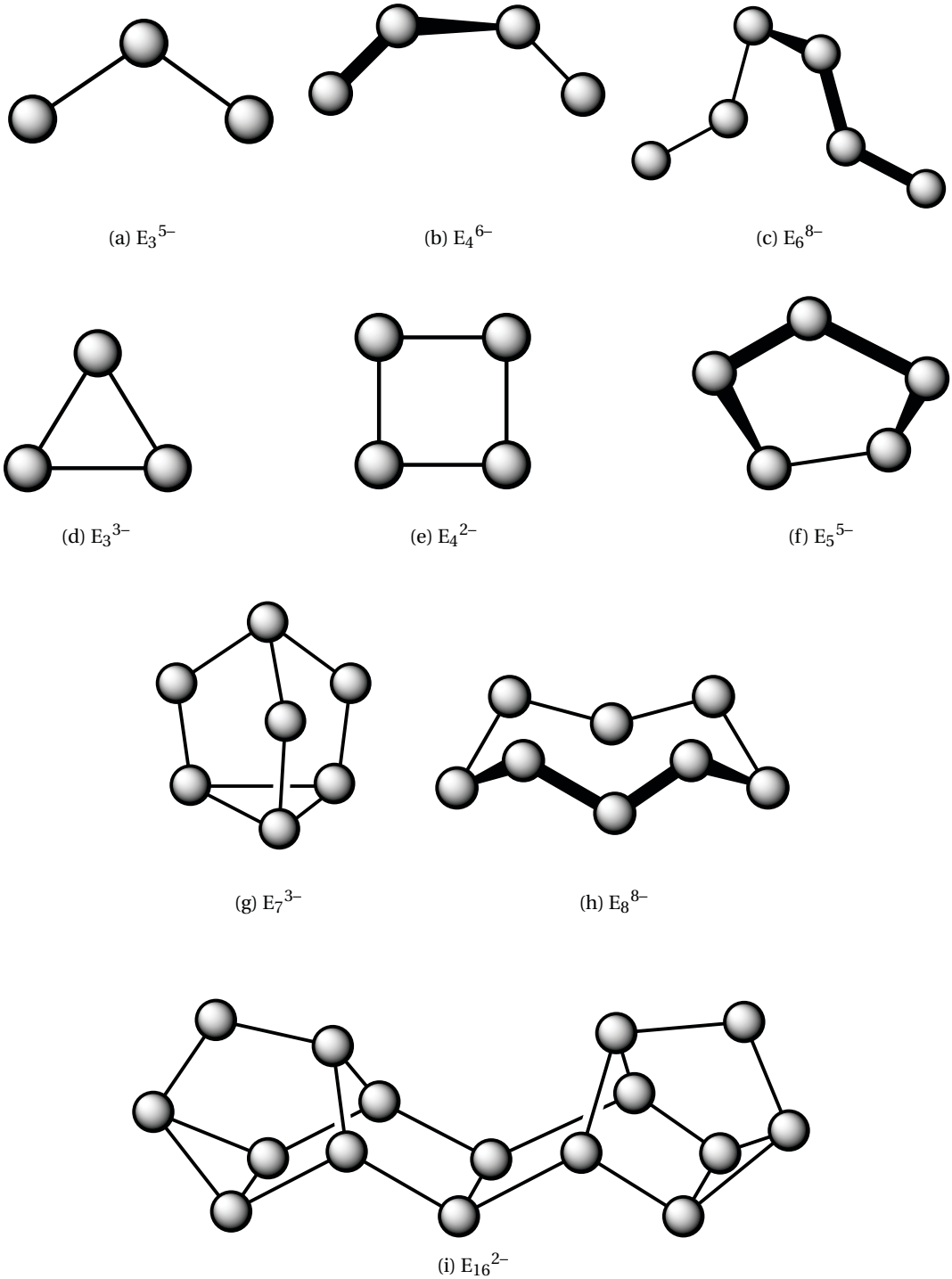

(a) E_3^{5-} (b) E_4^{6-} (c) E_6^{8-}

(d) E_3^{3-} (e) E_4^{2-} (f) E_5^{5-}

(g) E_7^{3-} (h) E_8^{8-}

(i) E_{16}^{2-}

Figure 1.4: Structures of selected E^{15} polyanions

1.3 From Zintl Phases to Distinct Cluster Anions

1.3.1 The Intermetallic

The area of intermetallic phases is vast and continuously expanding. Within it multiple classifications have been made according to structural constitution, VEC and physical properties. These "phenomenological" classifications gave rise to four distinct groupings, which are explained in this section briefly.

Heusler phases

Heusler phases are ternary intermetallic phases in which ferromagnetic or anti-ferromagnetic properties arise from the formation of a face centered cubic (fcc) super-lattice. In principle two binary compounds XY and XZ (ideally with CsCl-structure) form a phase with the composition X_2YZ. However, the elements used in the formation of the phase are not ferromagnetic themselves. Their magnetic properties solely arise from their order in the solid state. Heusler phases are mainly ferromagnetic and contain Cu/Ni/Co (X), Mn (Y) and Al/In/Sn/Sb/Bi (Z). In the case a joint fcc sub-lattice is vacant *semi*-Heusler phases of the composition XYZ may form. [13,51]

Hume-Rothery phases

Hume-Rothery phases are closely related to the different modifications of brass. Their VEC determines the structure. If more and more Zn is added to Cu the VEC rises. If the VEC is between 1 and 1.36 (α phase) Zn is statistically distributed resulting in a solid solution of Zn in Cu. At a VEC of 1.50 (β phase) a bcc structure (also W-structure) is adopted. Whereas at a VEC of 1.75 a hcp structure is adopted (ϵ phase). According to their VEC an isotype structure is adopted by various other alloys of transition metals with main group metals. As the VEC rises, electrons have to assume higher energy levels, the Fermi limit rises. At approx. 1.36 the delimitation of the first Brillouin zone is reached, increasing the VEC above this delimitation would mean to occupy states in a higher energy band, therefore the transition into another structure type (from α to β phase) is favored. [47,52]

Laves phases

Laves phases are perfectly packed alloy-like solid solutions of two metals with the general molecular formula AB_2 (e.g. KNa_2, $CaMg_2$). A atoms usually are electropositive metals like alkali or alkaline earth metals, whereas B atoms usually are less electropositive metals from

phase	formula	VE	atoms	VEC
β	AgZn	1 + 2	2	3 : 2 = 21 : 14 = 1.50
	Cu_5Sn	5 + 4	6	9 : 6 = 21 : 14 = 1.50
ϵ	$CuZn_3$	1 + 6	4	7 : 4 = 21 : 12 = 1.75
	Cu_3Sn	3 + 4	4	7 : 4 = 21 : 12 = 1.75

Table 1.4: Examples of Hume-Rothery phases and their VEC

groups 4-6. The ratio of the atomic radii of the two metals is ideal at $\frac{r_A}{r_B} = \sqrt{\frac{3}{2}} \approx 1.225$, although this packing can be realised between a value of 1.1 to 1.7 for $\frac{r_A}{r_B}$. Laves phases are densely packed and can be cubic or hexagonal. A atoms are ordered in a diamond or hexagonal diamond structure, B atoms form closely packed tetrahedra around the A atoms. There are three structure types for Laves phases: the $MgCu_2$-type (space group $Fd\bar{3}m$, see Figure 1.5 (a)) features a cubic diamond structure for A atoms with B_4 tetrahedra at all tetrahedral sites. The $MgZn_2$-type (space group $P6_3/mmc$, see Figure 1.5 (b)) features a hexagonal diamond structure of A atoms with B atoms building up face and vertex linked tetrahedra. The third structure type is the $MgNi_2$-type (space group $P6_3/mmc$) and can be viewed as a combination of the latter two structures. Due to their almost ideal packing (volume density of 0.71) Laves phases show metal-like electrical conductivity, but are hard and brittle and cannot be deformed at room temperature. Therefore, Laves phases have similarities to Zintl phases (formally they possess homonuclear B_4 tetrahedra), but they do not fulfill the valence rules for Zintl phases in general and should not be considered as part of Zintl phases (see section 1.3.1 on the next page). [13,47,52,53]

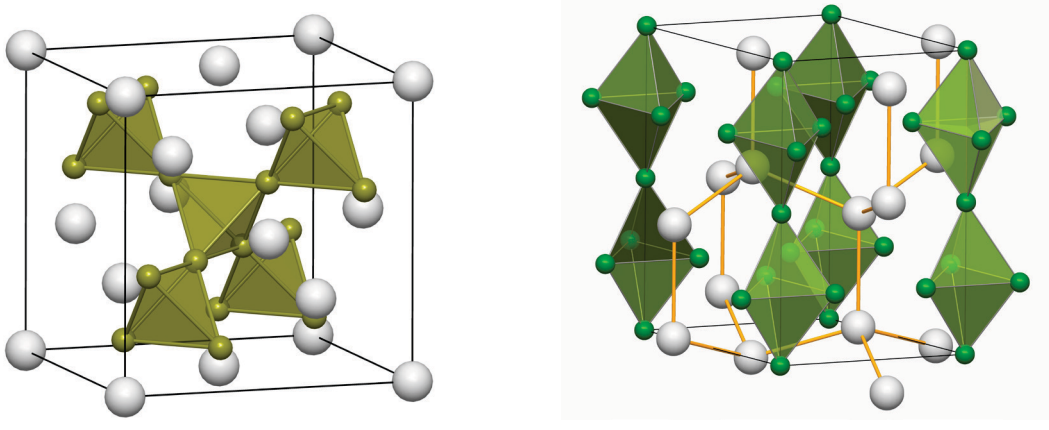

(a) $MgCu_2$ (b) $MgZn_2$

Figure 1.5: Unit cells of the Laves phases $MgCu_2$ and $MgZn_2$

Zintl phases

As opposed to Hume-Rothery phases, Zintl phases in general contain one more electropositive element A and greatly exceed the VEC of Hume-Rothery phases (up to a VEC of 2.5).[54] Zintl proposed to consider an electron transfer from the more electropositive element A to element X instead of an averaged VEC – resulting in the general formula A_mX_n or $(A_m)^+X_n{}^{m-}$. The logical consequence of an electron transfer to element X is the formation of covalent bonds resulting in polyanionic covalently bonded structures.[49,55,56] The number of neighboring atoms is determined by the octet rule, therefore an atom with N valence electrons (including formally transferred electrons from the electropositive partner) must have $8 - N$ covalent bonds. Therefore NaTl can be regarded as Na^+Tl^- with covalently bonded Tl^- units, which build up a diamond-like structure (see Figure 1.6). Tl^- has four valence electrons and hence builds four $(8 - 4 = 4)$ bonds to its neighboring atoms. The presence of covalent bonds in an intermetallic phase is a sharp delimitation to the previously described classes of intermetallics.[52]

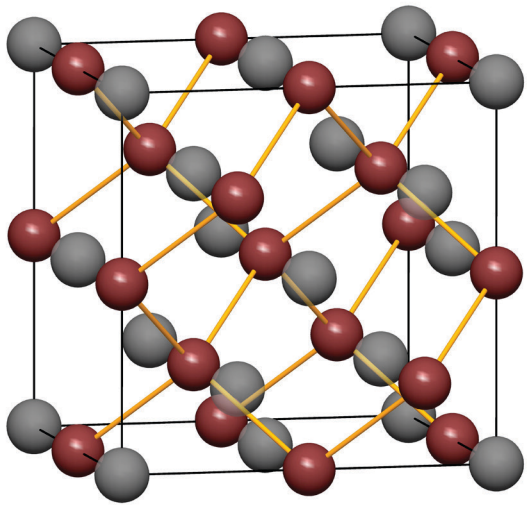

Figure 1.6: Unit cell of the Zintl phase NaTl with Tl^- units connected

1.3.2 Delimitation of the Zintl Phase

In general Zintl phases contain a metal A and a meta-metal X. Unfortunately the definition of a meta-metal as being the elements between classic metals and non-metals is not decisive. Whereas the limit to classic metals in the periodic table is quite easy to establish the limit towards the non-metals is not. Elements such as P, Se and Te have non-metallic and metallic

modifications making a clear assignment difficult. The original definition of a Zintl phase is quite sharp, but confines the term to phases of metals and meta-metals in which homonuclear X–X bonds are present. [56] Historically, the Zintl line separates the electropositive elements A in Zintl phases from the main group meta-metals X and runs along the border between the triel and tetrel elements in the periodic table (see Table 1.5). Elements left of the Zintl line should form intermetallic phases with electropositive elements, whereas elements right of it should form salt-like compounds with more or less extended anionic structures. As simple as this definition and delimitation along the Zintl line seems, it restricts the term to a very low number of known phases. The Zintl line is no strict delimitation and should be considered as an outdated term. Therefore Klemm proposed additions to Zintl's strict rules which are described in Section 1.3.3.

1	**2**	**3**	**4**	**5**	**6**	**7**	**8**	**9**	**10**	**11**	**12**	**13**	**14**	**15**	**16**	**17**	**18**
H																	He
Li	Be											B	C	N	O	F	Ne
Na	Mg											Al	Si	P	S	Cl	Ar
K	Ca	Sc	Ti	V	Cr	Mn	Fe	Co	Ni	Cu	Zn	Ga	Ge	As	Se	Br	Kr
Rb	Sr	Y	Zr	Nb	Mo	Tc	Ru	Rh	Pd	Ag	Cd	In	Sn	Sb	Te	I	Xe
Cs	Ba	La	Hf	Ta	W	Re	Os	Ir	Pt	Au	Hg	Tl	Pb	Bi	Po	At	Rn
Fr	Ra																

Table 1.5: Periodic table of elements with visualised Zintl line

1.3.3 The Zintl-Klemm Formalism

Due to the presence of covalent homonuclear bonds in Zintl phases, they show characteristics of valence compounds. They therefore show a relationship between chemical and electronic structure. In non-electron-deficient compounds short homonuclear contacts can be described as 2c2e bonds. These 2c2e bonded polyanions $X_n{}^{m-}$ fulfill the octet rule by forming bonds and undergoing reduction by electron transfer from the electropositive metal.
By accepting an electron from their electropositive partner, the anionic component formally reaches the valence electron configuration of the next higher group in the periodic table. Hence, they can be viewed as pseudo-atoms of this group or as a pseudo element of it and the anionic sub-lattice can adopt structures and connectivities assumed by this element – they are isostere. [57,58,59] Although this concept can be explained quite easily, it had large implications

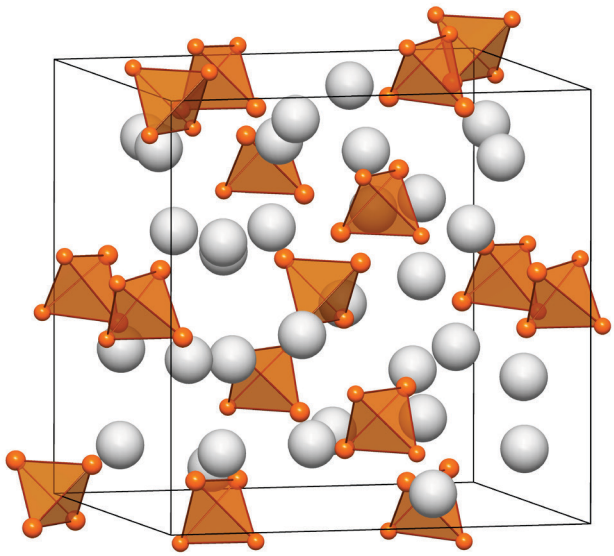

Figure 1.7: Unit cell of the Zintl phase KGe with connected $(Ge_4)^{4-}$ tetrahedra

on the view of many phases and compound. According to R. Hoffmann [60] this concept is *"the single most important theoretical concept in solid state chemistry of this century"*, and yet it is still reinterpreted and extended to new classes of compounds, for example for cations in oxides. [61]

As previously described Tl^- in NaTl adopts a diamond structure and, hence, acts as carbon. In $CaSi_2$ the single negative charged Si atom forms hexagonal $(Si^-)_n$ networks like in the structure of grey As. [52] In the case of KGe the Ge^- units form $Ge_4{}^{4-}$ tetrahedra analogous to white phosphorus (see Figure 1.7). [62] The Zintl-Klemm formalism can be seen as a valence electron counting scheme for the solid state. Zintl phases not only depend on the existence of X–X bonds and chemical constitution, but also on their compliance to the Zintl-Klemm formalism. Nesper [54] defined three criteria for Zintl phases that combine the Zintl-Klemm formalism with chemical and physical properties demonstrated by ideal Zintl phases:

1. A well-defined relationship between geometry and electronic structure must exist. This implies the validity of valence electron counting schemes for at least a part of the structure.

2. They are semiconductors with a band gap of less than 2 eV or show increasing electrical conductivity with increasing temperature.

3. Zintl phases are mostly diamagnets, if paramagnetic they should not show temperature-

dependent paramagnetism.

A consequence of these criteria is that Zintl phases possess very narrow homogeneity widths in a phase diagram (line compounds), they are not alloys and not insulators but are structured solids and therefore cannot be deformed without breaking (brittleness).

1.3.4 Crossing the Zintl Line

The delimitation between electropositive elements A and (meta)metals X is not a harsh criterion for Zintl phases any more but a reminder where to expect a "classic" Zintl phase with well-developed X–X bonding. Especially by inclusion of transition metals (the early transition metals on the side of electropositive elements) and the late transition metals (on the metal side), we can understand novel phases and apply the Zintl-Klemm formalism in new contexts. When combining elements of the far sides of the periodic table to a Zintl phase the electronegativity of the elements is quite different and is considered when formally transferring electrons within the counting scheme. When moving closer to the Zintl line from both ends of the periodic table, elements with small differences in electronegativity are combined. In this area phases deviate more and more from the Zintl-Klemm formalism as the fundamental idea behind the electron counting scheme does not apply any more. The well known realgar (P_4S_3,[63] see Figure 1.8 (a)) can be considered as an example: Although we have well localised 2c2e bonds the Zintl-Klemm concept cannot be applied due to the small differences in electronegativity – no significant electron transfer takes place. No electron transfer takes place and there is no electropositive partner present. However, a nortricyclan topology is found that is also known from Zintl phases like Li_3P_7 (see Figure 1.8 (b)).[64]

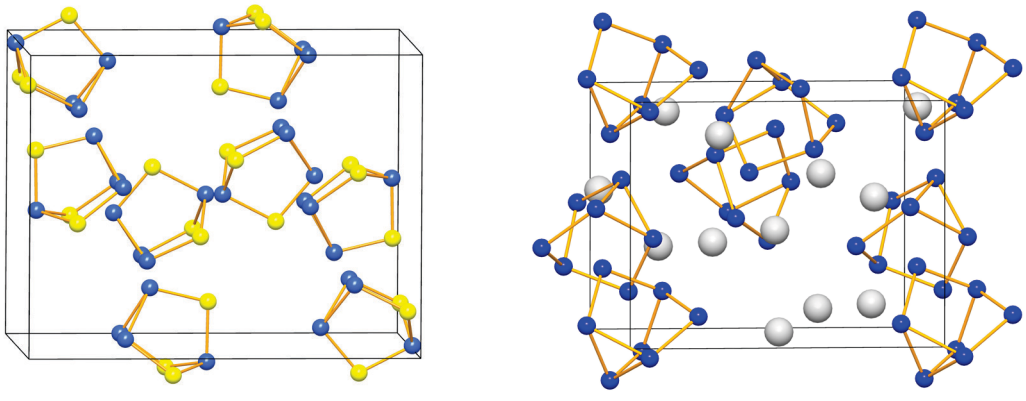

(a) P_4S_3 (b) Li_3P_7

Figure 1.8: Unit cell of realgar P_4S_3 and Li_3P_7

1.3.5 Limits of the Zintl-Klemm Formalism

The Zintl-Klemm formalism is very useful when considering the VEC of compounds for their bonding analysis; in simple cases like in NaTl[65] their connectivity has an analog in an elemental modification (see Section 1.3.1 on page 11). However, it cannot explain structural transitions under pressure and in general the interaction between "cations" and "anions" in phases and ionic crystals.[66] LiTl, for example, crystallises in a CsCl structure. LiAl, LiGa and LiIn crystallise in a NaTl structure at ambient conditions.

1.3.6 "Phases" and Solid Mixture

The reaction towards cluster anions can either be started from a known Zintl phase or from a solid mixture comprised of elements, that might as well be part of a Zintl phase (typically a stoichiometric mixture). In the case of utilising a ATt_3 or ATt_9 phase (A = alkali metal, Tt = tetrel element) the cluster anions present in the solid state are generally extracted into solution. The higher the charge of the cluster anion, the lower is its solubility. In most cases a filtration upon extraction is therefore a mandatory step. For example a common source of Ge_9^{4-} are the phases K_4Ge_9 [67] and Cs_4Ge_9, [68] in which the cluster anions are present in the phase and can be extracted without further change to the cluster anion. Due to the high charge of the cluster anion of 4– the solubility is limited, hence, the yield of the extraction is low. Yet, there are also examples in which the extraction process cannot be described as a solution process of a pre-formed cluster anion present in the phase. In the case of the phase K_8SnSb_4 the cluster anion present in the solid state is a $(SnSb_4)^{8-}$ tetrahedron, but upon extraction in *en* the cluster anion $(Sn_2Sb_2)^{2-}$ was obtained as a $[K(crypt\text{-}222)]^+$ salt.[69] Hence, a transformation from $(SnSb_4)^{8-}$ to $(Sn_2Sb_2)^{2-}$ upon extraction occurred. This can be explained with the very high negative charge of the parent cluster anion of 8–, which cannot be obtained as a $[K(crypt\text{-}222)]^+$ salt due the sterically impossible task to arrange eight crypt-222 sequestered K^+ cations around a rather small tetrahedron. In solution $(SnSb_4)^{8-}$ decomposes under formation of the soluble $(Sn_2Sb_2)^{2-}$ and elemental Sb. The transition into a less charged and soluble cluster anion should be favored process. The mechanism of this reorganisation upon extraction is a black box to date. As reorganisation processes in favor of a charge reduction have been observed during cluster anion formation, it is reasonable to conclude that these processes are also on work when employing no pre-defined phase, but a solid mixture. The extraction of a single phase is then not a mandatory condition for the formation of cluster anions. $(Sn_2Bi_2)^{2-}$, for example, has been obtained upon extraction of a solid mixture of the composition KSnBi in en.[70] There is no known ordered single phase with this stoichiometry. This result opened the field for the synthesis of new solid mixtures in order to form new homo- and heteroatomic

cluster anions, but with the downside of having an mostly unknown reorganisation process in the reaction cascade. This approach has since been expanded to yield mixed E^{13}/E^{15} and E^{14}/E^{15} cluster anions in the Dehnen group.

1.3.7 Extraction Process

As mentioned above the extraction is an important step in cluster anion synthesis, but also a mostly unknown step. Consequentially, several factors might influence the cluster transformation during extraction:

- Reactions between multiple extracted cluster anions
- Solubility effects between extracted cluster anions and solvent
- Ion pairing effects between extracted clusters & cation (especially for the heavier alkali metals)
- Coordination effects between cluster anion and solvent
- Coordination effects between cation and solvent
- Surface effects between undissolved phase or solid mixture and cluster anions
- Disproportionation reactions of cluster anions
- Reduction of cluster anions from unreacted alkali metals in solid mixtures
- Extraction conditions itself (temperature, light and pressure)

As not only one but several or all of these factors might influence the formation of cluster anions upon extraction it is almost impossible to shed light on the whole framework of interdependent processes that occur during the extraction. In addition to this there has been no quantitative study on the solubility of Zintl phases and solid mixtures. In most reactions left over phases are filtered off, so the impact of surface effects upon cluster formation cannot be estimated. For example Corbett *et al.* [71] stated that the best yields were achieved when allowing the solution to stand over the solid mixture for one week or heating the whole extraction mixture to 35°C with the solid still present. As the extraction process normally takes between several hours and a few days, cluster reduction due to leftover alkali metals in solid mixtures and reactions on surfaces of the undissolved phase cannot be neglected. All in all the extraction process is the least understood step in cluster formation.

1.3.8 Dynamics in Solution

In terms of dynamics the family of homo-atomic E^{14} 9-vertex clusters has been investigated in great detail. For Sn_9^{4-} and Pb_9^{4-}, which are readily accessible from the A_4X_9 Zintl phases (A = K, Rb, Cs; X = Sn, Pb) [6,72,73] NMR spectroscopic measurements were conducted. For Sn_9^{4-} ^{119}Sn-NMR revealed that in solution even at lower temperatures (30°C to –40°C in *en*, NH_3) only a single resonance signal is present. [73] Judging from the solid state structure Sn_9^{4-} was expected to show three resonances with a 4:4:1 ratio as the cluster has a C_{4v} symmetry. [74] The occurrence of one resonance can be explained by dynamics in solution in which the cluster anion fluctuates between C_{4v} and D_{3h} on the NMR time scale (see Figure 1.9). This dynamic process found in homo-atomic E^{14} 9-vertex clusters has already been suggested for ML_9 coordination complexes. [75,76,77] As this dynamic behavior has been observed for coordination complexes and certain homo-atomic cluster anions alike, it is reasonable to conclude that this is also true for other homo-atomic cluster anions, for which NMR spectroscopy is not feasible due to the physical properties of the element (e.g. Ge with a nuclear spin of $\frac{9}{2}$) and heteroatomic clusters related to or exhibiting a similar connectivity as the Sn_9^{4-} cluster anion. At low temperatures this fluctuation is not observed. A ^{119}Sn Mössbauer study for the Sn_9^{4-} system at 77 K revealed three distinct Sn environments with a ratio of 4:4:1. [78] Yet, EXAFS and Raman spectroscopy for this system revealed that at lower and ambient temperature this fluctuation is present. [79] The previously discussed transition between C_{4v} and D_{3h} must therefore be considered as extreme cases, with the real situation being in between.

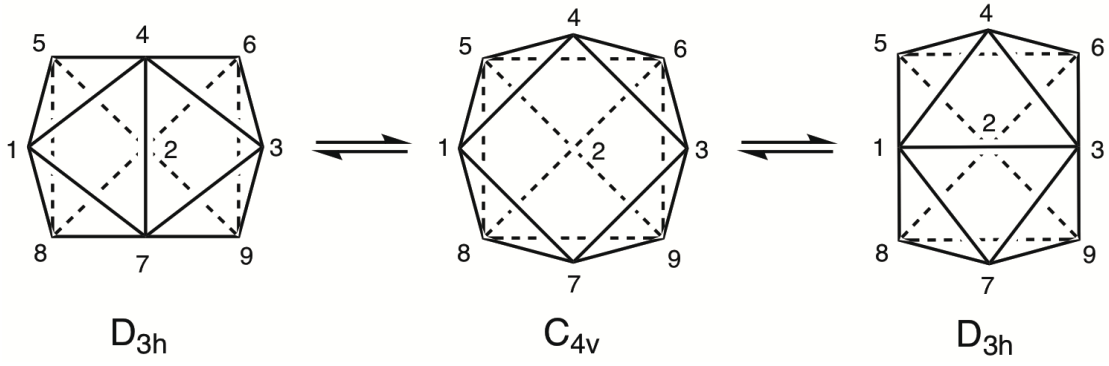

Figure 1.9: Dynamics of 9-vertex clusters: Transition between C_{4v} and D_{3h} symmetry

1.3.9 The Crystallisation Process

When considering the effects that extraction can have on product formation, it is not a surprise that crystallization conditions can also play a role. An irreversible transition between two cluster compounds in solution, from a tetrahedral $(Ge_2P_2)^{2-}$ to a 9-vertex cluster $(Ge_7P_2)^{2-}$ under

precipitation of red phosphorus, occurs in DMF over the time of two weeks. Yet, in *en* this process is slower and involves an so far unknown protonated species. In the case of $(Ge_2As_2)^{2-}$ in the presence of "Ta" atoms in *en* several multi-metallic clusters have been isolated from one reaction, suggesting a complex re-organisation process in solution. [80] One could argue that depending on the choice of counter-solvent and solvent, one species will crystallise more easily. Removing this species from the equilibrium could inhibit a further reactivity leading to a different product. Therefore the time allowed before starting the crystallisation process, the reaction conditions itself (like time and temperature) and the choice of counter-solvent in addition the crystallisation conditions (e.g. low temperature or ambient temperature) should be considered equal tunable parameters for obtaining a specific cluster compound. Careful optimisations for each parameter seem to be a quite tedious task, especially for only delicately manageable compounds, but would certainly help to understand certain pathways in the cluster building process.

1.4 Deltahedral and Non-Deltahedral Cluster Anions

1.4.1 Application of the VEC

A helpful classification for cluster ions in general is the VEC per cluster, that can be derived from the sum formula of the compound. For a VEC < 8 the cluster compound is anionic, for a VEC > 8 polycationic. In the case the VEC = 8 the compound is of a simple ionic nature. If the VEC is not an integer number, the bonding situation of the charged cluster compound is more complex, as the atoms within the cluster are not bonded equally throughout the anion. The VEC is therefore a simple tool to evaluate the overall constitution of the anion. In the case of the Zintl phase Ba_3Si_4 the VEC is 5.5. The average bond order b(XX) in Ba_3Si_4 of 2.5 is achieved for two Si atoms bonded two-fold and two Si atoms bonded three-fold. The VEC and average bond order are calculated as followed:

$$VEC(X) = \frac{3 \cdot 2(Ba) + 4 \cdot 4(Si)}{4} = \frac{22}{4} = \frac{11}{2} = 5.5$$
$$b(XX) = 8 - VEC(X) = 8 - 5.5 = 2.5$$

The cluster anion Si_4^{6-} has a butterfly structure (see Fig. 1.10 on the following page(a)). The already discussed P_7^{3-} cluster anion that is present in the Zintl phase Li_3P_7 has a VEC of 5.43 and features four three-fold bonded P atoms and three two-fold bonded P atoms resulting in an average bond order of b(XX) = 2.57 (see Fig. 1.10 on the next page(c)). The cluster anion Si_5^{2-} within the Zintl salt $[K(crypt\text{-}222)]_2(Si_5)$ has a VEC of 4.4 and an average bond order of 3.6 and has the shape of a tripodal bicapped pyramid. It is comprised of two apical three-fold bonded Si atoms and a base of three four-fold bonded Si atoms. The basal Si atoms are neutral, they fulfill their valence electron octet by four 2c2e bonds. The two apical Si atoms have a single negative charge (see Fig. 1.10 on the following page(b)).[81] However, especially when dealing with a non-integer VEC other factors need to be considered in case-specific studies: as shown by Wang *et al.*[82] Si_5^{2-} shows 3D-aromatic behavior, therefore the pure localisation of the negative charges on the apical Si atoms is not an accurate representation and rather a helpful simplification. For the anion Ge_4^{4-} the VEC is an integer (VEC = 5.0) and consequentially the atoms are bonded equally throughout the cluster.

In Table 1.6 on the next page more examples for frequently occurring structure motifs for cluster anions are shown. As the number of atoms in the cluster framework increases the variety of their topologies increases, too. For cluster anions X_n^{m-} with $n > 9$ the inner volume of the cluster can be occupied, too, giving birth to endohedral cluster anions, which are

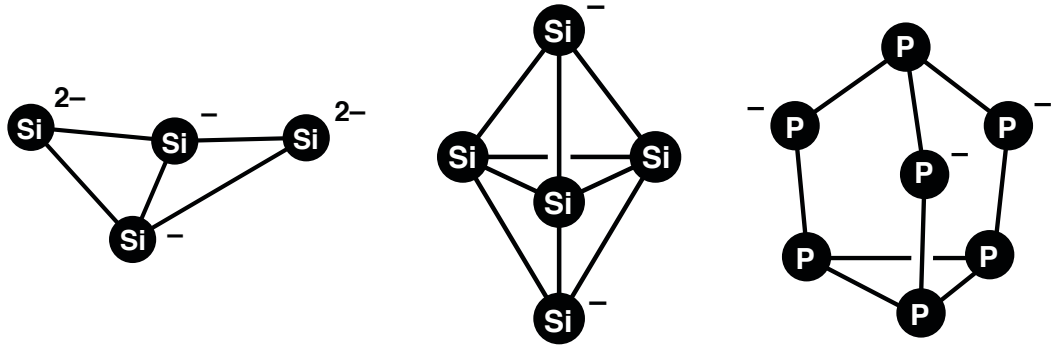

(a) Si_4^{6-} (b) Si_5^{2-} (c) P_7^{3-}

Figure 1.10: Selected Zintl anions with non-integer VEC (formal charges assigned)

discussed in Section 1.6.1 on page 32.

Cluster anion	VEC	b(XX)	symmetry (idealised)	structure
Si_4^{6-} [81]	5.50	2.50	C_{2v}	butterfly
Ge_4^{4-} [62]	5.00	3.00	T_d	tetrahedron
Si_5^{2-} [81]	4.40	3.60	D_{3h}	trigonal bipyramid
Tl_5^{7-} [83]	4.40	3.60	D_{3h}	trigonal bipyramid
P_7^{3-} [64]	5.43	2.57	C_{3v}	nortricyclane-like
Ge_9^{4-} [68]	4.44	3.56	C_{4v}	monocapped square antiprism
Ge_{10}^{2-} [84]	4.67	3.33	D_{4d}	bicapped square antiprism

Table 1.6: Examples of cluster anions: VEC, bond order, symmetry and structure

1.4.2 Nomenclature

The nomenclature of chemical compounds is a matter of great importance to the IUPAC. In the last decades several additions to the *Preferred IUPAC Names* (PIN) have been made. Although the nomenclature for organic compounds is very well developed, this is not true for inorganic compounds as they possess a high flexibility in terms of coordination number, oxidation states, bond order and topology. For Zintl phases like KGe the name potassium germanide is derived quite easily, but it does not give any structural information on the constitution of the solid phase. For the Zintl anion found in KGe, two sets of nomenclature rules might be considered: [85] cluster compounds may be viewed as polycycles or polynuclear clusters.
In the case of polycycles the name for the simple tetrahedral Zintl anion Ge_4^{4-} is tricyclo[1.1.0.$0^{2,4}$]-

tetragermane-tetraide. For Ge_5^{2-} the name pentacyclo[2.1.0.0^{1,3}.0^{2,4}.0^{2,5}]-pentagermane-3,5-diide is derived. As the assignment of rings and nodes to a cluster compound becomes much more difficult for larger clusters, very soon the effort to derive the name bears no proportion to the information it contains. Considering the nomenclature for polynuclear complexes the name [T_d-(13)-Δ^4-*closo*]-tetragermanium-tetraide is derived for Ge_4^{4-}. For Ge_5^{2-} the name is [D_{3h}-(131)-Δ^6-*closo*]-pentagermanium-3,5-diide. As the nomenclature for polynuclear clusters is derived from the *central structural unit* (CEP) as described in the Casey, Evans, Powell (CEP) system [86,87,88] for polyboron hydrides and the Wade-Mingos rules (see also Section 1.4.3), it is confined to the topology of *closo*, *nido*, *arachno*, etc. boranes, which are all based on deltahedral clusters. In the case of non-deltahedral clusters or endohedral clusters no set of rules can be applied to derive a name that is balanced between length and informational content. A new system of nomenclature for multi-metallic clusters would therefore be very useful in this steadily expanding field.

1.4.3 Polyhedral Skeletal Electron Pair Theory (PSEPT) – Wade-Mingos Rules

Wade and Mingos defined and revised a comprehensive set of rules to determine the structure of main group element cluster compounds. [89,90] Boranes and carboranes strictly comply with this set of rules, but it can also be used for metal-carbonyl clusters, metallo-boranes and -carboranes as well as for deltahedral polyanions of E^{13} and E^{14} elements and certain sulfur compounds.

The basis for these rules is a counting procedure for skeletal electrons. Main group elements can contribute three atom orbitals to the molecular orbital of the cluster. The total number of electrons is calculated for element E (v) and its ligand L (x) by the formula $v+x-2$ (where v is the number of valence electrons of element E and x is the number of electrons supplied by the ligand). For transition metals the formula is $v+x-12$, as transition metals can accommodate more ligands due to their *d*-oribtals. If the number of skeletal electrons is $2n+2$, a complete polyhedron with n vertices is the predicted structure (*closo*). When atoms and ligands can overcome the sufficient electrons for a *closo* polyhedron, polyhedra with one or more missing vertices are realised (see Table 1.8 on the following page). The polyhedra realised for certain numbers of vertices are listed in Table 1.7 on the next page. 1.11 on the following page shows textbook examples of *arachno* and *nido* type Wade clusters originating from an octahedron. For several polyanions the skeletal electron count was calculated according to Wade-Mingos rules. They are listed in Table 1.1 on page 4 and 1.2 on page 7.

Vertices	polyhedron
4	tetrahedron
5	trigonal bipyramid
6	octahedron
7	pentagonal bipyramid
8	dodecahedron
9	tricapped trigonal prism
10	bicapped square antiprism
11	octadecahedron
12	icosahedron

Table 1.7: Table of polyhedra realised for certain numbers of vertices

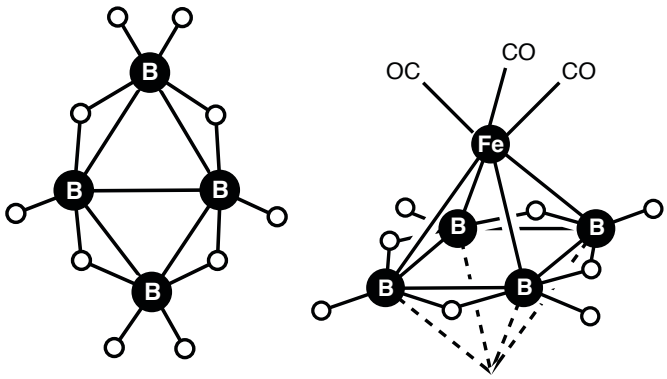

(a) B_4H_{10} (b) $B_4H_8Fe(CO)_3$

Figure 1.11: *arachno* B_4H_{10} (left) and *nido* $B_4H_8Fe(CO)_3$ (right)

Electron count	Name	Structure
$4n$+2	*closo*	polyhedron with n vertices
$4n$+4	*nido*	n + 1 vertex polyhedron, one vertex missing
$4n$+6	*arachno*	n + 2 vertex polyhedron, two vertices missing
$4n$+8	*hypho*	n + 3 vertex polyhedron, three vertices missing

Table 1.8: Skeletal electron count vs. predicted structure

1.4.4 Electron-Precise Clusters

In electron-precise clusters every bond can be described as a 2c2e bond, with left over electrons being assigned as formal atom charges. Although, Wade-Mingos rules (see Section 1.4.3 on page 23) can give us an idea about the shape of the cluster, it cannot be used to describe the electronic situation, as multi-centre-bonding, which is a foundation of the Wade-Mingos rules, does not apply without restrictions for electron-precise clusters. [81] For example the Si_4^{6-} anion can be classified as *arachno*-type according to Wade-Mingos rules (14 skeletal electrons, $2n+6$, $n=4$), therefore it can be described as a $n+2$ vertex polyhedron, with two vertices missing. Indeed we can explain the structure as an octahedron with two of its basal vertices removed. Whereas the electronic situation excludes multi-centre bonding due its angled structure and is best describes by 2c2e bonds with the two far-sided atoms bearing 2– charges (see Figure 1.10 on page 22(a)). More impressive is the comparison between Si_9^{4-} and Ge_9^{4-} (see Figure 1.12).

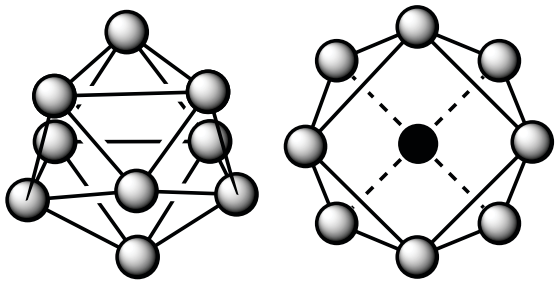

(a) electron-precise Si_9^{4-}

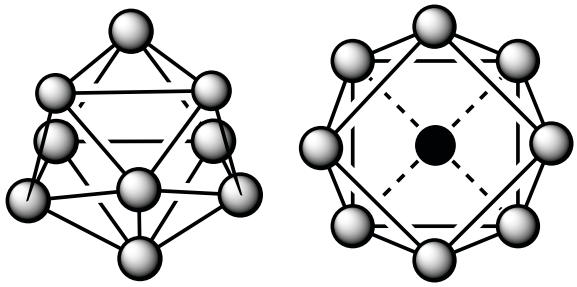

(b) non electron-precise Ge_9^{4-}

Figure 1.12: Comparison between Si_9^{4-} and Ge_9^{4-}

Whereas the structure of Ge_9^{4-} [72] can be described as accurately with Wade-Mingos rules, a quantum chemical calculation for Si_9^{4-} revealed, that this view is wrong for silicides. [91] Although the overall shape of this silicon cluster is apparently similar, and can be described as a *nido* Wade-Mingos cluster, its electronic situation is entirely different. All bonds in Si_9^{4-} are best described as electron-precise 2c2e bonds, with the negative charges localised on the three-fold bonded Si position (see Figure 1.12(a)).

1.4.5 Deltahedral Cluster Anions

Homo- and hetero-atomic Zintl anions of groups 13 (see Section 1.2.1 on page 3) and 14 (see Section 1.2.2 on page 5) have a deltahedral constitution. Their bonding interactions and topology can be explained by the PSEP theory (see Section 1.4.3 on page 23). In deltahedral clusters every face of the cluster topology resembles a triangle. The term *deltahedral* is derived from the majuscule Greek letter *delta* (Δ), which has the shape of an equilateral triangle. Deltahedral clusters have been found in the chemistry of boranes and their isolobal as well as iso-valence-electronic relatives. In general deltahedral clusters are observed when the skeletal electrons of the cluster are not able to form electron-precise 2c2e bonds throughout the cluster framework.[92,93,94] By utilising multi-centre bonding, 3c2e bonds, as known for the diborane B_2H_6, an overall bonding interaction results from the the combination of three atom orbitals to form one bonding, one non-bonding and one anti-bonding molecular orbital, in which the available two electrons occupy the bonding molecular orbital.

1.4.6 Non-Deltahedral Cluster Anions

In contrast to deltahedral cluster anions (see Section 1.4.5), non-deltahedral clusters possess faces, that are not triangular. They are not observed in classical homo-atomic group 13 (see Section 1.2.1 on page 3) or group 14 (see Section 1.2.2 on page 5) Zintl anions, as they all are electron deficient and form multi-centre bonded deltahedral polygons (or can be derived from them), in conformity with Wade-Mingos rules (see Section 1.4.3 on page 23). Non-deltahedral clusters have been observed upon reactions with homo-atomic Zintl anions with (metal-)organic reagents (see Section 1.6 on page 32), especially when a metal cation was incorporated into the centre of the cluster framework in which all atoms are (pseudo) E^{15} atoms (see Section 1.6.1 on page 32). Notable topologies in this context are 10, 12, 13 and 14-vertex clusters of group 14 and 15 elements like $[Co@Ge_{10}]^{3-}$ [95] (10 vertices), $[Ru@Ge_{12}]^{3-}$ [96] (12 vertices), $[La@Sn_4Bi_9]^{3-}$ [97] (13 vertices) and $[Eu@Sn_6Bi_8]^{4-}$ [98] (14 vertices). Their structures are shown in Figure 1.13 on the facing page.

1.4.7 Transformations between Deltahedral and Non-Deltahedral Cluster Anions

The transformation from deltahedral clusters to non-deltahedral clusters must be accompanied by a change in the electronic situation. In case of the transformation of electron-deficient clusters to electron-precise clusters this is a logical structural response upon the availability of additional electrons within the cluster framework to overcome electron-deficiency. In this case the transforation may either lead to the formation of an electron-precise cluster or to a cluster

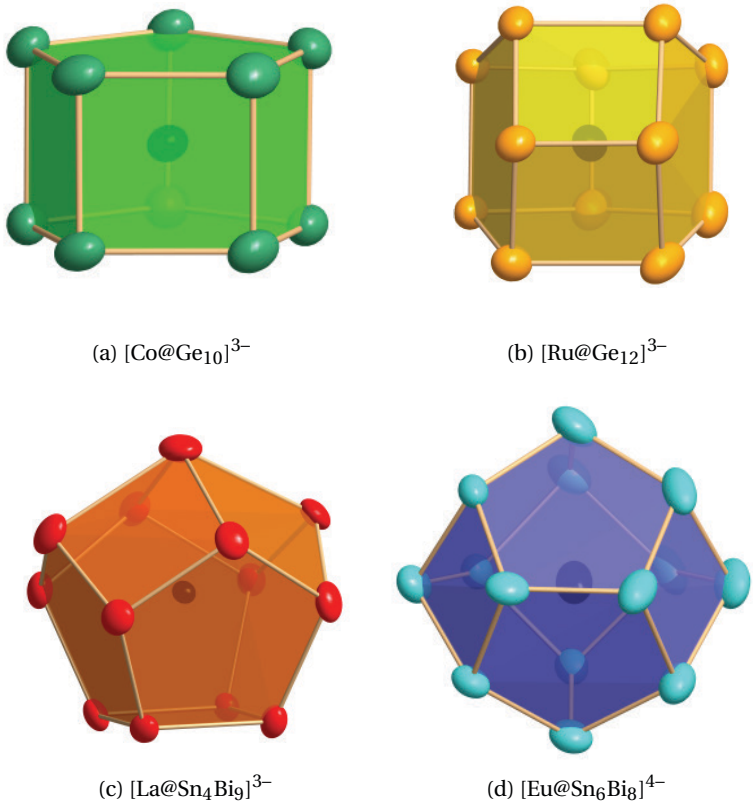

(a) $[Co@Ge_{10}]^{3-}$ (b) $[Ru@Ge_{12}]^{3-}$

(c) $[La@Sn_4Bi_9]^{3-}$ (d) $[Eu@Sn_6Bi_8]^{4-}$

Figure 1.13: Structures of selected non-deltahedral clusters

in-between electron-deficiency and electron-precision. However, the transformation from deltahedral to non-deltahedral clusters is exclusively one between all electron-precise clusters: a tetrahedral, electron-precise precursors like $(Sn_2Bi_2)^{2-}$ (20 valence electrons, all atoms are (pseudo) E^{15} elements) is reacted with a metal-organic reagent to give a larger non-deltahedral, electron-precise cluster. $[Eu@Sn_6Bi_8]^{3-}$ is a 14-vertex cluster, with 21 bonding interactions in its cluster framework. It is the product of the electron-precise tetrahedral $(Sn_2Bi_2)^{2-}$ Zintl anion with $[(C_5Me_4H)_3Eu]$. The cluster has 70 valence electrons overall. This cluster has 42 electrons available for skeletal bonding in its 21 bond framework. Therefore this cluster is electron-precise and forms a $(Sn_6Bi_8)^{6-}$ shell, which is counterbalanced from the inside with Eu^{3+} and from the outside by three sequestered K^+ cations. In the case of the multi-metallic cluster $[Ta@Ge_4As_8]^{3-}$, [80] there are 60 valence electrons present. It is derived from the reaction of $(Ge_2As_2)^{2-}$ with "Ta". The cluster has 36 skeletal electrons available for bonding in its 18 bond framework and is electron-precise, too. Its $(Ge_4As_8)^{8-}$ shell is compensated by V^{5+} from the inside and three sequestered K^+ cations from the outside.

The known transformations so far are not triggered by the compensation of electron-deficiency,

bur rather by the formation of new bonding interactions to generate a suitable cluster shell for the inner metal cation. The charge of the metal cation present may therefore support a certain species that evolves during complex cluster growing steps in solution, that leads to the crystallisation of the most stable species.

1.4.8 Superatoms and the Jellium Model

Upon evaluation of structure motifs calculated for boranes and post-transition metal clusters, it was found that post-transition metal clusters often possess other cluster topologies as energetic minima than the corresponding boranes. Ge_{11}^{2-} has a D_{3h} pentacapped trigonal prism as energy minimised structure, the corresponding borane $B_{11}H_{11}^{2-}$ a C_{2v} octadodecahedron. [99,100] This discrepancy can be explained by the involvement of electrons, that are disregarded in the Wade-Mingos rules as non-participating in the cluster bonding. In the PSEP theory (see Section 1.4.3 on page 23) these electrons are excluded because they are involved in ligand-bonding or belong to external lone pairs that cannot contribute to cluster bonding due to the symmetry of their orbitals. For post-transition metals, however, the exclusion as external lone pairs is not justified. The involvement of higher orbitals (d, f, g) causes a change in the electron count for closed-shell configurations due to the changed energetic order of the atomic orbitals. Classical noble gas configuration leads to closed-shell configuration for 2, 10, 18, 36, 54 and 86 cluster electrons. Under utilisation of the so-called *Jellium sphere* in free atoms the 1p and 1d levels are added between 1s and 2s. Between 2s and 3s the orbitals 1f, 2p, 1g and 2d are added. [101] This gives rise to the so called *magic numbers* in the Jellium model, which mark the new number of electrons needed for a close-shell configuration. This Jellium sphere can also be applied to cluster frameworks, giving rise to so-called superatoms. [102,103] In the context of this work the magic numbers 20 and 40 are of importance. White phosphorus P_4 and the tetrahedral Zintl anions E_4^{4-} (E = Si, Ge, Sn, Pb) both have 20 valence electrons species (as well as the binary E^{14}/E^{15}), all these Zintl anions have been found in Zintl phases as well as in solution. The Zintl anions In_{11}^{7-} and Ge_9^{4-} have 40 valence electrons; these species are found in Zintl phases as well as in solution. [101] Interestingly, E_5^{2-} and E_{10}^{2-} (E = Ge) Zintl anions, which have non-magic valence electron numbers, have not been reported as part of Zintl phases so far. The reason for this could be the lack of exceptional stability provided by a closed-shell configuration, as described by the Jellium model. The Jellium model can help to understand differences that arise for certain electron numbers and is helpful in addition to other models explained in this context.

1.5 Synthesis of Homo-Atomic Zintl Anions and Hetero-Atomic Clusters

In recent decades, the search for new Zintl anions and multi-metallic clusters has become an important field of modern inorganic chemistry. In particular, the chemistry of clusters of the tetrel elements received wide recognition after the synthesis of a novel meso-structured modification of germanium by Kanatzidis *et al.*[104] utilising Ge^{4-} and a hexagonal modification using a Ge_9^{2-}-polymer by Tolbert *et al.*[105]. A porous clartrate-II structure of Ge was also recently discovered.[106] Great success in the functionalisation of Zintl clusters has also been be achieved using Ge_9^{4-} as precursor (see also Section 1.6 on page 32).[94] Therefore this section will focus on the chemistry of and around E^{14} elements. A complete list of the Zintl anions available by solid state reactions and reactions in solution can be found in Table 1.2 on page 7.

1.5.1 Synthesis of Homo-Atomic Cluster Anions

Silicon

The synthesis of Si-based Zintl anions in solution relies heavily on the use of liquid ammonia as solvent. To date, all reported synthesis methods use liquid ammonia to extract Si-based Zintl anions from the solid phase, later steps are reported to involve pyridine as solvent. The tetrahedral Zintl anion Si_4^{4-} has not been crystallized from solution, but is accessible in solid state reactions that yielded the phases NaSi, KSi, RbSi, CsSi and $BaSi_2$.[94] Si_5^{2-} has only been synthesised in solution as $[K(crypt\text{-}222)]^+$ salts in liquid ammonia.[107] The cluster Si_9^{2-} was synthesised from $K_{12}Si_{17}$ upon reaction with Ph_3GeCl, Me_3SnCl or *t*-BuCl.[108] Si_9^{3-} was found to be a side product of the reaction that gives Si_5^{2-} and is also only available from solution based chemistry.[107] Si_9^{4-} can be synthesised in solution from extraction of $A_{12}Si_{17}$ (A = K, Rb, Cs) in liquid ammonia.[91,94,109]

Germanium

In contrast to silicon, Zintl anions of germanium can be synthesised at ambient temperatures and do not exclusively rely on liquid ammonia as solvent. Here *en* is frequently used as solvent for the extraction of solid phases. Like for Si, the tetrahedral species Ge_4^{4-} has not been crystallized from solution based chemistry, yet, but is accessible in the solid phase from the phases NaGe, KGe, RbGe, CsGe, $SrGe_2$, $BaGe_2$ and $Na_2Cs_2Ge_4$.[94] Ge_5^{2-} can be synthesised in solution from the extraction of the phase $KGe_{1.67}$ in *en*, thf and liquid ammonia.[110,111] Ge_9^{2-}

was synthesised only alongside Ge_9^{4-}.[112] The linking of Ge_9 species will be discussed at a later point (see Section 1.6.3 on page 35). The paramagnetic species Ge_9^{3-} is obtained by extraction of the phases $KGe_{2.25}$ and $RbGe_{2.25}$. Ge_9^{4-} is available from solid phases and in solution upon extraction of the solid phases A_4Ge_9 (A = K, Rb, Cs).[94] The pristine *closo*-Ge_{10}^{2-} anion was synthesised only recently by Fässler *et al.* from Rb_4Ge_9 and 7-amino-1-trimethylsilyl-5-aza-hepta-3-en-1-yne.[113]

Tin

The Zintl anions Sn_4^{4-}, Sn_5^{2-}, Sn_9^{3-} and Sn_9^{4-} are known. They can be synthesised in the case of Sn_4^{4-} and Sn_9^{4-} directly in the solid state and upon extraction of these phases in *en* and liquid ammonia.[94] Sn_5^{2-}[114] and Sn_9^{3-}[115] can be synthesised using the same pathway as for Ge_5^{2-} and Ge_9^{3-}.

Lead

As for all previously discussed elements, only the tetrahedral and 9-vertex species Pb_4^{4-} and Pb_9^{4-} can be obtained in the solid state and in solution.[94] Pb_5^{2-}[114] and Pb_9^{3-}[116] are obtained by similar pathways as for their related Ge species. Pb_{10}^{2-}[117] is obtained by oxidation of Pb_9^{4-} with $[(C_6H_5)P_3]AuCl$ in en.

1.5.2 Hetero-Atomic Cluster Anions

In principle, the synthesis of binary Zintl anions or hetero-atomic cluster anions does not differ from the synthesis of their homo-atomic analogies. They are obtained from extraction of a solid phase in *en* or liquid ammonia, which is in most cases not known by structure, and therefore better described as solid mixtures then a solid phase. Unsurprisingly, in this case ternary mixtures instead of binary phases are used for extraction. They are obtained obtained upon heating a ternary mixture of the elements in a sealed niobium or tantalum ampoule at temperatures that normally exceed 650 °C. Alternatively, the ternary precursors can be synthesised by heating the mixture in a silica glass ampoule in an oven or with a oxygen torch, or in an open crucible under inert gas flow. The resulting mixtures are stored under inert conditions. To date, the number of binary hetero-atomic cluster anions is not as extensive in comparison to the number of known compounds involving homo-atomic cluster anions. However, there is still room as several element combinations have not been synthesised so far. Only seven binary tetrahedral hetero-atomic Zintl anions were characterised upon crystallisation from the extraction of ternary mixtures.[94]

E^{13}/E^{14}	E^{13}/E^{15}	E^{14}/E^{15}
$(P_7Tl)^{2-}$	$(InBi_3)^{2-}$	$(Ge_2As_2)^{2-}$
$(As_7Tl)^{2-}$	$(GaBi_3]^{2-}$	$(Sn_2Sb_2)^{2-}$
$(P_{14}In)^{3-}$	$(In_4Bi_5)^{3-}$	$(Sn_2Bi_2)^{2-}$
		$(Pb_2Sb_2)^{2-}$
		$(Pb_2Bi_2)^{2-}$
		$(Sn_4Bi_4)^{4-}$
		$(Ge_7Sb_2)^{2-}$
		$(Sn_3Sb_4)^{6-}$
		$(Sn_7Bi_2)^{2-}$
		$(Pb_7Bi_2)^{2-}$
		$(Bi_5Sn_3)^{3-}$
		$(Ge_{16}Bi_2)^{4-}$
		$(Ge_{18}In)^{5-}$
		$(P_{15}Sn)^{3-}$
		$(P_{15}Pb)^{3-}$
		$(As_{14}Sn)^{4-}$

Table 1.9: List of binary E^{13}/E^{14}, E^{13}/E^{15} and E^{14}/E^{15} Zintl anions

In Table 1.9 the binary Zintl anions are sorted according to their classification as binary E^{13}/E^{14}, E^{13}/E^{15} and E^{14}/E^{15} cluster anions. Reactions involving binary precursors with (metal-)organic compounds are discussed in Section 1.6 on the following page. To date no Zintl phase containing these binary Zintl anions has been isolated. All reports show that they were obtained upon crystallisation from solution. Therefore it is still unknown if binary precursors can form upon extraction or are present in the solid phase at all. Only for the system K/Sn/Sb was it proven that the solid phase K_2SnSb_2 does not contain the $(Sn_2Sb_2)^{2-}$ anion. [69]

1.6 Paths to Hetero-Atomic Cluster Anions

In this section selected pathways to yield multi-metallic cluster anions are discussed. Clusters only protected by a shielding inert ligand shell, multi-metallic clusters in the gas phase and cluster cations in general will not be discussed here.
Three major cluster modifications are described in the following sections. Upon building larger clusters, the inner volume of the poly-atomic or poly-metallic framework passes a critical mark, after which it is enabled to harbour interstitial atoms and thereby form endohedral cluster anions. Reported results indicate that for a closed cluster framework the critical mark is passed with nine atoms atoms, with the 10-vertex cluster anion $[Fe@Ge_{10}]^{3-}$ being the smallest cluster to possess an endohedral metal cation.[118] Several reports have been published for larger cluster frameworks with 12, 13 and 14 vertices: $[Ru@Ge_{12}]^{3-}$ [96] (12 vertices), $[La@Sn_4Bi_9]^{3-}$ [97] (13 vertices) and $[Eu@Sn_6Bi_8]^{4-}$ [98] (14 vertices). See Section 1.6.1 for details. Another way to functionalise cluster anions is to attach (metal-)organic groups. Several interesting results have been reported, utilising Ph_2Zn and metal carbonyls among many other reagents (see Section 1.6.2 on the facing page). Also, cluster anions have been reported to form dimers as well as oligomeric and polymeric chains. This can be achieved by direct cluster-cluster coupling, metal-mediated coupling and even organic linkers (see Section 1.6.3 on page 35). Furthermore cluster can be transformed by oxidation or reduction with (metal-)organic reagents, as this transformation might as well be considered part of other classifications mentioned in this section, it will not be discussed separately here.

1.6.1 Incorporating Metal Atoms

Precursors like phosphine-stabilised metal halides and transition metal Cp-complexes are utilised to form endohedral multi-metallic clusters. In en, $[(C_5Me_4H)_3U]$ releases its $(C_5Me_4H)^-$ ligands in the presence of Bi_4^{2-} (formed in situ from $(GaBi_3)^{2-}$).[119] The ligands in here are replaced by three Bi_4 rings, resulting in a paramagnetic $[U@Bi_{12}]^{3-}$ cluster. The resulting cluster is therefore formally comprised of one U^{4+} cation surrounded by a radical Bi_{12}^{7-} shell. $[Ge_9Ni_2(PPh_3)]^{2-}$, in which one Ni atom is placed in the cluster centre, is synthesised from $[Ni(CO)_2(PPh_3)_2]$ and Ge_9^{4-} in en.[120] Upon reaction of $(Sn_2Bi_2)^{2-}$ with $Pd(dppe)_2$ in en, $[Pd_3Sn_8Bi_6]^{4-}$ was obtained, which features a 14-vertex topology and an endohedral Pd_3 triangle (see Figure 1.15 on page 34).[121] The endohedral cluster anion $[Eu@Sn_6Bi_8]^{4-}$ is also derived from $(Sn_2Bi_2)^{2-}$, here after reaction with $[(C_5Me_4H)_3Eu]$. It is believed that two nortricyclane-type $(Sn_3Bi_4)^{6-}$ anions form as intermediate and rearrange to incorporate the Eu^{3+} cation.[98] For V, Nb and Ta the formation of an endohedral cluster is also achieved without the need for (metal-)organic precursors. The respective 12- and 14-vertex cluster

anions $[V@Ge_4As_8]^{3-}$, $[Nb@Ge_6As_8]^{3-}$, $[Ta@Ge_4As_8]^{3-}$ and $[Ta@Ge_6As_8]^{3-}$ are obtained from quaternary solid mixtures.[80,122] The $[Pd_3@Ge_9(Sn\mathit{i}Pr_3)_3]^{2-}$ anion completes a series of species in which one, two and three group 10 atoms are embedded in one or two conjunct Ge_9 moieties.[123] [Ni(cod)] is used as reagent to incorporate single Ni atoms into the Ge_9 cluster framework resulting in $[Ni@Ge_9]^{3-}$. For the incorporation of more than one endohedral transition metal atom, the Ge_9 cluster framework is too small, resulting in an condensation of two Ge_9 moieties to increase the inner volume. Without additional stabilisation by $[(\mathit{i}Pr)_3Sn]$, the reaction of $[Pd(PPh_3)_4]$ with Ge_9^{4-} results in $[Pd_2@Ge_{18}]^{4-}$ (see Figure 1.14).[124] Hence, the $[(\mathit{i}Pr)_3Sn]$ ligands do not only decorate the cluster, but they have a notable influence on the reaction mechanism and thus the product spectrum. The formation of the Pd_3 unit is not understood so far, but seems to be a preferred arrangement of transition metal atoms in multi-metallic cluster anions. In $[Pd_2@Ge_{18}]^{4-}$ a Pd_2 dumbbell is incorporated between two Ge_9 half cups.

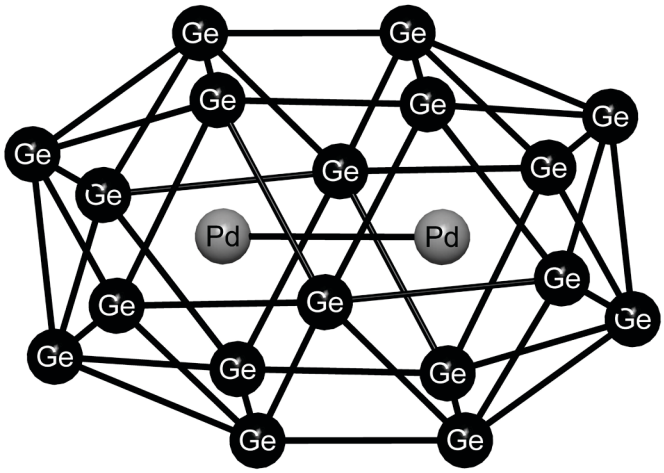

Figure 1.14: Structure of the $[Pd_2@Ge_{18}]^{4-}$ cluster anion

1.6.2 Attaching Functional Groups

Atoms can also be attached to pre-formed cluster anions in solution. This is due to the expected reduction of the cluster charge upon reaction with a (metal-)organic precursor. Sn_9^{4-} is reported to replace one NH_3 ligand from $[TiCp_2(NH_3)_2]^+$ in liquid ammonia to form the anionic complex $[TiCp_2(Sn_9)(NH_3)]^{3-}$. The Ti atom binds to one of the Sn atoms of the cluster only.[125] In DMF or liquid ammonia, the easily accessible Ge_9^{4-} anions can also exchange with a labile Cl^- ligand from phosphane-stabilised coinage metal halides[126] and various chlorosilanes.[127] By adding chlorotrimethylsilane, Ge_9^{4-} clusters can be silylated to yield di-silylated di-anionic[127] (see Figure 1.16 on the following page) and tri-silylated mono-anionic

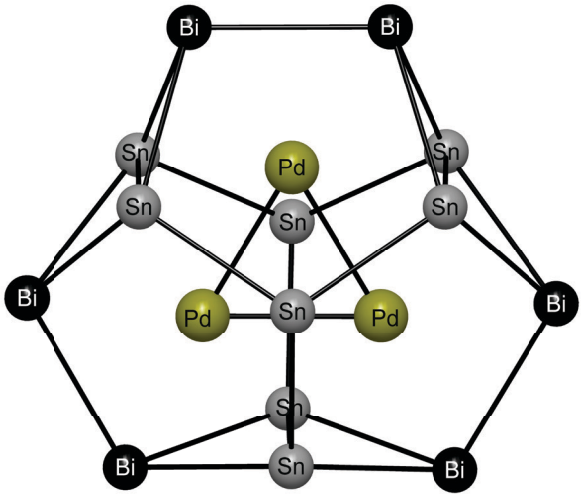

Figure 1.15: Structure of the $[Pd_3@Sn_8Bi_6]^{4-}$ cluster anion

clusters.[7] They are proven to be excellent starting materials for subsequent reactions with phosphane-stabilised metal halides and metal NHC complexes.[120,128,129] The reactivity of the silylated cages decreases, as one would expect, with the size of the silyl-groups, making this parameter a tunable property in the directed synthesis of multi-metallic clusters. The resulting clusters show different bonding modes depending on their ligands: Cu-NHC complexes retain their NHC ligand, resulting in a capping of the Ge_9 cage on one triangular face,[12] whereas phosphine-stabilised metal halides yielded more complex structures, that even involve a transformation of the complete cluster framework.[130] These were shown to reach from simple capping processes to the dimerisation of metal-capped fragments (see Section 1.6.3 on the next page). After silylation of the Ge_9^{4-} precursor and reaction with EtBr, a charge neutral, tetra-substituted cluster bearing an additional ethyl group is reported.[7]

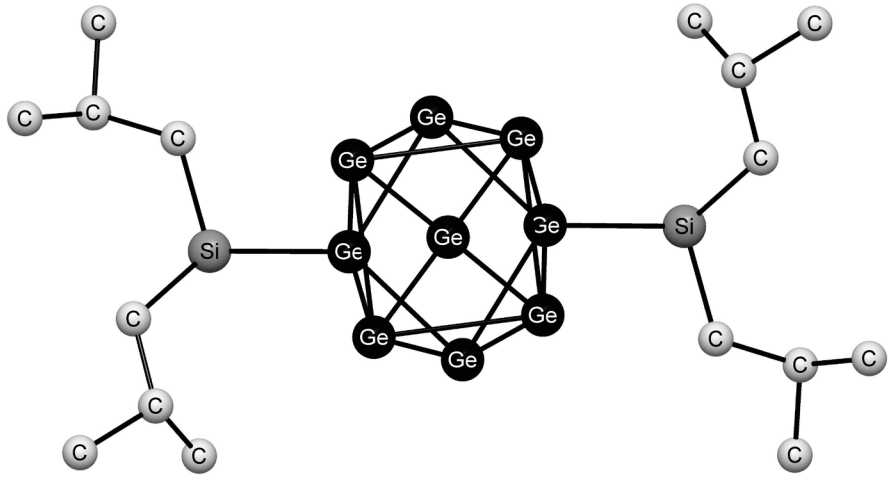

Figure 1.16: Structure of the twice silylated cluster anion $[Ge_9[Si(i\text{Bu})_3]_2]^{2-}$

1.6.3 Connecting Cluster Anions

Cluster moieties are also reported to build dimeric, trimeric, tetrameric and polymeric assemblies.[131] So far this is exclusively reported for Zintl anions of germanium. Cluster moieties can be connected by direct Ge–Ge bonds to yield $(Ge_9–Ge_9)^{6–}$ dimers,[31] $(Ge_9–Ge_9–Ge_9)^{6–}$ trimers[32] (here the outer two moieties are bound with two 2c2e bonds to the central Ge_9 unit, which in here is formally neutral, see also Figure 1.17) and a tetrameric structure[33] (see also Section 1.3 on page 6). Guloy *et al.* furthermore reported a $^{1}_{\infty}[Ge_9]^{2–}$ polymer upon oxidation of $Ge_9^{4–}$ (see Figure 1.2 on page 5).[34] The link can also be mediated by metal atoms and organic groups. Fässler *et al.* reported a polymeric structure of $^{1}_{\infty}[HgGe_9]^{2–}$ from the reaction of $Ge_9^{4–}$ with elemental mercury.[132] This is also achieved with Zn to form a trimeric chain.[133] Also, organic linkers like 1,4-bis(trimethylsilyl)butadiyne can be used to connect Ge_9 units.[134] Gold atoms were successfully employed to connect two Ge_9 units without structural changes to the cluster core: The reaction of $Ge_9^{4–}$ anions with $[Au(PPh_3)Cl]$ yielded a salt comprising $[Ge_{18}Au_3]^{5–}$ anions.[128] Here Ge_9 cage undergo a one–electron oxidation per Au atom added to the ensemble, hence reducing the overall charge of the cluster anion to 5–. Aurophilic interactions exist within the triangle that connects symmetrically in an eclipsed manner to two faces of the deltahedral Ge_9 clusters.

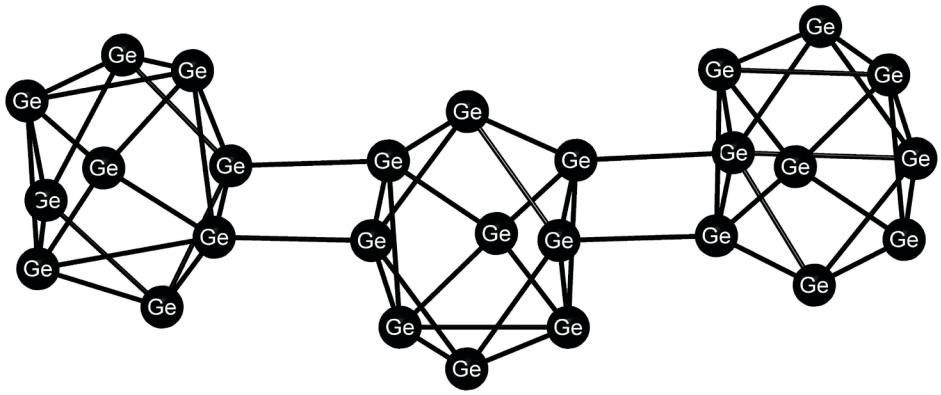

Figure 1.17: Structure of the trimeric $(Ge_9–Ge_9–Ge_9)^{6–}$ cluster anion

2 Motivation

The aim of this work is to synthesise novel binary Zintl anions of the tetrel and pentel elements with special focus on germanium and, upon the successful implementation of their synthesis, to explore the reactivity of these compounds towards (metal)organic reagents. As part of a binational cooperation the synthesis of the clusters was to be conducted in Marburg, whereas derivatisation reactions were to be performed at The University of Western Ontario, Canada. The previous research in the Dehnen group for the heavier E^{14}/E^{15} element combinations was meant to provide the foundation upon which new synthesis pathways for Zintl anions were to be developed. Prior to this project, the synthesis of the binary E^{14}/E^{15} Zintl anions $(Sn_2Sb_2)^{2-}$, $(Sn_2Bi_2)^{2-}$, $(Pb_2Sb_2)^{2-}$ and $(Pb_2Sb_2)^{2-}$ had been established. [69,71,135,136]

For the lighter tetrel elements Si and Ge as well as for the lighter pentel elements P and As only homo-atomic Zintl anions had been reported so far. [94] In contrast to the heavier binary Zintl anions, no ternary phases of alkali or alkaline earth metals with lighter E^{14} and E^{15} elements had been reported in the literature, with K_2GeAs_2 [137] being the only exception. For the elemental combination A/Ge/P (A = alkali or alkaline earth metal) no phase has been reported to date. This might be due to the less metallic character of germanium versus tin and lead and its much higher melting point (Ge 937 °C; Sn 232 °C, Pb 325 °C).

The most basic work for this project was to establish a synthetic route to stoichiometrically well balanced solid mixtures or a defined ternary phase. Subsequently, the extraction of the solid with ethylene diamine and liquid ammonia, which are both classical solvents in the context of Zintl anion chemistry should give birth to the first binary Zintl anions of lighter E^{14}/E^{15} elements. By utilisation of crown ethers and cryptands (e.g. 18-c-6 and crypt-222) and suitable counter-solvents, the extracted binary Zintl anions were to be crystallized and the obtained crystals to be analyzed by means of SCXD, ESI-MS, EDX and NMR (if applicable).

With this milestone being reached, a comprehensive study of reactivity against (metal)organic reagents was to be started. Previously reported derivatisations of homo-atomic and hetero-

atomic Zintl anions should be systematically tried on the novel binary compounds in order to develop a chemistry around them. The basic idea behind this approach is the pseudo-

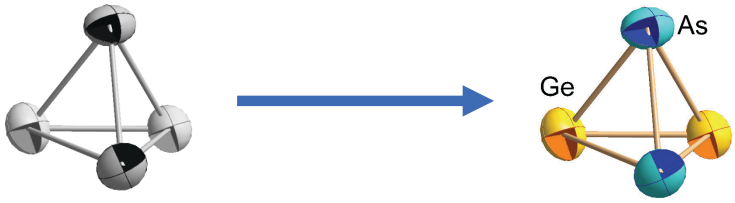

Figure 2.1: Charge reduction by binary precursors, Ge_4^{4-} to $(Ge_2As_2)^{2-}$

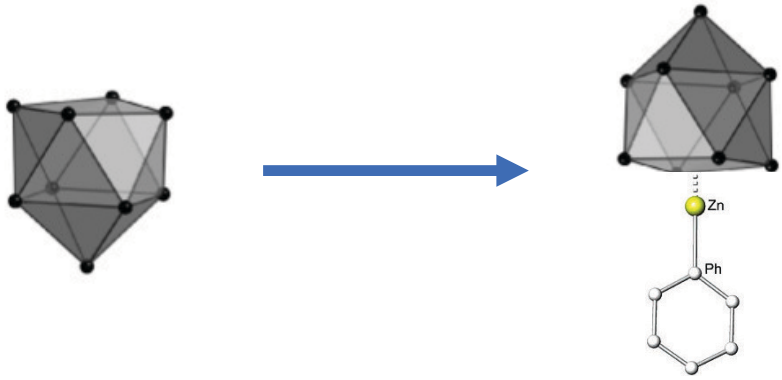

Figure 2.2: Charge reduction by metal-organic ligands

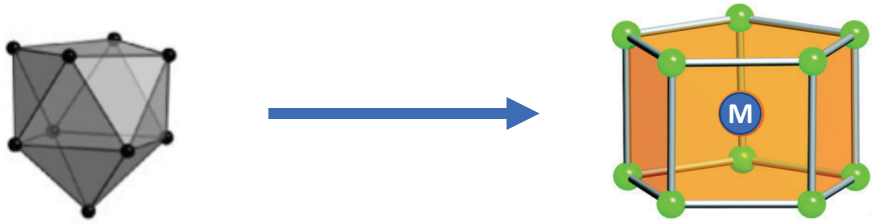

Figure 2.3: Charge reduction by formation of endohedral cluster anions

element concept by Klemm.[57] For the elements employed in this context, germanium can be reduced by an alkali metal to give "Ge^-", a species iso-valence-electronic to phosphorus. So, by moving from homo-atomic to hetero-atomic precursors the valence-electronic situation can be maintained and the cluster charge reduced simultaneously. Most of the so far developed Zintl chemistry is based on polyanionic homo-atomic species.

Employing binary instead of homo-atomic precursors is a suitable way to reduce the charge of the Zintl anion, as mentioned previously (see also Figure 2.1). In terms of Ge_4^{4-} the involvement of a group 15 element like P or As formally leads to the binary anions $(Ge_3P)^{3-}$,

$(Ge_2P_2)^{2-}$ and $(GeP_3)^-$ for phosphorus and $(Ge_3As)^{3-}$, $(Ge_2As_2)^{2-}$ and $(GeAs_3)^-$ for arsenic. Pathways to the synthesis of these compounds were to be explored as part of this work and depending upon their successful synthesis the reactivity towards (metal)organic compounds to be investigated.

The addition of a (metal)organic group itself may also be a way to reduce the charge of one species (see Figure 2.2). Homo-atomic precursors need several substituents bound to the cluster framework in order to reduce the compound's charge. In theory, a binary precursor may lead to equally functionalised, but less charged compounds, with a single-step synthesis. Hindermost, literature also reports the incorporation of metal cations into the centre of cluster anions, thereby forming endohedral clusters (see Figure 2.3). If applicable, this transformations were also to be employed for this project.

The following cumulative part will give a complete insight of the progress made in this project by re-printing published and submitted manuscripts.

3 Cumulative Part

3.1 $[V@Ge_8As_4]^{3-}$ & $[Nb@Ge_8As_6]^{3-}$: Encapsulation of Electron-poor Transition Metal Atoms

This article was published in Chem. Commun., 2015, **51**, 3866–3869.

The $[K(crypt\text{-}222)]^+$ salts of $[V@Ge_8As_4]^{3-}$ and $[Nb@Ge_8As_6]^{3-}$ were obtained by extraction of quaternary phases with *en*/crypt-222. The $[V@Ge_8As_4]^{3-}$ anion is the first Zintl anion incorporating a (formal) V^{5+} cation, thus the smallest cation ever embedded within a main group (semi-)metal cage. It represents the second example of a novel 12-vertex cluster architecture. The bonding situation was elucidated by quantum chemistry, also allowing for a precise assignment of Ge vs. As atoms, being indistinguishable by means of X-ray diffraction.

S. Mitzinger conceived and performed the synthesis, performed the characterisation and interpreted the analytical data. W. Massa was consulted for crystallographic advice and completed solution of the crystal structures. L. Broekaert and F. Weigend performed quantum chemical calculations. All authors co-wrote the manuscript.

Diese Arbeit wurde in der Zeitschrift Chem. Commun., 2015, **51**, 3866–3869 veröffentlicht.

Es wurden die $[K(crypt\text{-}222)]^+$-Salze der Clusteranionen $[V@Ge_8As_4]^{3-}$ und $[Nb@Ge_8As_6]^{3-}$ durch die Extraktion einer quaternären festen Mischung erhalten. Das $[V@Ge_8As_4]^{3-}$ Clusteranion ist die erste Zintl-Spezies, die ein formal fünffach positiv geladenes V-Kation enthält, damit ist es das kleinste jemals in Hauptgruppen-Metallcluster eingeführte Kation. Zudem ist diese Verbindung erst die zweite, welche eine neuartige 12-Vertex Cluster-Topologie aufweist. Die Bindungssituation wurde mit Hilfe quantenchemischer Methoden untersucht und erlaubte die definitive Zuordnung von Ge- und As-Atomen auf Positionen im Clustergerüst, welche durch Methoden der Röntgenbeugung nicht voneinander unterschieden werden können.

S. Mitzinger erdachte die Synthese und führte das Experiment sowie die Charakterisierung und die Interpretation der analytischen Daten durch. W. Massa wurde für die Vervollständigung der Lösung der kristallographischen Datensätze hinzugezogen und führte diese durch. L. Broekaert und F. Weigend führen die quantenchemischen Rechnungen und deren Auswertung durch. Alle Autoren haben das Manuskript gemeinsam verfasst.

ChemComm

COMMUNICATION

View Article Online
View Journal | View Issue

$[V@Ge_8As_4]^{3-}$ and $[Nb@Ge_8As_6]^{3-}$: encapsulation of electron-poor transition metal atoms†

Stefan Mitzinger,[a] Lies Broeckaert,[ac] Werner Massa,[a] Florian Weigend*[bc] and Stefanie Dehnen*[a]

Cite this: *Chem. Commun.*, 2015, 51, 3866

Received 17th December 2014,
Accepted 28th January 2015

DOI: 10.1039/c4cc10086g

www.rsc.org/chemcomm

$[K([2.2.2]crypt)]^+$ salts of $[V@Ge_8As_4]^{3-}$ and $[Nb@Ge_8As_6]^{3-}$ were obtained by extraction of quaternary phases with en/[2.2.2]crypt. The V–Ge–As anion is the first Zintl anion incorporating a (formal) V^{5+} cation, thus the smallest cation ever embedded within a main group (semi-)metal cage. It represents the second example of a novel 12-vertex cluster architecture. The bonding situation was elucidated by quantum chemistry, also allowing for a precise assignment of Ge *vs.* As atoms, being indistinguishable by X-ray diffraction.

The research on endohedral clusters, which comprise homo- or heteroatomic main group (semi-)metal cages with interstitial transition metal atoms, is a rapidly advancing field of modern inorganic, materials and theoretical chemistry.[1] This is not only triggered by the beauty of the resulting structures but also by the chemical and physical properties of the compounds that can be viewed as transition metal-doped main group (semi-)metal clusters, thus molecular models to doped (semi-)metals.[2]

Recent discoveries include clusters that form non-classical, non-deltahedral polyanions with group 14 element atoms[3] unexpectedly, since all known classical molecular Zintl anions of group 14 elements are electron deficient and form multicenter-bonded deltahedra. This clearly indicated a great impact of the interstitial atom on the electronic and structural properties of such molecules. The latest addition to this field has been the report on a new non-deltahedral 12-vertex cluster topology by Goicoechea *et al.*,[4] which was observed for a paramagnetic cluster $[Ru@Ge_{12}]^{3-}$ and could be shown to be more stable in this system than any further isomeric geometries, such as an icosahedron.

However, most endohedral clusters published to date are based on the inclusion of electron-rich transition metal atoms – most often in a d^{10} electronic configuration. Exclusions have been species with interstitial lanthanide ions,[2a,3c,d,5] $[Cp_5Ti_4Sn_{15}]$,[6a] and species detected *via* mass spectrometry, like $[V@Si_{16}]^+$.[6b] Combining two different main group elements within the cluster shell recently opened up a new direction, as the systems are free to adjust their charge by isolobal substitution of formal $(E^{14})^{2-}$ or $(E^{14})^-$ by $(E^{15})^{\pm0}$. This way, many new topologies have been observed that were not accessible with only one of the main group elements involved.[7]

In the present case, formal Ge^- besides As atoms served to compensate for the high charge of an interstitial group 5 metal ion M^{5+}, forming the first endohedral clusters comprising these extremely hard cations of electron-poor transition metals V and Nb. The resultant ternary clusters possess a −3 charge perfect for crystallization with $[K([2.2.2]crypt)]^+$ counterions.

The title compounds $[K([2.2.2]crypt)]_3[V@Ge_8As_4]\cdot2tol\cdot en$ (**1**, 12%) and $[K([2.2.2]crypt)]_3[Nb@Ge_8As_6]\cdot tol\cdot en$ (**2**, 22%) were obtained by extraction of solid mixtures K–Ge–As–V or K–Ge–As–Nb (with about 3 atom% of the group 5 metal according to EDX measurements) with ethane-1,2-diamine (en)/[2.2.2]crypt; the quoted solids were obtained by fusing equimolar amounts of K, Ge and As with about 0.1 equivalents of V in a silica glass ampoule, or by simply fusing K, Ge, and As in an Nb ampoule, respectively. After 3d at room temperature, the extracts were filtered and layered with toluene. The corresponding extraction of the ampoule material was previously observed for the only further known Nb-containing intermetallic complex within $[Rb([2.2.2]crypt)]_2\{Rb[NbAs_8]\}$.[8]

According to X-ray structure analyses,‡ both cluster anions exhibit non-deltahedral topologies (Fig. 1). The one observed in **1** accords with the novel 12-vertex topology of $[Ru@Ge_{12}]^{3-}$,[4] and the anion in **2** possesses the 14-vertex cage that has so far only been observed with interstitial lanthanide cations.[3]

The persistence of the cluster anions in the two compounds in solution and the gas phase was confirmed by ESI mass-spectrometry

[a] *Philipps-Universität Marburg, Fachbereich Chemie and Wissenschaftliches Zentrum für Materialwissenschaften (WZMW), Hans-Meerwein-Straße 4, 35043 Marburg, Germany. E-mail: dehnen@chemie.uni-marburg.de; Fax: +49 6421 2825653; Tel: +49 6421 2825751*

[b] *Institut für Nanotechnologie, Karlsruher Institut für Technologie (KIT), Hermann-von-Helmholtz-Platz 1, 76344 Eggenstein-Leopoldshafen, Germany*

[c] *Institut für Physikalische Chemie, Karlsruher Institut für Technologie (KIT), Fritz-Haber-Weg 2, 76131 Karlsruhe, Germany*

† Electronic supplementary information (ESI) available: Details of syntheses, X-ray crystallography (SCXRD and PXRD), energy dispersive X-ray spectroscopy (EDX), electrospray ionization mass spectrometry (ESI-MS), and DFT calculations. CCDC 1030791 and 1030792. For ESI and crystallographic data in CIF or other electronic format see DOI: 10.1039/c4cc10086g

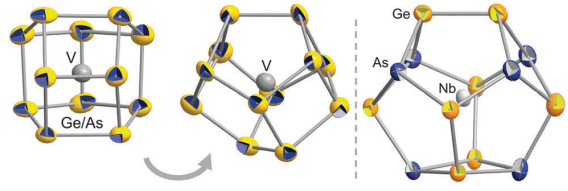

Fig. 1 Structures of the cluster anions $[V@Ge_8As_4]^{3-}$ (two views, left and center) and $[Nb@Ge_8As_6]^{3-}$ (right). Ellipsoids shown with 50% probability. Atomic distribution of Ge–As atoms in **2** as determined by perturbation theory calculations.[9]

on a fresh DMF–en solution (Fig. 2); the spectra further indicate that a complex mixture of species coexists (see ESI†), which explains the relatively low yields of **1** and **2**.

Perturbation theory treatment[9] based on DFT calculations[10,11] served to find the energetically most favorable distribution of atoms in the cluster anion in **2**, which is by $\geq$11 kJ mol^{-1} energetically preferred to other distributions (see ESI†). The result was used for the refinement of the atomic positions in **2** shown in Fig. 1, leading to mean interatomic distances of 2.4965 Å (Ge–As), 2.5011 Å (Ge–Ge), 2.8562 Å (Nb–As), and 2.9654 Å (Nb–Ge).

The $[V@Ge_8As_4]^{3-}$ anion in **1** is disordered over three orientations (82.6%, 9.0%, 8.4%) in the crystal. Additionally, calculations show that several preferable isomers are very close in energy (nine within 4.6 kJ mol^{-1}; see ESI†). Thus, all main group atom positions were refined with a mixed Ge : As occupation

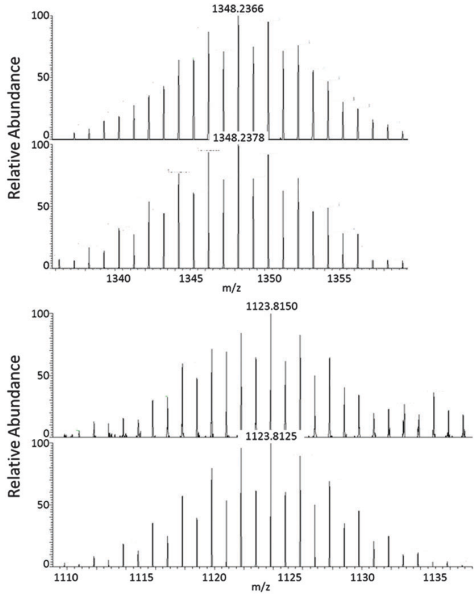

Fig. 2 ESI-MS(–) spectra (measured: top *versus* calculated: bottom) of $[K([2.2.2]crypt)][V@Ge_8As_4]^-$ (m/z = 1348.23; top) and $[Nb@Ge_8As_6]^-$ (m/z = 1123.81; bottom). The isotopic patterns are well reproduced by simulations, and all measured m/z values agree with the simulated ones within deviations of less than 0.003 m/z. The mass peaks are partially overlaid by mass peaks of further fragments, some of which could be assigned to other anions. The corresponding data are provided in the ESI.†

(0.67 : 0.33; mean distances (Ge–As)–(Ge–As) 2.515–2.521 Å, mean distances V–(Ge–As) 2.719–2.728 Å within the three orientations), and thermal ellipsoids are given as mixed sites in Fig. 1.

Both anion topologies are highly related: the two Ge–As cages differ only by two atoms, which complete a four-ring in **2** that replaces a two-atom unit in the anion in **1**. The close structural relationship might be a hint to both the stepwise formation of such clusters and the ability to adopt a certain cage size in accordance with the size of the interstitial metal atom.

Regarding the sizes of the involved metal atoms in the anions of **1** and **2** as well as in related intermetalloid clusters,[12] it seems plausible to find similar structures for elemental combinations with similar relative atomic sizes, such as for Nb–Ge–As *versus* Ln–Pb–Bi. However, the structural analogy found for V–Ge–As and Ru–Ge is not intuitive, as the Ru atom was reported to be a formal "Ru^{2-}" (d^{10} configuration, an atomic radius of Ru: 130 pm), thus being anionic in nature and much larger than formal V^{5+} (68 pm).

Inspired by this apparent contradiction, the electronic situation within the cluster anions in **1** and **2** was compared with the situation found at different elemental compositions by means of quantum chemistry.[10,11] For a better understanding of the rather new 12-vertex clusters, the calculations on hypothetical $[Rh@Ge_{12}]^{3-}$ and the diamagnetic analog to $[Ru@Ge_{12}]^{3-}$ were included.[4]

For both the (empty) 12-atom and 14-atom cluster shells, each atom is bonded to three neighbors. For electron precision, five electrons are thus required per atom, three for the bonds and two for the lone pair, which are necessary for the angular local geometry. This results in a 60 (70) electron system for the 12-atom (14-atom) shell, and can be realized, for instance, by 12 (14) Ge^- or As atoms in $[Ge_nAs_{N-n}]^{n-}$, N = 12, 14 and n = 0, 1, ... N. Electron precision, that is the presence of solely two-electron-two-center bonds and lone pairs, corresponds to the result of localization procedures carried out for the orbitals resulting from DFT calculations. These yield localized molecular orbitals (LMOs) that are centered to more than 97% at either one or two atoms.[13] If n is larger than the total charge q of an intermetalloid cluster anion $[M@Ge_nAs_{N-n}]^{q-}$, electron precision is achieved upon consideration of a maximum formal charge g at the interstitial transition metal atom from group g ($g = n - q$).

$[Nb@Ge_8As_6]^{3-}$ ($n - q = g = 5$) thus would be most likely described as a (formally) fivefold charged metal ion in an electron-perfect shell of group 15 or pseudo-group 15 elements. Calculated LMOs (Fig. 3a–d) support this, at least as a rough approximation: they are dominantly located at one or two atoms of the cage, but of course show (Mulliken[14]) contributions from the central atom. For LMOs representing lone pairs, these contributions amount to 5–8% (Fig. 3a and b), and for the Ge–As bonds to 5–12%. For the Ge–Ge bonds they are higher, 13–22% for the Ge–Ge bond perpendicular to the two nearly parallel ones with 22% Nb contribution (Fig. 3d). Clearly, the actual charge of the central atom – as far as it can be defined at all – is thus much smaller, but the formal charge of +5 is still justified as all LMOs are dominated by cage contributions.

This also holds for the 12-atom-cage cluster $[V@Ge_8As_4]^{3-}$, analyzed at its most stable As : Ge atomic distribution (Fig. 3e–h). The respective numbers of the contribution of the V atom are

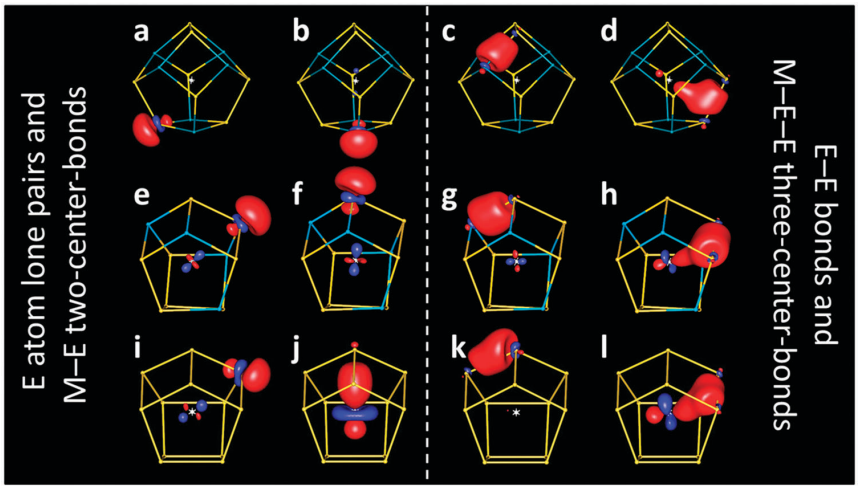

Fig. 3 Representative localized molecular orbitals for calculated clusters $[Nb@Ge_8As_6]^{3-}$ (top, a–d), $[V@Ge_8As_4]^{3-}$ (center, e–h) and $[Rh@Ge_{12}]^{3-}$ (bottom, i–l). For each type of LMOs, those with the lowest (a, e, i, c, g, and k) or highest (b, f, j, d, h, and l) contribution of the central atom are shown, respectively.

3–5% for LMOs representing lone pairs, 3–14% for As–Ge bonds and 12–21% for Ge–Ge bonds. Still, also for these anions, a description of formal M^{5+} in an electron-precise shell of solely group 15 and pseudo-group 15 elements with bonds between all neighboring main group atoms, assisted by (or delocalized towards) the valence orbitals of the central metal atom, is still justified, at least as an approximation.

However, this is no longer the case for interstitial transition metal atoms of electron-richer groups, such as presently hypothetical $[Rh@Ge_{12}]^{3-}$ (as the diamagnetic analog of paramagnetic $[Ru@Ge_{12}]^{3-}$ with 59 electrons in sum). For the Rh analog (g = 9), the above description would require a formal oxidation state of 9+ ("Rh^{9+}"), which is not reasonable. Indeed, LMOs reveal a different picture than found for the group 3 or 5 metal atoms. Here, only eight Ge atoms possess lone pairs (Fig. 3i), while the four remaining Ge atoms (the only ones connecting two four-rings of the cluster shell; Fig. 3j) form a two-center bond with the Rh atom in the center instead, which is polarized towards the latter (Ge : Rh contributions of 1 : 2). Thus, in contrast to the above compounds, four of the LMOs are not dominated by cage contributions, but by the d orbital contributions of the central atom. Accordingly, the respective four Ge atoms cannot be regarded as pseudo-group 15 element atoms anymore. Concerning Ge–Ge bonds, each bond again corresponds to an LMO, as for the compounds discussed above, but the trend towards Ge–Ge–Rh three-center bonds is further enhanced for most of them (Rh contributions up to *ca.* 27%; Fig. 3l). In analogy to the discussion above, *i.e.* by neglecting the Rh contributions to the Ge–Ge bonds, the formal charge of Rh is +1 if the four two-center LMOs shown in Fig. 3j are fully assigned to Rh, or even +5 if these are interpreted as bonds between Rh and Ge.

We note in passing that assignment of the formal charge calculated from population analyses based on the total electron density yields negative formal charges for the central atom, both for Rh and Ru.[4]

In conclusion, it was shown that electron-poor V and Nb atoms can be accommodated within endohedral clusters $[V@Ge_8As_4]^{3-}$ and $[Nb@Ge_8As_6]^{3-}$, the first members of an M–Ge–As cluster family. These possess non-deltahedral topologies, described recently for much larger metal ions (La, Ce, Nd, Gd, Tm, and Ru) within cages of either larger main group metal atoms (Sn, Pb, and Bi), or only Ge atoms. In line with the pseudo-element concept ($Ge^- \triangleq As^0$), V is encapsulated as V^{5+}, making it the hardest cation ever embedded within endohedral Zintl anions. Experiments and complementary DFT calculations showed that (a) an ionic description of the bonding situation within intermetalloid clusters is appropriate for interstitial metal atoms up to group 3 (and Ln), and qualitatively also for formally higher charged and thus more polarizing metal ions, such as M^{5+} from group 5. (b) Embedding electron-rich interstitial metal atoms (such as from groups 8 or 9) qualitatively changes the bonding situation: the resulting system does no longer exhibit a classical (pseudo-)group 15, three-bonded situation. Thus, in spite of identical total electron numbers that cause identical overall structures, the bonding situations can exhibit distinct differences.

This work was supported by the Alexander von Humboldt Stiftung and the Friedrich Ebert Stiftung.

Notes and references

‡ CCDC 1030791 (**1**) and 1030792 (**2**). DFT calculations with Turbomole[10] GGA exchange–correlation functional BP86,[11a,b] def-SVP basis sets,[11c,d] and effective core potentials (ECPs) for Sn, Bi, Nb, Ru, Rh,[11e,f] and COSMO.[11g,h] Contours drawn at 0.1 a.u. using gOpenMol.[13c]

1 (*a*) S. Scharfe, F. Kraus, S. Stegmaier, A. Schier and T. F. Fässler, *Angew. Chem., Int. Ed.*, 2011, **50**, 3630; (*b*) T. F. Fässler, *Struct. Bonding*, 2011, **140**, 91; (*c*) S. C. Sevov and J. M. Goicoechea, *Organometallics*, 2006, **25**, 5678; (*d*) F. S. Kocak, P. Zevalij, Y.-F. Lam and B. W. Eichhorn, *Inorg. Chem.*, 2008, **47**, 3515; (*e*) M. Ruck, *Angew. Chem., Int. Ed.*, 2001, **40**, 1182.

2 (*a*) F. Lips, M. Hołyńska, R. Clérac, U. Linne, I. Schellenberg, R. Pöttgen, F. Weigend and S. Dehnen, *J. Am. Chem. Soc.*, 2012, **134**, 1181; (*b*) N. Korber, *Angew. Chem., Int. Ed.*, 2009, **48**, 3216.
3 (*a*) B. Zhou, M. S. Denning, D. L. Kays and J. M. Goicoechea, *J. Am. Chem. Soc.*, 2009, **131**, 2802; (*b*) J.-Q. Wang, S. Stegmaier and T. Fässler, *Angew. Chem., Int. Ed.*, 2009, **48**, 1998; (*c*) F. Lips, R. Clérac and S. Dehnen, *Angew. Chem., Int. Ed.*, 2011, **50**, 960; (*d*) R. Ababei, W. Massa, B. Weinert, P. Pollak, X. Xie, R. Clérac, F. Weigend and S. Dehnen, *Chem. – Eur. J.*, 2015, **1**, 386.
4 G. Espinoza-Quintero, J. C. A. Duckworth, W. K. Myers, J. E. McGrady and J. M. Goicoechea, *J. Am. Chem. Soc.*, 2014, **136**, 1210.
5 (*a*) B. Weinert, F. Weigend and S. Dehnen, *Chem. – Eur. J.*, 2012, **18**, 13589; (*b*) B. Weinert, F. Müller, K. Harms, R. Clérac and S. Dehnen, *Angew. Chem., Int. Ed.*, 2014, **53**, 11979.
6 (*a*) C. B. Benda, M. Waibel and T. F. Fässler, *Angew. Chem., Int. Ed.*, 2015, **2**, 522; (*b*) P. Claes, E. Janssens, V. T. Ngan, P. Gruene, J. T. Lyon, D. J. Harding, A. Fielicke, M. T. Nguyen and P. Lievens, *Phys. Rev. Lett.*, 2011, **107**, 173401.
7 (*a*) F. Lips and S. Dehnen, *Angew. Chem., Int. Ed.*, 2009, **48**, 6435; (*b*) F. Lips and S. Dehnen, *Angew. Chem., Int. Ed.*, 2011, **50**, 955; (*c*) F. Lips, R. Clérac and S. Dehnen, *J. Am. Chem. Soc.*, 2011, **133**, 14168; (*d*) R. Ababei, J. Heine, M. Hołyńska, G. Thiele, B. Weinert, X. Xie, F. Weigend and S. Dehnen, *Chem. Commun.*, 2012, **48**, 11295.
8 H. G. von Schnering, J. Wolf, D. Weber, R. Ramirez and T. Meyer, *Angew. Chem., Int. Ed.*, 1986, **25**, 353.
9 (*a*) F. Weigend, C. Schrodt and R. Ahlrichs, *J. Chem. Phys.*, 2004, **121**, 10380; (*b*) F. Weigend and C. Schrodt, *Chem. – Eur. J.*, 2005, **11**, 3559; (*c*) F. Weigend, *J. Chem. Phys.*, 2014, **141**, 134103.
10 TURBOMOLE Version 6.6, © TURBOMOLE GmbH 2014. TURBOMOLE is developed by the University of Karlsruhe and Forschungszentrum Karlsruhe 1989–2007, TURBOMOLE GmbH since 2007; available from http://www.turbomole.com.
11 (*a*) D. Becke, *Phys. Rev. A: At., Mol., Opt. Phys.*, 1988, **38**, 3098; (*b*) J. P. Perdew, *Phys. Rev. B: Condens. Matter Mater. Phys.*, 1996, **33**, 8822; (*c*) K. Eichkorn, O. Treutler, H. Öhm, M. Häser and R. Ahlrichs, *Chem. Phys. Lett.*, 1995, **242**, 652; (*d*) K. Eichkorn, F. Weigend, O. Treutler and R. Ahlrichs, *Theor. Chem. Acc.*, 1997, **97**, 119; (*e*) M. Dolg, H. Stoll, A. Savin and H. Preuss, *Theor. Chim. Acta*, 1989, **75**, 173; (*f*) H. Stoll, B. Metz and M. Dolg, *J. Comput. Chem.*, 2002, **23**, 767; (*g*) A. Klamt and G. Schüürmann, *J. Chem. Soc., Perkin Trans. 2*, 1993, 799–805; (*h*) A. Schäfer, A. Klamt, D. Sattel, J. C. W. Lohrenz and F. Eckert, *Phys. Chem. Chem. Phys.*, 2000, **2**, 2187.
12 (*a*) B. Cordero, V. Gómez, A. E. Platero-Prats, M. Revés, J. Echeverría, E. Cremades, F. Barragán and S. Alvarez, *Dalton Trans.*, 2008, 2832; (*b*) R. D. Shannon, *Acta Crystallogr., Sect. A: Cryst. Phys., Diffr., Theor. Gen. Crystallogr.*, 1976, **32**, 751.
13 (*a*) S. F. Boys, *Rev. Mod. Phys.*, 1960, **32**, 296; (*b*) J. M. Foster and S. F. Boys, *Rev. Mod. Phys.*, 1960, **32**, 300; (*c*) D. L. Bergman, L. Laaksonen and A. Laaksonen, *J. Mol. Graphics Modell.*, 1997, **15**, 301.
14 R. S. Mulliken, *J. Chem. Phys.*, 1955, **23**, 1833.

Supporting Information

$[V@Ge_8As_4]^{3-}$ and $[Nb@Ge_8As_6]^{3-}$: Unprecedented Encapsulation of Electron-Poor Transition Metal Atoms†

S. Mitzinger,[a] L. Broeckaert,[a,b] W. Massa,[a] F. Weigend,[b]* and S. Dehnen[a]*

[a] *Fachbereich Chemie, Wissenschaftliches Zentrum für Materialwissenschaften, Philipps-Universität Marburg, Hans-Meerwein-Straße, 35043 Marburg, Germany, email: dehnen@chemie.uni-marburg.de*;

[b] *Institut für Nanotechnologie, Karlsruher Institut für Technologie (KIT) Hermann-von-Helmholtz-Platz 1, 76344 Eggenstein-Leopoldshafen, Germany, email: florian.weigend@kit.edu*

Contents:

1. Synthesis details

1.1 General

All manipulations and reactions were performed under dry Ar atmosphere by using standard Schlenk or glovebox techniques. All solvents were dried and freshly distilled prior to use. [2.2.2]crypt[1] (Merck) was dried *in vacuo* for at least 18 h.

A phase with a nominal composition "KGeAs" was addressed by combining K, Ge and As in equimolar amounts in a niobium ampoule. The ampoule was then sealed by arc-welding and was placed in an oven at 950 °C. The resulting solid was ground in a mortar. To our surprise, the EDX analysis revealed the presence of Nb with 3.1 atom-% within the intermetallic phase. This accords with a stoichiometry near to "$K_{10}Ge_{10}As_{10}Nb$", thus close to the Ge:As:Nb ratio found in the $[Nb@Ge_8As_6]^{3-}$ anion (see below). The other elements appeared in near to equimolar ratios, as expected.

Upon the synthesis of the Nb compound (see below), we attempted to generate a homologue V compound. For this, the phase "$K_8Ge_8As_6V$" was approached by fusing K, Ge, As and V in an 8:8:6:1 stoichiometric ratio – thereby adopting the As amount to the stoichiometric ratio observed in the $[Nb@Ge_8As_6]^{3-}$ anion – in a silica glass ampoule with an oxygen torch. The resulting solid was thoroughly ground in a mortar prior to further use. EDX analysis confirmed the presence of V with 3.0 atom-% in the intermetallic phase, indicating a smaller amount to be included in the intermetallic phase than attempted. The other elements appeared in the expected molar ratios.

1.2 Syntheses

1.2.1 Synthesis of $[K([2.2.2]crypt]_3[V@Ge_8As_4]\cdot 2tol\cdot en$ (1)

139 mg (0.1 mmol) of the K/Ge/As/V intermetallic solid and 139 mg of [2.2.2]crypt were weighed out into a Schlenk tube. Then *en* (ethane-1,2-diamine, 4 mL) was added. The reaction mixture was allowed to stir for 2 days. The liquid was filtered through a standard glass frit, yielding a orange solution that was carefully layered by *tol* (toluene, 7 mL). After 21 days, yellow plate shaped crystals of $[K([2.2.2]crypt]_3[V@Ge_8As_4]\cdot 2tol\cdot en$ (**1**) were obtained.

1.2.2 Synthesis of $[K([2.2.2]crypt]_3[Nb@Ge_8As_6]\cdot tol\cdot en$ (2)

187 mg (1 mmol) of the K/Ge/As/Nb intermetallic solid and 141 mg [2.2.2]crypt (0.375 mmol) were weighed out into a Schlenk tube. Then *en* (ethane-1,2-diamine, 4 mL) was added. The reaction mixture was allowed to stir for 2 days. The liquid was filtered through a standard glass frit, yielding a dark red solution that was carefully layered by

tol (toluene, 7 mL). After 7 days dark red block shaped crystals of K([2.2.2]crypt]$_3$[Nb@Ge$_8$As$_6$]·*tol*·*en* (**2**) were obtained.

2. Single crystal X-ray crystallography

The data for the X-ray structural analyses were collected at T = 100(2) K with Mo-K$_\alpha$-radiation ($\lambda_{Mo\text{-}K\alpha}$= 0.71073 Å) on an area detector system Stoe IPDS2. The structures were solved by direct methods (SHELXS-97[2]), and refined by full-matrix-least-squares methods against F^2 with program SHELXL-2013.[2] Crystallographic data for the two structures reported in this paper have been deposited with the Cambridge Crystallographic Data Center as supplementary publications nos. CCDC-1030791 (**1**) and CCDC-1030792 (**2**). The crystal data and experimental parameters of the structure determinations are collected in Table S1.

Table S1. Crystal data and details of the structure determinations of **1** and **2**.

Compound	**1**	**2**
empirical formula	$C_{70}H_{132}As_4Ge_8K_3N_8O_{18}V$	$C_{63}H_{124}As_6Ge_8K_3N_8NbO_{18}$
formula weight [g mol^{-1}]	2422.47	2522.14
crystal color, shape	block, red	block, red
crystal size [mm^3]	0.48 × 0.31 × 0.20	0.50 × 0.50 × 0.40
crystal system	triclinic	triclinic
space group	$P\bar{1}$	$P\bar{1}$
a [Å]	11.9985(7)	16.1475(7)
b [Å]	16.7415(11)	16.7769(6)
c [Å]	25.3291(18)	18.0373(8)
α [°]	80.709(6)	89.184(3)
β [°]	88.755(5)	80.452(3)
γ [°]	69.258(5)	79.420(3)
V [Å^3]	4692.3(6)	4736.1(3)
Z, ρ_{calc} [g cm^{-3}]	2	2
μ (Mo$_{K\alpha}$) [mm^{-1}]	4.215	4.889
absorption correction type	Gaussian	Gaussian
2θ range [°]	2.55-25.00	3.01-26.00
total reflns	41618	66699
unique reflns [R_{int}]	16426	18581
obs. reflns [$I > 2\sigma(I)$]	4761	8558
parameters	880	945
wR_2 (all data)/ R_1 [$I > 2\sigma(I)$]	0.1138/0.0568	0.0630/0.0346
GooF (all data)	0.694	0.636
max peak/hole, [e Å^{-3}]	0.888/–0.749	1.085/–0.520

2.1. Details of the structure determination of [K([2.2.2]crypt]$_3$[V@Ge$_8$As$_4$]·2*tol*·*en* **(1)**

A numerical absorption correction has been applied based on crystal faces optimized by the XSHAPE procedure in XAREA (Stoe 2013).

Cluster anion: The main component is a V-centered 12-atom cluster with the composition [V@Ge$_8$As$_4$]$^{3-}$ according to theoretical calculations (see section 5). After refinement of this cluster anion, five residual electron density maxima were observed and could be refined as Ge/As atoms with occupations up to 13%. *Vice versa*, underoccupations of up to 13% were observed for several of the 12 main cluster atoms. This feature can be explained by assuming disorder over two additional orientations. Refinement of a respective disorder model gave occupations for the three orientations of 80.62(2), 9.71(1), and 9.30(2)%, respectively. The critical refinement of many close metal positions was stabilized by applying geometrical restraints favouring the same geometry for all three cluster shells (SAME option in SHELXL). Atoms with neighbours closer than 1 \%A were refined with the same anisotropic displacement parameters. In the final cycles all metal positions were refined with the expected overall ratio Ge/As 8:4. As Ge and As have virtually the same scattering power with Mo radiation, errors in the assignment would not influence the quality of the refinement. In Figure 1 of the main document, only the main component of the anion is shown with Ge/As attributions according to the perturbation theoretical calculations (see section 5). Its bond lengths are given in Table S2. In Figure S1, the complete disorder model is shown with the labelling scheme.

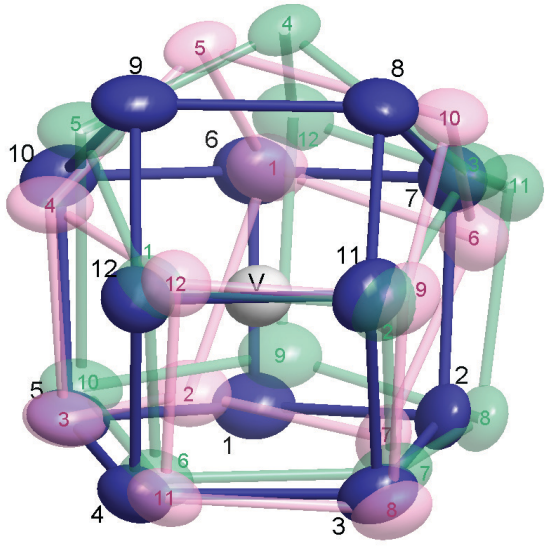

Figure S1. $[V@Ge_8As_4]^{3-}$ anion in **1** disordered over three orientations (blue 80.62%, red 9.71%, green 9.30%). Displacement ellipsoids at the 50% probability level.

Table S2. Interatomic distances [Å] in the anion of **1** (main orientation).

atom numbers		atom numbers		atom numbers	
1 – 2	2.526(3)	3 – 11	2.536(5)	7 – 8	2.490(3)
1 – 5	2.468(3)	4 – 5	2.460(4)	8 – 9	2.631(3)
1 – 6	2.526(3)	4 – 12	2.519(5)	9 – 10	2.500(2)
2 – 3	2.473(5)	5 – 10	2.581(2)	9 – 12	2.526(3)
2 – 7	2.547(3)	6 – 7	2.467(3)	11 – 12	2.495(7)
3 – 4	2.601(6)	6 – 10	2.436(4)	average	**2.517**
V – 1	2.881(2)	V – 5	2.682(3)	V – 9	2.660(2)
V – 2	2.612(3)	V – 6	2.801(3)	V – 10	2.742(2)
V – 3	2.711(3)	V – 7	2.716(3)	V – 11	2.756(4)
V – 4	2.703(4)	V – 8	2.616(2)	V – 12	2.784(5)
				average	**2.722**

Cations: Two of three $[K([2.2.2]crypt)]^+$ cations are well localized. A third one shows disorder over two positions shifted by about 1 Å. For it only isotropic displacement parameters could be refined common by pairs. All cations were refined using geometrical restraints on the bond lengths and 1,3-distances but leaving conformational freedom (SAME option of SHELXL). This explains the large number of restraints. Figure S2 shows all three cations.

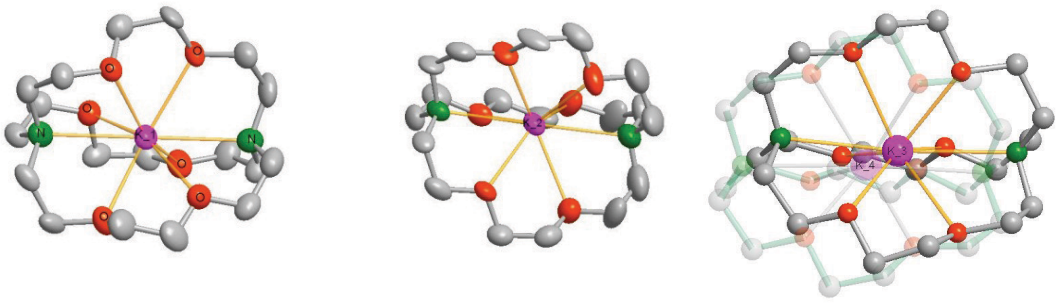

cation 1 cation 2 1:1 disordered cation 3

Figure S2. The three independent $[K([2.2.2]crypt)]^+$ cations in **1**. Displacement ellipsoids for cations 1 and 2 at the 50% probability level, for 3 arbitrary radii.

Solvent: Around the unit cell origin, a large void remained with diffuse electron densities corresponding to about 140 electrons/asymm. unit. Thus, similar to the structure of **2**, solvent contents of toluene and *en* molecules are assumed, probably two toluene and one *en* molecules according to the electron count. As we were not able to establish a sensible disorder model for this region, its contribution was subtracted by back Fourier transform (PLATON SQUEEZE) from the data set. Thus, the solvent molecules are missing in the parameter list leading to several error messages in the PLATON CHECKCIF procedure.

Packing: The three independent cations form layers parallel to the (0-11) plane. In between, the anion clusters are inserted (Figure S3), as well as the disordered solvent molecules.

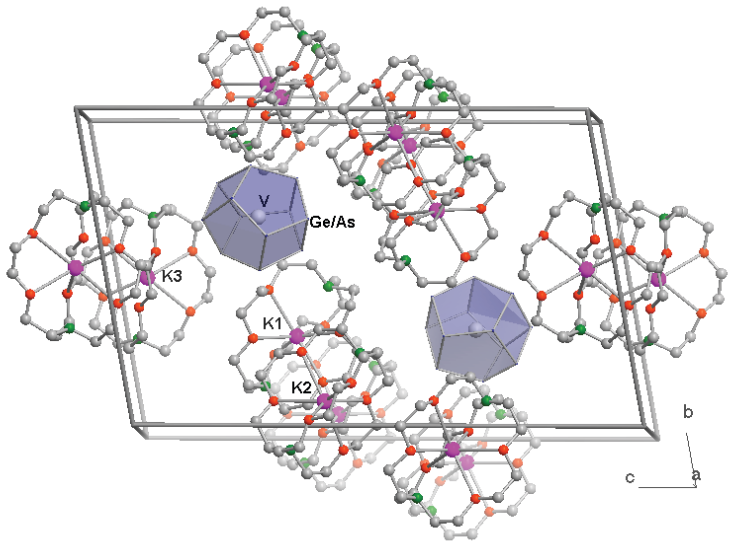

Figure S3. Unit cell of **1** with neighborhood. Arbitrary radii; polyhedra: anionic clusters (main orientation), pink: K, green: N, red: O, grey: C. Note that the empty space around the cell origin contains non-localized, disordered toluene and *en* solvent molecules.

2.2. Details of the structure determination of $[K([2.2.2]crypt]_3[Nb@Ge_8As_6]\cdot tol\cdot en$ **(2)**

As for **1,** a numerical absorption correction has been applied based on crystal faces optimized by the XSHAPE procedure in XAREA (Stoe 2013).

The anion revealed as a pure $[Nb@Ge_8As_6]^{3-}$ cluster. The Ge/As assignment (Figure 1 and Figure S4) was done based on the perturbation theoretical calculations (section 5). The interatomic distances are collected in Table S3. The three independent $[K([2.2.2]crypt)]^+$ cations are all well localized (Figure S5). Even the solvent content, a toluene and an *en* molecule, could be localized and refined. Only the *en* molecule had to be refined with restraints of the bond lengths and with isotropic displacement parameters.

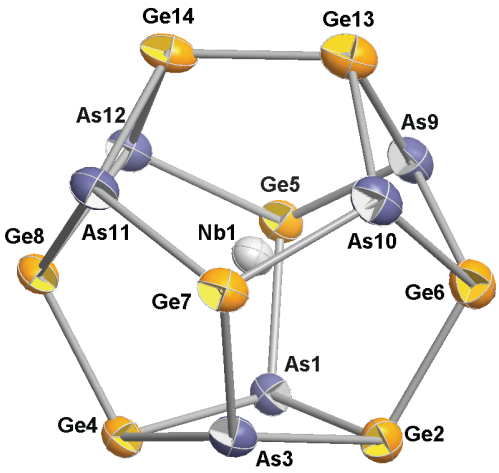

Figure S4. $[Nb@Ge_8As_6]^{3-}$ anion in **2**. Displacement ellipsoids at the 50% probability level.

Table S3. Interatomic distances [Å] in the anion of **2.**

atom numbers		atom numbers		atom numbers	
As1 – Ge2	2.5110(9)	Ge4 – Ge8	2.4817(9)	Ge8 – As11	2.4948(9)
As1 – Ge4	2.5125(9)	Ge5 – As9	2.4732(9)	Ge8 – As12	2.4949(9)
As1 – Ge5	2.4804(9)	Ge5 – As12	2.5048(9)	As9 – Ge13	2.5101(10)
Ge2 – As3	2.5079(9)	Ge6 – As9	2.4958(9)	As10 – Ge13	2.5216(10)
Ge2 – Ge6	2.4762(10)	Ge6 – As10	2.5008(10)	As11 – Ge14	2.5055(9)
As3 – Ge4	2.5198(9)	Ge7 – As10	2.5010(10)	As12 – Ge14	2.5005(9)
As3 – Ge7	2.4741(9)	Ge7 – As11	2.5220(10)	av. Ge – As av. Ge – Ge	**2.5017** **2.4790**
Nb – As1	2.7784(8)	Nb – Ge6	2.9994(9)	Nb – As11	2.8487(8)
Nb – Ge2	3.0326(9)	Nb – Ge7	2.9321(8)	Nb – As12	2.8480(8)
Nb – As3	2.8096(8)	Nb – Ge8	2.9414(8)	Nb – Ge13	3.0410(9)

Nb – Ge4	3.0769(9)	Nb – As9	2.8246(8)	Nb – Ge14	2.9734(9)
Nb – Ge5	2.9441(8)	Nb – As10	2.8095(8)	av. Nb – Ge av. Nb – As	**2.9926** **2.8198**

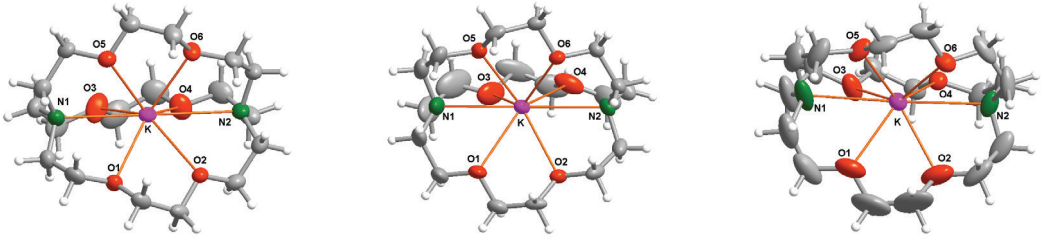

cation 1 cation 2 cation 3

Figure S5. The three independent $[K[2.2.2]crypt]^+$ cations in **2**. Displacement ellipsoids at the 50% probability level.

Packing: The $[K([2.2.2]crypt)]^+$ cations form a honeycomb-like packing with channels along the [11-1] direction, in which the anion clusters are aligned (Figure S6).

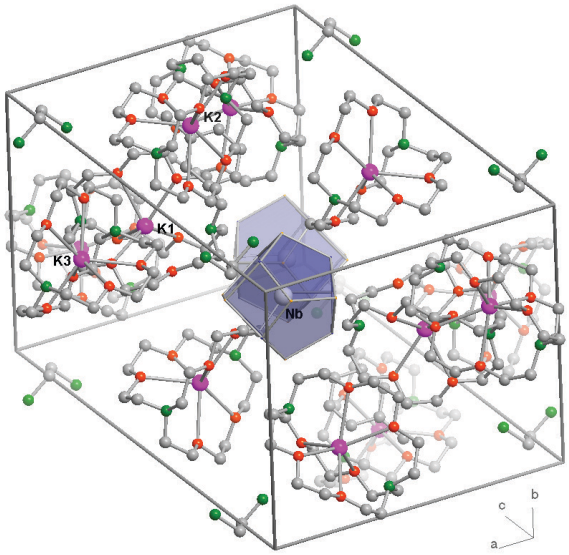

Figure S6. Unit cell of **1** with neighborhood. Arbitrary radii; blue polyhedra: anion clusters, pink: K, green: N, red: O, grey: C.

3. Energy dispersive X-ray spectroscopy (EDX) analysis

EDX analyses were performed to support the elemental composition that was suggested based on the XRD experiments. These were carried out using an EDX-device Voyager 4.0 of Noran Instruments coupled with an electron microscope CamScan CS 4DV. Data acquisition was performed with an acceleration voltage of 20 kV and 100 s accumulation time. The radiation emitted by the atoms was analyzed: K-K, Ge-K, As-K, V-K and Nb-L. To minimize surface effects in the measurement, the K-lines were preferably used to calculate the elemental composition. Results are summarized in Table S4.

Table S4. EDX analysis of **1** and **2** (K, Ge, As, V/Nb)

Element	k-ratio	ZAF	Atom%	Atomic ratio observed (calc)	Element wt %	wt % Err. (1-sigma)
[K([2.2.2]crypt]$_3$[Ge$_8$As$_4$V]·2*tol*·*en* (1)						
K-K	0.1131	1.180	22.07	3.73 (3)	13.35	+/- 0.26
Ge-K	0.4835	1.033	44.47	7.23 (6)	49.95	+/- 1.77
As-K	0.3113	1.037	27.86	4.00 (4)	32.29	+/- 1.91
V-K	0.0413	1.068	5.60	0.97 (1)	4.41	+/- 0.27
Total			100	15.93 (14)	100	
[K([2.2.2]crypt]$_3$[Ge$_8$As$_6$Nb]·*tol*·*en* (2)						
K-K	0.1174	1.226	24.43	4.77 (3)	14.40	+/- 0.21
Ge-K	0.4140	1.028	38.90	7.59 (8)	42.57	+/- 1.15
As-K	0.3363	1.032	30.74	6.00 (6)	34.72	+/- 1.37
Nb-L	0.0444	1.873	5.94	1.16 (1)	8.32	+/- 0.38
Total			100	19.52 (18)	100	

The results of the EDX investigations confirm the Ge:As ratios of the investigated substances within the expected accuracy, as well as the presence of V and Nb, respectively, in the crystalline material.

4. Electrospray Ionization Mass Spectrometry (ESI-MS) Investigations

ESI(–) mass spectrometry has been performed on a Finnigan LTQ-FT spectrometer by Thermo Fischer Scientific in the negative ion mode: Spray voltage 3.90 kV, capillary temperature 300°C, capillary voltage –11 V, tube lens voltage –140 V, sheath gas flow rate 25 arb, sweep gas flow rate 0 arb. For the measurements, the filtered solutions were dried *in vacuo* and re-dissolved in dry DMF. During the ESI-MS investigations fast decomposition was observed during the injection, resulting in black precipitate in the Hamilton syringe as well as a decreased flow rate into the ESI chamber. Additional peaks observed in the ESI(–) spectrum show incomplete isotopic patterns and are believed to belong to decomposition products and fragments formed by a dynamic re-organization of the cluster anions and their fragments in solution under ESI-MS conditions. As it is common for Zintl anions and intermetallic cluster anions, the observed fragments have been detected as oxidized, singly charged species. In summary, despite analytical challenges the existence of the cluster anions of **1** and **2** could be proven (see below).

4.1 ESI-MS investigation of [K([2.2.2]crypt)]$_3$[Ge$_8$As$_4$V] (1)

The ESI(–)MS spectrum of **1** (Figure S7) revealed the (protonated) cluster anion $[Ge_8As_4VH]^-$ (m/z = 933.01) to be present along with the $[K([2.2.2]crypt)]^+$ adduct $[Ge_8As_4VC_{18}H_{37}N_2O_6K]^-$ (m/z = 1348.23) of the trimetallic cluster $[Ge_8As_4V]^{3-}$ found in SCXD (Figures S8, S9). Furthermore, the anions $(Ge_2As_2H)^-$ (m/z = 296.69), $(Ge_7As_2)^-$ (m/z = 658.30), $(Ge_7As_2C_{18}H_{36}N_2O_6K)^-$ (m/z = 1073.52), and $(Ge_{10}C_{18}H_{36}N_2O_6K)^-$ (m/z = 1141.44) and were identified (Figures S10-S12). They are believed to origin from the formation of the multimetallic cluster itself during extraction, and they likely represent intermediates which could not be crystallized. In some spectra, unidentified components that may derive from fragmentations partially overlay the peak of the named species.

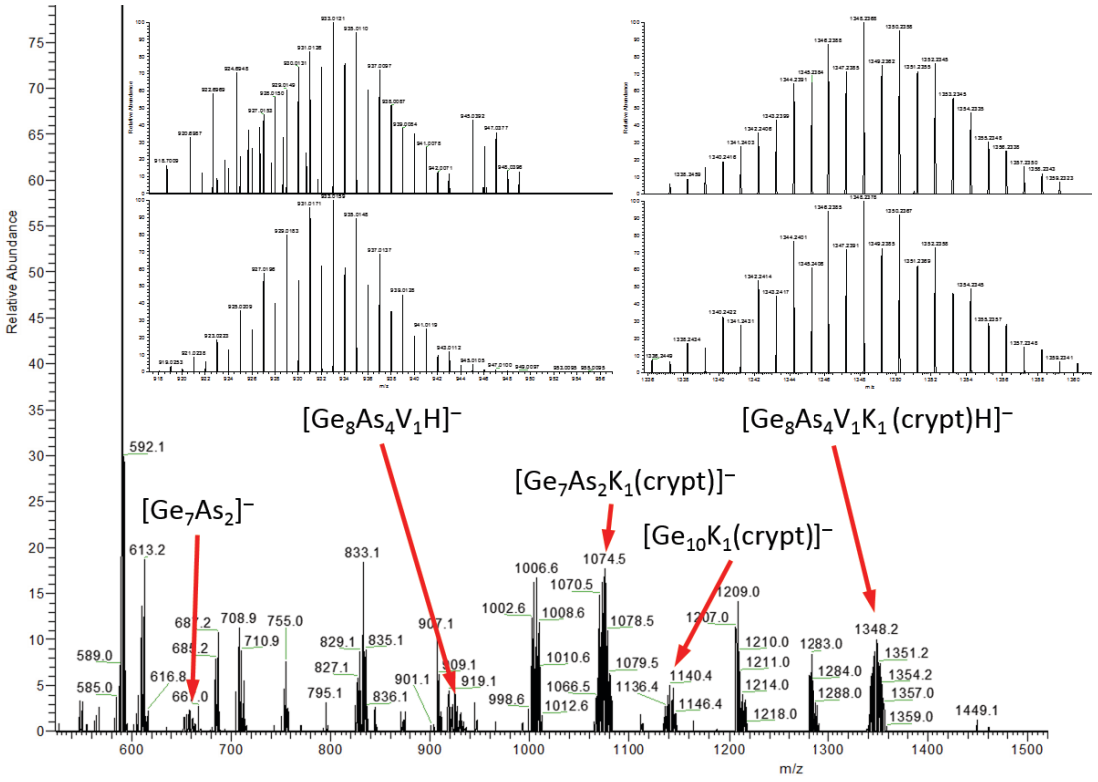

Figure S7. ESI-MS(–) overview spectrum

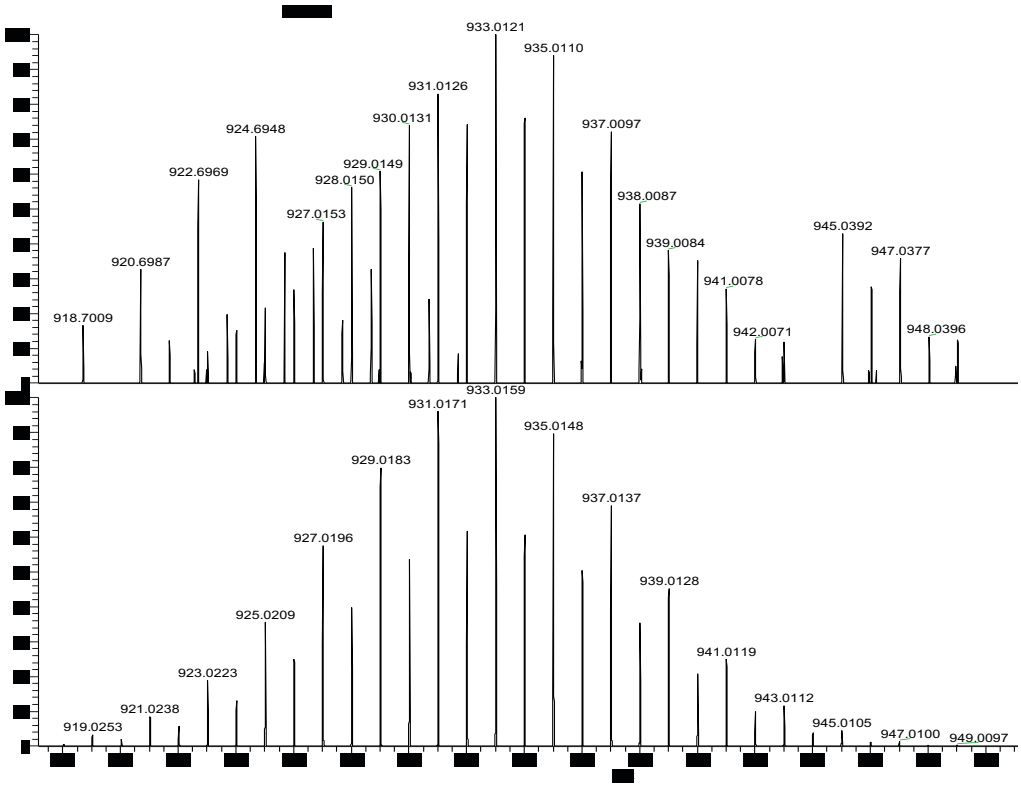

Figure S8. ESI-MS(–) mass peak of the $[Ge_8As_4VH]^-$ anion. Measured (top) vs. calculated (bottom) spectrum. The partially overlaid species could not be identified.

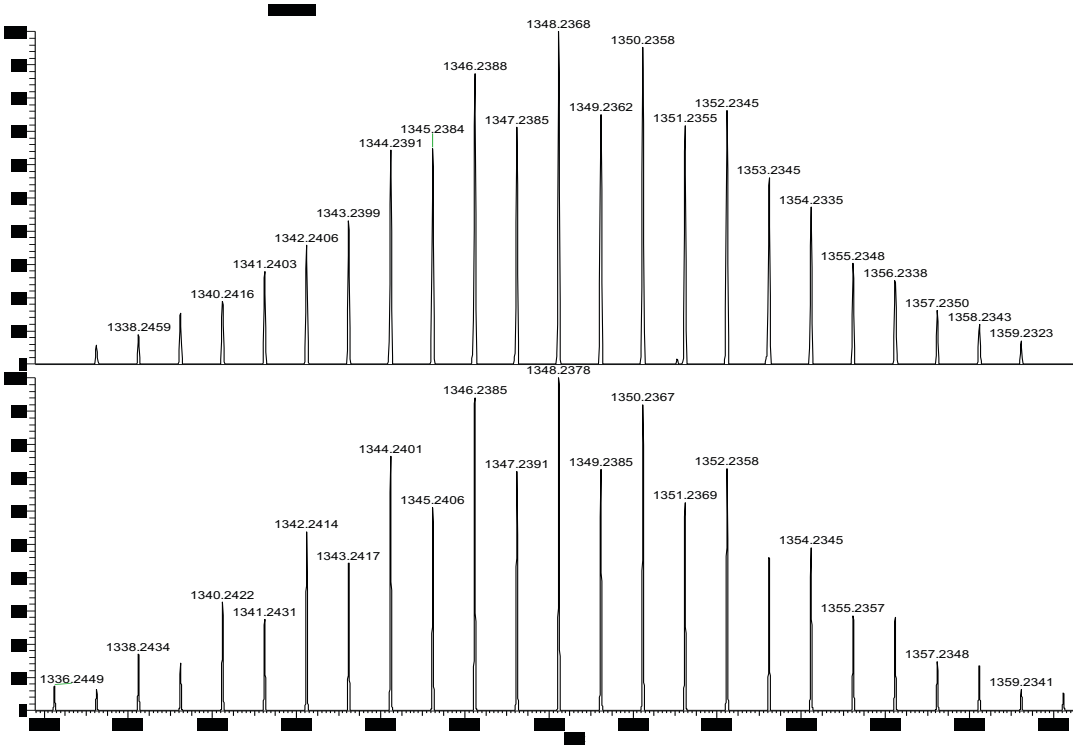

Figure S9. ESI(–) mass peak of $[Ge_8As_4VC_{18}H_{37}N_2O_6K]^-$. Measured (top) vs. calculated (bottom) spectrum.

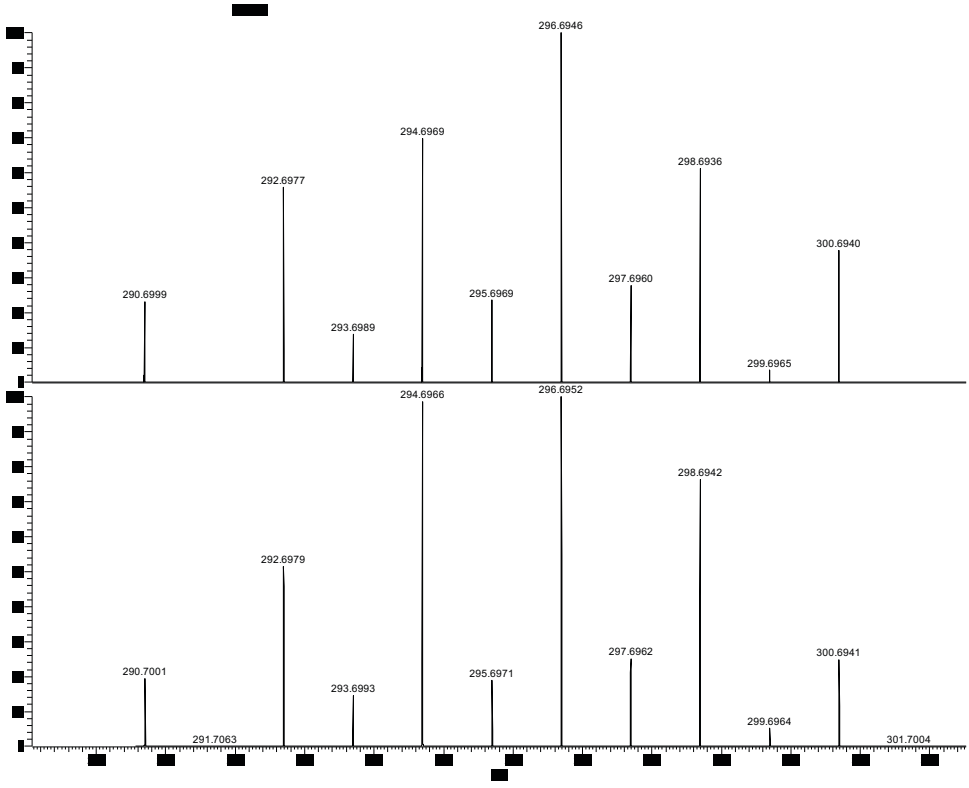

Figure S10. ESI(–) mass peak of $(Ge_2As_2H)^-$. Measured (top) vs. calculated (bottom) spectrum.

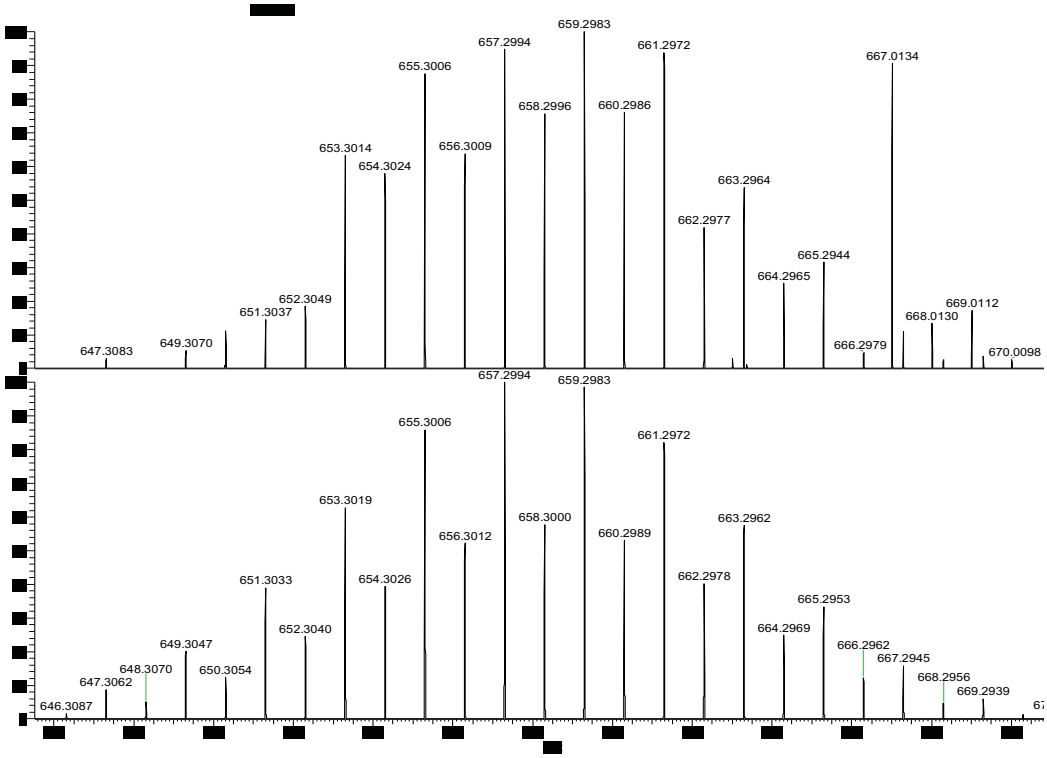

Figure S11. ESI(–) mass peak of $(Ge_7As_2)^-$. Measured (top) vs. calculated (bottom) spectrum.

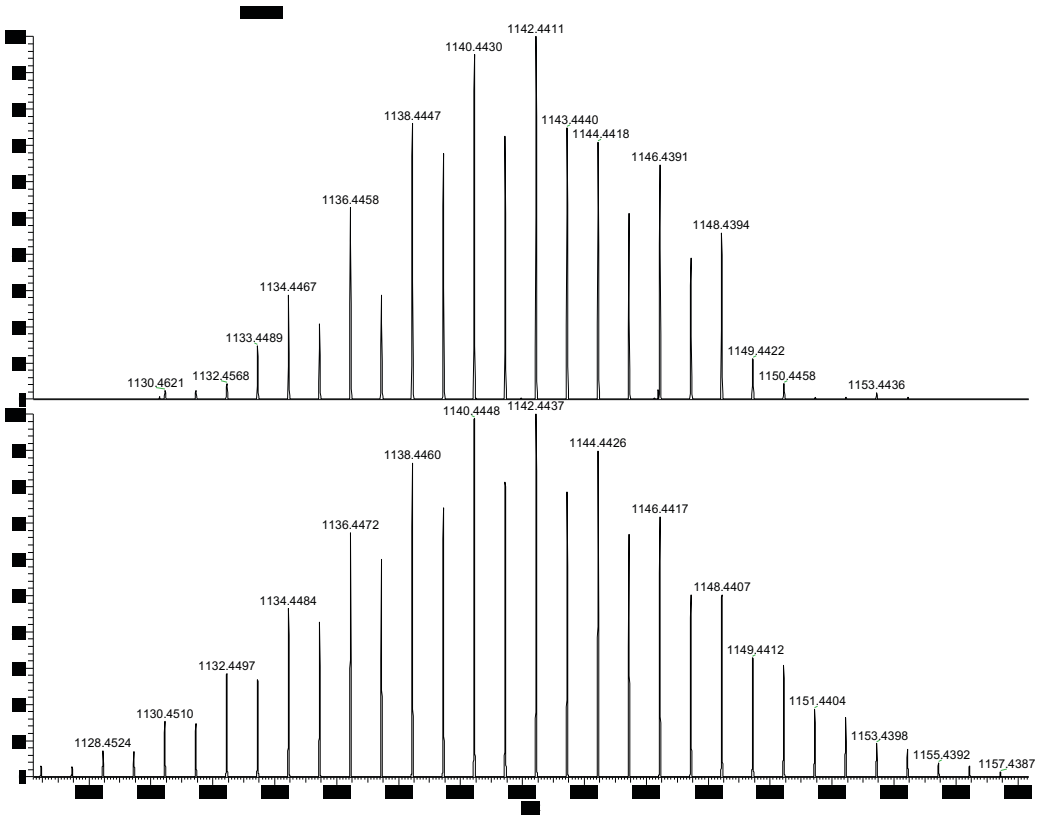

Figure S12. ESI(–) mass peak of $(Ge_{10}C_{18}H_{36}N_2O_6K)^-$. Measured (top) vs. calculated (bottom) spectrum.

4.2 ESI-MS Investigation of [K([2.2.2]crypt)]$_3$[Ge$_8$As$_6$Nb] (2)

The ESI(–)MS spectrum of **2** (Figure S13) revealed the cluster $[Ge_8As_6Nb]^-$ (m/z = 1123.81), which corresponds to the trimetallic cluster $[Ge_8As_6Nb]^{3-}$ found in SCXD (Figure S14). Furthermore the mass peaks of $(Ge_2As_2H)^-$ (m/z = 296.69) was identified in the ESI(–) spectrum (Figure S15). Also mass peaks corresponding to a cluster with the composition $[Ge_6As_6Nb]^-$ (m/z = 975.97) and an overlay (mixture) of the following species were found: $[Ge_7As_6NbH]^-$ / $[Ge_7As_6Nb]^-$ / $[Ge_6As_7NbH]^-$ / $[Ge_6As_7Nb]^-$ (m/z = 1051.89) (Figures S16, S17); the latter could, however, not be assigned unambiguously, and have not been confirmed yet by crystalline products. Nevertheless, these indicate further species to possibly co-exist in a complicated equilibrium in solution.

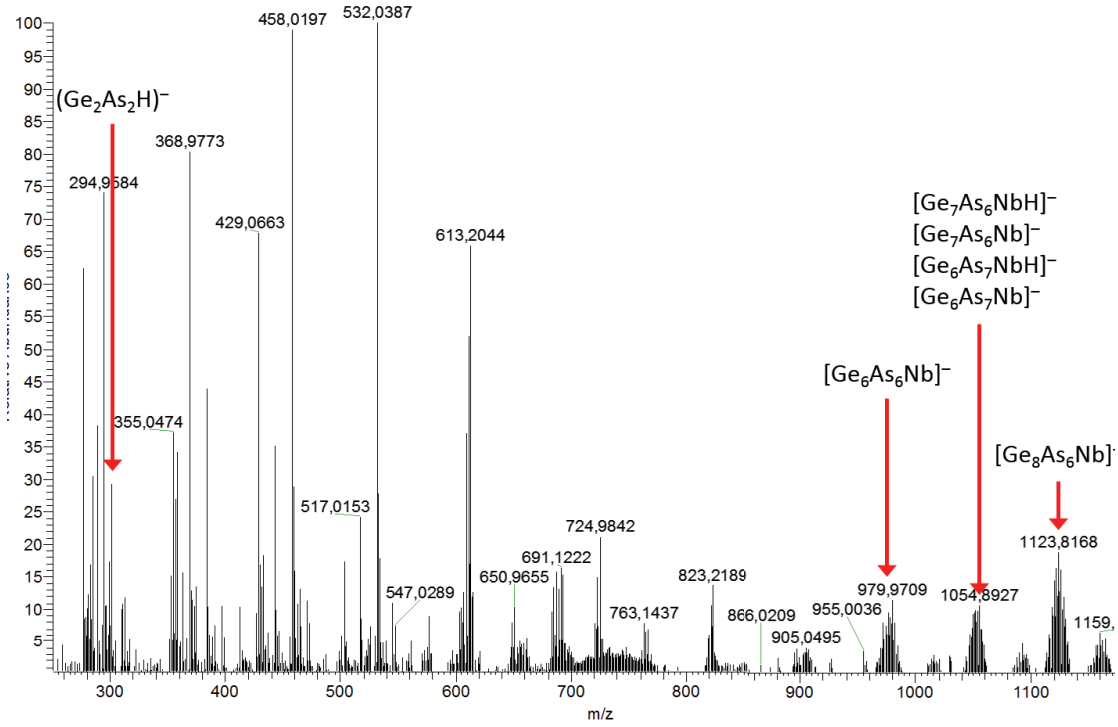

Figure S13. ESI-MS(–) overview spectrum

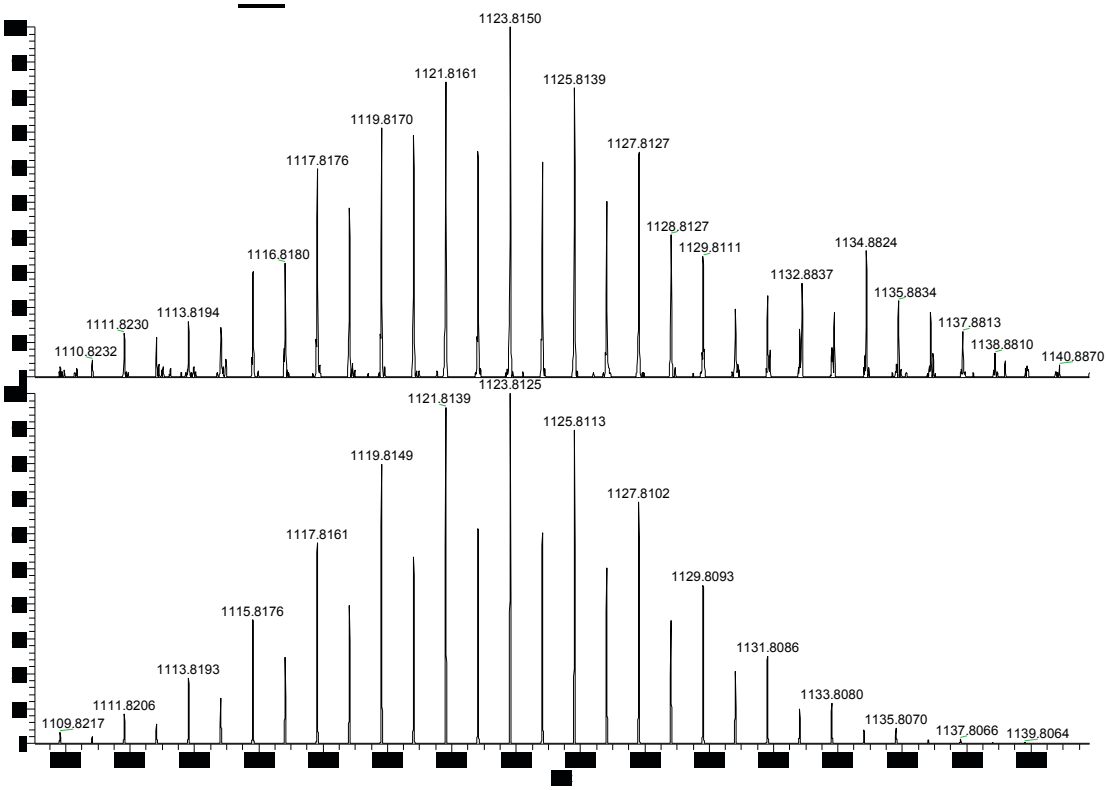

Figure S14. ESI(–) mass peak of $[Ge_8As_6Nb]^-$. Measured (top) vs. calculated (bottom) spectrum.

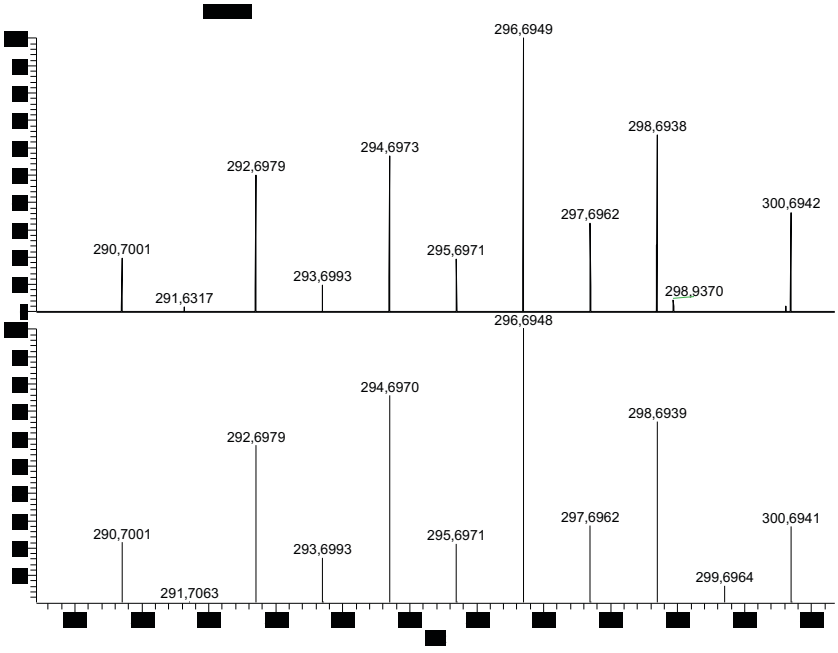

Figure S15. ESI(–) mass peak of $(Ge_2As_2H)^-$. Measured (top) vs. calculated (bottom) spectrum.

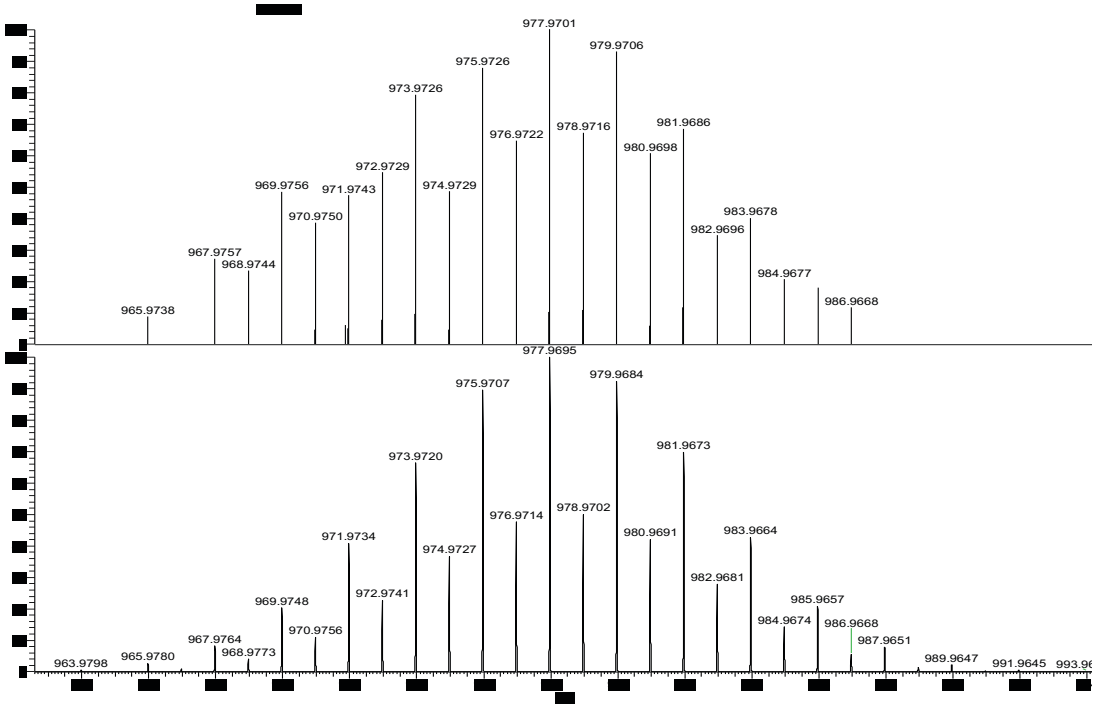

Figure S16. ESI(–) mass peak of $[Ge_6As_6Nb]^-$. Measured (top) vs. calculated (bottom) spectrum.

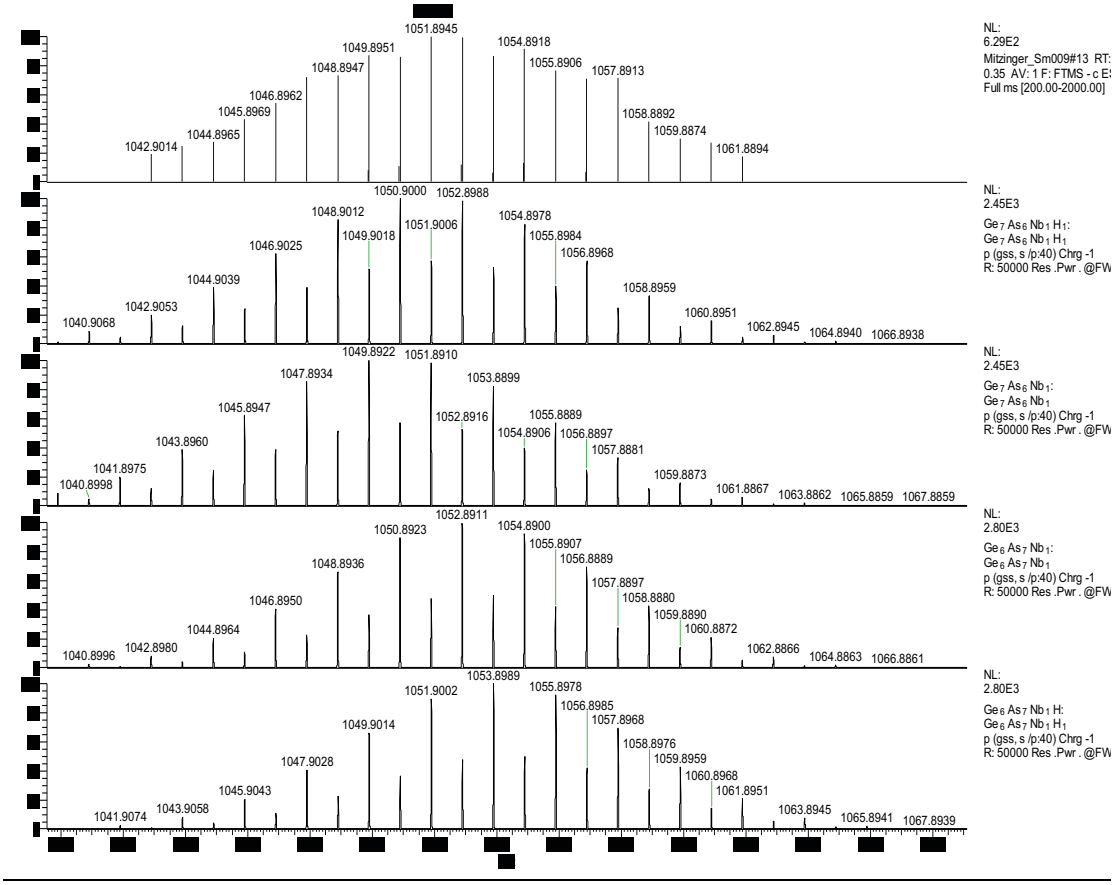

Figure S17. ESI(–) mass peak likely corresponding to $[Ge_7As_6Nb]^-$ / $[Ge_7As_6NbH]^-$ / $[Ge_6As_7Nb]^-$ / $[Ge_6As_7NbH]^-$. Measured (top) vs. calculated (below) spectra.

5. Quantum Chemical Investigations

5.1 Methods

The DFT calculations were performed with the program system Turbomole.[3] The GGA exchange-correlation functional BP86 was applied,[4] together with a def-SVP basis set[5] and corresponding effective core potentials (ECPs) for Sn, Bi, Nb, Ru, Rh and Lu.[6] COSMO was used with default parameters to compensate for the negative charge of the clusters.[7] Localization of MOs was done following the procedure by Boys.[8] Mulliken[9] and NPA (Natural Population Analysis)[10] charges were calculated at the same level of theory. Contours in Figures 3 and 4 are drawn at 0.1 a.u. by using gOpenMol.[11]

5.2 Perturbation theory study for atom assignment in the anions of 1 and 2

The optimal distribution of the different atom types (Ge/As) to the positions in the (trimetallic) cluster anions of compounds **1** and **2** was done using first-order perturbation theory.[12,13] The (first-order) estimation for the preference of Ge and As to the different positions requires only the calculation of the electrostatic potential at the respective positions, $V_i = V(\mathbf{R}_i)$, without the contribution of the nucleus located at this position $\mathbf{R}_i$. As atoms (more right in the periodic table) are assigned to the sites with the lower electrostatic potential, Ge atoms are assigned to the remaining positions with a higher electrostatic potential. A detailed theoretical background of this method can be found in refs. 11 and 12.

The anion of **1**, $[V@Ge_8As_4]^{3-}$, which is depicted in Figure S18, left hand side, has the highest electrostatic potential at positions (1)-(8) and the calculated values vary between –156.379 and –156.380 Hartree; Ge atoms were placed here. For positions (9)-(12) the lowest electrostatic potential was calculated (between –160.700 and –160.696 Hartree) and the four As atoms were assigned to these points.

For the anion of **2**, $[Nb@Ge_8As_6]^{3-}$, depicted in Figure S18, right hand side, the electrostatic potential was the highest at positions (1)-(8) and varies between –156.576 and –156.572 Hartree; the Ge atoms were placed here. Positions (9)-(14) have the lowest electrostatic potential (between –160.926 and –160.921 Hartree) and the six As atoms were assigned to these points.

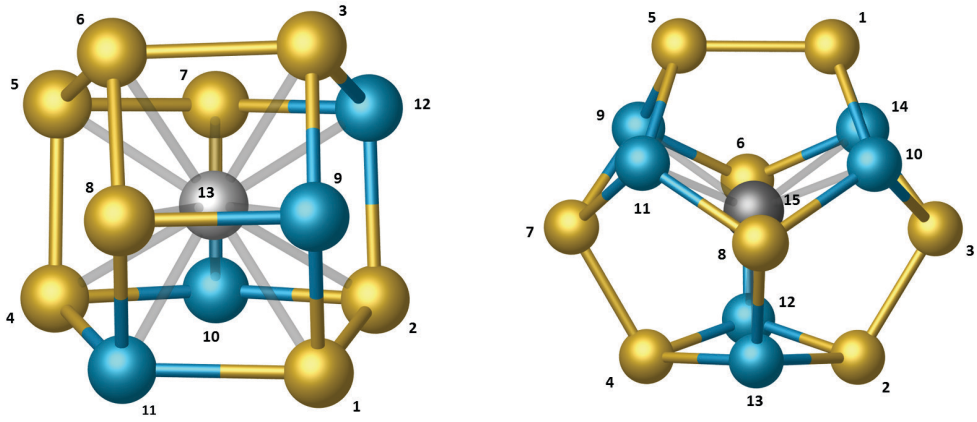

Figure S18. Left: Calculated minimum structure of the $[V@Ge_8As_4]^{3-}$ anion in **1**. The (Ge/As) atomic distribution results from perturbation theory calculations, as described above. Ge atoms are drawn in yellow and As atoms in blue. Right: Calculated minimum structure of the $[Nb@Ge_8As_6]^{3-}$ anion in **2**. The (Ge/As) atomic distribution results from perturbation theory calculations, as described above. Ge atoms are drawn in yellow and As atoms in blue.

5.3 Population analyses

Tables S5 and S6 summarize atomic charges of the 14-atom and 12-atom cluster anions $[Lu@Pb_6Bi_8]^{3-}$, $[Nb@Ge_8As_6]^{3-}$, and $[Nb@Ge_8As_4]^{3-}$ or $[V@Ge_8As_4]^{3-}$, and $[Rh@Ge_{12}]^{3-}$, respectively, as calculated by means of Mulliken[8] or Natural Population Analysis (NPA).[9] The charges are expressed as multiples of the elementary charge ***e*** (values in a.u.).

Table S5. Atomic charges for two different cluster anions with main group metal shells containing 14 atoms: $[Nb@Ge_8As_6]^{3-}$ and $[Lu@Pb_6Bi_8]^{3-}$ (values in a.u.). The atom numbering accords with the positions indicated in Figure S18.

$[Nb@Ge_8As_6]^{3-}$	Mulliken	NPA	$[Lu@Pb_6Bi_8]^{3-}$	Mulliken	NPA
Ge (1)	-0.044	-0.018	Pb (1)	-0.207	0.042
Ge (2)	-0.044	-0.018	Pb (2)	-0.207	0.042
Ge (3)	-0.044	-0.018	Pb (3)	-0.207	0.042
Ge (4)	-0.044	-0.018	Pb (4)	-0.212	0.040
Ge (5)	-0.044	-0.018	Pb (5)	-0.212	0.040
Ge (6)	-0.005	+0.081	Pb (6)	-0.207	0.042
Ge (7)	-0.044	-0.018	Bi (7)	-0.218	-0.363
Ge (8)	-0.005	+0.081	Bi (8)	-0.218	-0.363
As (9)	-0.218	-0.316	Bi (9)	-0.246	-0.276
As (10)	-0.218	-0.316	Bi (10)	-0.246	-0.276
As (11)	-0.218	-0.316	Bi (11)	-0.245	-0.275
As (12)	-0.218	-0.316	Bi (12)	-0.247	-0.276
As (13)	-0.218	-0.316	Bi (13)	-0.247	-0.276
As (14)	-0.218	-0.316	Bi (14)	-0.244	-0.275
Nb (15)	-1.418	-1.159	Lu (15)	+0.162	-0.869

Table S5. Atomic charges for two cluster anions with main group metal shells containing 12 atoms, $[V@Ge_8As_4]^{3-}$, $[Nb@Ge_8As_4]^{3-}$, and $[Rh@Ge_{12}]^{3-}$ (values given in a.u.). The atom numbering accords with the positions indicated in Figure S18.

$[V@Ge_8As_4]^{3-}$	Mulliken	NPA	$[Nb@Ge_8As_4]^{3-}$	Mulliken	NPA	$[Rh@Ge_{12}]^{3-}$	Mulliken	NPA
Ge (1)	-0.153	-0.157	Ge (1)	-0.066	+0.010	Ge (1)	+0.009	-0.157
Ge (2)	-0.153	-0.157	Ge (2)	-0.065	+0.010	Ge (2)	-0.098	-0.244
Ge (3)	-0.179	-0.141	Ge (3)	-0.068	+0.029	Ge (3)	-0.097	-0.243
Ge (4)	-0.179	-0.141	Ge (4)	-0.068	+0.029	Ge (4)	-0.098	-0.244
Ge (5)	-0.246	-0.385	Ge (5)	-0.179	-0.175	Ge (5)	-0.098	-0.244
Ge (6)	-0.246	-0.385	Ge (6)	-0.179	-0.175	Ge (6)	+0.010	-0.157
Ge (7)	-0.165	-0.098	Ge (7)	-0.041	+0.040	Ge (7)	-0.097	-0.244
Ge (8)	-0.165	-0.098	Ge (8)	-0.041	+0.040	Ge (8)	-0.097	-0.243
As (9)	-0.278	-0.451	As (9)	-0.215	-0.305	Ge (9)	+0.009	-0.157
As (10)	-0.278	-0.451	As (10)	-0.215	-0.305	Ge (10)	+0.009	-0.157
As (11)	-0.271	-0.463	As (11)	-0.231	-0.270	Ge (11)	-0.097	-0.243
As (12)	-0.271	-0.463	As (12)	-0.231	-0.270	Ge (12)	-0.097	-0.243
V (13)	-0.418	+0.392	Nb (13)	-1.401	-1.660	Rh (13)	-2.258	-0.423

6. References for the supplementary information

[1] 4,7,13,16,21,24-Hexaoxa-1,10-diazabicyclo[8.8.8]hexacosane / Kryptofix 222

[2] G. M. Sheldrick, *Acta Crystallogr*. **2008**, A**64,** 112 – 122.

[3] TURBOMOLE Version 6.6, © TURBOMOLE GmbH 2014. TURBOMOLE is a development of University of Karlsruhe and Forschungszentrum Karlsruhe 1989 − 2007, TURBOMOLE GmbH since 2007; available from http://www.turbomole.com.

[4] (a) D. Becke, *Phys. Rev. A* 1988, **38**, 3098 – 3100; (b) J. P. Perdew, *Phys. Rev. B* 1996, **33**, 8822 – 8824.

[5] (a) K. Eichkorn, F. Weigend, O. Treutler, R. Ahlrichs, *Theor. Chem. Acc.*, 1997, **97**, 119 – 124; (b) K. Eichkorn, O. Treutler, H. Öhm, M. Häser and R. Ahlrichs, *Chem. Phys. Lett.*, 1995, **242**, 652 – 660.

[6] (a) M. Dolg, H. Stoll, A. Savin, H. Preuss, *Theor. Chim. Acta* 1989, **75**, 173 – 194; (b) H. Stoll, B. Metz, M. Dolg, *J. Comput. Chem*. 2002, **23**, 767 – 778.

[7] (a) A. Klamt, G. Schürmann, *J. Chem. Soc. Perkin Trans.* 1993, **2**, 799 − 805; (b) A. Schäfer, A. Klamt, D. Sattel, J. C. W. Lohrenzc and F. Eckert, *Phys. Chem. Chem. Phys.*, 2000, **2**, 2187 – 2193.

[8] (a) S. F. Boys, *Rev. Mod. Phys.* 1960*,* **32**, 296 – 299 *;* (b) J. M. Foster, S. F. Boys, *Rev. Mod. Phys.* 1960*,* **32***,* 300 – 302.

[9] R. S. Mulliken, *J. Chem. Phys.* 1955, **23**, 1833 – 1840.

[10] A. E. Reed, R. B. Weinstock, and F. Weinhold, *J. Chem. Phys.* 1985, **83**, 735 – 746.

[11] D. L. Bergman, L. Laaksonen, and A. Laaksonen, *J. Mol. Graph. Model.* 1997, **15**, 301−306.

[12] (a) F. Weigend, C. Schrodt, and R. Ahlrichs*, J. Chem. Phys.* 2004, **121,** 10380 – 10384; (b) F. Weigend, and C. Schrodt*, Chem. Eur. J.* 2005, **11,** 3559 – 3564.

[13] F. Weigend, *J. Chem. Phys.* 2014, **141**, 134103.

3.2 Understanding of Multimetallic Cluster Growth

This article was published in Nature Commun., 2016, **7**:10480.

The elucidation of formation mechanisms is mandatory for understanding and planning of synthetic routes. For (bio-)organic and organometallic compounds, this has long been realised even for very complicated molecules, whereas the formation of ligand-free inorganic molecules has widely remained a black box to date. This is due to poor structural relationships between reactants and products and the lack of structurally related intermediates arising from the comparably high coordination flexibility of involved atoms. Here investigations on the stepwise formation of multimetallic clusters, based on a series of crystal structures and complementary quantum-chemical studies of $(Ge_2As_2)^{2-}$, $(Ge_7As_2)^{2-}$, $[Ta@Ge_6As_4]^{3-}$, $[Ta@Ge_8As_4]^{3-}$ and $[Ta@Ge_8As_6]^{3-}$ are reported. The study makes use of efficient quantum-chemical tools, enabling the first detailed screening of the energy hypersurface along the formation of ligand-free inorganic species for a semi-quantitative picture. The results can be generalised for an entire family of multimetallic clusters.

S. Mitzinger conceived and performed the synthesis, performed the characterisation and interpreted the analytical data. W. Massa was consulted for crystallographic advice and completed solution of the crystal structures. L. Broekaert and F. Weigend performed quantum chemical calculations. All authors co-wrote the manuscript.

Dieser Artikel wurde in der Zeitschrift Nature Commun., 2016, **7**:10480 veröffentlicht.

Für ein System aus Ta-, Ge- und As- haltigen Metallclustern konnte nun zum ersten Mal durch die geschickte Kombination von modernsten quantenchemischen Rechnungen und anorganischer Synthese die Bildung von Metallclustern ausgehend vom $(Ge_2As_2)^{2-}$ hin zum $[Ta@(Ge_8As_6)]^{3-}$ beleuchtet werden. Das Spektrum der vorgefundenen Cluster reicht dabei vom kleinen tetraedrischen $(Ge_2As_2)^{2-}$, über einen 9-Atom-Käfig der Zusammensetzung $(Ge_7As_2)^{2-}$, hin zu den endohedralen Clustern $[Ta@Ge_8As_4]^{3-}$ und [Ta@Ge8As6]$^{3-}$. Jedoch ermöglichte es erst der Fund einer Zwischenstufe, nämlich des Clusters $[Ta@Ge_6As_4]^{3-}$, den Reaktionspfad der Clusterbildung nachzuvollziehen. Mit Hilfe einer kürzlich entwickelten quantenchemischen Methode zur Berechnung der günstigsten Energie von Isomeren multimetallischer Systeme (GA-RP) sowie der erstmaligen Modellierung ihrer Reaktionspfade gelang schließlich der Schluss des Kreises und die Einordnung der Cluster in eine Reaktionskaskade zur intermetalloiden Clusterbildung. Dieser Fund erlaubt die Einordnung der vorgefundenen Zwischenstufe als einen „gemeinsamen Vorfahren“ der bisher bekannten endohedralen homo- und multi-metallischen Tetrelcluster aus 10, 12, 13 und 14 Atomen in der Clusterhülle. Darüber hinaus lieferte die Studie erstmals eine quantenchemisch fundierten Vorschlag für die Reorganisation von deltaedrischen zu nicht-deltaedrischen Clustern.

S. Mitzinger erdachte die Synthese und führte das Experiment sowie die Charakterisierung und die Interpretation der analytischen Daten durch. W. Massa wurde für die Vervollständigung der Lösung der kristallographischen Datensätze hinzugezogen und führte diese durch. L. Broekaert und F. Weigend führen die quantenchemischen Rechnungen und deren Auswertung durch. Alle Autoren haben das Manuskript gemeinsam verfasst.

nature COMMUNICATIONS

ARTICLE

Received 23 Jul 2015 | Accepted 14 Dec 2015 | Published 25 Jan 2016

DOI: 10.1038/ncomms10480 OPEN

Understanding of multimetallic cluster growth

Stefan Mitzinger[1], Lies Broeckaert[1,2], Werner Massa[1], Florian Weigend[2] & Stefanie Dehnen[1]

The elucidation of formation mechanisms is mandatory for understanding and planning of synthetic routes. For (bio-)organic and organometallic compounds, this has long been realized even for very complicated molecules, whereas the formation of ligand-free inorganic molecules has widely remained a black box to date. This is due to poor structural relationships between reactants and products and the lack of structurally related intermediates—due to the comparably high coordination flexibility of involved atoms. Here we report on investigations of the stepwise formation of multimetallic clusters, based on a series of crystal structures and complementary quantum-chemical studies of $(Ge_2As_2)^{2-}$, $(Ge_7As_2)^{2-}$, $[Ta@Ge_6As_4]^{3-}$, $[Ta@Ge_8As_4]^{3-}$ and $[Ta@Ge_8As_6]^{3-}$. The study makes use of efficient quantum-chemical tools, enabling the first detailed screening of the energy hypersurface along the formation of ligand-free inorganic species for a semi-quantitative picture. The results can be generalized for an entire family of multimetallic clusters.

[1] Fachbereich Chemie and Wissenschaftliches Zentrum für Materialwissenschaften, Universität Marburg, Hans-Meerwein-Straße, D-35043 Marburg, Germany. [2] Institut für Nanotechnologie, Karlsruher Institut für Technologie, Hermann-von-Helmholtz Platz 1, D-76344 Eggenstein-Leopoldshafen, Germany. Correspondence and requests for materials should be addressed to F.W. (email: florian.weigend@kit.edu) or to S.D. (email: dehnen@chemie.uni-marburg.de).

The evaluation of reaction mechanisms is not only useful but also essential for understanding, planning and optimizing chemical reactions in a reasonable and also efficient and economical way. In organic chemistry, this is a highly common procedure that allowed for the development of the retro-synthetic approach for systematic access of complex target molecules from simpler precursor fragments in the 1980s (ref. 1). However, neither this procedure nor any kind of systematic mechanistic study has so far been applied to the formation of inorganic molecules. Especially for polynuclear complexes or clusters, the formation mechanisms have widely remained unexplored to date. This is usually due to a poor structural relationship between reactants and product molecules. Furthermore, the flexibility of the metal atoms within a cluster regarding coordination numbers and geometry allows for a relatively quick re-organization, which usually prohibits monitoring of the processes and the detection of structurally related intermediates—at least in homoatomic cases, which lack any kind of 'tracer' atom.

Metal clusters in general have been subject of countless studies over the past decades, the more as monodisperse species came into sight as veritable and controllable quantum dots[2,3], which have also been used to generate novel nanostructured solids[4–6]. In particular, multimetallic clusters have attracted much attention by chemists and physicists in the recent past as they represent monodisperse intermetallic particles with superatom characteristics[7] and fine-tunable opto-eletronic as well as magnetic properties[8–10]. For this, these clusters can be viewed as molecular models to doped metals or bimetallic, catalytically active nanostructures[11,12].

However, the design of such clusters has appeared to be very challenging, since for reactions in condensed matter, the very first steps in the formation starting out from atomic, molecular or solid state precursors have essentially remained unexplored so far. It would thus be of great benefit to elucidate these processes to make such particles more generally available. A profound knowledge of all evolutionary steps would allow for overcoming the challenges of a reproducible synthesis, controlling the shape and size as well as the fine-tuning of chemical and physical properties.

A recently active investigated class of corresponding multimetallic compounds are intermetalloid clusters, that is, main-group (semi-)metal cages embedding transition metal atoms[13–16]. A large variety of different cluster structures has been presented over the last two decades, with ever larger and more complex architectures, that are usually obtained in solution by reaction of homoatomic or heteroatomic Zintl anions with transition metal complexes. Here, in some cases, intermediate complexes have been isolated that allowed for some understanding of the stepwise release of organic ligands from the used transition metal complexes[17–21], but it was not possible to trace back the complicated re-arrangement processes of the smaller Zintl anions in the presence of transition metal atoms.

The lack of knowledge regarding the relationship between reactants and products becomes particularly obvious for non-deltahedral cluster architectures including group 14 metal atoms[11,22–27], since all known precursors have been deltahedral main-group element polyanions so far.

Herein, we report on the synthesis and isolation of a series of compounds containing heterometallic or intermetalloid polyanions of different sizes, $(Ge_2As_2)^{2-}$, $(Ge_7As_2)^{2-}$, $[Ta@Ge_8As_4]^{3-}$ and $[Ta@Ge_8As_6]^{3-}$. During these studies, we additionally crystallized an unprecedented intermediate, $[Ta@Ge_6As_4]^{3-}$, of the corresponding intermetalloid cluster anions. This result prompted us to investigate the reaction by a systematic exploration of the energy hypersurface with recently developed tools for the search of low-lying minima in mixed-metallic systems[28] and for the optimization of transition pathways[29]. This way, we shed light on the complex formation processes behind non-deltahedral multimetallic clusters in a semi-quantitative manner.

Results

Experimental findings. The study started out with the synthesis of a precursor compound with a binary anion, $[K([2.2.2]crypt)]_2(Ge_2As_2)\cdot en$ (**1**), which was carried out according to the syntheses of homologous or isoelectronic compounds[30–34], by fusion of K, Ge and As (1:1:1) in Ta tubes at high temperatures, slow cooling to room temperature and subsequent extraction with *en*/[2.2.2]crypt at room temperature. The only difference from previous procedures was the application of a somewhat higher maximum temperature, 950 °C instead of 600 °C at the fusion step, which we initially chose in regard of the higher melting temperature of germanium as compared with those of tin or lead, and which turned out to be necessary to gain Ta atoms from the bulk (see below). As in many other cases before, we also crystallized a compound with a 9-atom binary polyanion from the extraction solution, $[K([2.2.2]crypt)]_2(Ge_7As_2)$ (**2**), and we detected a known homoatomic 10-atom cage $(Ge_{10})^{2-}$ (**A**)[35], along with **1** (compound **2** was also gained starting from a K/Ge/As phase generated in silica ampoules, indicating that Ta is not needed for its synthesis). However, the procedure also afforded two further compounds, which comprise ternary intermetalloid clusters with Ta atoms inside, $[K([2.2.2]crypt)]_3[Ta@Ge_6As_4]\cdot 2tol$ (**3**) and $[K([2.2.2]crypt)]_5[K([2.2.2]crypt)(en)][Ta@Ge_8As_4]_{1.21}[Ta@Ge_8As_6]_{0.79}\cdot en$ (**4**).

Obviously, the higher temperature at the beginning of the synthesis and the particular elemental combination enabled the reaction with the tube material and subsequent incorporation of Ta^{5+} (as confirmed by X-ray absorption spectroscopy (EDX) analyses of the resulting solid). The highly polarizing nature of the hard Ta^{5+} ion, which increases the covalent character of the bonds between transition metal and main-group (semi-) metal atoms, is made responsible in turn for the possibility to isolate fragmentary/intermediate complexes such as the anion in **3**. According structures are not likely to be isolated in the presence of less-polarizing cations, such as the Ln^{3+} series used before.

We thereupon developed a systematic access to these phases by addition of Ta powder. All four compounds were isolated from the extraction solution in single-crystalline form, and experimentally characterized by energy dispersive EDX (Supplementary Fig. 1, Supplementary Tables 1 and 2), X-ray diffraction (Fig. 1, Supplementary Figs 2–13, Supplementary Tables 3–7) and electrospray ionization mass spectrometry (ESI-MS, Supplementary Figs 14–26). The elucidation of single-crystal structures was not trivial here as it faced the following complications: (I) indistinguishability of Ge and As atoms by MoKα radiation, inhibiting the experimental assignment of Ge/As atomic positions, (II) positional disorder of the anions (**2** and **4**) and (III) co-crystallization of diverse anions of different structures (**3**) or composition (**4**), in the latter case arising along with complication (II).

From crystal structures to a sketched formation mechanism. Besides $[K([2.2.2]crypt]^+$ cations, the compounds comprise a tetrahedral $(Ge_2As_2)^{2-}$ anion (**1**), a nine-atom anion $(Ge_7As_2)^{2-}$ (**2**) with the topology of the well-known $(Ge_9)^{4-}$ cage[13], two different isomers of $[Ta@Ge_6As_4]^{3-}$ with so far unprecedented 10-atom architectures (**3**), as well as the clusters $[Ta@Ge_8As_4]^{3-}$ and $[Ta@Ge_8As_6]^{3-}$ (**4**). One of the co-crystallizing anions in **4** is based on a 12-atom cage with a rare non-deltahedral topology,

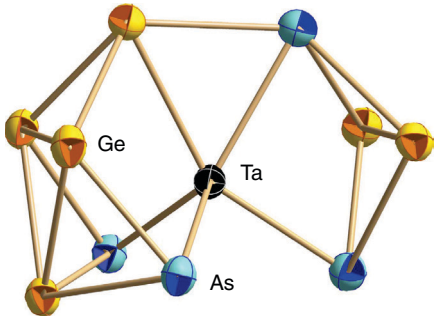

Figure 1 | Molecular structure of the predominant anionic component in 3. Thermal ellipsoids are shown at 50% probability. Selected distances [Å]: Ge/As–Ge/As 2.4770(7)-2.761(1); Ta–Ge/As 2.496(1)-2.719(1). Owing to non-distinguishability of Ge and As atoms for X-rays, the refinement was done based on the assignment of Ga or As atoms resulting from DFT calculations. The minority component isomer is shown in Supplementary Fig. 7b.

reported recently by Goicoechea and co-workers for the binary cluster $[Ru@Ge_{12}]^{3-}$ (ref. 36), and for $[V@Ge_8As_4]^{3-}$ produced in our lab[37]. The Ge/As shell of the second anion in **4** adopts the stable 14-atom enneahedron of main-group metals, which was observed recently for several lanthanide-centered examples, $[Ln@Sn_xBi_{14-x}]^{4-}$ (Ln/x = Eu/6; La/7, Ce/7)[25,26]. While the topology of the latter is known, the corresponding cluster in **4** comprises the smallest 14-atom cage known to date (Ø 5.7…5.8 Å), and it is the second intermetalloid cluster of this type that does not embed a lanthanide cation but a group 5 metal ion besides $[Nb@Ge_8As_6]^{3-}$ (ref. 37). Hence, whereas the topologies of the anions in **1**, **2** and **4** are known for other elemental compositions, neither the composition nor the structures of the anions in **3** have been known so far. Figure 1 shows the molecular structure of the predominant component (90%) of the two isomeric anions in **3** (for the minority component isomer, see Supplementary Fig. 7b). The crystal structures of all other anions are presented in Fig. 2 and in Supplementary Figs 3,5,10 and 11. Full crystallographic details can be gained from Supplementary Table 3 and Supplementary Data 1–4.

According to these results, the uncommon cluster structure can be described as being composed of two parts, a 6-atom (Ge_4As_2) unit and a 4-atom (Ge_2As_2) unit, attached to a Ta atom. As will be discussed in the following, we claim this anion to be the key species for the formation of non-deltahedral, multimetallic clusters. This leads us to the following general formation protocol (equation (1)) including all observed anionic compositions, as well as Ta metal (represented by atoms here):

$$\begin{aligned}&(\mathbf{Ge_2As_2})^{2-} + (\mathbf{Ge_{10}})^{2-} + \mathbf{Ta}\\ &\rightarrow (\mathbf{Ge_7As_2})^{2-} + \mathbf{Ta}\\ &\rightarrow [\mathbf{Ta@Ge_6As_4}]^{3-}\\ &\rightarrow [\mathbf{Ta@Ge_8As_6}]^{3-} + [\mathbf{Ta@Ge_8As_4}]^{3-} \qquad (1)\end{aligned}$$

to use the information gained so far for understanding of the formation mechanism along the steps indicated in the above equation, we systematically investigated the energy hypersurface of all of the given anions. This was realized with the programme system Turbomole[38] by a genetic algorithm (GA)[39–43] based on density functional theory (DFT) with the functional by Becke and Perdew, BP86 (refs 44, 45), and polarized split-valence basis sets, def-SVP (refs 46-48), and further employing the conductor-like

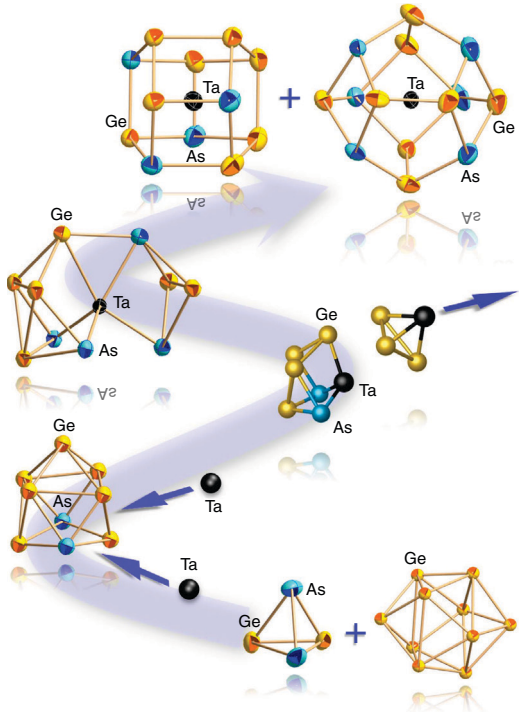

Figure 2 | Outline of the stepwise formation of non-deltahedral intermetalloid Ta/Ge/As clusters. The shown pathway starts out from the $(Ge_2As_2)^{2-}$ anions in **1** and the $(Ge_{10})^{2-}$ anion[40] (bottom) under consideration of all isolable species, hence the anions in **2** (2nd from bottom), in **3** (2nd from top) and in **4** (top), plus the calculated, hypothetic anions $[Ta@Ge_4As_2]^-$ and $(TaGe_3)^-$ (centre). The minimum structures of the latter are shown in a different style of representation for easier tracking.

screening model (COSMO)[49] with standard settings for charge compensation. Within the GA, one is faced with the problem of assigning Ge and As to the atomic positions in the energetically best way. This (re)assignment of atoms to places was done by first-order perturbation theory (RP), with the difference in nuclear charges of the two elements as perturbation parameter[50,51]. The resulting procedure, called GA-RP[28] was applied to all systems with the settings given in ref. 28. The resulting local minimum structures for each isomer were subsequently re-optimized employing the functional by Tao, Perdew, Staroverov and Scuseria, TPSS (ref 52), with polarized triple zeta valence basis sets[53] and Dirac-Hartree-Fock effective core potentials[54], dhf-TZVP, which for main-group element clusters yields results close to that of coupled-cluster calculations[55]. We note in passing that the influence of different types of functionals is small, barrier heights with BP86 are lower by typically 3.8 kJ mol^{-1}, maximal by 9.1 kJ mol^{-1}; differences to the functional by Perdew, Burke and Ernzerhof (PBE)[56] or to the hybrid functional by Tao, Perdew, Staroverov and Scuseria (TPSSh)[57] functionals are even smaller, see Supplementary Tables 8 and 9. The global minima obtained from the GA-RP procedures possess topologies that are identical with those of the experimentally determined structures throughout, and all structural parameters agree well. For the species $(Ge_2As_2)^{2-}$/$(Ge_7As_2)^{2-}$/$[Ta@Ge_6As_4]^{3-}$/$[Ta@Ge_8As_6]^{3-}$/$[Ta@Ge_8As_4]^{3-}$ the mean deviations amount to 0.027/0.019/0.012/0.017/0.033 Å, the maximum deviations to 0.062/0.097/0.037/0.074/0.104 Å. This indicates both the reliability of the

procedure for their identification and the reliability of TPSS/dhf-TZVP for the description of the energy hypersurface at 0 K (disregarding zero-point energy). For all cases of interest, connecting pathways between isomers were calculated with an iterative method based on a local quadratic approximation of the energy hypersurface[29]. Subsequently, all minima and maxima of two of these pathways were re-optimized, which leads to a small increase of energies for barriers (by ca. 2 kJ mol^{-1}). We convinced ourselves that all transitions in fact represent reaction coordinates. This was done by distorting each maximum along its imaginary mode in positive and negative direction and subsequently optimizing the distorted structures (minimum search). In all cases we verified that the two resulting structures are identical to the minimum structures right and left to the maximum. Moreover, thermal corrections from energies at 0 K to free enthalpies were calculated from partition sums within the standard harmonic oscillator approximation[58] for each molecule in the gas phase; vibrational frequencies were used non-scaled. The resulting data are given in Supplementary Figs 27 and 28, Supplementary Tables 10 and 11 for $T = 298$, 500, 700 and 900 K. For these temperatures, mean changes in barrier heights amount to $+0.6/+3.8/+6.4/+10.1$ kJ mol^{-1}, maximum changes to $+3.2/+7.7/+12.7/+18.3$ kJ mol^{-1}, respectively. The overall changes of the barrier heights resulting from the bare inspection of the pathway to those obtained when considering the above effects (individual optimization of minima/maxima, functional dependence and temperature dependence) thus are estimated to be smaller than 10 kJ mol^{-1} at room temperature and below 20 kJ mol^{-1} at $T = 900$ K; changes for relative energies of minima are even smaller. These—rather moderate—effects thus were not considered in the following and reaction barriers were taken directly from the optimized reaction pathways.

Furthermore, the GA-RP procedure was used to determine the global minimum structures of further fragments that resulted from hypothetic withdrawal of atoms from the experimentally observed larger clusters. Two of such hypothetical fragments, $[Ta@Ge_4As_2]^-$ and $(TaGe_3)^-$, turned out to be reasonable candidates for missing links in the reaction cascade, considered to form on interaction of $(Ge_7As_2)^{2-}$ with Ta atoms. They were, however, not detected in the experimental studies, presumably owing to their (high) reactivity. Figure 2 provides an illustration of the stepwise cluster formation as suggested based on the preliminary results regarding all of the named species and their topologies.

Deeper insight into the formation pathway. Although the relative amounts of isolated products are dependent to some extent on the K:Ge:As ratio of the reactants (besides an approximately constant amount of released Ta tube material of ca. 4%), the fusing temperature, the amount of solvent, the extraction time and the layering technique, it was not possible so far to isolate the separate species stepwise in real time. Mass spectrometry experiments indicate that the final clusters that co-crystallize in compound **4** can be already detected in the first spectrum recorded after injection of fresh extracts of the solid precursor phase. This indicates that either all of the detected species are formed side by side during cooling of the melt (the Ta-containing ones on contact of the K/Ge/As alloy with the Ta tube material or Ta powder), or that those reactions that occur in solution are rather quick. As explained and quantified below, the first steps leading from the anion in **1** through that in **2** to the first Ta-containing anion, $[Ta@Ge_4As_2]^-$, require higher temperatures, as they finally come along with the release of Ta atoms from Ta metal. The formation of the anion in **3** can follow in the solid or in solution at room temperature, given that *en* would sufficiently stabilize the $[Ta@Ge_4As_2]^-$ species. The last step, leading from the anion in **3** to the anions in **4**, is very likely a reaction in solution. For the processes being considerably rapid, we were definitely lucky to find a system that enabled the crystallization of reactants and diverse synthons along with the final products. Still, as more experimental information cannot be gained here due to the complicated and fast rearrangement processes within complex reaction mixtures, and owing to the lack of energetic information, a complementary quantum-chemical analysis of the formation process was necessary for a refined and at least semi-quantitative picture.

In this comprehensive study, we did not only consider all species mentioned above plus $(Ge_3As)^{3-}$ and $(As_2)^{2-}$ as additional leaving groups, but also the energetically higher isomers of the involved anions, which resulted from the GA-RP procedure; although the latter were not observed in stable crystals, they may play a role as reactive intermediates. Reaction energies were calculated for those steps of the reaction with atom- and charge-balance for educts and products, since only for these cases, the dependency of the calculated energy differences on the dielectric constant chosen in the COSMO approach is reasonably small (Supplementary Table 12). Reaction pathways were calculated with an iterative method based on a local quadratic approximation of the energy hypersurface[29].

Here, we will focus on three general aspects: First, the initial step that leads to the formation of the ubiquitous nine-atomic anion $(Ge_7As_2)^{2-}$ from the four-atomic and ten-atomic precursor anions $(Ge_2As_2)^{2-}$ and $(Ge_{10})^{2-}$. Second, the formation of the $[Ta@Ge_6As_4]^{3-}$ anion in **3** from $(Ge_7As_2)^{2-}$ through $[Ta@Ge_4As_2]^-$. These steps are apparently intuitive regarding the development of the structures (Fig. 2), thus we will use this part of the mechanism mainly to indicate the role of the transition metal atom. The final step to form $[Ta@Ge_8As_4]^{3-}$ and $[Ta@Ge_8As_6]^{3-}$ from $[Ta@Ge_6As_4]^{3-}$ lacks an according structural relationship. Hence, we explored the availability and the role of possible isomers of $[Ta@Ge_6As_4]^{3-}$ in the third part of the following discussion.

We note in advance that the formation pathway that we derived from our combined experimental and extensive quantum-chemical study represents only one of several possible routes, but obviously a very plausible one, as it is based on 'smooth' inter- or intramolecular re-arrangements; these are feasible with energies that are significantly smaller than those of uncompensated bond-breaking, like breaking an As–As bond in As_4, which amounts to 179 kJ mol^{-1} (calculated as $(E(As_4) - 4\,E(As))/6$) at level TPSS/dhf-TZVP), or breaking a Ge–Ge bond (188 kJ mol^{-1})[59]. The presented route leads to a topological relation between all structures therein, and as it also bridges to all previously known non-deltahedral clusters (see below).

Ta-independent first step. The co-existence of $(E^{14}{}_2E^{15}{}_2)^{2-}$, $(E^{14}{}_{10})^{2-}$ and $(E^{14}{}_7E^{15}{}_2)^{2-}$ anions in solutions of ternary $K/E^{14}/E^{15}$ phases[25,26,30,33,34] is very obvious, but has heretofore never been explained. Thus, we inspected this step in detail, which at the same time represents the initial step in the intermetalloid cluster formation pathway shown in Fig. 2. The energy difference for the formation of two $(Ge_7As_2)^{2-}$ anions from $(Ge_{10})^{2-}$ and two $(Ge_2As_2)^{2-}$ anions cannot be calculated reliably owing to missing charge balance (see above). For that, we performed the calculation with a total charge of 4– throughout, thus formally considering a partially oxidized precursor anion '$(Ge_2As_2)^-$'. The latter, which actually represents the electronic configuration of the species found under ESI-MS conditions, was calculated to be a global minimum with an elongated Ge…Ge

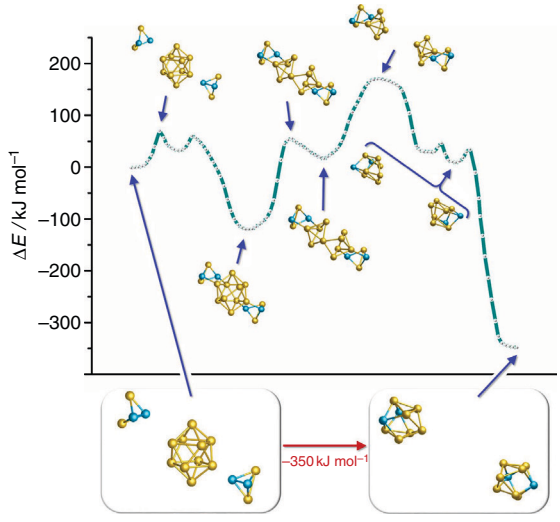

Figure 3 | Formation of two $(Ge_7As_2)^{2-}$ anions from $\{(Ge_2As_2)\ldots(Ge_{10})\ldots(Ge_2As_2)\}^{4-}$. The pathway was modelled based on the initial arrangement of three separate anions (bottom left), the final separate $(Ge_7As_2)^{2-}$ anions (bottom right) and an intermediate, local minimum structure, in which the two $(Ge_2As_2)^{-}$ species are attached to the $(Ge_{10})^{2-}$ cage in topologically reasonable way regarding the products (marked with an asterisk). Selected structures along the pathway are shown.

edge, according with the fact that the HOMO of $(Ge_2As_2)^{2-}$ represents the Ge–Ge bond. Although we cannot exclude that the oxidation takes place later on during this step, an early oxidation right at the beginning seems to be reasonable in terms of easier approach of the anionic species.

The reaction pathway from an initial arrangement of three separate species $\{(Ge_2As_2)\ldots(Ge_{10})\ldots(Ge_2As_2)\}^{4-}$ to the final arrangement of two separate anions $\{(Ge_7As_2)\ldots(Ge_7As_2)\}^{4-}$ (Fig. 3) was calculated[29] using 53 intermediate structures at level TPSS/dhf-TZVP (refs 52–54), including one intermediate optimized local minimum structure, in which the two (Ge_2As_2) species are attached to the (Ge_{10}) cage. An asterisk in Fig. 3 marks this intermediate. The chosen type of attachment is the one that requires minimum re-arrangement for the $(Ge_7As_2)^{2-}$ products (that is, further types of attachment cannot be excluded, but would cause higher barriers). The reaction pathway is summarized as follows. The intermediate is more stable than the initial arrangement by ca. 120 kJ mol^{-1}, and achievable by a small barrier of ca. 70 kJ mol^{-1} (and a second, smaller one). The final arrangement in turn is more stable than the intermediate by ca. 240 kJ mol^{-1}, but separated from the latter by two barriers, amounting to 180 kJ mol^{-1} and 160 kJ mol^{-1}, respectively (besides some further, much smaller ones). The first of the two barriers comes along with a significant break-up of the central Ge_{10} cage. The reason for a still rather small barrier in spite of the loss of a total of five Ge–Ge contacts can be explained by changes in nature and quality of the Ge–Ge bonds. The marked isomer exhibits electron-deficient multi-centre bonding, as reflected by an average coordination number of 4.8 for the 10 Ge atoms in the central part, whereas for the higher-energy state these atoms are in a nearly electron-precise situation with an average coordination number of 3.8 (including the exo-Ge–As bonds for both cases). Thus, the decreasing number of bonds is accompanied by an increasing bond order for the remaining bonds. The second barrier mainly reflects the cleavage of the remaining Ge–Ge bond between the two newly formed fragments. The dissociation energy is in the range of a Ge–Ge single bond (188 kJ mol^{-1}) (ref. 59). These newly formed fragments show a rather low-average coordination number (3.3), which increases to 3.6 as two pairs of Ge atoms approach each other (second image from right in Fig. 3) and finally to 4.0 in the nine-atom cages; the As atoms are three-bonded throughout the path before they turn into four-bonded ones during the final process. The entire reaction is exothermal by ca. 350 kJ mol^{-1}, and the barriers are conquerable in the high-temperature flux.

Inclusion of Ta and formation of the key anion in 3. Due to its shape, the $[Ta@Ge_6As_4]^{3-}$ anion in **3** is most reasonably described as $[Ta@Ge_4As_2]^{-}\cdot(Ge_2As_2)^{2-}$. This may be viewed as the result of an insertion of the $[Ta@Ge_4As_2]^{-}$ part of the anion in **3** into the As–As bond (that is, the LUMO) of the original $(Ge_2As_2)^{2-}$ tetrahedron. During this step, Ta is thus formally oxidized from a +3 to a +5 state. The fusion of these two parts to the anion in **3** is exothermic by 331 kJ mol^{-1} (Supplementary Table 12). The formation of the preceding species, $[Ta@Ge_4As_2]^{-}$, is intuitively considered as the reaction of Ta atoms with $(Ge_7As_2)^{2-}$ during the high-temperature reaction, as the former can be derived from the latter by replacement of a $(Ge_3)^{2-}$ ring with Ta; the $(Ge_3)^{2-}$ unit is thereby trapped by a second Ta atom to form $(TaGe_3)^{-}$ under 1-e^{-} oxidation; this species was not experimentally isolated; it should be reactive enough to immediately react with half an equivalent of $(As_2)^{2-}$, released in the formation of $[Ta@Ge_8As_4]^{3-}$ (see final step below) to form the experimentally proven $(Ge_3As)^{3-}$ anion (Supplementary Fig. 19). The formation of $[Ta@Ge_4As_2]^{-}$ and $(TaGe_3)^{-}$ from $(Ge_7As_2)^{2-}$ and two Ta atoms is exothermic by 903 kJ mol^{-1} (Supplementary Table 12). Of course, the Ta atoms need to be liberated previously from the bulk phase, that is, the wall of the reaction tube. The enthalpy of atomization of Ta metal amounts to 782 kJ mol^{-1} per atom[59], which may be the upper limit. However, for a surface atom, this energy is much smaller, in particular when considering defects like edges or corners. It should be significantly smaller than the dissociation energy of (formally) quadruple-bonded Ta_2, 504 kJ mol^{-1} (energy difference to separated atoms at TPSS/dhf-TZVP level), so that the overall reaction will be exothermic.

If the subsequent formation of **3** takes place in solution, that is, during or shortly on the extraction step, a chelating solvent—such as *en*—is absolutely essential to intermediately stabilize the quoted interim species like $[Ta@Ge_4As_2]^{-}$ or $(TaGe_3)^{-}$ by coordinating to the valence-unsaturated Ta atom; according *en* complexes are presumably not stable enough for detection (at least under the conditions that we applied in our measurements), but indeed, other solvents than *en* did not lead to any identifiable products in this study. Alternatively, all initial steps might already occur in the flux, such that the anions in **1–3** co-exist in the solid prior to extraction.

Independent from the very reaction conditions, the described process involves species with stepwise increasing formal oxidation state at the Ta atoms (0, +3 and +5), which is in line with the idea of successive redox cascades involving the transition metal atom.

Isomerization processes and final step. The formation of the two clusters in **4**, $[Ta@Ge_8As_4]^{3-}$ and $[Ta@Ge_8As_6]^{3-}$, is not possible starting from $[Ta@Ge_6As_4]^{3-}$ in its experimentally observed shape (see Fig. 1) as neither the topology nor the Ge/As distribution match. Instead, higher-energy isomers of $[Ta@Ge_6As_4]^{3-}$ with more suitable topologies and Ge/As distributions with regard to the larger clusters should be the reactive ones in subsequent reactions with $(Ge_2As_2)^{2-}$ (to obtain

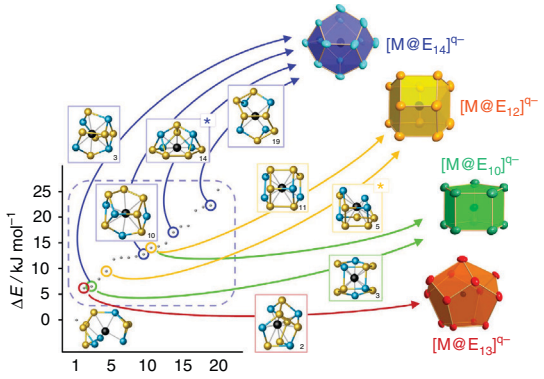

Figure 4 | Illustration of the low-energy re-arrangement of the anion in 3 to form isomers. In addition to the global minimum structure, the energies (dashed blue box) and selected structures of the 19 isomers following in energy are given. The drawn isomers represent exact fragments of the known non-deltahedral intermetalloid cluster topologies (for references see text). Two isomers are marked with an asterisk, symbolizing those that are discussed as direct precursors to the cluster with 12 atoms (isomer 5, yellow) or 14 atoms (isomer 14, blue), respectively.

the minimum structure of $[Ta@Ge_8As_4]^{3-}$ and $(As_2)^{2-}$ or the minimum structure of $[Ta@Ge_8As_6]^{3-}$ and $2e^-$). In principle, these isomers might form as kinetic products directly from the precursors $(Ge_2As_2)^{2-}$ and $(Ge_{10})^{2-}$, or the $(Ge_7As_2)^{2-}$ nine-atom cage in an alternative way than shown here; however, as this hypothesis requires much more assumptions and is not based on further experimental proof, we rather suggest a re-arrangement starting out from the experimentally observed global minimum structure of $[Ta@Ge_6As_4]^{3-}$.

For this purpose, we inspected the lowest 20 isomers resulting from the GA-RP procedure. These isomers are higher than the minimum by ca. 5–25 kJ mol^{-1}, thus their temporary existence is plausible. Many of them are fragments of regular $[M@E_n]$ anionic polyhedra ($n = 10$–14), that is, they have topologies fitting to all experimentally known non-deltahedral intermetalloid clusters containing tetrel atoms, as illustrated in Fig. 4. This finding extends the meaningfulness of this work to a more general understanding of multimetallic cluster formation.

As mentioned above, for a subsequent reaction to $[Ta@Ge_8As_4]^{3-}$ or to $[Ta@Ge_8As_6]^{3-}$, additionally a matching Ge/As distribution is required. This is the case, for the fifth-stable isomer of $[Ta@Ge_6As_4]^{3-}$ (isomer 5; +9 kJ mol^{-1}; marked with a yellow asterisk in Fig. 4), which is the lowest energy isomer representing an exact fragment of the experimentally found topology and global minimum Ge/As distribution of $[Ta@Ge_8As_4]^{3-}$. The latter (and additionally the reactive intermediate $(As_2)^{2-}$, see above) is formed from this fragment with $(Ge_2As_2)^{2-}$ in a near isoenergetic step (−1 kJ mol^{-1}). Similarly, the fourteenth-stable isomer (isomer 14; +17 kJ mol^{-1}; marked with a blue asterisk in Fig. 4) is identical to the upper part of the most favourable $[Ta@Ge_8As_6]^{3-}$ structure. Hence, for completion of this cluster, only a (Ge_2As_2) unit is lacking; since the latter is originally provided in its dianionic form, an oxidation has to take place. As this reaction thus yields different charges for educts and products, the corresponding energy could not be reliably calculated (see above). However, similar energetics can be expected as for the reaction towards $[Ta@Ge_8As_4]^{3-}$.

For the described steps, it remained to find possible pathways between the global minimum of $[Ta@Ge_6As_4]^{3-}$, our 'start structure', and the two most promising reactive species, the fifth and the fourteenth-stable isomer, called 'end structures'. Here, we started from an initial pathway consisting of 14 intermediate structures obtained from interpolation between start and end structure, followed by an iterative optimization; in each iteration the gradients are calculated for each of the 14 structures. The number of possible pathways between any two isomers of $[Ta@Ge_6As_4]^{3-}$ amounts to $6! \cdot 4! = 17{,}280$, as there are 6! ways to connect corresponding the 6 Ge atoms of the start and end structure, and similarly 4! ways for the 4 As atoms. For the two isomerizations, initial pathways were calculated for all possibilities; however, the costly optimization procedure was only carried out for those with interatomic distances not shorter than 1.6 Å for all atoms in all interpolated structures of the initial pathways. The discarded pathways will most probably not be favourable in the end, and furthermore, quantum-chemical calculations for atom distances far away from equilibrium are often problematic. For the remaining ca. 700 pathways (for each of the two isomerizations), 35 iterations were carried out with economic DFT settings BP86 (refs 44,45)/def-SVP (refs 46–48). Thereupon, the pathways with lowest barriers were refined with a larger number (53) of intermediate structures at the more accurate level TPSS/dhf-TZVP (refs 52–54) until convergence. For each of the two isomerizations, the finally resulting pathway with lowest barriers is shown in Fig. 5. Isomer 5 (fragment of $[Ta@Ge_8As_4]^{3-}$) can be reached from the global minimum via three barriers with heights of 76/63/46 kJ mol^{-1}. For isomer 14 (fragment of $[Ta@Ge_8As_4]^{3-}$), the first barrier amounts to 92 kJ mol^{-1}, followed by five barriers of 14/50/48/72/40 kJ mol^{-1}. All barriers are obviously high enough to allow for (low yield) crystallization of the $[Ta@Ge_6As_4]^{3-}$ anion in **3**, but also low enough to be finally overcome at the isomerization into suitable fragments as precursors of the two clusters in **4**. Interestingly, no direct pathway was found between isomer 5 and isomer 14, thus indicating that the subsequent reactions into the global minimum structures of $[Ta@Ge_8As_4]^{3-}$ or $[Ta@Ge_8As_6]^{3-}$, respectively (Supplementary Figs 29 and 30), are straight forward then.

One of the most important lessons we learned from these investigations is surprisingly obvious in its retrospective. Different from the preliminary assumption, and probably different from further suggestion on cluster formation pathways to be found in the literature, we deduce the following, general statement from our findings: clusters that are observed in crystalline 'intermediates' are not necessarily directly involved in further cluster growth, but they can play a key role in the reaction cascade upon isomerization, such as found in the present case. Here, several intermediate compositions co-exist in nearly isoenergetic isomeric forms, with higher-energy isomers being naturally more reactive—thus not being detectable or at least not isolable, and most probably being the species that are actually involved in the reaction cascade, whereas the global minimum species rather represent thermodynamic sinks. We note in passing that the exact tracing of the re-arrangement between the respective isomers was facilitated by the presence of two different elements in the present case.

With respect to the known charges of the involved species, a cascade of redox steps needs to be taken into consideration. A final overview of atom and electron balances along the pathway is provided in Fig. 6. Following our assumptions, we can explain the whereabouts of all electrons during the complex process—except for two electrons to be released at the initial step, which does not seem to be problematic regarding the variety of small polyanionic by-products formed alongside the reaction, detectable by means of ESI-mass spectrometry (Supplementary Figs 14,18 and 24).

In summary, our findings strongly suggest that the transition metal atoms come into play early in the cluster formation process,

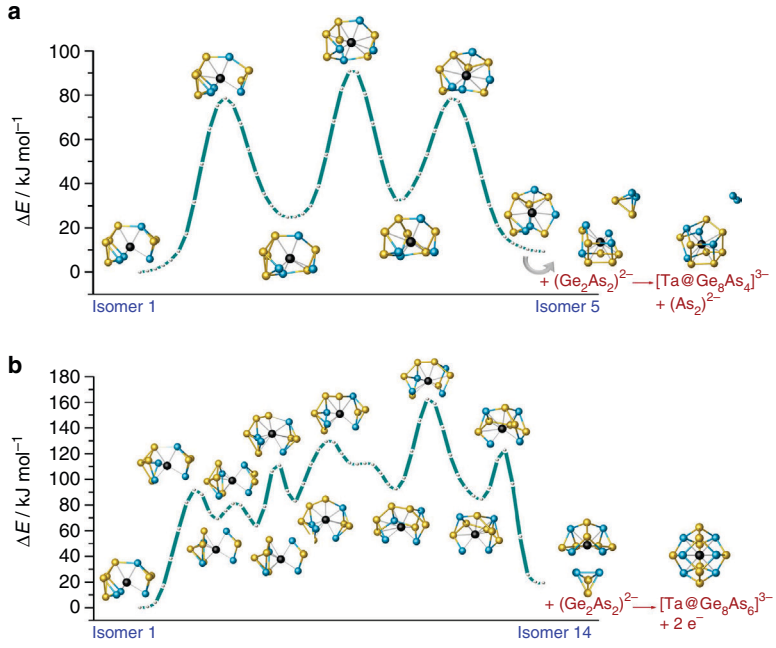

Figure 5 | Stepwise re-arrangements of the most stable anion isomer in 3. (**a**) Re-arrangement into isomer 5. (**b**) Rearrangement into isomer 14. The final topologies are suitable for uptake of another $(Ge_2As_2)^{2-}$ unit from **1** to form the clusters $[Ta@Ge_8As_4]^{3-}$ (top) or $[Ta@Ge_8As_6]^{3-}$ (bottom) in **4**. Detailed explanations are given in the text.

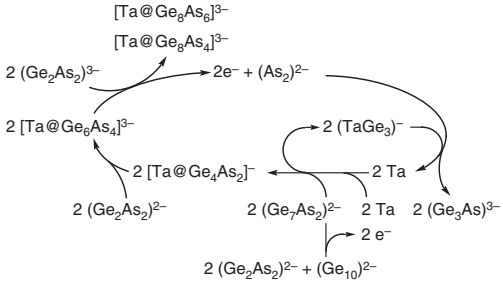

Figure 6 | Formation cycle for the generation of Ta/Ge/As clusters. The scheme gives an overview of atom and electron balances along the pathway for the formation of multimetallic clusters $[Ta@Ge_8As_6]^{3-}$ and $[Ta@Ge_8As_4]^{3-}$ starting out from $(Ge_2As_2)^{2-}$, $(Ge_{10})^{2-}$ and Ta.

that they are redox-active if delivered as neutral atoms, and that they are needed to weaken the bonds between the main-group atoms for easier fragmentation in their oxidized form. This clearly serves to explain the role of the transition metal atoms in such reactions in general, such that they can be viewed as catalysts triggering bond-breaking and bond-formation steps during the observed re-arrangements. Different from the behaviour of a common catalyst, at least a fraction of the transition metal atoms rather act as templates, such that they are finally surrounded by a rather stable, closed cluster shell, while another fraction seems to behave like a veritable catalyst, being involved in the formation of small fragments, which are anticipated to leave the formation pathway for being re-used again. Hence, we show that at least for the considered cluster family, the main-group atom shell is rather built stepwise around the transition metal atom instead of a transition metal atom entering a pre-formed, entire cluster shell.

Discussion

With this study, we contributed to a more detailed and at least semi-quantitative understanding of ligand-free, multimetallic cluster formation by providing deeper insight into possible processes. This was possible by a combination of new experimental findings on binary and ternary anionic clusters with comprehensive quantum-chemical investigations applying a new methodology (GA-RP)[28]. We identified several isomers of a previously unknown key synthon, which are topologically identical with exact fragments of all known non-deltahedral intermetalloid clusters containing tetrel atoms. Additionally, the study rationalized why all of the reactions of $(E^{14}{}_2E^{15}{}_2)^{2-}$ anions pass the $(E^{14}{}_7E^{15}{}_2)^{2-}$ step, and why and how these, as well as reactions that start out from $(E^{14}{}_9)^{4-}$, can proceed toward anions of the quoted type and composition by thorough screening of the energy hypersurface. This allowed shedding light on the formation of multimetallic clusters in general, not only for the compounds presented herein.

Our study still leaves room for further extension. In this regard, alternative pathways have to be explored that lead into other cluster families, such as the deltahedral ones. The uncountable variety of isomers with larger atom numbers and their re-arrangements into each other via energy barriers are likewise part of an exhaustive ongoing study, which has now become realistic by the development of the efficient methodology. The technique is applicable to all other systems dealing with binary or multinary cluster compounds, hence allowing for a detailed insight into cluster formation pathways. This way, we hope to finally contribute to a comprehensive understanding of inorganic reaction mechanisms in general, and to illuminate the former 'black box'.

Methods

General synthetic methods. All manipulations and reactions were performed under dry Ar atmosphere by using standard Schlenk or glovebox techniques. All

solvents were dried and freshly distilled prior to use. [2.2.2]crypt (4,7,13,16,21,24-Hexaoxa-1,10-diazabicyclo[8.8.8]hexacosane, purchased as Kryptofix 222 from Merck) was dried *in vacuo* for at least 18 h. The synthesis of ternary phases $K_1Ge_1As_x$ ($x = 0.5$, 1) were approached by fusing K, Ge and As in the respective stoichiometric ratios in a silica glass ampoule with an oxygen torch or in a tantalum ampoule within an oven at 950 °C, respectively.

Fusion reactions. The generation of a solid mixture with the nominal composition of 'KGeAs' was approached by combining K, Ge and As in equimolar amounts in a tantalum ampoule, which was sealed by arc-welding within the glove box. The ampoule was then placed in an oven for 48 h with initial heating to 950 °C and subsequent slow cooling to room temperature (heating and cooling rates of $50\,K\,h^{-1}$). The resulting solid was thoroughly ground in a mortar prior to further use As confirmed by EDX spectroscopy results (Supplementary Fig. 1a and Supplementary Table 1), the solid product contains ~4 atom-% of Ta. For this, the precursor phase will be denoted as 'KGeAs:Ta' (precursor phase 1) in the following. The synthesis of the 'KGeAs' solid was also performed in a silica glass ampoule with an oxygen torch (precursor phase 2). Results of EDX spectroscopy are provided in Supplementary Fig. 1b and Supplementary Table 1.

Conjoint synthesis of 1–4. A total of 150 mg (0.81 mmol) of 'KGeAs:Ta' (precursor phase 1) and 460 mg (1.22 mmol) of [2.2.2]crypt were weighed out into a Schlenk tube. Then 1,2-diaminoethane (*en*, 4 ml) was added to result in a dark red suspension. The reaction mixture was allowed to stir for 2 days. The liquid was filtered through a standard glass frit, yielding a red solution that was carefully layered by toluene (*tol*, 7 ml). Crystals of **1** form within 3 days. After 10 days, four distinct kinds of crystals (**1–4**) can be identified in the Schlenk tube (Supplementary Fig. 2). Due to the variety of crystals obtained in this reaction specific yields for **1–4** could not be determined with certainty. The overall yield of crystalline material is ~19% (based on [2.2.2]crypt). $[K([2.2.2]crypt)]_5[K([2.2.2]crypt)(en)][Ta@Ge_8As_4]_{1.21}[Ta@Ge_8As_6]_{0.79}\cdot en$ (**4**) is the major product of this reaction according to visual inspection of the Schlenk tube (~60% of crystalline material).

Conjoint synthesis of 1 and 2. For proving that the presence of Ta is not mandatory for the formation of salts of the $(Ge_2As_2)^{2-}$ and $(Ge_7As_2)^{2-}$ anion, 150 mg (0.81 mmol) of 'KGeAs' prepared in a silica glass ampoule (precursor phase 2) and 460 mg (1.22 mmol) of [2.2.2]crypt were weighed out into a Schlenk tube and then suspended in *en* (4 ml). The reaction mixture was allowed to stir for 1 day. The orange mixture was filtered through a standard glass frit, and the resulting solution was carefully layered by *tol* (7 ml). After 7 days, black-looking, block-like crystals of **2** as well as orange plates of **1** were obtained. On cutting the dark blocks into a size suitable for single-crystal X-ray diffraction, they split off into orange plates (Supplementary Fig. 2, centre), which had only been agglomerated. Due to the crystal mixture, specific yields for **1** and **2** could not be determined with certainty. The overall yield of crystalline material is ~24% (based on [2.2.2]crypt).

Energy dispersive X-ray spectroscopy analyses. EDX analyses were performed to support the elemental composition that was suggested based on the single-crystal X-ray diffraction experiments. These were carried out using an EDX-device Voyager 4.0 of Noran Instruments coupled with an electron microscope CamScan CS 4DV. Data acquisition was performed with an acceleration voltage of 20 kV and 100 s accumulation time. The radiation emitted by the atoms was analysed: K-K, Ge-K, As-K and Ta-M/L. To minimize surface effects in the measurement, the K-lines were preferably used to calculate the elemental composition.

The spectra measured on the precursor phases 1 and 2 are shown in Supplementary Fig. 1, the results are summarized in Supplementary Table 1. Supplementary Table 2 summarizes the results for the precursor phases and compounds **1–4**, respectively. The results of the EDX investigations confirm the element ratios of the investigated substances within the expected accuracy.

Crystallographic study of 1–4. Single-crystal X-ray diffraction data were collected on STOE imaging plate systems IPDS2 or IPDS2T, using graphite-monochromized Mo-Kα radiation ($\lambda_{Mo-K\alpha} = 0.71073$ Å) at 100 K. The structures were solved by direct methods, using SHELXS-97 (ref. 60) or SIR2011 (ref. 61), and refined by full-matrix-least-squares methods against F^2 with SHELXL-2013 software[60]. Crystal data: (**1**) $C_{38}H_{80}As_2Ge_2K_2N_6O_{12}$, $M_r = 1186.3$, triclinic, space group $P1$, $a = 10.9738(4)$ Å, $b = 11.9313(4)$ Å, $c = 12.6146(6)$ Å, $\alpha = 118.021(3)°$, $\beta = 108.361(4)°$, $\gamma = 96.476(3)°$, $V = 1{,}315.07(10)$ Å^3, $Z = 1$, $\rho_{calc} = 1.498\,g\,cm^{-3}$, $\mu(Mo_{K\alpha}) = 2.608\,mm^{-1}$, 23,683 reflections were measured, 10,275 of which were unique, $R(int) = 0.065$, R_1 ($I > 2\sigma(I)$) $= 0.0454$, wR_2 (all data) $= 0.1189$, S (all data) $= 1.075$. (**2**) $C_{36}H_{72}As_2Ge_7K_2N_4O_{12}$, $M_r = 1{,}489.14$, trigonal, space group $P\bar{3}c1$, $a = 11.8653(3)$ Å, $c = 22.3848(9)$ Å, $V = 2729.2(2)$ Å^3, $Z = 2$, $\rho_{calc} = 1.812\,g\,cm^{-3}$, $\mu(Mo_{K\alpha}) = 5.212\,mm^{-1}$, 3,581 reflections were measured, 1,942 of which were unique, $R(int) = 0.035$, R_1 ($I > 2\sigma(I)$) $= 0.0521$, wR_2 (all data) $= 0.1048$, S (all data) $= 0.958$. (**3**) $C_{68}H_{124}As_4Ge_6K_3N_6O_{18}Ta$, $M_r = 2347.19$, monoclinic, space group $P2_1/n$, $a = 13.7543(2)$ Å, $b = 28.6077(5)$ Å, $c = 22.9845(4)$ Å, $\beta = 92.489(1)°$, $V = 9{,}035.4(3)$ Å^3, $Z = 4$, $\rho_{calc} = 1.725\,g\,cm^{-3}$, $\mu(Mo_{K\alpha}) = 4.829\,mm^{-1}$, 148,425 reflections were measured, 19,185 of which were unique, $R(int) = 0.070$, R_1 ($I > 2\sigma(I)$) $= 0.0346$, wR_2 (all data) $= 0.0838$, S (all data) $= 0.884$. (**4**) $C_{56}H_{116}As_{4.79}Ge_8K_3N_8O_{18}Ta$, $M_r = 2{,}427.40$, triclinic, space group $P\bar{1}$, $a = 16.6082(5)$ Å, $b = 22.6960(8)$ Å, $c = 23.9068(8)$ Å, $\alpha = 94.960(3)°$, $\beta = 94.036(3)°$, $\gamma = 91.402(3)°$, $V = 8951.2(5)$ Å^3, $Z = 4$, $\rho_{calc} = 1.801\,g\,cm^{-3}$, $\mu(Mo_{K\alpha}) = 5.819\,mm^{-1}$, 64,236 reflections were measured, 31,253 of which were unique, $R(int) = 0.057$, R_1 ($I > 2\sigma(I)$) $= 0.0735$, wR_2 (all data) $= 0.1973$, S (all data) $= 0.990$. Further details are given in Supplementary Table 3. Cambridge Crystallographic Data Centre deposition codes are provided in the Accession codes section.

Details of the structure determination of 1. The structure of $[K([2.2.2]crypt)]_2[Ge_2As_2]\cdot en$ (**1**) comprises two independent $[K[2.2.2]crypt)]^+$ cations, a tetrahedral $(Ge_2As_2)^{2-}$ anion (Supplementary Fig. 3) and a disordered *en* molecule. The space group is indeed $P1$ with pseudo-symmetry $P\bar{1}$. The tetrahedral $(Ge_2As_2)^{2-}$ anion breaks the centro-symmetry. At $Z = 1$ it would appear disordered on the atomic positions of a cube in case of true centro-symmetry, which is not the case here. Since Ge and As cannot be distinguished by X-ray diffraction using Mo-Kα radiation, all four sites are half-occupied by Ge and As. Supplementary Table 4 summarizes interatomic distances and angles. The cations form a honeycombe-like packing with channels along a in which the $(Ge_2As_2)^{2-}$ anions are aligned together with the disordered *en* molecules (Supplementary Fig. 4).

Details of the structure determination of 2. Compound $[K([2.2.2]crypt)]_2[Ge_7As_2]$ (**2**) crystallizes in space group $P\bar{3}c1$ with the $[K[2.2.2]crypt)]^+$ cation on a threefold axis (site 3d) and the $(Ge_7As_2)^{2-}$ anion on the 2a site with symmetry 32 (D_3). The Ge/As occupation 7:2 as confirmed by mass spectrometry (MS) and density functional theory (DFT) investigations was fixed for each cluster atom. Around the 2a site, 24 metal positions could be located. This can be explained by orientational disorder of a 9-atom anion cluster (Supplementary Fig. 5a) over three positions generated by the threefold axis along [001] with Ge/As1 common for two orientations (Supplementary Fig. 5b). The large displacement ellipsoids let us assume that the C_2 axis (or C_4 axis with indistinguishable Ge/As) of the $(Ge_7As_2)^{2-}$ anion does not coincide exactly with the C_2 axes of the crystallographic 2a site. Thus the disorder model is really an overlay of six instead of three orientations and the refined geometry may appear adulterated, therefore. Supplementary Table 5 summarizes interatomic distances and angles. Similar to compound **1**, but with trigonal symmetry, the cations form a honeycombe-like packing with the disordered anions in channels along the c axis (Supplementary Fig. 6).

Details of the structure determination of 3. The structure of $[K([2.2.2]crypt)]_3[Ta@Ge_6As_4]\cdot 2tol$ (**3**) in space group $P2_1/n$ is built by a $[Ta@Ge_6As_4]^{3-}$ anion showing statistical overlay of two isomers with occupations of 87.7(1) and 12.3(1)% (Supplementary Fig. 7, Supplementary Table 6), three independent $[K([2.2.2]crypt)]$ cations (Supplementary Fig. 8) and two toluene solvent molecules. The interpretation of the disorder model of the anion isomers and attribution of Ge and As to the atom sites has been done based on theoretical calculations. The large anisotropic displacement parameters of Ge7A, Ge8A and Ge9A suggest additional orientational disorder of the tetrahedral $(Ge_3As)^{3-}$ group of isomer 2. The bond lengths in this region may therefore be adulterated. The left hand side of the isomer might derive from an intermediately formed $(Ge_6As_3)^-$ nine-atom cage, homologues of which had been observed in previous studies with Sn/Bi or Pb/Bi anions[25,26,34]. The formation of $(Ge_6As_3)^-$, in turn, is attributed on another relative orientation of $(Ge_2As_2)^{2-}$ and $(Ge_{10})^{2-}$ during the respective attack in the first step of the reaction cascade. The complicated packing of cations, anions and toluene molecules in compound **3** is shown in Supplementary Fig. 9.

Details of the structure determination of 4. The triclinic centrosymmetric structure of $[K([2.2.2]crypt)]_5[K([2.2.2]crypt)(en)][Ta@Ge_8As_4]_{1.21}[Ta@Ge_8As_6]_{0.79}\cdot en$ (**4**) shows severe disorder effects on the two independent anion positions as well as at some of the six independent cations. The anions are on two independent sites. On site one, superposition of a $[Ta@Ge_8As_4]^{3-}$ cluster (89.4%) and a $[Ta@Ge_8As_6]^{3-}$ cluster (10.6%) has been found. The occupations by Ge and/or As were taken according to information from EDX spectroscopy, mass spectrometry, the most stable configurations of DFT calculations and their probable disordered orientations (Supplementary Fig. 10). Bond lengths are given in Supplementary Table 7. On site 2, a $[Ta@Ge_8As_6]^{3-}$ cluster is dominating (68.5%) superimposed by a $[Ta@Ge_8As_4]^{3-}$ cluster in two different orientations (12.9 and 18.6%). By this complicated disorder with many approximately common positions, the individual geometrical data appear adulterated and are not listed, therefore. The structures are given in Supplementary Fig. 11. Five of the six cations are $[K[2.2.2](crypt)]$ cations like in the structures of compounds **1–3**. The refinement of these [2.2.2]crypt molecules in the presence of many heavy atoms was performed using geometrical restraints on the bond lengths and 1,3- distances. The anisotropic displacement ellipsoids show sometimes irregular shape as they include disorder effects (Supplementary Fig. 12a–d). They were refined with restraints to avoid too anisotropic displacement parameters. For one [2.2.2]crypt ligand with strong disorder, no sensible disorder model could be established. Its contribution was subtracted, therefore, by the back Fourier transform method from the data set. A sixth

cation has an *en* molecule coordinated to K^+ in addition to the [2.2.2]crypt ligand (Supplementary Fig. 12e). In addition, a non-coordinated *en* molecule was located. The packing of molecules in the structure of compound **4** is shown in Supplementary Fig. 13.

Electrospray ionization mass spectrometry investigations. ESI-MS measurements have been performed on a Finnigan LTQ-FT spectrometer by Thermo Fischer Scientific in the negative ion mode: Spray voltage 3.90 kV, capillary temperature 300 °C, capillary voltage −11 V, tube lens voltage −140 V, sheath gas flow rate 25 arb, sweep gas flow rate 0 arb. As it is common for Zintl anions and intermetallic cluster anions, the observed fragments have been detected as oxidized, singly charged species.

ESI-MS of the *DMF/en/*[2.2.2]crypt extract of 'KGeAs'. The ESI(−) mass spectrum of the extract of 'KGeAs' (precursor phase 2, prepared in a silica glass ampoule) in DMF/*en* in presence of [2.2.2]crypt was measured after 18 h of extraction time (Supplementary Fig. 14). The study confirms the concurrent presence of the singly charged cluster species $(Ge_2As_2H)^-$—(m/z = 296.69, Supplementary Fig. 15), obviously formed under ESI-MS conditions by protonation of the anion in **1,** as well as $(Ge_7As_2)^-$ (m/z = 658.29, Supplementary Fig. 16) side by side with $(Ge_{10})^-$ (m/z = 726.22, Supplementary Fig. 17) in the same solution. The concurrent presence of these polyanions strongly supports the assumption that the 9-atom cluster $(Ge_7As_2)^{2-}$ is the product of the reaction of two $(Ge_2As_2)^{2-}$ clusters with one $(Ge_{10})^{2-}$. Also adducts of K^+ and $[K([2.2.2]crypt)]^+$ were detected: $(Ge_7As_2K)^-$ (m/z = 697.26), $(Ge_{10}C_{18}H_{36}N_2O_6K$; m/z = 1141.44).

ESI-MS of the *en/*[2.2.2]crypt extract of 'KGeAs:Ta' . The ESI(−) mass spectra of the extract of 'KGeAs:Ta' (precursor phase 1, prepared in a Ta ampoule) in *en* in the presence of [2.2.2]crypt was measured after 3 h of extraction time. The overview spectrum (Supplementary Fig. 18) confirms the presence of a variety of clusters in solution. Remarkable is the presence anions of **1** and intermediate **3** in the solution after just 3 h of extraction. Due to fragmentation of the high-mass isotopic patterns and increasing degradation of the solution during injection the observed intensity of the isotopic pattern decreased during the measurement. In the reaction mixture, the presence of $(Ge_2As_2H)^-$ (m/z = 296.69) beside $(Ge_3As)^-$ (m/z = 292.68) was confirmed (Supplementary Fig. 19). The isotopic patterns of $(Ge_6As_4Ta)^-$ (m/z = 916.17), $(Ge_6As_4TaK)^-$ (m/z = 955.13) and $(Ge_6As_4TaK_2)^-$ (m/z = 994.09, Supplementary Figs 20–22) were identified as well as these of $[K([2.2.2]crypt)]^+$ adducts. In addition, the isotopic pattern of $(Ge_5As_3C_{18}H_{36}N_2O_6K_3)^-$ (m/z = 1082.5) was identified (Supplementary Fig. 23).

ESI-MS of a DMF/*en* solution of 4. In the spectrum, various anions with and without $[K([2.2.2]crypt)]^+$ were identified (Supplementary Fig. 24). The following species, representing oxidized clusters of $[Ta@Ge_8As_4]^{3-}$ and $[Ta@Ge_8As_6]^{3-}$ were found: $(Ge_8As_4TaC_{36}H_{72}N_4O_{12}K_2)^-$ (m/z = 1892.46, Supplementary Fig. 25) and $(Ge_8As_6TaC_{18}H_{36}N_2O_6K)^-$ (m/z = 1627.07, Supplementary Fig. 26).

Quantum-chemical methods. All calculations were done with the programme system TURBOMOLE (ref. 38). Global minimum searches were carried out with a DFT-based GA (refs 42,43) extended[28] by an atom-to-place re-assignment step[50,51] with the following settings: Population size $P = 20$ structures; cross-over after optimization of 10 structures, leading to the formation of $P = 10$ new (child) structures. The mutation probability was set to 1%. The procedure was stopped after 30 generations. Optimizations of reaction pathways were done with an iterative method based on a local quadratic approximation of the energy hypersurface[29]. For these steps bases of polarized split-valence quality, def-SV(P)[46,47] (with an effective core potential of Wood-Boring type for Ta (ref. 48) and the generalized gradient approximation DFT functional (BP86) by Becke[44] and Perdew[45] were chosen for reasons of economy. The resulting best structures and best pathways were re-optimized using more flexible polarized triple zeta valence basis sets dhf-TZVP (ref. 53; with an effective core potential of the Dirac-Hartree-Fock type for Ta)[54] and the meta-generalized gradient approximation functional by Tao, Perdew, Staroverov and Scuseria (TPSS)[52]. For comparison, also PBE[56] and TPSSh[57] functionals were applied, with the results given in Supplementary Tables 8, 9 and 12. For all cases, the negative charges of the clusters were compensated by using the COSMO[49], with the dielectric constant ε set to infinity (default). Thermochemical data were calculated from partition sums within the standard harmonic oscillator approximation for molecules in the gas phase[58]. The vibrational frequencies were used non-scaled. The RI approximation was used throughout[62]. Molecules were visualized with the programme CYLView[63].

References

1. Corey, E. J. The logic of chemical synthesis: multistep synthesis of complex carbogenic molecules (nobel lecture). *Angew. Chem. Int. Ed.* **30,** 455–465 (1991).
2. Okrut, A. *et al.* Selective molecular recognition by nanoscale environments in a supported iridium cluster catalyst. *Nat. Nanotechnol.* **9,** 459–465 (2014).
3. Bals, S. *et al.* Atomic scale dynamics of ultrasmall germanium clusters. *Nat. Commun.* **3,** 897 (2012).
4. Qian, M. *et al.* Cluster-assembled materials: toward nanomaterials with precise control over properties. *ACS Nano* **4,** 235–240 (2009).
5. Armatas, G. S. & Kanatzidis, M. G. Mesostructured Germanium with cubic pore Symmetry. *Nature* **441,** 1122–1125 (2006).
6. Guloy, A. *et al.* A guest-free germanium clathrate. *Nature* **443,** 320–323 (2006).
7. Luo, Z. & Castleman, A. W. Special and general superatoms. *Acc. Chem. Res.* **47,** 2931–2940 (2014).
8. Grubisic, A., Ko, Y. J., Wang, H. & Bowen, K. H. Photoelectron spectroscopy of lanthanide-silicon cluster anions $LnSi_n^-$ ($3 \leq n \leq 13$; Ln = Ho, Gd, Pr, Sm, Eu, Yb): prospect for magnetic silicon-based clusters. *J. Am. Chem. Soc.* **131,** 10783–10790 (2009).
9. Wagner, F. R., Noor, A. & Kempe, R. Ultrashort metal–metal distances and extreme bond orders. *Nat. Chem.* **1,** 529–536 (2009).
10. Kong, X.-J., Long, L.-S., Zheng, Z., Huang, R.-B. & Zheng, L.-S. Keeping the ball rolling: fullerene-like molecular clusters. *Acc. Chem. Res.* **43,** 201–209 (2010).
11. Korber, N. The Shape of germanium clusters to come. *Angew. Chem. Int. Ed.* **48,** 3216–3217 (2009).
12. Zhou, S., McIlwrath, K., Jackson, G. & Eichhorn, B. W. Enhanced CO tolerance for hydrogen activation in au–pt dendritic heteroaggregate nanostructures. *J. Am. Chem. Soc.* **128,** 1780–1781 (2006).
13. Fässler, T., Scharfe, S., Kraus, F., Stegmaier, S. & Schier, A. Zintl Ions, cage compounds, and intermetalloid clusters of group 14 and group 15 elements. *Angew. Chem. Int. Ed.* **50,** 3630–3670 (2011).
14. Butovskii, M. V. *et al.* Molecules containing rare-earth atoms solely bonded by transition metals. *Nat. Chem.* **2,** 741–744 (2010).
15. Lips, F. & Dehnen, S. $[Zn_6Sn_3Bi_8]^{4-}$: expanding the intermetalloid zintl anion concept to ternary systems. *Angew. Chem. Int. Ed.* **48,** 6435–6438 (2009).
16. Lips, F., Clérac, R. & Dehnen, S. $[Pd_3Sn_8Bi_6]^{4-}$: A 14-vertex Sn/Bi cluster embedding a Pd_3 triangle. *J. Am. Chem. Soc.* **133,** 14168–14171 (2011).
17. Wang, J.-Q., Stegmaier, S., Wahl, B. & Fässler, T. Step-by-step synthesis of the endohedral stannaspherene $[Ir@Sn_{12}]^{3-}$ via the capped cluster anion $[Sn_9Ir(cod)]^{3-}$. *Chem. Eur. J.* **16,** 1793–1798 (2010).
18. Moses, M. J., Fettinger, J. & Eichhorn, B. W. Charged molecular alloys: synthesis and characterization of the binary anions $Pd_7As_{16}^{4-}$ and $Pd_2As_{14}^{4-}$. *J. Am. Chem. Soc.* **124,** 5944–5945 (2002).
19. Kesanli, B. *et al.* Cluster growth and fragmentation in the highly fluxional platinum derivatives of Sn_9^{4-}: synthesis, characterization, and solution dynamics of $Pt_2@Sn_{17}^{4-}$ and $Pt@Sn_9H^{3-}$. *J. Am. Chem. Soc.* **129,** 4567–4574 (2007).
20. Schnöckel, H. Metalloid Al- and Ga-clusters: a novel dimension in organometallic chemistry linking the molecular and the solid-state areas? *Dalton Trans.* 3131–3136 (2005).
21. Benda, C. B., Waibel, M. & Fässler, T. F. On the formation of intermetalloid clusters: titanocene(III)diammin as a versatile reactant toward nonastannide zintl clusters. *Angew. Chem. Int. Ed.* **54,** 522–526 (2015).
22. Wang, J.-Q., Stegmaier, S. & Fässler, T. $[Co@Ge_{10}]^{3-}$: an intermetalloid cluster with archimedean pentagonal prismatic structure. *Angew. Chem. Int. Ed.* **48,** 1998–2002 (2009).
23. Zhou, B., Denning, M. S., Kays, D. L. & Goicoechea, J. M. Synthesis and isolation of $[Fe@Ge_{10}^{3-}]$: a pentagonal prismatic zintl ion cage encapsulating an interstitial iron atom. *J. Am. Chem. Soc.* **131,** 2802–2803 (2009).
24. Krämer, T. *et al.* Structural trends in ten-vertex endohedral clusters, $M@E_{10}$ and the synthesis of a new member of the family, $[Fe@Sn_{10}]^{3-}$. *Dalton Trans.* **42,** 12120–12129 (2013).
25. Lips, F., Clérac, R. & Dehnen, S. $[Eu@Sn_6Bi_8]^{4-}$: a mini-fullerane-type zintl anion containing a lanthanide ion. *Angew. Chem. Int. Ed.* **50,** 960–964 (2010).
26. Lips, F. *et al.* Doped semimetal clusters: ternary, intermetalloid anions $[Ln@Sn_7Bi_7]^{4-}$ and $[Ln@Sn_4Bi_9]^{4-}$ (Ln = La, Ce) with adjustable magnetic properties. *J. Am. Chem. Soc.* **134,** 1181–1191 (2012).
27. Weinert, B., Weigend, F. & Dehnen, S. Subtle impact of atomic ratio, charge and lewis basicity on structure selection and stability: the Zintl anion $[(La@In_2Bi_{11})(\mu\text{-}Bi)_2(La@In_2Bi_{11})]^{6-}$. *Chem. Eur. J.* **18,** 13589–13595 (2012).
28. Weigend, F. Extending DFT-based genetic algorithms by atom-to-place re-assignment via perturbation theory: a systematic and unbiased approach to structures of mixed-metallic clusters. *J. Chem. Phys.* **141,** 134103 (2014).
29. Plessow, P. Reaction path optimization without NEB springs or interpolation algorithms. *J. Chem. Theory Comput.* **9,** 1305–1310 (2013).
30. Critchlow, S. C. & Corbett, J. D. Heteropolyatomic anions of the post transition metals. Synthesis and structure of the ditindibismuthide(2–) anion, $Sn_2Bi_2^{2-}$. *Inorg. Chem.* **21,** 3286–3290 (1982).
31. Corbett, J. D. Polyatomic Zintl anions of the post-transition elements. *Chem. Rev.* **85,** 383–397 (1985).
32. Xu, L. i. & Sevov, S. C. Heteroatomic deltahedral clusters of main-group elements: synthesis and structure of the Zintl ions $[In_4Bi_5]^{3-}$, $[InBi_3]^{2-}$, and $[GaBi_3]^{2-}$. *Inorg. Chem.* **39,** 5383–5389 (2000).

33. Lips, F., Schellenberg, I., Pöttgen, R. & Dehnen, S. The subtle influence of binary versus homoatomic Zintl ions: the phenyl-ligated trimetallic cage $[Sn_2Sb_5(ZnPh)_2]^{3-}$. *Chem. Eur. J.* **15,** 12968–12973 (2009).
34. Ababei, R. *et al.* Making practical use of the pseudo-element concept: an efficient way to ternary intermetalloid clusters by an isoelectronic Pb^{-}–Bi combination. *Chem. Commun.* **48,** 11295–11297 (2012).
35. Belin, C., Mercier, H. & Angilella, V. Homoatomic polyanions of post transition elements. synthesis and structure of salts containing the decagermanide Ge_{10}^{2-} and the paramagnetic Ge_5^{3-} anions. *New J. Chem.* **15,** 931–938 (1991).
36. Espinoza-Quintero, G., Duckworth, J. C. A., Myers, W. K., McGrady, J. E. & Goicoechea, J. M. Synthesis and characterization of $[Ru@Ge_{12}]^{3-}$: an endohedral 3-connected cluster. *J. Am. Chem. Soc.* **136,** 1210–1213 (2014).
37. Mitzinger, S., Broeckaert, L., Massa, W., Weigend, F. & Dehnen, S. $[V@Ge_8As_4]^{3-}$ and $[Nb@Ge_8As_6]^{3-}$: unprecedented encapsulation of electron-poor transition metal atoms. *Chem. Commun.* **51,** 3866–3869 (2015).
38. TURBOMOLE 6.6, TURBOMOLE GmbH 2014. University of Karlsruhe and Forschungszentrum Karlsruhe, 1989-2007, TURBOMOLE GmbH since 2007.
39. Wales, D. J. & Doye, J. P. K. Global optimization by basin-hopping and the lowest energy structures of Lennard-Jones clusters containing up to 110 atoms. *J. Phys. Chem. A* **101,** 5111–5116 (1997).
40. Froemming, N. S. & Henkelman, G. Optimizing core-shell nanoparticle catalysts with a genetic algorithm. *J. Chem. Phys.* **131,** 234103 (2009).
41. Hartke, B. Geometry optimization of clusters using genetic algorithms. *J. Phys. Chem.* **97,** 9973–9976 (1993).
42. Deaven, D. M. & Ho, K. M. Molecular geometry optimization with a genetic algorithm. *Phys. Rev. Lett.* **75,** 288–291 (1995).
43. Sierka, M. *et al.* Unexpected structures of aluminum oxide clusters in the gas phase. *Angew. Chem. Int. Ed.* **46,** 3372–3375 (2007).
44. Becke, A. D. Density-functional exchange-energy approximation with correct asymptotic behavior. *Phys. Rev. A* **38,** 3098–3100 (1988).
45. Perdew, J. P. Density-functional approximation for the correlation energy of the inhomogeneous electron gas. *Phys. Rev. B* **33,** 8822–8824 (1986).
46. Schäfer, A., Horn, H. & Ahlrichs, R. Fully optimized contracted Gaussian basis sets for atoms Li to Kr. *J. Chem. Phys.* **97,** 2571 (1992).
47. Eichkorn, K., Weigend, F., Treutler, O. & Ahlrichs, R. Auxiliary basis sets for main row atoms and transition metals and their use to approximate coulomb potentials. *Theor. Chem. Acc.* **97,** 119–124 (1997).
48. Andrae, D., Haeussermann, U., Dolg, M., Stoll, H. & Preuss, H. Energy-adjusted ab initio pseudopotentials for second and third row transition elements. *Theor. Chim. Acta* **77,** 123–141 (1990).
49. Klamt, A. & Schüürmann, G. COSMO: a new approach to dielectric screening in solvents with explicit expressions for the screening energy and its gradient. *J. Chem. Soc. Perkin Trans.* **2,** 799–805 (1993).
50. Weigend, F., Schrodt, C. & Ahlrichs, R. Atom distributions in binary atom clusters: a perturbational approach and its validation in a case study. *J. Chem. Phys.* **121,** 10380–10384 (2004).
51. Weigend, F. & Schrodt, C. Atom-type assignment in molecules and clusters by perturbation theory—a complement to X-ray structure analysis. *Chem. Eur. J.* **11,** 3559–3564 (2005).
52. Tao, J., Perdew, J. P., Staroverov, V. N. & Scuseria, G. E. Climbing the density functional ladder: nonempirical meta–generalized gradient approximation designed for molecules and solids. *Phys. Rev. Lett.* **91,** 146401 (2003).
53. Weigend, F. & Baldes, A. Segmented contracted basis sets for one- and two-component Dirac-Fock effective core potentials. *J. Chem. Phys.* **133,** 174102 (2010).
54. Figgen, D., Peterson, K. A., Dolg, M. & Stoll, H. Correlation consistent basis sets: the transition metals Hf—Pt. *J. Chem. Phys.* **130,** 164108 (2009).
55. Drebov, N., Weigend, F. & Ahlrichs, R. Structures and properties of neutral gallium clusters: a theoretical investigation. *J. Chem. Phys.* **135,** 044314 (2011).
56. Perdew, J. P., Burke, K. & Ernzerhof, M. Generalized gradient approximation made simple. *Phys. Rev. Lett.* **77,** 3865–3868 (1996).
57. Staroverov, V. N., Scuseria, G. E., Tao, J. & Perdew, J. P. Comparative assessment of a new nonempirical density functional: molecules and hydrogen-bonded complexes. *J. Chem. Phys.* **119,** 12129–12137 (2003).
58. McQuarrie, D. A. & Simon, J. D. *Molecular Thermodynamics* ISBN 978-1891389054 (University Science Books, 1999).
59. James, A. M. & Lord, M. P. in *Macmillan's Chemical and Physical Data* (Macmillan, 1992).
60. Sheldrick, G. M. A short history of SHELX. *Acta Crystallogr.* **A64,** 112–122 (2008).
61. Burla, M. C. *et al.* SIR2011: a new package for crystal structure determination and refinement. *J. Appl. Crystallogr.* **45,** 357–361 (2012).
62. Weigend, F. Accurate coulomb-fitting basis sets for H to Rn. *Phys. Chem. Chem. Phys.* **8,** 1057–1065 (2006).
63. Legault, C. Y. CYLView. 1.0b (Université de Sherbrooke, 2009).

Acknowledgements

This work was supported by the Alexander von Humboldt Foundation, the Friedrich-Ebert-Stiftung and the Deutsche Forschungsgemeinschaft (DFG). We thank R. Riedel for X-ray data collection.

Author contributions

S.M. conceived and performed the synthetic experiments and further analyses (XRD, EDX spectroscopy and ESI-mass spectrometry). W.M. solved and refined the structures. L.B. and F.W. planned and performed all quantum-chemical investigations. S.D. co-planned and supervised the work. All authors co-wrote the paper.

Additional information

Accession codes: The X-ray crystallographic coordinates for structures reported in this Article have been deposited at the Cambridge Crystallographic Data Centre, under deposition numbers 1016136-1016139. These data can be obtained free of charge from The Cambridge Crystallographic Data Centre via www.ccdc.cam.ac.uk/data_request/cif.

Supplementary Information accompanies this paper at http://www.nature.com/naturecommunications

Competing financial interests: The authors declare no competing financial interests.

Reprints and permission information is available online at http://npg.nature.com/reprintsandpermissions/

How to cite this article: Mitzinger, S. *et al.* Understanding of multimetallic cluster growth. *Nat. Commun.* 7:10480 doi: 10.1038/ncomms10480 (2016).

Supporting Information

Understanding of Multimetallic Cluster Growth

Stefan Mitzinger,[a] Lies Broeckaert,[a,b] Werner Massa,[a] Florian Weigend,*[b] and Stefanie Dehnen*[a]

[a] Fachbereich Chemie, Wissenschaftliches Zentrum für Materialwissenschaften, Philipps-Universität Marburg, Hans-Meerwein-Straße, 35043 Marburg, Germany, email: dehnen@chemie.uni-marburg.de;

[b] Institut für Nanotechnologie, Karlsruher Institut für Technologie (KIT) Hermann-von-Helmholtz-Platz 1, 76344 Eggenstein-Leopoldshafen, Germany, email: florian.weigend@kit.edu

Contents:

1. Synthesis details

1.1 General remarks

All manipulations and reactions were performed under dry Ar atmosphere by using standard Schlenk or glovebox techniques. All solvents were dried and freshly distilled prior to use. [2.2.2]crypt[1] (Merck) was dried *in vacuo* for at least 18 h.

1.1 Fusion reactions and energy dispersive X-ray spectroscopy (EDX) analyses

The generation of a solid mixture with the nominal composition of “KGeAs” was approached by combining K, Ge and As in equimolar amounts in a tantalum ampoule, which was sealed by arc-welding within the glove box. The ampoule was then placed in an oven for 48 hours, with initial heating to 950 °C and subsequent slow cooling to room temperature (heating and cooling rates of 50 K/h). The resulting solid was thoroughly ground in a mortar prior to further use As confirmed by energy dispersive X-ray (EDX) spectroscopy results (Figure S1, top, and Table S1), the solid product contains approximately 4 atom-% of Ta. For this, the precursor phase will be denoted as “KGeAs:Ta” (precursor phase 1) in the following.

The synthesis of the “KGeAs” solid was also performed in a silica glass ampoule with an oxygen torch (precursor phase 2). Results of EDX spectroscopy are provided in Figure 1, bottom, and Table S1.

The EDX experiments were carried out on powder samples, using an EDX-device Voyager 4.0 of Noran Instruments coupled with an electron microscope CamScan CS 4DV. Data acquisition was performed with an acceleration voltage of 20 kV and 100 s accumulation time. The radiation emitted by the atoms was analyzed: K-K, Ge-K, As-K. To minimize surface effects in the measurement, the K-line of As was used to calculate the elemental composition.

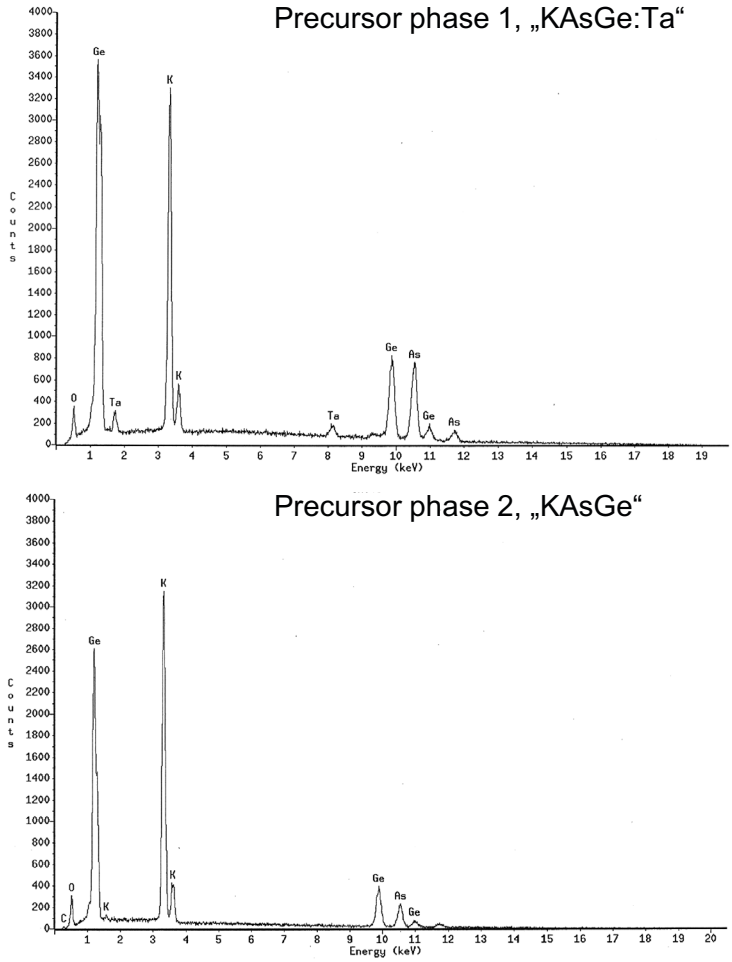

Figure S1. EDX spectra of the solid products upon melting a K:Ge:As mixture (1:1:1) in a T ampoule (precursor phase 1, top), or in a silica glass ampoule (precursor phase 2, bottom).

Table S1. EDX analysis results of the solid products upon melting a K:Ge:As mixture (1:1:1) in a Ta ampoule (precursor phase 1), or in a silica glass ampoule (precursor phase 2).

Element	k-ratio	ZAF	Atom%	Ratio	wt %	wt % Err.
Precursor phase 1						
K-K	0.1808	1.210	36.44	1.24 (1)	21.88	+/- 0.19
Ge-K	0.2704	1.260	30.56	1.04 (1)	34.07	+/- 0.33
As-K	0.3245	1.037	29.26	1.00 (1)	33.67	+/- 1.00
Ta-M	0.0410	2.531	3.73	0.08	10.38	+/- 0.37
Total			100	3.28 (3)	100	
Precursor phase 2						
K-K	0.2251	1.169	40.22	1.42 (1)	15.61	+/- 0.47
Ge-K	0.3616	1.056	31.44	1.11 (1)	61.24	+/- 2.99
As-K	0.3352	1.060	28.34	1.00 (1)	23.15	+/- 3.01
Total			100	3.54 (3)	100	

1.3 Conjoint Synthesis of [K([2.2.2]crypt)]$_2$[Ge$_2$As$_2$]·en (1), [K([2.2.2]crypt)]$_2$[Ge$_7$As$_2$] (2), [K([2.2.2]crypt)]$_3$[Ta@Ge$_6$As$_4$]·2tol (3), and [K([2.2.2]crypt)]$_5$[K([2.2.2]crypt)(en)][Ta@Ge$_8$As$_4$]$_{1.21}$[Ta@Ge$_8$As$_6$]$_{0.79}$·en (4)

150 mg (0.81 mmol) of "KGeAs:Ta" (precursor phase 1) and 460 mg (1.22 mmol) of [2.2.2]crypt were weighed out into a Schlenk tube. Then *en* (1,2-diaminoethane, 4 mL) was added to result in a dark red suspension. The reaction mixture was allowed to stir for 2 days. The liquid was filtered through a standard glass frit, yielding a red solution that was carefully layered by toluene (*tol*, 7 mL). After 10 days, four distinct kinds of crystals were identified in the Schlenk tube (Figure S2):

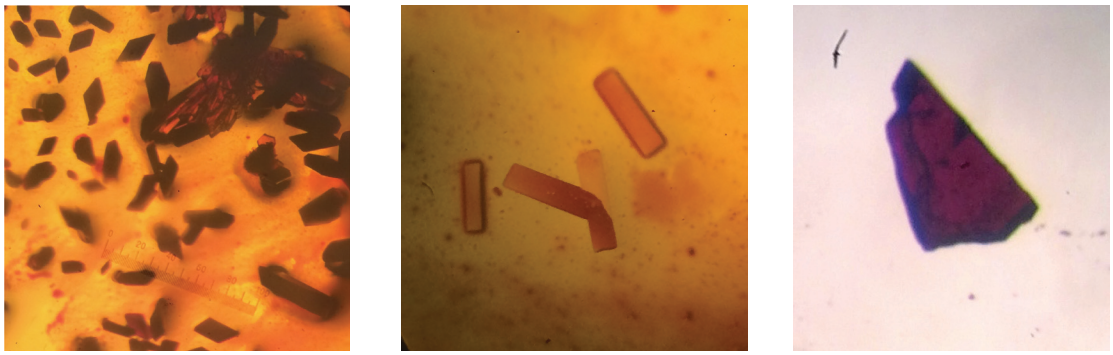

Figure S2. Rhombic, dark crystals of **4** along with stacked plate-shaped, red crystals of **1** (left), rectangular, orange-red crystals of **2** (center), and red, block-type single crystal of **3** (right).

Due to the variety of crystals obtained in this reaction specific yields for **1** - **4** could not be determined with certainty. The overall yield of crystalline material is approx. 19% (based on [2.2.2]crypt). [K([2.2.2]crypt)]$_5$[K([2.2.2]crypt)(en)][Ta@Ge$_8$As$_4$]$_{1.21}$-[Ta@Ge$_8$As$_6$]$_{0.79}$·en (**4**) is the major product of this reaction according to visual inspection of the Schlenk tube (approx. 60% of crystalline material).

1.4 Conjoint Synthesis of [K([2.2.2]crypt)]$_2$[Ge$_2$As$_2$]·en (1) and [K([2.2.2]crypt)]$_2$[Ge$_7$As$_2$] (2)

For proving that the presence of Ta is *not* mandatory for the formation of salts of the [Ge$_2$As$_2$]$^{2-}$ and [Ge$_7$As$_2$]$^{2-}$ anion, 150 mg (0.81 mmol) of "KGeAs" prepared in a silica glass ampoule (precursor phase 2) and 460 mg (1.22 mmol) of [2.2.2]crypt were weighed out into a Schlenk tube and then suspended in *en* (4 mL). The reaction mixture was allowed to stir for 1 day. The orange mixture was filtered through a standard glass frit, and the resulting solution was carefully layered by *tol* (7 mL). After 7 days, black-looking, block-like crystals of **2** as well as orange plates of **1** were obtained. On cutting

the dark blocks into a size suitable for single-crystal X-ray diffraction (SCXD), they split off into orange plates (see Figure S2, center), which had only been agglomerated. Due to the crystal mixture, specific yields for **1** and **2** could not be determined with certainty. The overall yield of crystalline material is approx. 24% (based on [2.2.2]crypt).

2. Single crystal X-ray crystallography

The data for the X-ray structural analyses were collected at T = 100(2) K with Mo-K_α-radiation ($\lambda_{Mo\text{-}K\alpha}$= 0.71073 Å) on area detector systems Stoe IPDS/2T or Stoe IPDS/2 . The structures were solved by direct methods (SHELXS-97[1] or SIR2011[2]), and refined by full-matrix-least-squares methods against F^2 with program SHELXL-2013.[1] Crystallographic data for the four structures reported in this paper have been deposited with the Cambridge Crystallographic Data Center as supplementary publications nos. CCDC-1016136–1016139. The crystal data and experimental parameters of the structure determinations are collected in Table S2.

Table S2. Crystallographic data for the X-ray structure analyses of compounds **1 - 4**

Compound	1	2	3	4
empirical formula	$C_{38}H_{80}As_2Ge_2K_2N_6O_{12}$	$C_{36}H_{72}As_2Ge_7K_2N_4O_{12}$	$C_{68}H_{124}N_6O_{18}K_3Ge_6As_4Ta$	$C_{56}H_{116}N_8O_{18}K_3As_{4.79}Ge_8Ta$
formula weight [g mol^{-1}]	1186.30	1489.14	2347.19	2427.40
crystal color, shape	orange block	orange block	red plate	black block
crystal size [mm^3]	0.34×0.28×0.19	0.32×0.30×0.20	0.50×0.33×0.12	0.30×0.09×0.08
crystal system	triclinic	trigonal	monoclinic	triclinic
space group	$P\bar{1}$	$P\bar{3}c1$	$P2_1/n$	$P\bar{1}$
a [Å]	10.9738(4)	11.8653(3)	13.7543(2)	16.6082(5)
b [Å]	11.9313(4)	11.8653(3)	28.6077(5)	22.6960(8)
c [Å]	12.6146(6)	22.3848(9)	22.9845(4)	23.9068(8)
α [°]	118.021(3)			94.960(3)
β [°]	108.361(4)		92.489(1)	94.036(3)
γ [°]	96.476(3)			91.402(3)
V [Å^3]	1315.07(10)	2729.2(2)	9035.4(3)	8951.2(5)
Z, ρ_{calc} [g cm^{-3}]	1	2	4	4
μ ($Mo_{K\alpha}$) [mm^{-1}]	2.608	5.212	4.829	5.819
absorption correction type	Gaussian	Gaussian	Gaussian	Gaussian
2θ range [°]	2.68-26.82	1.82-26.76	1.42-26.80	2.55-25.00
total reflns	23683	3581	148425	64236
unique reflns [R_{int}]	10275 [0.065]	1942 [0.034]	19185 [0.070]	31253 [0.057]
obs. reflns [$I > 2\sigma(I)$]	9372	783	13496	16662
parameters	579	119	982	1597
R_1 [$I > 2\sigma(I)$]	0.0454	0.0521	0.0346	0.0735
wR_2 (all data)	0.1189	0.1048	0.0795	0.1973
GooF (all data)	1.076	0.958	0.884	0.991
max peak/hole, [e Å^{-3}]	1.17/ -0.80	0.65/ -0.45	1.20/ -0.62	3.38/ -1.72

2.1 Details of the structure determination of [K([2.2.2]crypt)]$_2$[Ge$_2$As$_2$]·en (1)

The structure is built by two independent [K[2.2.2]crypt)] cations, a tetrahedral $(Ge_2As_2)^{2-}$ anion (Figure S3), and a disordered *en* molecule. The space group is indeed *P*1 with pseudo-symmetry $P\bar{1}$. The tetrahedral $(Ge_2As_2)^{2-}$ anion breaks the centro-symmetry. At *Z* = 1 it would appear disordered on the atomic positions of a cube in case of true centro-symmetry, which is not the case here. As Ge and As cannot be distinguished by X-ray diffraction using MoKα radiation, all four sites were half-occupied by Ge and As. Table S3 summarized interatomic distances and angles.

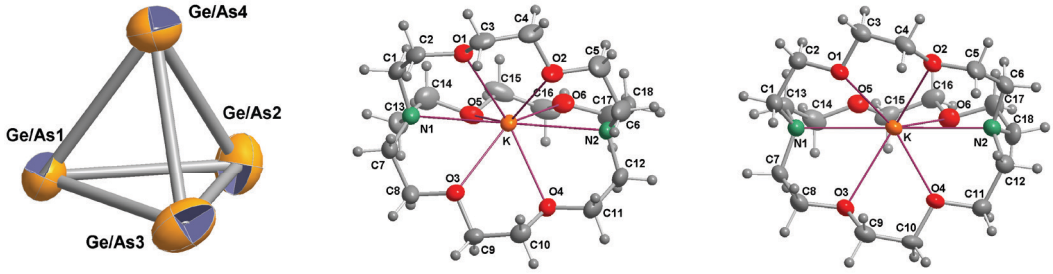

a **b** **c**

Figure S3. a) $[Ge_2As_2]^{2-}$ Anion in (**1**). b) Cation 1 in (1). c) Cation 2 in (1) Displacement ellipsoids at the 50% probability level.

Table S3. Interatomic distances /Å in the $(Ge_2As_2)^{2-}$ anion. Angles are 58.30(3) – 62.71(3)°.

atom numbers		atom numbers	
1 – 2	2.459(1)	2 – 4	2.568(1)
1 – 3	2.503(1)	3 – 4	2.517(1)
1 – 4	2.477(1)		
2 – 3	2.572(1)	average	**2.516(1)**

The cations form a honeycombe-like packing with channels along *a* in which the $[Ge_2As_2]^{2-}$ anions are aligned together with the disordered *en* molecules (Figure S4).

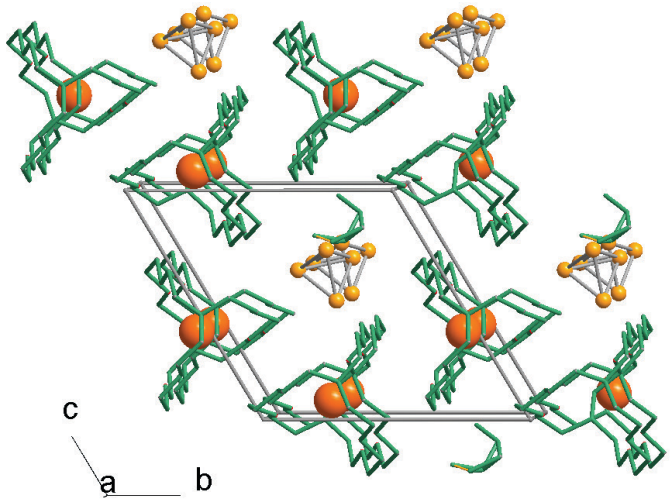

Figure S4. Packing in the structure of compound **1**. Arbitrary radii: Ge/As yellow, K orange, cryptand ligands and *en* green wire-model.

2.2 Details of the structure determination of [K([2.2.2]crypt)]$_2$[Ge$_7$As$_2$] (2)

Structure (**2**) crystallizes in space group $P\bar{3}c1$ with the [K[2.2.2]crypt)] cation on a 3-fold axis (site 3d) and the (Ge_7As_2) Anion on the 2a site with symmetry 32.(D_3).
The Ge/As occupation 7:2 as confirmed by MS and DFT investigations was fixed for each cluster atom. Around the 2a site, 24 metal positions (see Figure S5b) could be located. This can be explained by orientational disorder of a 9-atom anion cluster (Figure S5a) over three positions generated by the 3-fold axis along [001] with Ge/As1 common for two orientations (Figure S5b). The large displacement ellipsoids let us assume that the C2 axis (or C4 axis with indistinguishable Ge/As) of the [Ge7As2] anion does not coincide exactly with the C2 axes of the crystallographic 2a site. Thus the disorder model is really an overlay of six instead of three orientations and the refined geometry may appear adulterated, therefore. Table S4 summarized interatomic distances and angles.

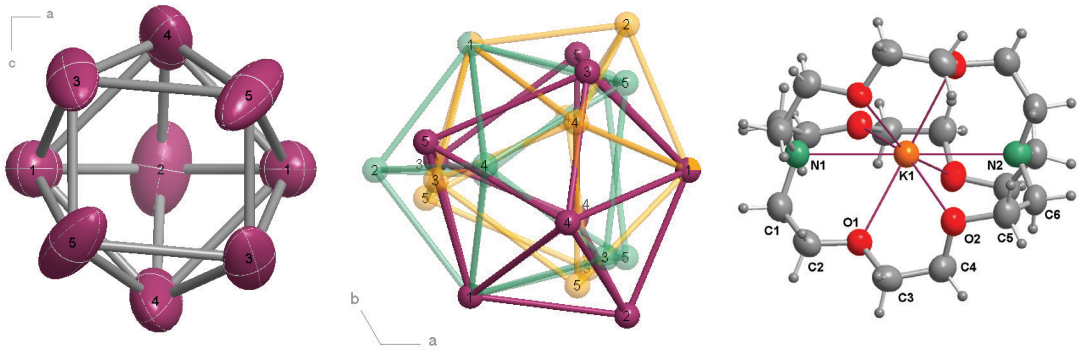

a **b** **c**

Figure S5. a) $(Ge_7As_2)^{2-}$ anion in (**2**) projected along the 2-fold axis. Displacement ellipsoids at the 50% probability level. b) The three orientations of the anion generated by the 3-fold axis (arbitrary radii). c) C_3-symmetric cation in (**2**). Displacement ellipsoids at the 50% probability level.

Table S4. Interatomic distances /Å in the $(Ge_7As_2)^{2-}$ anion (Figure S4a).

atom numbers		atom numbers	
1 – 2	2.416(3)	2 – 4	2.612(5)
1 – 3	2.542(5)	3 – 4	2.409(7)
1 – 4	2.729(3)	3 – 5	2.708(9)
1 – 5	2.696(5)	4 – 5	2.643(8)
		average	**2.594**

Similar to compound **1**, but with trigonal symmetry, the cations form a honeycombe-like packing with the disordered anions in channels along the *c* axis (see Figure S6).

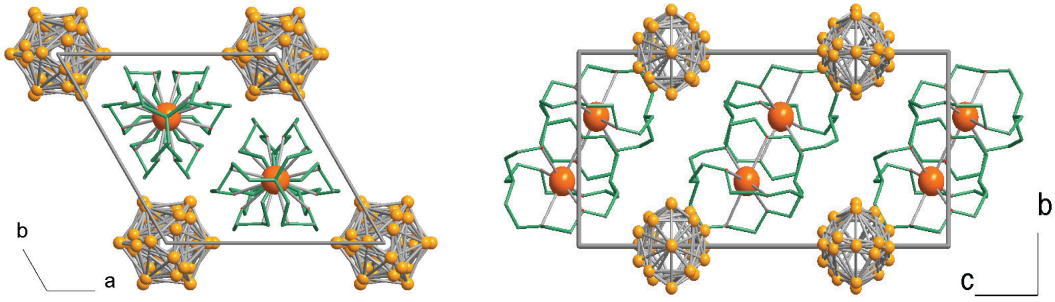

a **b**

Figure S6. Packing in the structure of compound **2**. Arbitrary radii, Ge/As yellow, K orange, cryptand ligands green wire-model. a) Projection along [001], b) Projection along [100].

2.3 Details of the structure determination of [K([2.2.2]crypt)]$_3$[Ta@Ge$_6$As$_4$]·2tol (3

The structure of compound **3** in space group $P2_1/n$ is built by three independent [K([2.2.2]crypt)] cations (Figure S8), a $[Ta@Ge_6As_4]^{3-}$ anion showing statistical overlay of two isomers with occupations of 87.7(1) and 12.3(1)% (Figure S7, Table S5), and two toluene solvent molecules. The interpretation of the disorder model of the anion isomers and attribution of Ge and As to the atom sites has been done based on theoretical calculations. The large anisotropic displacement parameters of Ge7A,Ge8A and Ge9A suggest additional orientational disorder of the tetrahedral [Ge$_3$As] group of isomer 2. The bond lengths in this region may therefore be adulterated. The left hand side of the isomer might derive from an intermediately formed $(Ge_6As_3)^-$ nine-atom cage, homologs of which had been observed in previous studies with Sn/Bi or Pb/Bi anions.[3] The formation of $(Ge_6As_3)^-$, in turn, is attributed on another relative orientation of $(Ge_2As_2)^{2-}$ and $(Ge_{10})^{2-}$ during the respective attack in the first step of the reaction cascade.

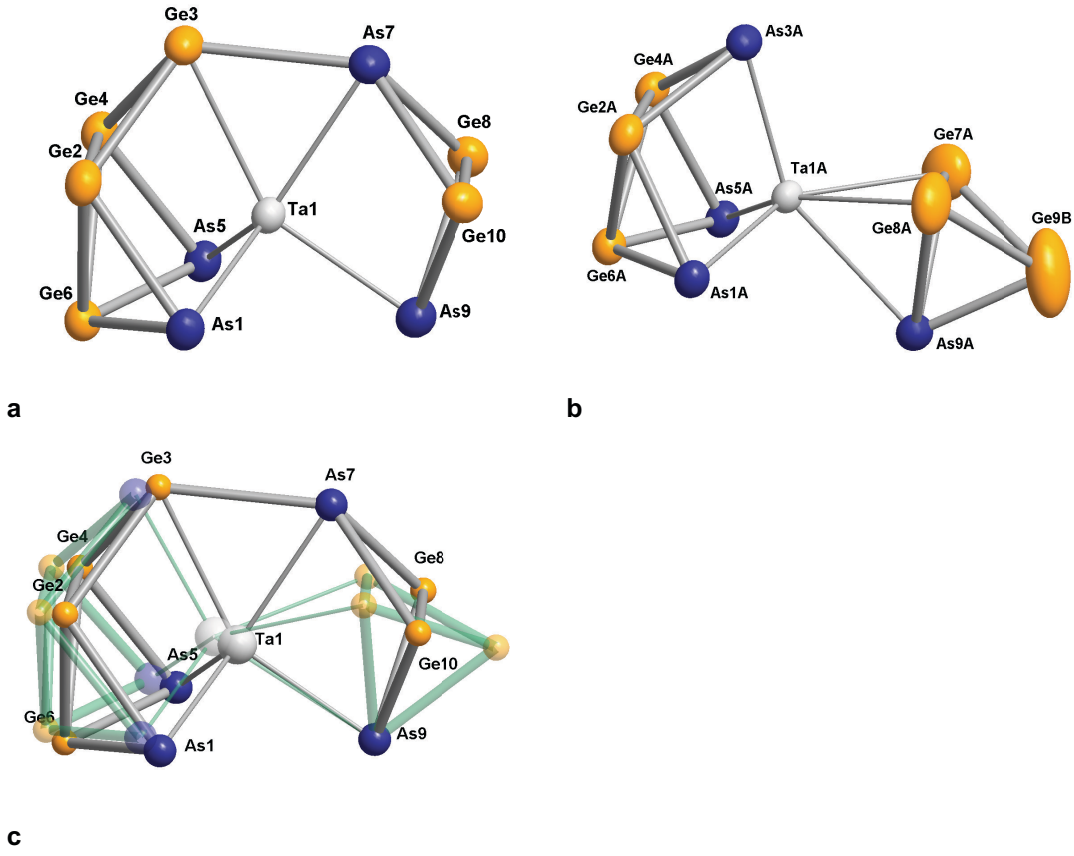

Figure S7. a) Isomer 1 (87.7%) of the $[TaGe_6As_4]^{3-}$ Anion in **3**. b) Isomer 2 (12.3%). Displacement ellipsoids at the 50% level. c) Disorder model by superposition of a and b. Arbitrary radii, second isomer transparent with green bonds.

Table S5. Interatomic distances /Å in the two isomers of the $[Ta@Ge_6As_4]^{3-}$ anion (Figure S6).

isomer 1					
Ta1 – As1	2.505(1)	Ta1 ⋯ Ge10	3.1222(7)	Ge4 – Ge3	2.519(1)
Ta1 – Ge3	2.719(1)	As1 – Ge6	2.525(2)	Ge3 – As7	2.627(1)
Ta1 – As5	2.496(1)	As5 – Ge6	2.522(1)	As7 – Ge8	2.519(1)
Ta1 – As7	2.6229(7)	Ge2 – Ge6	2.733(1)	As7 – Ge10	2.505(1)
Ta1 ⋯ Ge8	3.1089(8)	Ge4 – Ge6	2.761(1)	As9 – Ge8	2.4908(8)
Ta1 – As9	2.5413(6)	Ge2 – Ge3	2.543(1)	As9 – Ge10	2.4770(7)
isomer 2					
Ta1A – As1A	2.46(1)	As1A – Ge6A	2.53(1)	Ge7A – Ge8A	2.600(8)
Ta1A – As3A	2.52(1)	As5A – Ge6A	2.44(1)	Ge7A – Ge9B	2.53(1)
Ta1A – As5A	2.494(8)	Ge6A – Ge2A	2.67(1)	Ge7A – As9A	2.594(7)
Ta1A – Ge7A	2.746(7)	Ge6A – Ge4A	2.56(1)	Ge8A – As9A	2.705(7)
Ta1A – Ge8A	2.699(6)	As3A – Ge2A	2.47(1)	Ge9B – As9A	2.349(9)
Ta1A – As9A	2.906(3)	As3A – Ge4A	2.47(1)	Ge9B – Ge8A	2.53(1)

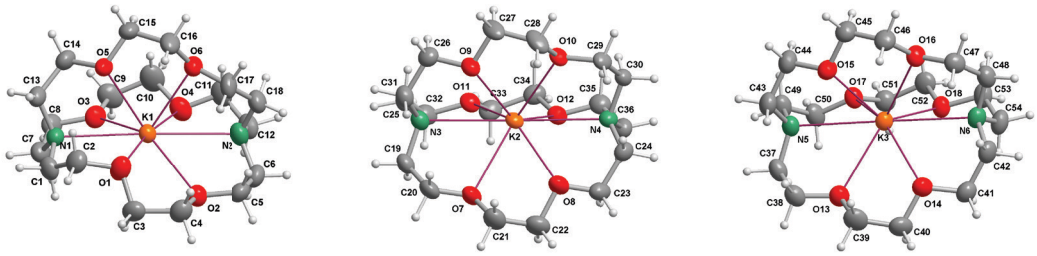

Figure S8. The three independent $[K([2.2.2]crypt)]^+$ cations in **3** (a - c). Displacement ellipsoids at the 50% level.

The complicated packing of cations, anions and toluene molecules in compound **3** is shown in Figure S9.

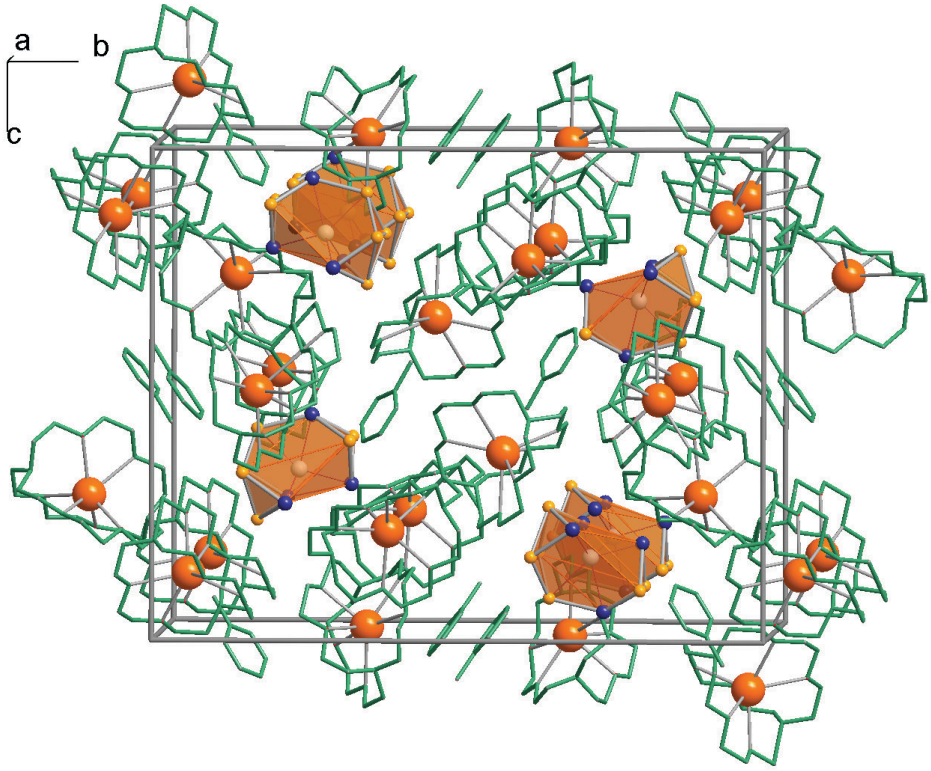

Figure S9. Packing in the structure of compound **3**. Arbitrary radii: Ta grey, Ge yellow, As blue, K orange, cryptand ligands and toluene molecules green wire-model.

2.4 Details of the structure determination of [K([2.2.2]crypt)]$_5$[K([2.2.2]crypt)(en)][Ta@Ge$_8$As$_4$]$_{1.21}$[Ta@Ge$_8$As$_6$]$_{0.79}$·en (4)

The triclinic centrosymmetric structure of compound **4** shows severe disorder effects on the two independent anion positions as well as at some of the six independent cations. The anions are on two independent sites. On site 1, superposition of a $[Ta@Ge_8As_4]^{3-}$ cluster (89.4%) and a $[Ta@Ge_8As_6]^{3-}$ cluster (10.6%) has been found. The occupations by Ge and/or As were taken according to information from EDX spectroscopy, mass spectrometry, the most stable configurations of DFT calculations, and their probable disordered orientations (Figure S10). Bond lengths are given in Table S6.

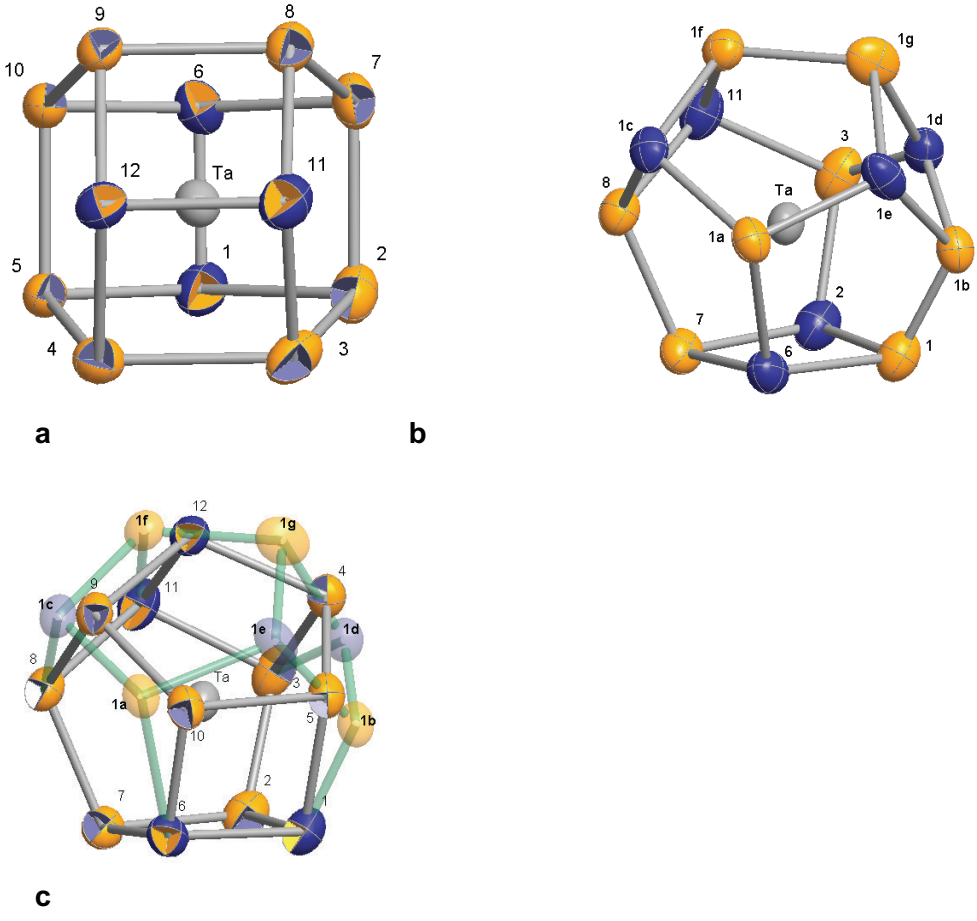

Figure S10. Anion site 1 in **4**: a) 12-atom cluster $[Ta@Ge_8As_4]^{3-}$. Yellow surface: 75%Ge, 25%As; blue surface: 50%Ge, 50%As. b) 14-atom cluster $[Ta@Ge_8As_6]^{3-}$. Yellow: Ge, blue: As. c) Disorder model: Overlay of a) (grey bonds) and b) (transparent, with green bonds). All displacement ellipsoids at the 50% probability level.

Table S6a. Interatomic distances /Å in the $[Ta@Ge_8As_4]^{3-}$ anion in **4** (Figure S10a).

Ta – 1	2.842(1)	Ta – 6	2.790(1)	Ta – 11	2.824(2)
Ta – 2	2.708(1)	Ta – 7	2.790(1))	Ta – 12	2.795(2)
Ta – 3	2.727(1)	Ta – 8	2.731(1)		
Ta – 4	2.759(2)	Ta – 9	2.742(2)	average	**2.763**
Ta – 5	2.706(1)	Ta – 10	2.739(1)		
1 – 2	2.571(2)	3 – 11	2.572(2)	7 – 8	2.533(2)
1 – 5	2.574(2)	4 – 5	2.526(2)	8 – 9	2.600(2)
1 – 6	2.491(2)	4 – 12	2.530(2)	9 – 10	2.541(2)
2 – 3	2.515(2)	5 – 10	2.591(2)	11 – 12	2.527(2)
2 – 7	2.639(2)	6 – 7	2.509(2)		
3 – 4	2.678(2)	6 – 10	2.482(2)	average	**2.555**

Table S6b. Interatomic distances /Å in the $[Ta@Ge_8As_6]^{3-}$ anion in **4** (Figure S10b).

Ta – Ge1	2.842(1)	Ta – Ge8	2.731(1)	Ta – As1d	2.729(12
Ta – As2	2.708(1)	Ta – As11	2.824(1)	Ta – As1e	3.037(11)
Ta – Ge3	2.727(1)	Ta – Ge1a	3.193(12)	Ta – Ge1f	3.037(15)
Ta – As6	2.790(1)	Ta – Ge1b	2.906(12)	Ta – Ge1g	3.125(14)
Ta – Ge7	2.790(1)	Ta – As1c	3.097(15)		
			average	Ta – Ge/As	**2.895**
Ge1 – As2	2.571(2)	As6 – Ge1a	2.816(12)	Ge1a – As1e	2.49(2)
Ge1 – Ge1b	2.108(13)	Ge7 – Ge8	2.533(2)	Ge1b – As1d	2.48(2)
Ge1 – As6	2.491(2)	Ge8 – As11	2.542(2)	Ge1b – As1e	2.35(2)
As2 – Ge3	2.515(2)	Ge8 – As1c	2.32(1)	As1c – Ge1f	2.47(2)
As2 – Ge7	2.639(2)	As6 – Ge7	2.509(2)	As1d – Ge1g	2.50(2)
Ge3 – As1d	2.064(11)	As11 – Ge1f	2.33(1)	As1e – Ge1g	2.48(2)
Ge3 – As11	2.572(2)	As6 – Ge1a	2.816(12)	Ge1g – Ge1f	2.49(2)
As6 – Ge7	2.509(2)	Ge1a – As1c	2.60(2)		
			average	Ge/As – Ge/As	**2.472**

On site 2, a $[Ta@Ge_8As_6]^{3-}$ cluster is dominating (68.5%) superimposed by a $[Ta@Ge_8As_4]^{3-}$ cluster in two different orientations (12.9% and 18.6%). By this complicated disorder with many approximately common positions, the individual geometrical data appear adulterated and are not listed, therefore. The structures are given in Figure S11.

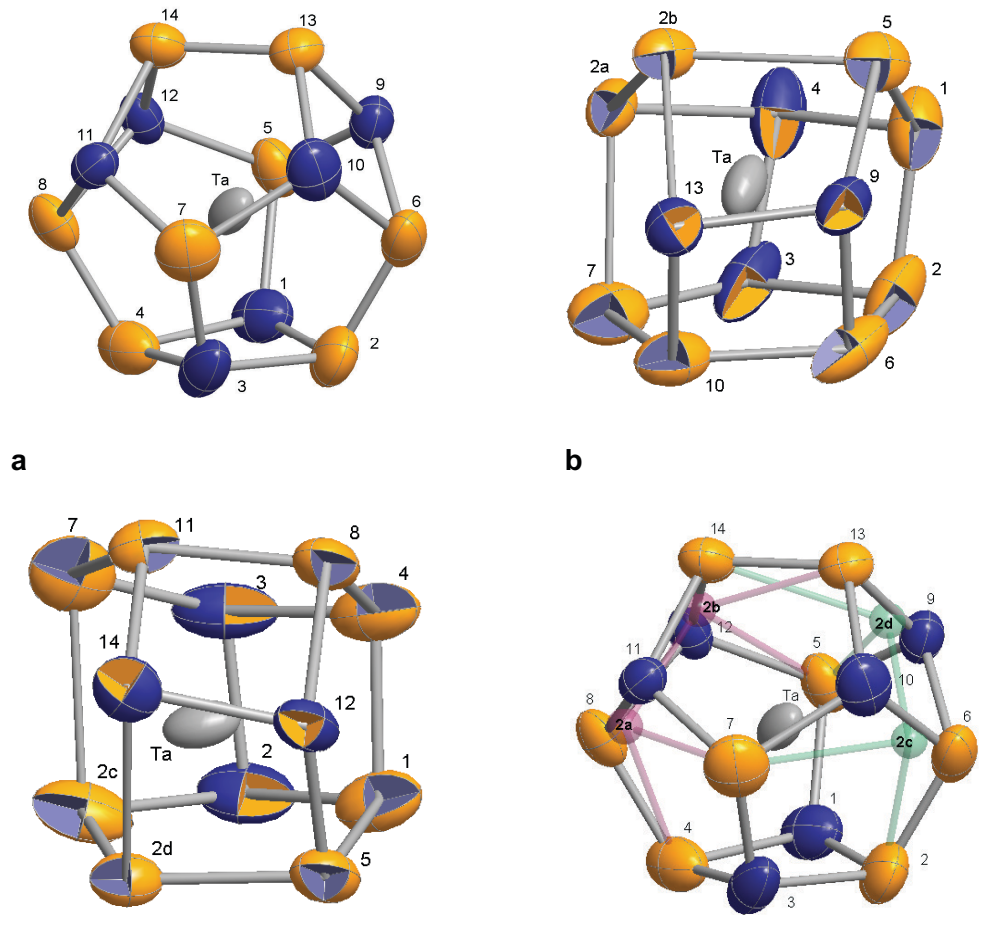

Figure S11. Anion site 2 in **4**. a) 14-atom cluster 2a $[Ta@Ge_8As_6]^{3-}$. b) 12-atom cluster $[Ta@Ge_8As_4]^{3-}$, first orientation. c) 12-atom cluster $[Ta@Ge_8As_4]^{3-}$, second orientation. d) Overlay of all three components. Red transparent: additional atoms for component b, Green transparent: additional atoms for component c. All displacement ellipsoids at the 50% probability level. Color codes are the same as in Figure S10.

Five of the six cations are [K[2.2.2](crypt)] cations like in the structures of compounds **1** - **3**. The refinement of these cryptand molecules in the presence of many heavy atoms was performed using geometrical restraints on the bond lengths and 1,3-distances. The anisotropic displacement ellipsoids show sometimes irregular shape as they include disorder effects (Figure S12a-d). They were refined with restraints to avoid too anisotropic displacement parameters. For one cryptand ligand with strong disorder, no sensible disorder model could be established. Its contribution was subtracted, therefore, by the back Fourier transform method from the data set. A sixth cation has an *en* molecule coordinated to K^+ in addition to the cryptand ligand (Figure S12e). In addition, a non-coordinated *en* molecule has been located.

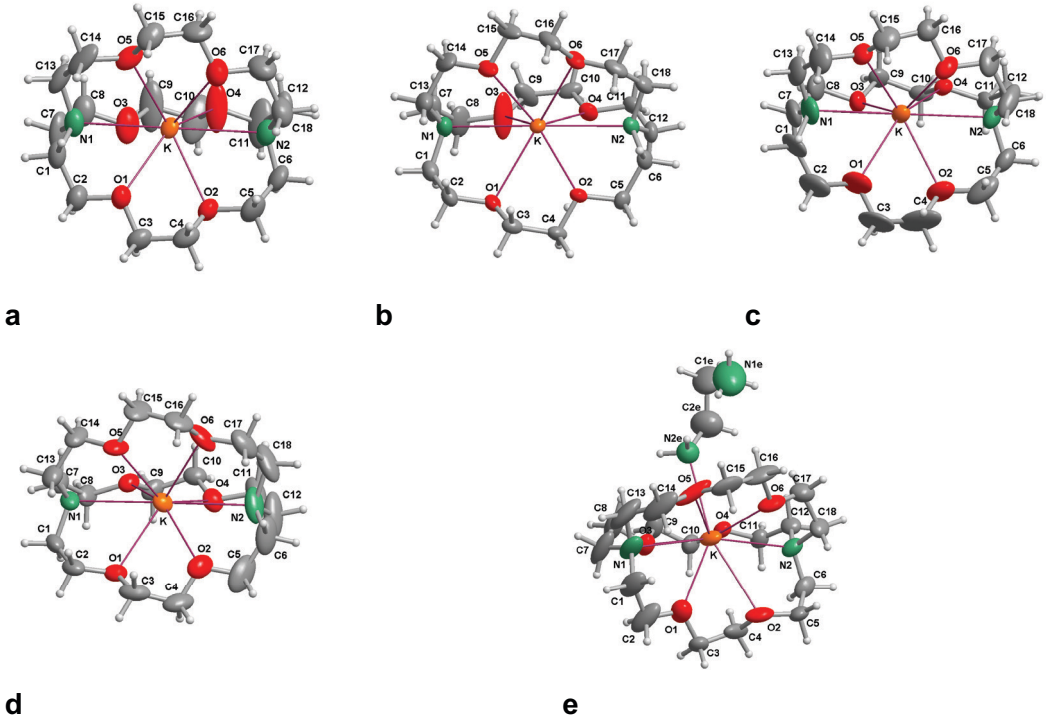

Figure S12. a) - d) The four localized $[K[2.2.2](crypt)]^+$ cations (of five). e) The $[K[2.2.2](crypt)(en)]^+$ cation in **4**. H-atoms at N1e with 2/3 occupation. All displacement ellipsoids at the 30% probability level.

The packing of molecules in the structure of compound **4** is shown in Figure S13.

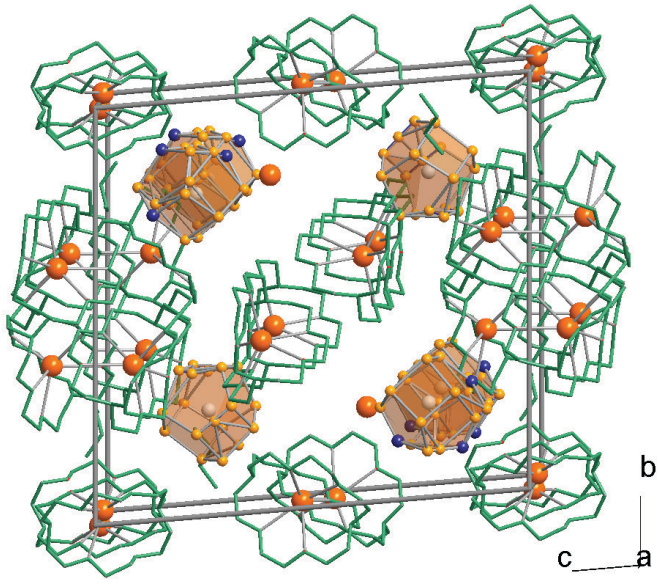

Figure 13. Packing of cations and anions in the structure of compound **4** with arbitrary radii: Anionic clusters as polyhedra; Ta grey, Ge yellow, As blue, K orange, cryptand ligands and en molecules green wire-model. Note one cryptand ligand missing due to heavy disorder.

3. Energy dispersive X-ray spectroscopy (EDX) analysis

EDX analyses were performed to support the elemental composition that was suggested based on the SCXD experiments. As for the solids presented in section 1.1, these were carried out using an EDX-device Voyager 4.0 of Noran Instruments coupled with an electron microscope CamScan CS 4DV. Data acquisition was performed with an acceleration voltage of 20 kV and 100 s accumulation time. The radiation emitted by the atoms was analyzed: K-K, Ge-K, As-K, Ta-M/L. To minimize surface effects in the measurement, the K-lines were preferably used to calculate the elemental composition. Table S7 summarizes the results.

Table S7. EDX analysis of single crystals of compounds **1**, **2**, **3**, and **4** (K, Ge, As, Ta).

Element	k-ratio	ZAF	Atom%	Atomic ratio obs. (calc)	Element wt %	wt % Err. (1-sigma)
[K([2.2.2]crypt)]$_2$(Ge$_2$As$_2$)·en (1)						
K-K	0.1519	1.056	26.48	1.50 (2)	16.04	+/- 0.42
Ge-K	0.4166	1.035	38.34	2.17 (2)	43.12	+/- 4.29
As-K	0.3918	1.042	35.18	2.00 (2)	40.84	+/- 3.43
Total			100	5.67 (6)	100	
[K([2.2.2]crypt)]$_2$(Ge$_7$As$_2$) (2)						
K-K	0.1318	1.247	25.72	2.58 (2)	15.61	+/- 0.47
Ge-K	0.5929	1.019	54.37	5.45 (7)	61.24	+/- 2.99
As-K	0.2232	1.018	19.91	2.00 (2)	23.15	+/- 3.01
Total			100	10.03 (11)	100	
[K([2.2.2]crypt)]$_3$[Ta@Ge$_6$As$_4$]·2tol(3)						
K-K	0.1595	1.247	35.90	7.02 (3)	19.89	+/- 0.34
Ge-K	0.3518	1.019	34.85	6.81 (6)	35.85	+/- 1.84
As-K	0.2135	1.018	20.47	4.00 (4)	21.73	+/- 1.86
Ta-M	0.1997	1.128	8.78	1.72 (1)	22.53	+/- 1.89
Total			100	19.55 (14)		
[K([2.2.2]crypt)]$_5$[K([2.2.2]crypt)(en)][Ta@Ge$_8$As$_4$]$_{1.21}$[Ta@Ge$_8$As$_6$]$_{0.79}$·en (4)						
K-K	0.0813	1.258	17.87	3.05 (3)	9.73	+/- 0.36
Ge-K	0.3848	1.001	47.65	6.19 (8)	46.40	+/- 2.42
As-K	0.3205	1.001	28.53	5.00 (5)	28.86	+/- 2.72
Ta-M	0.0759	2.528	5.96	1.24 (1)	15.01	+/- 0.99
Total			100	15.48 (17)	100	

The results of the EDX investigations confirm the Ge:As ratios of the investigated substances within the expected accuracy.

4. Electrospray Ionization Mass Spectrometry (ESI-MS) Investigations

ESI-MS has been performed on a Finnigan LTQ-FT spectrometer by Thermo Fischer Scientific in the negative ion mode: Spray voltage 3.90 kV, capillary temperature 300°C capillary voltage –11 V, tube lens voltage –140 V, sheath gas flow rate 25 arb, sweep gas flow rate 0 arb.

The ESI(–) mass spectra on an extract of "KGeAs" prepared in a silica glass ampoule (precursor phase 2) in DMF/*en* in the presence of [2.2.2]crypt (= $C_{18}H_{36}N_2O_6$; measured after 18h of extraction time; Figures S14-S17) confirm the concurrent presence of the singly charged cluster species $(Ge_2As_2H)^-$ (m/z = 296.69), $(Ge_7As_2K)^-$ (m/z = 697.26) and $(Ge_{10})^-$ (m/z = 726.22) in the same solution. The concurrent presence of these polyanions strongly supports the assumption that the 9-atom cluster $(Ge_7As_2)^{2-}$ is the product of the reaction of two $(Ge_2As_2)^{2-}$ clusters with one $(Ge_{10})^{2-}$.

The ESI(–) mass spectra on an extract of "KGeAs:Ta" prepared in a Ta ampoule (precursor phase 1) in *en* in the presence of [2.2.2]crypt (measured after 3h of extraction time; Figures S18-S23) confirm the concurrent presence of multiple singly charged cluster species in one single solution, such as: $(Ge_2As_2H)^-$ (m/z = 296.69), $(Ge_6As_4Ta)^-$ (m/z = 916.17), $(Ge_6As_4TaK)^-$ (m/z = 955.13), and $(Ge_6As_4TaK_2)^-$ (m/z = 994.09). It was shown hence that the 12- and 14-atom clusters $[Ta@Ge_8As_4]^{3-}$ and $[Ta@Ge_8As_6]^{3-}$ can be obtained from the same solution that also contains the intermediate $[Ta@Ge_6As_4]^{3-}$.

In a solution of $[K([2.2.2]crypt)]_3[Ta@Ge_8As_6]$ / $[K([2.2.2]crypt)]_3[Ta@Ge_8As_4]$ (**4**) in DMF/*en* (Figures S24-S26), the isotopic patterns of $(Ge_8As_4TaC_{36}H_{72}N_4O_{12}K_2)^-$ (m/z = 1892.46) and $(Ge_8As_6TaC_{18}H_{36}N_2O_6K)^-$ (m/z = 1627.07) were identified by ESI(–) mass spectrometry.

The ESI(–) mass spectra of the polyanionic compounds show fragmentation of the material and formation of further species; this may be due to both – a dynamic re-organisation of the cluster and its fragments in solution, and the ESI-MS conditions. As it is common for Zintl anions and intermetallic cluster anions, the observed fragments have been detected as oxidized, singly charged species.

4.1 ESI-MS Investigation of the extract of "KGeAs" (precursor phase 2, prepared in a silica glass ampoule) in DMF / en in presence of [2.2.2]crypt

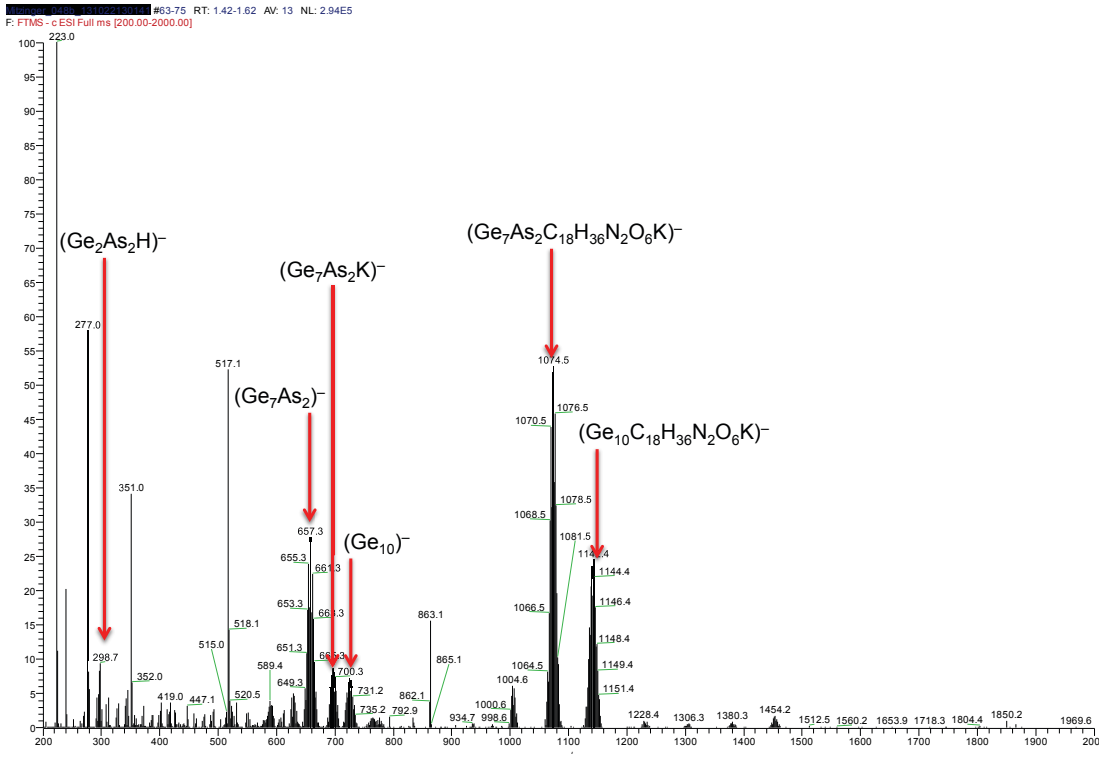

Figure S14. ESI-MS(–) overview spectrum of the extract of "KGeAs" (precursor phase 2, prepared in a silica glass ampoule) in DMF / *en* in presence of [2.2.2]crypt.

In the ESI-MS spectrum (Figure S14) of the extract of "KGeAs" (precursor phase 2, prepared in a silica glass ampoule) in *en* the isotopic patterns confirm the presence of $(Ge_2As_2H)^-$ (m/z = 296.69) (Figure S15), that was obviously formed under ESI-MS conditions from the anion in **1,** as well as the presence of $(Ge_7As_2)^-$ (m/z = 658.29) (Figure S16) side by side with $(Ge_{10})^-$ (m/z = 726.22) (Figure S17). Also adducts of K^+ and $[K([2.2.2]crypt)]^+$ were detected: $(Ge_7As_2K)^-$ (m/z = 697.26), $(Ge_{10}C_{18}H_{36}N_2O_6K)$ (m/z = 1141.44).

The isotopic pattern of $(Ge_2As_2H)^-$ (m/z = 296.69) (Figure S15) was also identified in all spectra containing the anions in **2, 3** or **4** that were formed under ESI-MS conditions (as seen in overview spectra below).

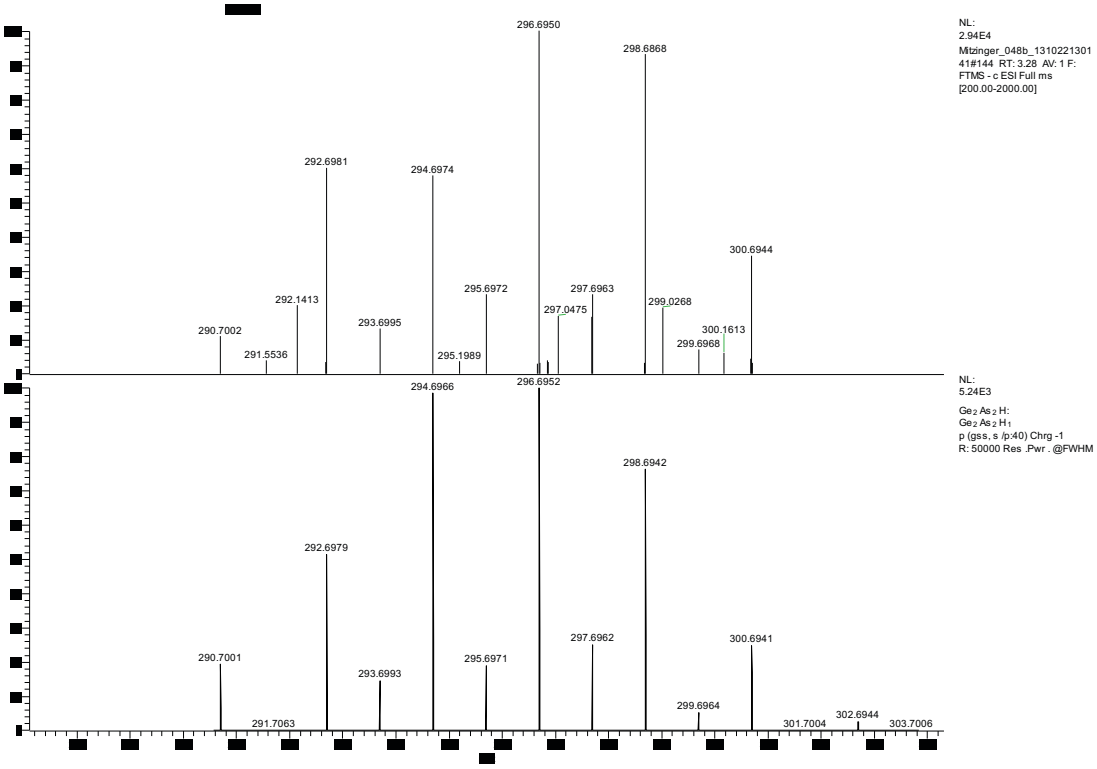

Figure S15. ESI(–) mass peak of $(Ge_2As_2H)^-$. Measured (top) vs. calculated (bottom) spectrum.

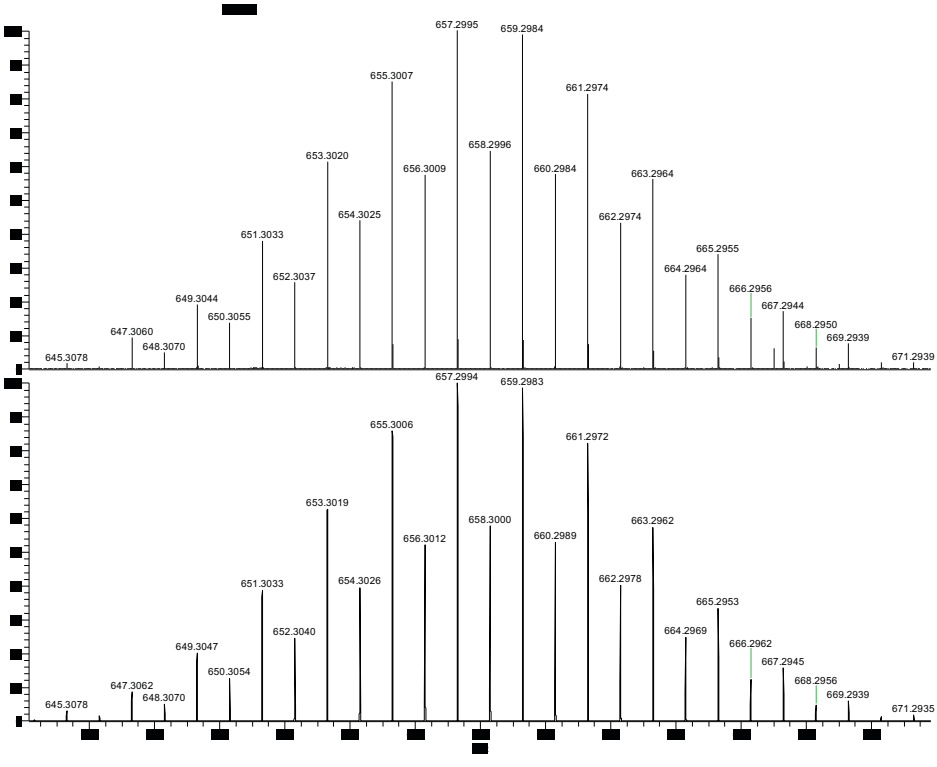

Figure S16. ESI(–) mass peak of $(Ge_7As_2)^-$. Measured (top) vs. calculated (bottom) spectrum.

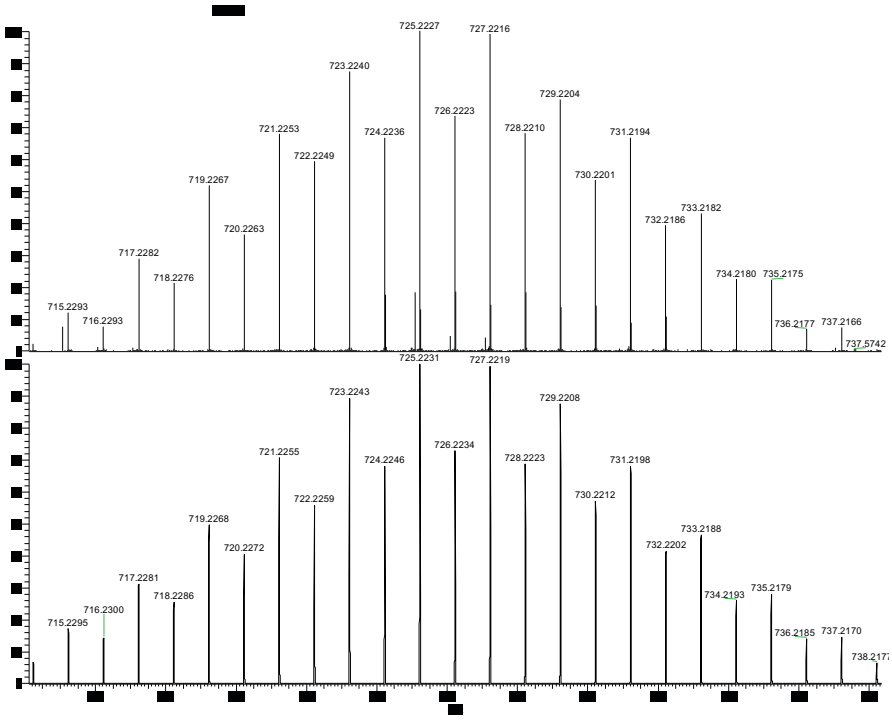

Figure S17. ESI(–) mass peak of $(Ge_{10})^-$. Measured (top) vs. calculated (bottom) spectrum.

4.2 ESI-MS Investigation of the extract of "KGeAs:Ta" (precursor phase 1, prepared in a Ta ampoule) in en in the presence of [2.2.2]crypt

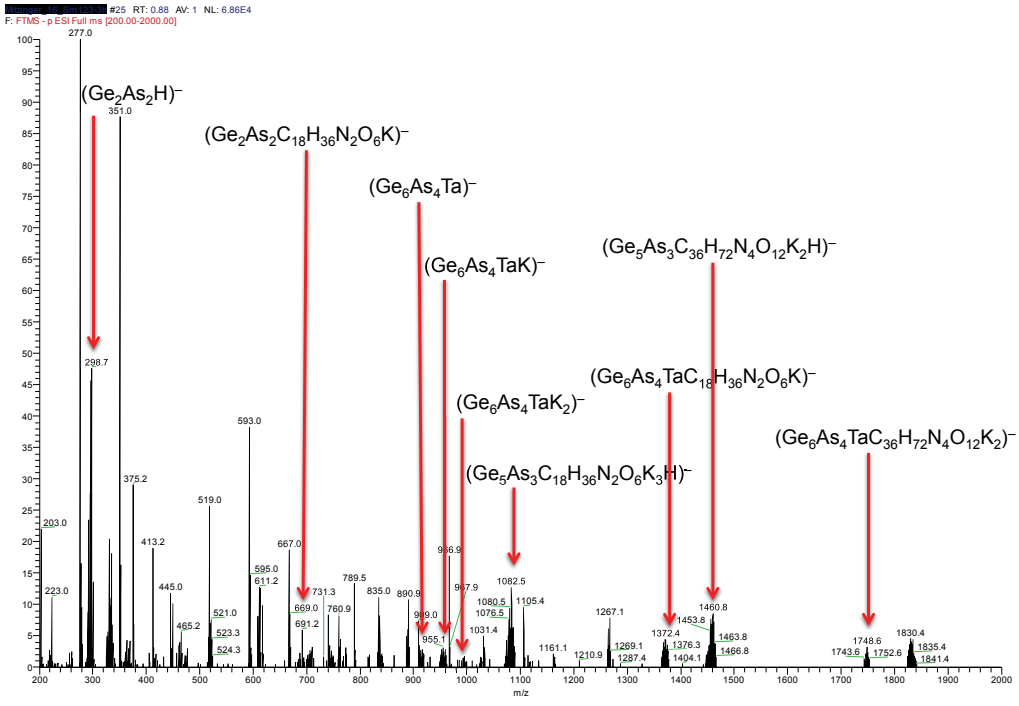

Figure S18. ESI-MS(–) overview spectrum of the reaction mixture after 3h of extraction time of the precursor phase "KGeAs:Ta" (precursor phase 1, prepared in a Ta ampoule) in 1,2-diaminoethane in presence of [2.2.2]crypt

The overview spectrum (Figure S18) confirms the presence of a variety of clusters in solution: Remarkable is the presence of the under ESI-MS conditions formed anions of **1** and intermediate **3** in the solution after just 3h of extraction. The different number of K^+ or $[K([2.2.2]crypt)]^+$ adducts indicates that Ta is present herein in various oxidation states: Presumably "+5" in $(Ge_6As_4Ta)^-$, "+4" in $(Ge_6As_4TaK)^-$ / $(Ge_6As_4TaC_{18}H_{36}N_2O_6K)^-$ and "+3" in $(Ge_6As_4TaK_2)^-$ / $(Ge_6As_4TaC_{36}H_{72}N_4O_{12}K_2)^-$.
Due to fragmentation of the high-mass isotopic patterns and increasing degradation of the solution during injection the observed intensity of the isotopic pattern decreased during the measurement. In the reaction mixture the presence of $(Ge_2As_2H)^-$ (m/z = 296.69) beside $(Ge_3As)^-$ (m/z = 292.68) was confirmed (Figure S19). The isotopic patterns of $(Ge_6As_4Ta)^-$ (m/z = 916.17), $(Ge_6As_4TaK)^-$ (m/z = 955.13) and $(Ge_6As_4TaK_2)^-$ (m/z = 994.09) (Figures S20-S22), which were obviously formed from the $[Ta@Ge_6As_4]$ cluster, were identified as well as these of $[K([2.2.2]crypt)]^+$ adducts. In addition, the isotopic pattern of $(Ge_5As_3C_{18}H_{36}N_2O_6K_3)^-$ (m/z = 1082.5) was identified (Figure S23).

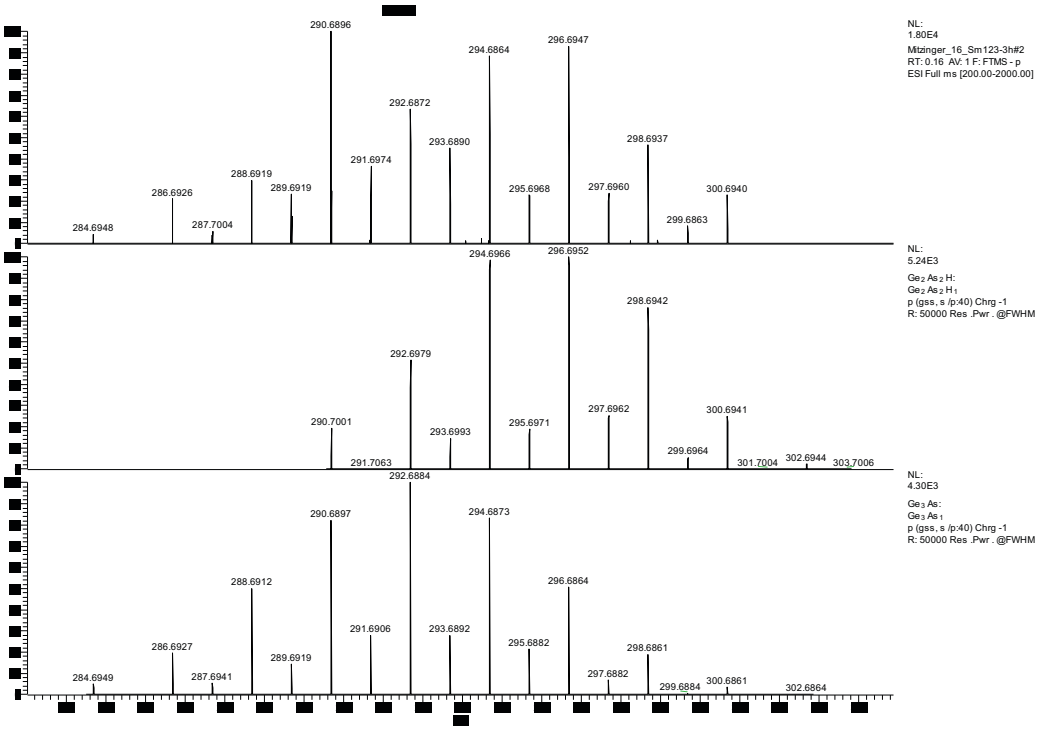

Figure S19. ESI(–) mass peak of $(Ge_2As_2H)^-$ and $(Ge_3As)^-$. Measured (top) vs. calculated (mid/bottom) spectrum.

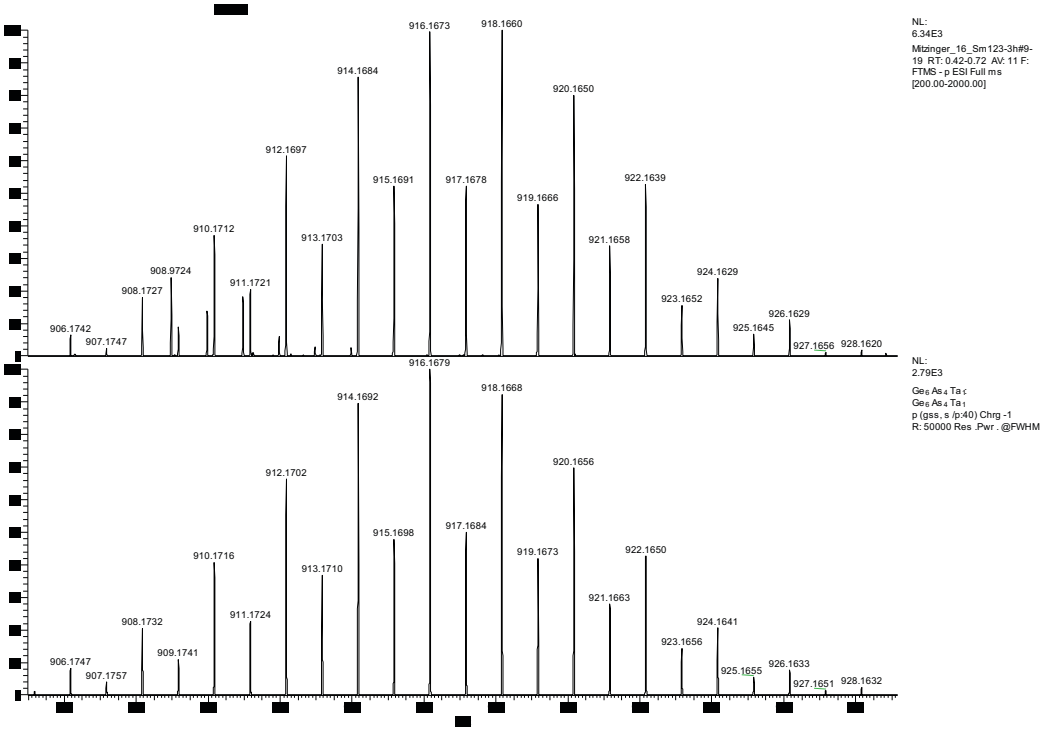

Figure S20. ESI(–) mass peak of $(Ge_6As_4Ta)^-$. Measured (top) vs. calculated (bottom) spectrum.

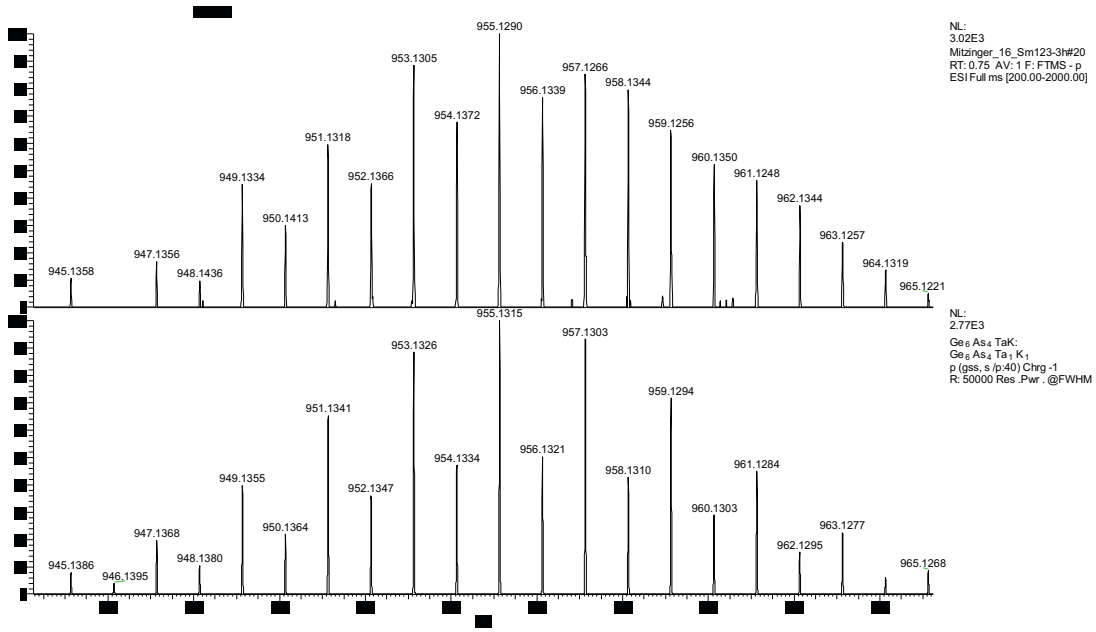

Figure S21. ESI(–) mass peak of $(Ge_6As_4TaK)^-$. Measured (top) vs. calculated (bottom) spectrum.

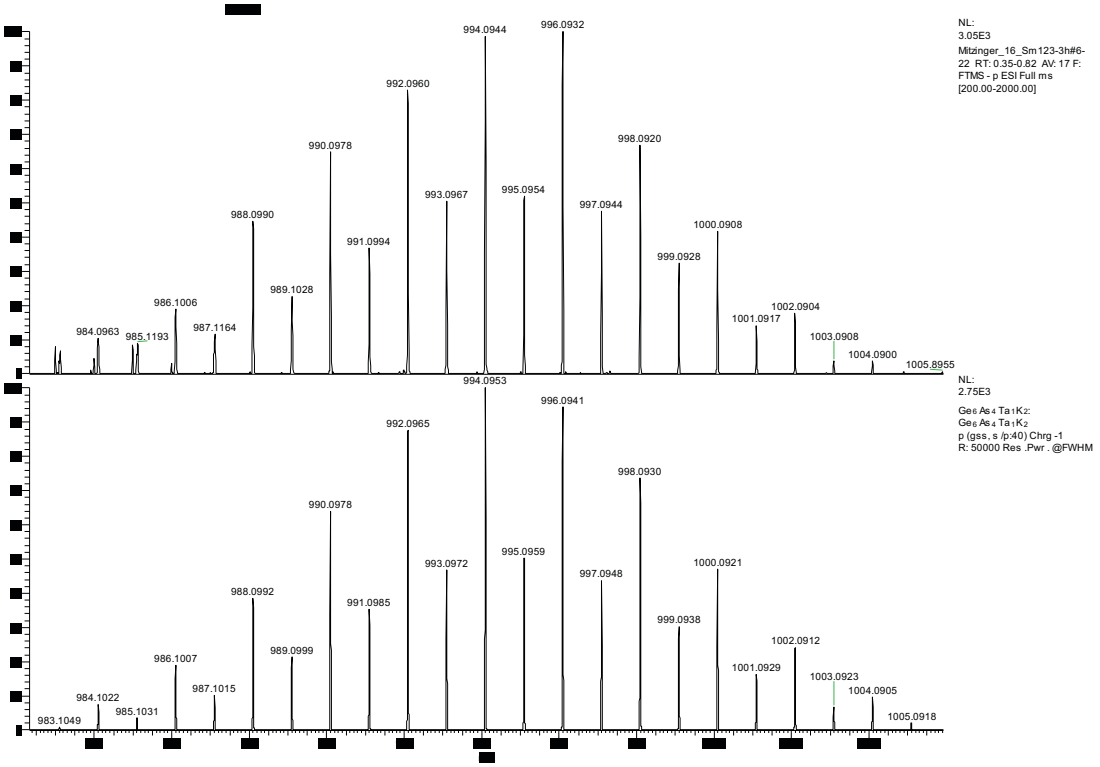

Figure S22. ESI(–) mass peak of $(Ge_6As_4TaK_2)^-$. Measured (top) vs. calculated (bottom) spectrum.

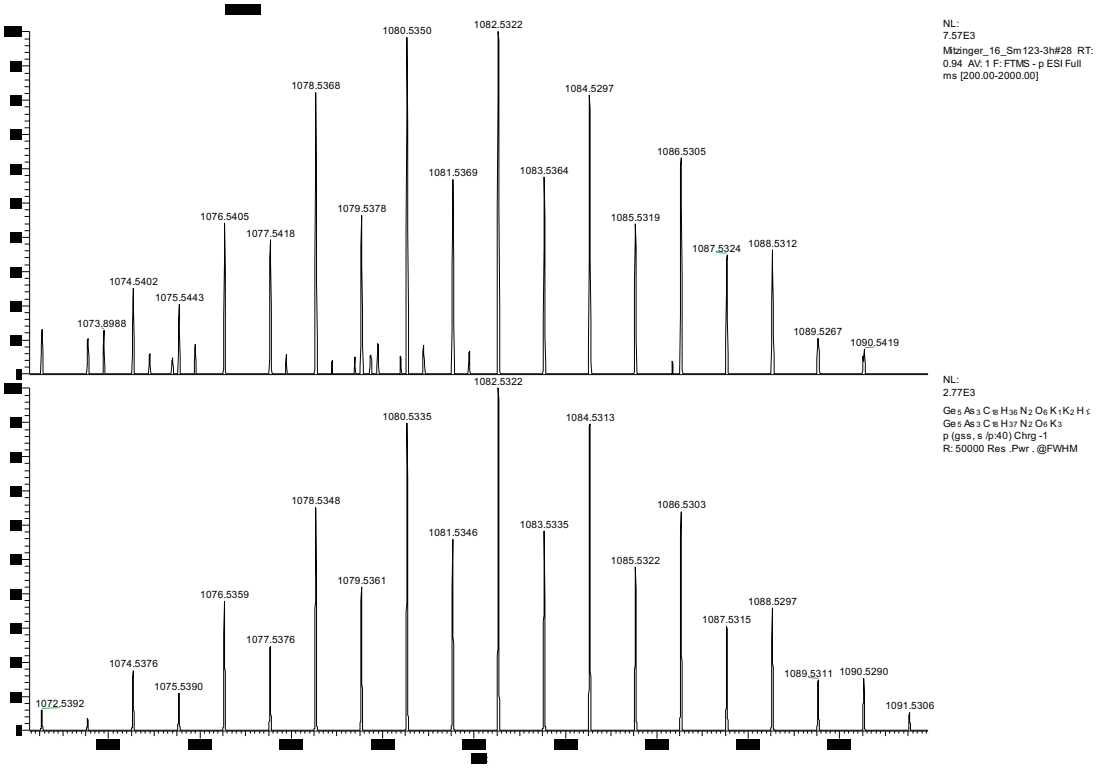

Figure S23. ESI(–) mass peak of $(Ge_5As_3C_{18}H_{36}N_2O_6K_3)^-$. Measured (top) vs. calculated (bottom) spectrum.

4.3 ESI-MS Investigation of 4

Upon ESI-MS investigation of **4**, dissolved in DMF/*en*, the following species, representing oxidized clusters of $[Ta@Ge_8As_4]^{3-}$ and $[Ta@Ge_8As_6]^{3-}$ were found: $(Ge_8As_4TaC_{36}H_{72}N_4O_{12}K_2)^-$ (m/z = 1892.45, Figure S25) and $(Ge_8As_6TaC_{18}H_{36}N_2O_6K)^-$ (m/z = 1625.07, Figure S26). Various related anions with and without $[K([2.2.2]crypt)]^+$ were also identified (Figure S24).

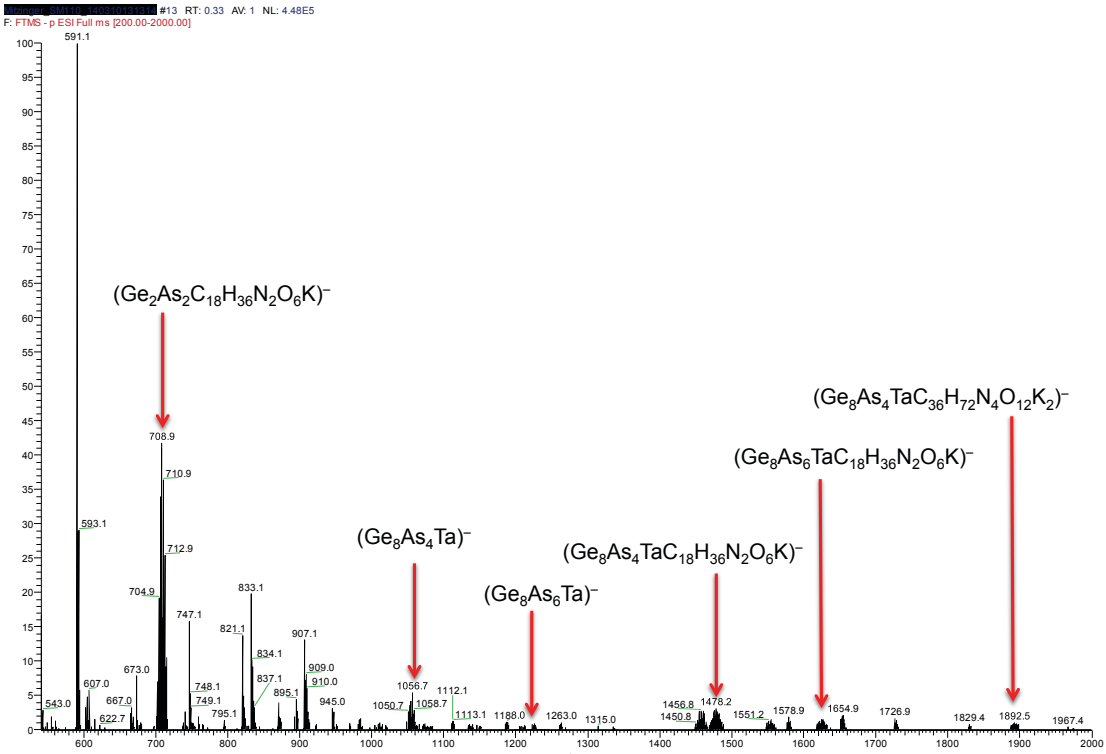

Figure S24. ESI-MS(–) overview spectrum of a solution of **4** in DMF/en

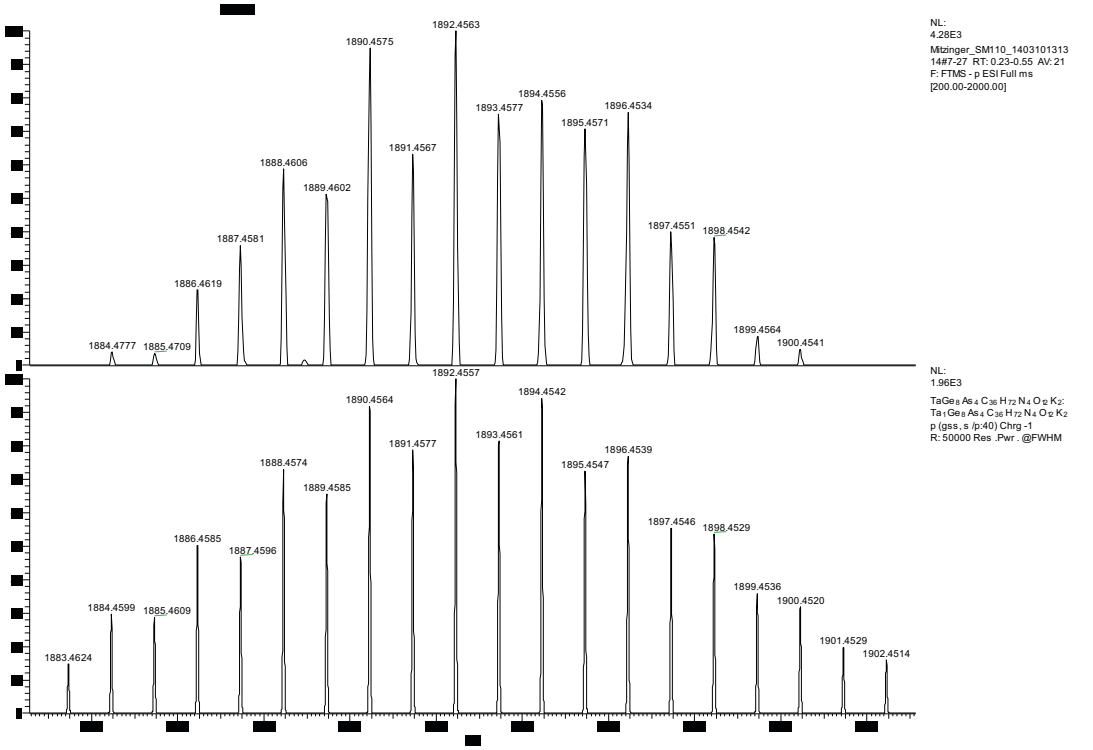

Figure S25. ESI(–) mass peak of $(TaGe_8As_4C_{36}H_{72}N_4O_{12}K_2)^-$. Measured (top) vs. calculated (bottom) spectrum.

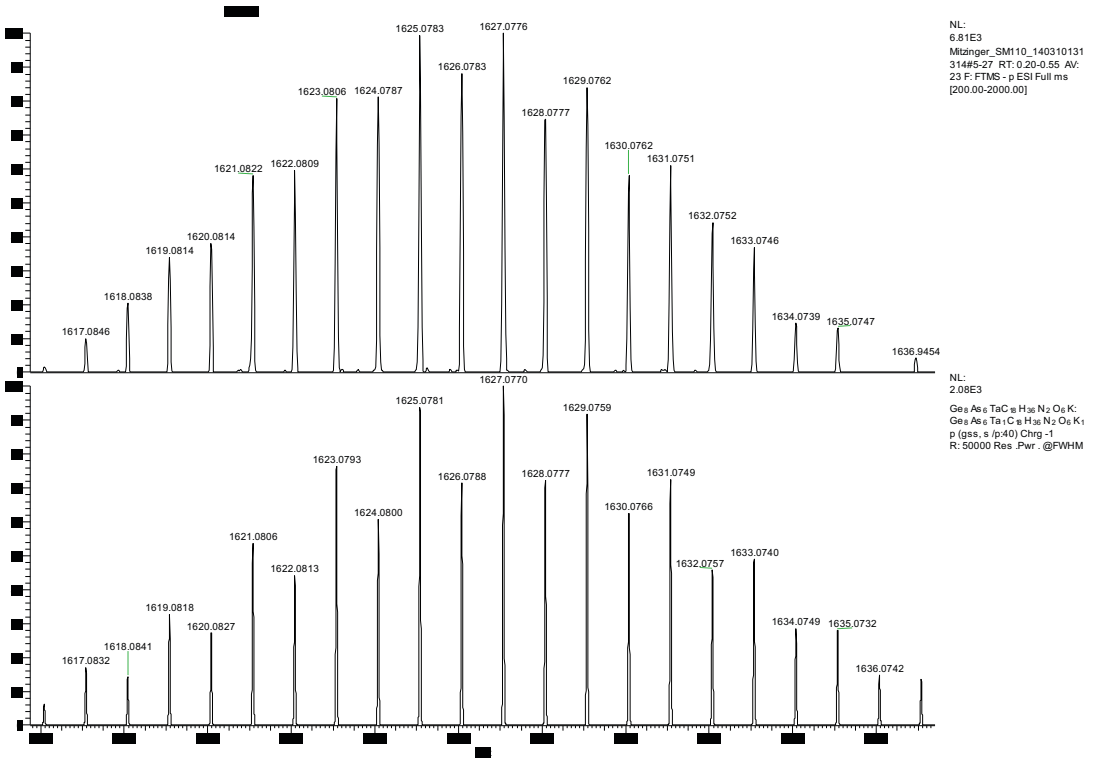

Figure S26. ESI(–) mass peak of $(TaGe_8As_6C_{18}H_{36}N_2O_6K)^-$. Measured (top) vs. calculated (bottom) spectrum.

5. Quantum Chemical Investigations

5.1 Methods

All calculations were carried out with the program system TURBOMOLE.[4] For the atom-type assignment procedure[5,6], the genetic algorithm[7-9] and the pre-optimization of reaction pathways (by the WOELFLING reaction path finder[8]),bases of polarized split-valence quality, def-SV(P)[11,12] (with an effective core potential of Wood-Boring type for Ta[13] and the generalized gradient approximation (GGA) DFT functional by Becke[14] and Perdew[15] were chosen for reasons of economy. The resulting best structures and best pathways were re-optimized using more flexible polarized triple zeta valence basis sets dhf-TZVP[16] (with an effective core potential of the Dirac-Hartree-Fock type for Ta)[17] and the meta-GGA functional by Tao, Perdew, Staroverov and Scuseria (TPSS).[18] For all cases, the resolution-of-the-identity approximation for the Coulomb part is employed,[19] the negative charges of the clusters were compensated by using the Conductor-like Screening Model (COSMO).[20] The dielectric constant ε was set to infinity (default) as well as to 13.5, which is the value for 1,2-diaminoethane. All energies given in this work, also the bond energy of Ta_2 are calculated with these settings (TPSS/dhf-TZVP/COSMO).

For the genetic algorithm,[7-9] the following settings were applied: Population size P = 20 structures; cross-over after 10 structures having been optimized (including the atom-type re-assignment step was carried out after 10 optimization cycles), GA-RP, leading to the formation of p = 10 new (child) structures. The mutation probability was set to 1%. The procedure was stopped after 30 generations.

Reaction pathways were investigated with the WOELFLING reaction path finder,[10] starting from an initial pathway consisting of 14 intermediate structures obtained from interpolation between start and end structure. Initial pathways were calculated for all possibilities, the optimization procedure was carried out for those with interatomic distances not shorter than 160 pm for all atoms in all interpolated structures of the initial pathways. For these pathways 35 iterations were carried out with economic DFT settings BP86/def-SV(P)/COSMO.[11-15] Thereupon, the pathways with lowest barriers were refined with a larger number (53) of intermediate structures at more accurate level TPSS/dhf-TZVP/COSMO[16-18] until convergence.

The structures were visualized with the CYLView Software.[21]

5.2 Reaction energies of charge-conserving steps

Table S8 summarizes the reaction energies for the charge-conserving second and the third step of the mechanism proposed in the manuscript.

Table S8. Reaction energies for the charge-conserving second and the third step of the mechanism proposed in the manuscript. The dielectric constant, ε, in the COSMO model was set to infinity (default) as well as to 13.5, which is the value for 1,2-diaminoethane.

ΔE/ kJ mol^{-1}	BP86/def-SVP	TPSS/dhf-TZVP	
	$\varepsilon = \infty$	$\varepsilon = \infty$	$\varepsilon = 13.5$
2: $(Ge_7As_2)^{2-} + 2\ Ta \rightarrow [Ta@Ge_4As_2]^- + (TaGe_3)^-$	–815.6	–902.9	–917.1
3: $[Ta@Ge_4As_2]^- + (Ge_2As_2)^{2-} \rightarrow [Ta@Ge_6As_4]^{3-}$	–312.4	–330.6	–300.6

5.3 Energetically higher isomers of $[Ta@Ge_8As_4]^{3-}$ and $[Ta@Ge_8As_6]^{3-}$

Global minimum structures for $[Ta@Ge_8As_4]^{3-}$ and $[Ta@Ge_8As_6]^{3-}$ obtained from GA-RP calculations are represented in Figures 2 and 4 in the manuscript, energetically higher isomers are shown in Figures S27 and S28, respectively.

In case of $[Ta@Ge_8As_6]^{3-}$, energetically next isomers (up to +40 kJ/mol) differ from the minimum only by their occupations, for $[Ta@Ge_8As_4]^{3-}$ the energetically next isomers are open cage structures, with varying occupation.

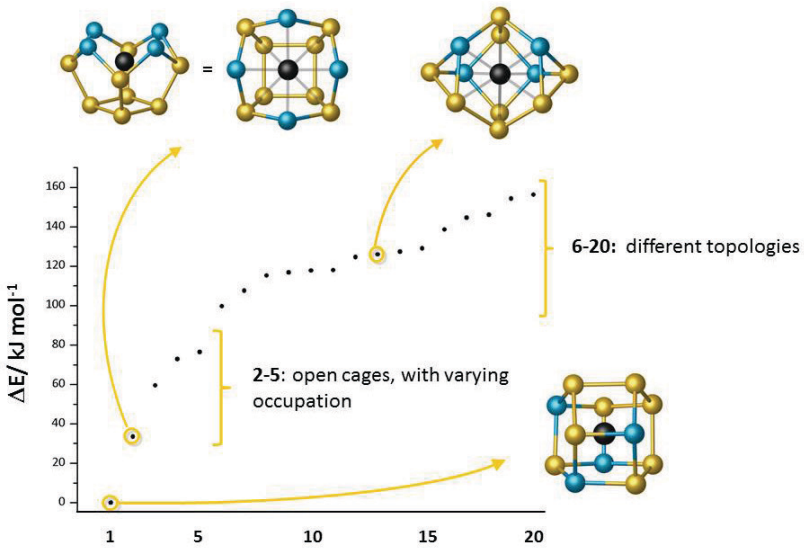

Figure S27. Minimum structures for $[Ta@Ge_8As_4]^{3-}$ from GA-RP calculations.

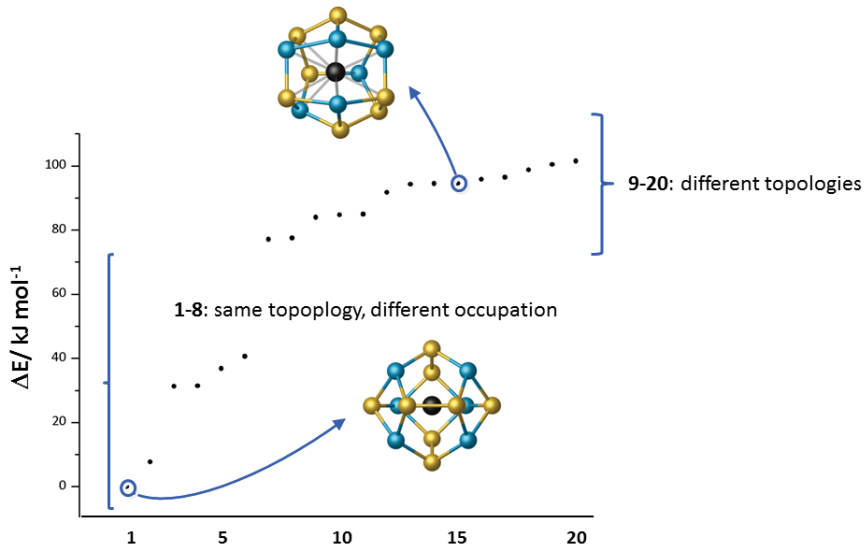

Figure S28. Minimum structures for $[Ta@Ge_8As_6]^{3-}$ from GA-RP calculations.

6. References for the supplementary information

[1] G. M. Sheldrick A short history of SHELX. *Acta Crystallogr*. **A64,** 112 – 122 (2008).

[2] M. C. Burla *et al.* SIR2011: a new package for crystal structure determination and refinement. *J. Appl. Crystallogr.* **45**, 357-361 (2012).

[3] Lips, F., Clérac, R. & Dehnen, S. $[Eu@Sn_6Bi_8]^{4-}$: A Mini-Fullerane-Type Zintl Anion Containing a Lanthanide Ion. *Angew. Chem. Int. Ed.* **50**, 960–964 (2010).

[4] TURBOMOLE Version 6.6, © TURBOMOLE GmbH 2014. TURBOMOLE is a development of University of Karlsruhe and Forschungszentrum Karlsruhe 1989 − 2007, TURBOMOLE GmbH since 2007.

[5] Weigend, F., Schrodt, C. & Ahlrichs, R. Atom distributions in binary atom clusters: A perturbational approach and its validation in a case study. *J. Chem. Phys.* **121,** 10380–10384 (2004).

[6] Weigend, F. & Schrodt, C. Atom-Type Assignment in Molecules and Clusters by Perturbation Theory — A Complement to X-ray Structure Analysis. *Chem. Eur. J.,* **11,** 3559–3564 (2005).

[7] Deaven, D. M. & Ho, K. M. Molecular Geometry Optimization with a Genetic Algorithm. *Phys. Rev. Lett.* **75**, 288-291 (1995).

[8] Sierka, M. *et al.* Unexpected structures of aluminum oxide clusters in the gas phase. A*ngew. Chem. Int. Ed.* **46**, 3372-3375 (2007).

[9] Weigend, F. Extending DFT-based genetic algorithms by atom-to-place re-assignment via perturbation theory: A systematic and unbiased approach to structures of mixed-metallic clusters. *J. Chem. Phys.* **141**, 134103 (2014).

[10] Plessow. P. Reaction Path Optimization without NEB Springs or Interpolation Algorithms. *J. Chem. Theory Comput.,* **9 (3),** 1305-1310, (2013).

[11] Schäfer, A., Horn, H. & Ahlrichs, R. Fully optimized contracted Gaussian basis sets for atoms Li to Kr. *J. Chem. Phys.* **97**, 2571 (1992).

[12] Eichkorn, K., Weigend, F., Treutler, O. & Ahlrichs, R. Auxiliary basis sets for main row atoms and transition metals and their use to approximate coulomb potentials. *Theor. Chem. Acc.,* **97**, 119-124, (1997).

[13] Andrae, D. *et al.* Energy-adjusted ab initio pseudopotentials for second and third row transition elements. *Theor. Chim. Acta* **77**, 123-141 (1990).

[14] Becke, A. D. Density-functional exchange-energy approximation with correct asymptotic behavior. *Phys. Rev. A* **38,** 3098-3100 (1988).

[15] Perdew, J. P. Density-functional approximation for the correlation energy of the inhomogeneous electron gas. *Phys. Rev. B* **33**, 8822-8824 (1986).

[16] Weigend, F, & Baldes, A. Segmented contracted basis sets for one- and two-component Dirac-Fock effective core potentials. *J. Chem. Phys.* **133**, 174102 (2010).

[17] Figgen, D., Peterson, K. A., Dolg, M. & Stoll, H. Correlation consistent basis sets: the transition metals Hf – Pt. *J. Chem. Phys*. **130,** 164108 (2009).

[18] Tao, J., Perdew, J. P., Staroverov, V. N. & Scuseria, G. E. Climbing the density functional ladder: nonempirical meta–generalized gradient approximation designed for molecules and solids. *Phys. Rev. Lett.* **91**, 146401 (2003).

[19] Weigend, F. Accurate coulomb-fitting basis sets for H to Rn. *Phys. Chem. Chem. Phys.* **8**, 1057-1065 (2006).

[20] Klamt, A. & Schüürmann, G. COSMO: a new approach to dielectric screening in solvents with explicit expressions for the screening energy and its gradient. *J. Chem. Soc., Perkin Trans.* **2**, 799-805, (1993).

[21] Legault, C. Y. CYLView 1.0b. Université de Sherbrooke, 2009.

3.3 $(Ge_2P_2)^{2-}$: A Binary Analogue of P_4 as a Precursor to the Ternary Cluster Anion $[Cd_3(Ge_3P)_3]^{3-}$

This manuscript was accepted at Chem. Commun. on the 21st of December 2017.

The novel binary P_4 analogue $(Ge_2P_2)^{2-}$ proved to be a suitable precursor for hetero-atomic cluster synthesis. Over time in solution, it rearranges to form $(Ge_7P_2)^{2-}$, as shown by NMR studies and X-ray diffraction. Reactions of $(Ge_2P_2)^{2-}$ with $CdPh_2$ afford $[Cd_3(Ge_3P)_3]^{3-}$, comprising an unprecedented trimeric ternary cluster anion with a triangular Cd_3 moiety.

S. Mitzinger conceived and performed the synthesis, J. Bandemehr performed the synthesis under supervision of S. Mitzinger. S. Mitzinger performed the characterisation and interpreted the analytical data. X. Xie performed ^{113}Cd and ^{31}P NMR spectroscopic measurements of **3** and interpreted the data. K. Reiter and F. Weigend performed quantum chemical calculations. S. Mitzinger, K. Reiter, S. McIndoe, X. Xie, F. Weigend, J. Corrigan and S. Dehnen co-wrote the manuscript.

Dieses Manuskript wurde bei Chem. Commun. am 21. Dezember 2017 zur Veröffentlichung angenommen.

Das neue binäre Zintl-Anion $(Ge_2P_2)^{2-}$, welches isovalenzelektronisch zu P_4 ist, hat sich als geeignetes Edukt zur Synthese multi-metallischer Cluster erwiesen. Es konnte durch NMR-spektroskopische Untersuchungen und Einkristallröntgendiffraktometrie gezeigt werden, dass sich $(Ge_2P_2)^{2-}$ über die Zeit in $(Ge_7P_2)^{2-}$ umwandelt. Die Reaktion von $(Ge_2P_2)^{2-}$ mit $CdPh_2$ ergab $[K(crypt\text{-}222)]_3[Cd_3(Ge_3P)_3]$, ein trimeres, multi-metallisches Clusteranion, welches eine bisher unbekannte Cd_3-Dreieckseinheit besitzt.

S. Mitzinger erdachte die Synthese und führte diese durch. J. Bandemehr führte die Synthese unter Anleitung von S. Mitzinger durch. S. Mitzinger führte die Charakterisierung und die Interpretation der analytischen Daten durch. X. Xie führte ^{113}Cd und ^{31}P NMR spektroskopische Messungen an Verbindung **3** durch und interpretierte die Messdaten. K. Reiter und F. Weigend führten quantenchemische Rechnungen durch und werteten die Ergebnisse aus. S. Mitzinger, K. Reiter, S. McIndoe, X. Xie, F. Weigend, J. Corrigan und S. Dehnen haben das Manuskript gemeinsam verfasst.

ChemComm

COMMUNICATION

$(Ge_2P_2)^{2-}$: a binary analogue of P_4 as a precursor to the ternary cluster anion $[Cd_3(Ge_3P)_3]^{3-}$†

Cite this: DOI: 10.1039/c7cc08348c

Received 30th October 2017,
Accepted 21st December 2017

DOI: 10.1039/c7cc08348c

rsc.li/chemcomm

Stefan Mitzinger,[ab] Jascha Bandemehr,[a] Kevin Reiter,[c] Scott J. McIndoe,[d] Xiulan Xie,[a] Florian Weigend,*[c] John F. Corrigan*[b] and Stefanie Dehnen*[a]

The novel binary P_4 analogue $(Ge_2P_2)^{2-}$ proved to be a suitable precursor for heteroatomic cluster synthesis. Over time in solution, it re-arranges to form $(Ge_7P_2)^{2-}$, as shown by NMR studies and X-ray diffraction. Reactions of $(Ge_2P_2)^{2-}$ with $CdPh_2$ afford $[K(crypt\text{-}222)]_3[Cd_3(Ge_3P)_3]$, containing an unprecedented ternary cluster anion with a triangular Cd_3 moiety.

Homoatomic polyanions of germanium, Ge_9^{4-} and Ge_4^{4-}, are actively used for the synthesis of binary transition metal-main group metal complexes and intermetalloid clusters. Their relative stability and yet demonstrated reactivity towards organic and inorganic compounds has been reported for numerous examples,[1–4] like the silylated cages $[Ge_9(SiPh_2CHCH_2)_3]^-$,[5] metal complexes like $[(Ge_9\{Si(TMS)_3\}_2)tBu_2P]Au(NHC^{Dipp})$,[6] or the intermetalloid cluster $[Ru@Ge_{12}]^{3-}$.[7] Within the last decade, a large variety of novel compounds were thus discovered that are exemplary for the high chemical flexibility of these homoatomic systems, which also includes mixed Ge/Si or Ge/Sn intertetrelide species.[8]

A complementary branch of transition metal-main group element cluster chemistry is based on the activation and derivatization of white phosphorus (P_4) as a reagent, which has led to a multitude of beautiful and spectacular new compounds and molecular architectures.[9–13]

We transferred this concept to binary analogs[14] by using the isoelectronic $(E_2^{14}E_2^{15})^{2-}$ species $(Ge_2As_2)^{2-}$,[16] $(Sn_2Sb_2)^{2-}$,[17,18] $(Sn_2Bi_2)^{2-}$,[19–21] or $(Pb_2Bi_2)^{2-}$.[22] This way, the two aforementioned areas of research are bridged, with significant electronic and structural consequences for the reaction products. Isoelectronic substitution has proven a very powerful tool in the formation of intermetalloid cluster anions and heterometallic complexes in the recent past.[22–27] The inclusion of E^{15} atoms to produce binary $(E_2^{14}E_2^{15})^{2-}$ anions reduces their charge relative to their E^{14} analogues, $(E_4^{14})^{4-}$, while retaining the overall valence electron number. The solubility is thus significantly enhanced. However, to date all studies with binary Zintl anions have so far addressed (semi-)metals of the fourth period upwards. In this work, we intended to approach the intriguing P_4 chemistry even more closely by explicitly including this element type while retaining the Zintl anion style of chemistry.

A solid mixture of potassium, germanium and red phosphorus of the nominal composition "$K_2Ge_2P_2$" was formed by fusing the elements in a 1:1:1 ratio at 950 °C in an Nb ampoule. According to a comprehensive time-dependent electrospray ionization mass spectrometry (ESI-MS) study of the extraction process of "$K_2Ge_2P_2$"/crypt-222 in ethane-1,2-diamine (ethylene diamine, en), the $(Ge_2P_2)^{2-}$ anion is the only Zintl anion detected at the beginning of the extraction. It was detected as its protonated, mono-charged derivative $(Ge_2P_2H)^-$ (Fig. S10 and S13, ESI†), as a typical consequence of the ESI procedure of (especially light element) Zintl ions from en solutions, and in contrast to some anions that were intrinsically protonated and even crystallized in this form.[28,29] Upon extracting the solid mixture with en/crypt-222 and subsequent layering with toluene, $[K(crypt\text{-}222)]_2(Ge_2P_2)\cdot en$ (**1**) crystallized as yellow tabular prisms in approximately 20% yield within 3 days (Fig. S1, ESI†). Larger amounts of **1** can be obtained by enforcing its precipitation by the rapid addition of THF to the filtered extraction mixture (yield approx. 70%). If undisturbed, dark orange cubes of $[K(crypt\text{-}222)]_2(Ge_7P_2)$ (**2**) also crystallize, in approximately 10% yield after two weeks (Fig. S2, ESI†). If left undisturbed for several weeks, crystals of **1** dissolve completely and larger amounts of **2** crystallize. As the $(Ge_7P_2)^{2-}$ cluster anion contained in **2** has not been detected in the ESI(−) mass

[a] Fachbereich Chemie and Wissenschaftliches Zentrum für Materialwissenschaften, Philipps-Universität Marburg, Hans-Meerwein-Str. 4, 35043 Marburg, Germany
[b] The University of Western Ontario, Department of Chemistry, 1151 Richmond Street, London, ON, N6A 5B7, Canada
[c] Karlsruhe Institute of Technology (KIT), Institute of Nanotechnology, Hermann-von-Helmholtz-Platz 1, 76344 Eggenstein-Leopoldshafen, Germany
[d] University of Victoria, Department of Chemistry, Elliott Building Room 301, Finnerty Road, Victoria, BC, V8P 5C2, Canada

† Electronic supplementary information (ESI) available: Synthesis details, crystallography, EDX spectroscopy, ESI mass spectrometry, NMR spectroscopy, quantum chemical calculations. CCDC 1579583–1579585. For ESI and crystallographic data in CIF or other electronic format see DOI: 10.1039/c7cc08348c

spectrum upon fresh extraction of the solid mixture in en, we anticipate its formation upon oxidation in solution over time.

The reactivity of the $(Ge_2P_2)^{2-}$ cluster anion towards d-block metal compounds was demonstrated by the addition of $CdPh_2$, giving rise to the formation of $[K(crypt\text{-}222)]_3[Cd_3(Ge_3P)_3]\cdot tol$ (**3**). A reaction with the lighter homologue, $ZnPh_2$, has not afforded identifiable products so far. Compound **1** crystallizes as red, elongated square prisms that dendritically agglomerate into a leaf-like morphology (Fig. S3, ESI†). **3** represents a new example of the rare family of compounds that contain direct Cd–Ge contacts, such as $[CdGe(SiMe_3)_3]_2I_3$[30] and $[Ge_9(Si(SiMe_3)_3)_3]_2Cd$.[2] At the same time the anion in **3** is the first species comprising more than two Cd atoms within an intermetalloid cluster structure.

The compositions of **1–3** were confirmed by means of ESI(−)-MS and energy-dispersive X-ray (EDX) spectroscopy. Their crystal structures were determined by means of single-crystal X-ray diffraction[31,32] (see ESI† for details).

1 crystallizes with one molecule of en per unit cell in the triclinic space group $P\bar{1}$ (Z = 1). The bond lengths of the tetrahedral anion were found to vary between 2.387(2) and 2.635(2) Å. The shortest bond is thus notably longer than the P–P bonds in white phosphorus (2.209(5) Å),[33] while the longest contact is slightly longer than the Ge–Ge bonds in the Ge_4^{4-} anion in K_4Ge_4 (2.563(3) Å).[34] However, the bond lengths are similar to known Ge–P distances (*e.g.*, 2.34 Å for a Ge atom coordinated to a P_4 unit;[35] *e.g.*, 2.50–2.52 Å for Ge atoms coordinated to a P_7 unit).[36] Due to intrinsic disorder in the solid state structure, we cannot discriminate between specific Ge–P, Ge–Ge and P–P bonds.

The ^{31}P-NMR spectrum, measured on a fresh solution of **1** in DMF-d_7 at room temperature, shows a singlet at δ = −432 ppm (Fig. 1, bottom). This is slightly less shifted upfield than the values reported for white phosphorus itself (−488 to −527 ppm).[37] However, the comparison of these values is problematic due to very different solvent environments. Recently, a planar Ge_2P_2 four-membered ring was reported that was synthesized *via* CO elimination of a phosphaketenyl germylene. For this compound, the ^{31}P-NMR spectrum shows a singlet at 131.9 ppm, hence significantly deshielded in comparison with its parent molecule, which exhibits a singlet at −301.7 ppm before decarbonylation.[38] However, a comparison with the anion in **1** is questionable for the Ge_2P_2 moiety being planar and not charged. A butterfly-type Ge_2P_2 motif was reported in a Ge(II) phosphinidene dimer, which also exhibits a low-field resonance ^{31}P-NMR signal at 270.2 ppm.[39] Here, the P atoms form four bonds each, again complicating a direct comparison with **1**. The NMR data of $(Ge_2P_2)^{2-}$ compare best with butterfly-shaped Ge–P heterocycles reported by Drieß *et al.*: with all P atoms bound three-fold, the ^{31}P-NMR resonance singlet is observed at −365 ppm,[40] hence between the values reported herein for **1** and **2**. This confirms the angles and the number of bonds to be the most important parameters for controlling the (de)shielding of the P atoms.

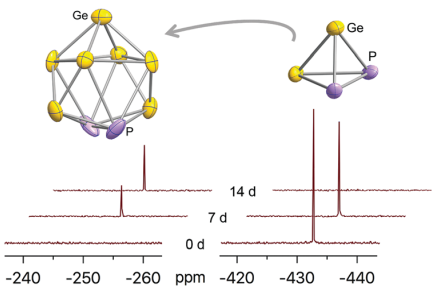

Fig. 1 Time-dependent ^{31}P NMR spectroscopy, indicating full conversion of $(Ge_2P_2)^{2-}$ anions to $(Ge_7P_2)^{2-}$ anions in the course of 14 days. The spectrum at the bottom was measured on a fresh solution of single crystals of compound **1** in DMF-d_7, and comprises the singlet signal of the $(Ge_2P_2)^{-}$ anion (see structure diagram to the right) at −432.38 ppm only. The spectrum in the centre was recorded from the same sample after 7 days, the topmost spectrum after 14 days. The latter comprises the singlet signal of the $(Ge_7P_2)^{2-}$ anion (see structure diagram to the left) at −252.21 ppm only, which is identical to the signal measured from single crystals of **2**.

Time-dependent ^{31}P-NMR spectroscopy in DMF-d_7 in a flame-sealed NMR tube (Fig. 1) indicates the continuous formation of a second species over time. As mentioned above, this species was identified as the $(Ge_7P_2)^{2-}$ anion by crystallization of compound **2**. The NMR data showed a complete conversion of $(Ge_2P_2)^{2-}$ to $(Ge_7P_2)^{2-}$ anions after two weeks, together with precipitation of red phosphorus, consistent with the lower relative phosphorus content in $(Ge_7P_2)^{2-}$ (3.5 : 1) with regard to that in $(Ge_2P_2)^{2-}$ (1 : 1). The loss of phosphorous by precipitation is reflected by a decrease of the ^{31}P-NMR signal intensity. The ^{31}P-NMR spectrum of the products features a singlet at δ = −252 ppm, in accordance with the less shielding chemical environment of seven neighboring Ge atoms with a total charge of 2− in $(Ge_7P_2)^{2-}$, opposed to only two neighboring Ge atoms with the same total charge in $(Ge_2P_2)^{2-}$. The ESI(−) mass spectrum recorded after the described conversion (Fig. S11, ESI†) exhibits peaks for the corresponding single charged species $(Ge_7P_2H)^{-}$ and $\{[K(crypt\text{-}222)](Ge_7P_2)\}^{-}$, respectively, in agreement with the described formation of $(Ge_2P_2)^{2-}$ into $(Ge_7P_2)^{2-}$. Noteworthy, this result supports a recent assumption regarding the formation mechanism of the *nido*-type cages from tetrahedral anions, which was made based on quantum chemical calculations.[15] Some calculations have also been done on the structure of neutral $[Ge_2P_2]$,[41] which are in full agreement with the known feature of an two-electron oxidation of the tetrahedral anions to result in the cleavage of the E^{14}–E^{14} bond, which represents the clusters' HOMO.[19]

Compound **2** crystallizes in the trigonal space group $P\bar{3}c1$ (Z = 2). The cluster anion is disordered over three positions around a common center of gravity (Fig. S5 and S6, ESI†). Each orientation shares two atom positions with another orientation. Its crystallographic constitution is therefore similar to that of the homologous $(Ge_7As_2)^{2-}$ cluster anion.[15] The Ge–Ge distances are in accordance with those observed in the $(Ge_7As_2)^{2-}$ homolog.

The ternary cluster compound **3** crystallizes in the hexagonal space group $P6_522$ (Z = 6). Two cluster orientations, that can be converted into each other by a two-fold rotation, are disordered

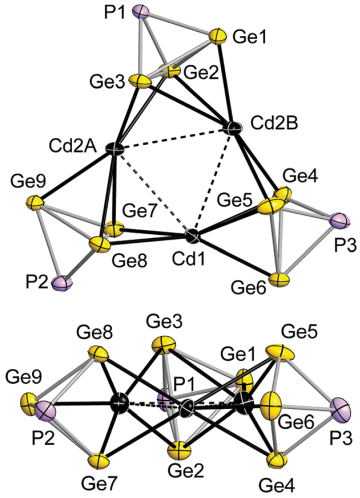

Fig. 2 Top view (left) and side view (right) of the molecular structure of the anion in **3**, shown for one of the two disordered positions. Selected distances [Å] and angles [°]: Cd1···Cd2A 2.985(3), Cd1···Cd2B 3.251(3), Cd2A···Cd2B 3.358(3), Cd–Ge 2.686(4)–3.170(4), Ge–Ge 2.232(6)–2.566(5), Ge–P 2.309(9)–2.440(14); Cd···Cd···Cd 10.70(4), 35.35(14), Ge–P–Ge 66.2(2)–71.5(6), Ge–Ge–Ge 57.3(2)–66.68(11), P–Ge–Ge 51.48(19)–57.01(17). Dashed Cd···Cd contacts are not meant to represent bonds.

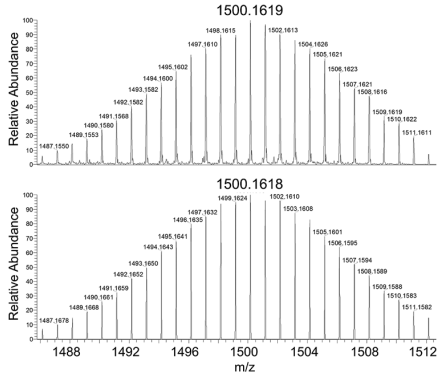

Fig. 3 High resolution ESI mass peak of the $[Cd_3(Ge_3P)_3]^{3-}$ anion in **3**, detected as $\{[K(crypt\text{-}222)]H[Cd_3(Ge_3P)_3]\}^-$ at *m*/*z* 1500. Top: Measured spectrum. Bottom: Calculated spectrum.

on the same anionic position, with site occupation factors of 0.5 for all atoms (Fig. S9, ESI†). The structure of one of the orientations is shown in Fig. 2. The crystallographic assignment of Ge and P atoms is supported by quantum chemical calculations as well as ^{31}P-NMR and ^{113}Cd-NMR studies (see below).

The anion in compound **3** is based on three Cd atoms forming a nearly isosceles triangle (Cd···Cd 2.985(3)–3.358(3) Å) that is coordinated and thereby connected by three $(Ge_3P)^{3-}$ tetrahedra. Notably, only Ge atoms of the latter interact with the Cd atoms, while the P atoms point outwards. Each of the Cd atoms interacts with two of the neighboring $(Ge_3P)^{3-}$ units, one coordinating in a η^3-type fashion, thereby forming a $P(Ge_3)Cd$ bipyramid, the other one coordinates in a η^2-type manner. This leads to an idealized C_{3h} symmetric structure, which is, however, perturbed by the irregularity of the central Cd_3 ring.

Quantum chemical calculations of the anion that are carried out without symmetry restrictions did not reproduce the exact structure as global energy minimum, but a diversity of similar ones within 30 kJ mol^{-1}, exhibiting weak modes (below 10 cm^{-1}) for a rotation of the $(Ge_3P)^{3-}$ unit about the virtual $Cd\cdots P_{opposite}$ axes (see Fig. S19, ESI†). This indicates a high fluxionality of the cluster at least under the given experimental conditions, which is in agreement with the NMR spectroscopic data of the cluster in solution.

The ^{113}Cd-NMR spectrum of a solution of **3** in DMF-d_7 revealed only one signal (δ = 636 ppm (t), $^2J_{^{113}Cd-^{31}P}$ = 72 Hz; see Fig. S18, ESI†). The ^{31}P-NMR is more complex and consists of a central singlet at −129 ppm with two symmetric satellites (72 Hz apart) and symmetric shoulders. After evaluation of several couplings enabled due to various Cd isotopes, an integral distribution of 2 : 19 : 58 : 19 : 2 was calculated and also observed in the experimental spectrum (see ESI† for more details). The value of the ^{113}Cd–^{31}P coupling of 72 Hz is similar to ^2J coupling constants reported for Cd-enriched enzyme phosphate complexes (30 Hz),[42] whereas it deviates by more than one order of magnitude from reported values for a $^1J_{^{113}Cd-^{31}P}$ coupling (1123–2960 Hz).[43,44] This supports the assignment of the P atoms in the $(Ge_3P)^{3-}$ moiety in **3** as pointing outwards.

The originally unexpected presence of $(Ge_3P)^{3-}$ units in the molecular structure of the anion in **3** was unambiguously confirmed by SCXRD as well as by ESI(−)-MS of re-dissolved single-crystals (Fig. 3), and it is in perfect agreement with the total 3 − charge of that anion that results from a combination of three $(Ge_3P)^{3-}$ units with three Cd^{2+} ions, balanced by three $[K(crypt\text{–}222)]^+$ cations. Therefore, we propose that upon addition of $CdPh_2$, the $(Ge_2P_2)^{2-}$ anions undergo a transformation into $(Ge_3P)^{3-}$ anions and some phosphorus species, such as $(GeP_3)^-$ (for the simplest possible way to comply with atom and charge balance), or some yet unidentified polyphosphides.

Moreover, in a detailed mass spectrometric study of the Ge/P system under different solvent conditions, we found evidence for "GeP_3" moieties with solvent fragments (Fig. S14, ESI†), which may support this first assumption. In our previous study of the Ge/As system[15] a corresponding "(Ge_3As)" moiety was detected in the ESI mass spectrum, which suggests that a similar process in solution is occurring in Ge/As and Ge/P systems. The mechanism of and the stimulus for this transformation remains puzzling and needs further investigation.

In conclusion, we were able to demonstrate the successful use of the novel P_4 homolog $(Ge_2P_2)^{2-}$ for the synthesis of multi-metallic clusters using $CdPh_2$ as a reagent. The novel trimeric cluster anion comprises an unusual triangular Cd geometry and a new $(Ge_3P)^{3-}$ fragment which forms from $(Ge_2P_2)^{2-}$ in solution at a so far unknown pathway, that most probably releases $(Ge_3P)^{3-}$ and $(GeP_3)^-$ fragments. The tetrahedral cluster anion $(Ge_2P_2)^{2-}$ undergoes an irreversible

transformation in solution resulting in the 9-vertex-cluster anion $(Ge_7P_2)^{2-}$. The novel homolog of P_4 can be synthesized as the $[K(crypt\text{-}222)]^+$ salt in high purity with approx. 70% yield and is therefore a good precursor for the development of new binary Ge/P cluster compounds. Although many questions remain unanswered in this process, we can conclude that these binary Zintl-type clusters possess a rich chemistry in solution. Their reactivity is to a degree solvent-specific, and they can undergo transformations into larger binary clusters. The quantitative understanding of this process alone would be of great value to develop a comprehensive chemistry around the so far selective knowledge we possess of multi-metallic clusters. This will be addressed in the future.

This article is dedicated to Professor Philip P. Power on the occasion of his 65th birthday. We thank Rhonda Stoddard and Dr Eric Janusson at the University of Victoria, British Columbia, Canada, for their help in utilizing various mass spectrometry methods, and Dr Mathew Willans at the University of Western Ontario, Ontario, Canada, for ^{31}P-NMR and preliminary ^{111}Cd-NMR and ^{113}Cd-NMR measurements. This work was supported by the Friedrich-Ebert-Stiftung (S. M.), the German Research Foundation (Deutsche Forschungsgemeinschaft, DFG; S. D.), and the Natural Sciences and Engineering Research Council of Canada (NSERC; S. M. and J. F. C.).

Conflicts of interest

There are no conflicts to declare.

Notes and references

1 S. C. Sevov and J. M. Goicoechea, *Organometallics*, 2006, **25**, 5678–5692.
2 F. Henke, C. Schenk and A. Schnepf, *Dalton Trans.*, 2009, 9141–9145.
3 L. G. Perla and S. C. Sevov, *J. Am. Chem. Soc.*, 2016, **138**, 9795–9798.
4 K. Mayer, L.-A. Jantke, S. Schulz and T. F. Fässler, *Angew. Chem., Int. Ed.*, 2017, **56**, 2350–2355.
5 K. Mayer, L. J. Schiegerl, T. Kratky, S. Günther and T. F. Fässler, *Chem. Commun.*, 2006, 11798–11801.
6 F. S. Geitner, J. V. Dums and T. F. Fässler, *J. Am. Chem. Soc.*, 2017, **139**, 11933–11940.
7 G. Espinoza-Quintero, J. C. A. Duckworth, W. K. Myers, J. E. McGrady and J. M. Goicoechea, *J. Am. Chem. Soc.*, 2014, **136**, 1210–1213.
8 M. Waibel, C. B. Benda, B. Wahl and T. F. Fässler, *Chem. – Eur. J.*, 2011, **17**, 12928–12931.
9 M. Scheer, G. Balázs and A. Seitz, *Chem. Rev.*, 2010, **110**, 4236–4256.
10 C. Schwarzmaier, A. Schindler, C. Heindl, S. Scheuermayer, E. V. Peresypkina, A. V. Virovets, M. Neumeier, R. Gschwind and M. Scheer, *Angew. Chem., Int. Ed.*, 2013, **52**, 10896–10899.
11 C. Schwarzmaier, A. Y. Timoshkin, G. Balázs and M. Scheer, *Angew. Chem., Int. Ed.*, 2014, **53**, 9077–9081.
12 J. D. Masuda, W. W. Schoeller, B. Donnadieu and G. Bertrand, *Angew. Chem., Int. Ed.*, 2007, **46**, 7052–7055.
13 J. D. Masuda, W. W. Schoeller, B. Donnadieu and G. Bertrand, *J. Am. Chem. Soc.*, 2007, **129**, 14180–14181.
14 B. Weinert and S. Dehnen, Binary and Ternary Intermetalloid Clusters, in *Clusters – Contemporary Insight in Structure and Bonding. Structure and Bonding*, ed. S. Dehnen, Springer, Cham, 2017, vol. 174.
15 S. Mitzinger, L. Broeckaert, W. Massa, F. Weigend and S. Dehnen, *Chem. Commun.*, 2015, **51**, 3866–3869.
16 S. Mitzinger, L. Broeckaert, W. Massa, F. Weigend and S. Dehnen, *Nat. Commun.*, 2016, **7**, 10480.
17 F. Lips, I. Schellenberg, R. Pöttgen and S. Dehnen, *Chem. – Eur. J.*, 2009, **15**, 12968–12973.
18 R. J. Wilson, L. Broeckaert, F. Spitzer, F. Weigend and S. Dehnen, *Angew. Chem., Int. Ed.*, 2016, **55**, 11775–11780.
19 S. C. Critchlow and J. D. Corbett, *Inorg. Chem.*, 1982, **21**, 3286–3290.
20 F. Lips, M. Raupach, W. Massa and S. Dehnen, *Z. Anorg. Allg. Chem.*, 2011, **637**, 859–863.
21 U. Friedrich, M. Neumeier, C. Koch and N. Korber, *Chem. Commun.*, 2012, **48**, 10544–10546.
22 R. Ababei, J. Heine, M. Hołyńska, G. Thiele, B. Weinert, X. Xie, F. Weigend and S. Dehnen, *Chem. Commun.*, 2012, **48**, 11295–11297.
23 B. Weinert, A. R. Eulenstein, R. Ababei and S. Dehnen, *Angew. Chem., Int. Ed.*, 2014, **53**, 4704–4708.
24 N. Lichtenberger, R. J. Wilson, A. R. Eulenstein, W. Massa, R. Clérac, F. Weigend and S. Dehnen, *J. Am. Chem. Soc.*, 2016, **138**, 9033–9036.
25 N. Lichtenberger, N. Spang, A. Eichhöfer and S. Dehnen, *Angew. Chem., Int. Ed.*, 2017, **56**, 778.
26 R. J. Wilson and S. Dehnen, *Angew. Chem., Int. Ed.*, 2017, **56**, 3098–3102.
27 Y. Wang, Q. Qin, J. Wang, R. Sang and L. Xu, *Chem. Commun.*, 2014, **50**, 4181.
28 B. Weinert, F. Müller, K. Harms and S. Dehnen, *Angew. Chem., Int. Ed.*, 2014, **53**, 11979–11983.
29 F. S. Kocak, D. O. Downing, P. Zavalij, Y.-F. Lam, A. N. Vedernikov and B. Eichhorn, *J. Am. Chem. Soc.*, 2012, **134**, 9733–9740.
30 S. P. Mallela, F. Schwan and R. A. Geanangel, *Inorg. Chem.*, 1996, **35**, 745–748.
31 A. Linden, *Acta Crystallogr., Sect. C: Struct. Chem.*, 2015, **71**, 1–2.
32 O. V. Dolomanov, L. J. Bourhis, R. J. Gildea, J. A. K. Howard and H. Puschmann, *J. Appl. Crystallogr.*, 2009, **42**, 339–341.
33 A. Simon, H. Borrmann and H. Craubner, *Phosphorus, Sulfur Silicon Relat. Elem.*, 1987, **30**, 507–510.
34 H. G. V. Schnering, J. Llanos, J. H. Chang, K. Peters, E. M. Peters and R. Nesper, *Z. Kristallogr. - New Cryst. Struct.*, 2005, **220**, 324–326.
35 J. W. Dube, C. M. E. Graham, C. L. B. Macdonald, Z. D. Brown, P. P. Power and P. J. Ragogna, *Chem. – Eur. J.*, 2014, **20**, 6739–6744.
36 G. E. Quintero, I. Paterson-Taylor, N. H. Rees and J. M. Goicoechea, *Dalton Trans.*, 2016, **45**, 1930–1936.
37 O. Kühl, *Phosphorus-31 NMR Spectroscopy*, Springer, Berlin/Heidelberg, 2008.
38 Y. Wu, L. Liu, J. Su, J. Zhu, Z. Ji and Y. Zhao, *Organometallics*, 2016, **35**, 1593–1596.
39 W. A. Merrill, E. Rivard, J. S. DeRopp, X. Wang, B. D. Ellis, J. C. Fettinger, B. Wrackmeyer and P. P. Power, *Inorg. Chem.*, 2010, **49**, 8481–8486.
40 M. Drieß, H. Pritzkow and U. Winkler, *Chem. Ber.*, 1992, **125**, 1541–1546.
41 F. Hao, Y. Zhao, X. Jing, X. Li and F. Liu, *THEOCHEM*, 2006, **764**, 47–52.
42 J. D. Otvos, J. R. Alger, J. E. Coleman and I. M. Armitage, *J. Biol. Chem.*, 1979, **254**, 1778–1780.
43 B. E. Mann, *Inorg. Nucl. Chem. Lett.*, 1971, **7**, 595–597.
44 D. Dakternieks and C. L. Roll, *Inorg. Chim. Acta*, 1985, **105**, 213–217.

Supporting Information

$(Ge_2P_2)^{2-}$: A Binary Analogue of P_4 as a Precursor to the Ternary Cluster Anion $[Cd_3(Ge_3P)_3]^{3-}$

Stefan Mitzinger,[a,b] Jascha Bandemehr,[a] Kevin Reiter,[c] Scott McIndoe,[d] Florian Weigend,[c] Xiulan Xie,[a] John Corrigan[b] and Stefanie Dehnen*[a]

[a] Fachbereich Chemie, Philipps-Universität Marburg
Hans-Meerwein-Str., 35043 Marburg, Germany
E-mail: dehnen@chemie.uni-marburg.de

[b] The University of Western Ontario, Department of Chemistry,
1151 Richmond Street, London, ON, N6A 5B7, Canada

[c] Karlsruhe Institute of Technology (KIT), Institute of Nanotechnology,
Hermann-von-Helmholtz-Platz 1, 76344 Eggenstein-Leopoldshafen, Germany

[d] University of Victoria, Department of Chemistry,
Elliott Building Room 301, Finnerty Road, Victoria, BC, V8P 5C2, Canada

Contents:

1. Synthesis details

1.1. General

All manipulations and reactions were performed under dry Ar atmosphere by using standard Schlenk or glovebox techniques. Ethane-1,2-diamine (ethylenediamine, *en*) was distilled over CaH_2 and stored over molecular sieves. Toluene and tetrahydrofurane (THF) were distilled over Na/K alloy and stored over molecular sieves. crypt-222[1] (Merck) was dried *in vacuo* for at least 18 h. Ge and P (red) of a purity of 99.99% or higher was used.

The solid mixture with a nominal composition "$K_2Ge_2P_2$" was accessed by combining K, Ge and P (red) in equimolar amounts in a niobium ampoule. The ampoule was sealed by arc-welding, and then stored in silica glass ampoule, which was sealed under vacuum, before heating in an oven at 950°C for 2 d. The resulting solid was pulverized in a mortar thoroughly prior to further use.

1.2. Syntheses

1.2.1. Synthesis of $[K([crypt\text{-}222]_2(Ge_2P_2)\cdot en$ (1) and $[K([crypt\text{-}222]_2(Ge_7P_2)$ (2)

0.2 mmol of "$K_2Ge_2P_2$" and 0.2 mmol of crypt-222 were weighed out into a Schlenk tube. Then *en* (ethane-1,2-diamine, 6 mL) was added. The reaction mixture was allowed to stir at room temperature for 3 h. The liquid was filtered through a standard glass frit (D3), yielding a yellow solution that was carefully layered with *tol* (toluene, 12 mL). After 3 days, clear yellow tabular prisms of $[K(crypt\text{-}222)]_2(Ge_2P_2)\cdot en$ (**1**) crystallized. Yield: approx. 21%.

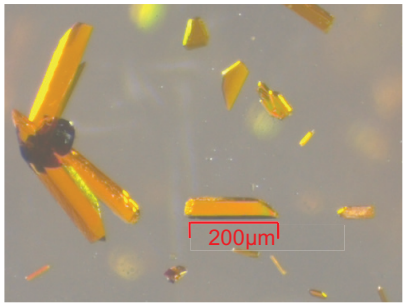

Figure S1. Crystals of $[K(crypt\text{-}222)]_2(Ge_2P_2)\cdot en$ (**1**).

If the Schlenk tube is left undisturbed for a longer time (>7 days), dark orange cubes of $[K(crypt\text{-}222)]_2(Ge_7P_2)$ (**2**) crystallize beside the clear yellow tabular prisms of **1** in approx. 10% yield.

After several weeks, all crystals of **1** have disappeared, and the only visible crystals are dark red cubes of **2**. Yield: approx. 20%.

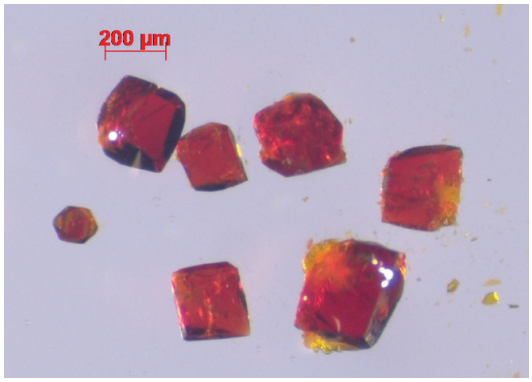

Figure S2. Crystals of [K([crypt-222]$_2$(Ge_7P_2) (**2**).

To obtain **1** in high purity and yield the extraction process is stopped after 3 h. After filtration through a standard glass frit (D3) a large volume of dry THF is added. **1** precipitates and is separated by filtration. The filtrate is cooled at 5°C over night. After a second filtration, the combined precipitates are dried *in vacuo*. A bright yellow solid is obtained at 70% yield.

1.2.2. Synthesis of [K(crypt-222)]$_2$[(Ge_3P)$_3$$Cd_3$] (3)

0.05 mmol of **1** are dissolved in 3 ml of *en*. Then 0.05 mmol of Ph_2Cd (or small excess) were added. After 3 h of stirring at room temperature the solution is filtered through a standard glass frit (D3) and layered with *tol*. After one week elongated red square prisms that dendritically agglomerate into a leaf-like morphology crystallized. They had to be broken down to single crystalline fragments for SCXD. Yield: approx. 24%.
The synthesis of **3** can also be addressed directly from "$K_2Ge_2P_2$" and Ph_2Cd in the presence of crypt-222 in *en*.

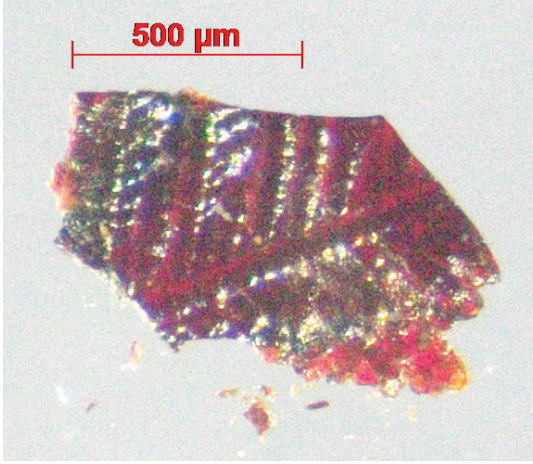

Figure S3. Crystals agglomerates of $[K(crypt\text{-}222)]_3[(Ge_3P)_3Cd_3]\cdot tol$ (**3**).

2. Single crystal X-ray crystallography

The data for the X-ray structural analyses were collected at T = 100(2) K with Mo-K_α-radiation ($\lambda_{Mo\text{-}K\alpha}$= 0.71073 Å) on an area detector system Stoe IPDS2 or Stoe IPDS2T or with a CCD detector system on a Bruker QUEST. The structures were solved by direct methods (SHELXS-97[2]), and refined by full-matrix-least-squares methods against F^2 with program SHELXL-2013.[2] Crystallographic data for the three structures reported in this paper have been deposited with the Cambridge Crystallographic Data Center as supplementary publications No. CCDC 1579583 (**1**), CCDC 1579584 (**2**) and CCDC 1579585 (**3**). The crystal data and experimental parameters of the structure determinations are collected in Table S1. Supplementary Figures are provided in Figures S4-S10 and selected structural parameters are listed in Tables S2-S4.

Table S1. Crystal data and details of the structure determinations of **1** - **3**.

Compound	**1**	**2**	**3**
empirical formula	$C_{38}H_{82}Ge_2K_2N_6O_{12}P_2$	$C_{36}H_{72}Ge_7K_2N_4O_{12}P_2$	$C_{61}H_{116}Cd_3Ge_9K_3N_6O_{18}P_3$
formula weight [g mol^{-1}]	1100.41	1401.24	2422.53
crystal color, shape	Yellow tabular prism	Dark red cube	Dark red block
crystal size [mm^3]	0.59×0.34×0.30	0.075×0.097×0.116	0.054×0.171×0.189
crystal system	triclinic	trigonal	hexagonal
space group	*P*1	*P*–3*c*1	$P6_522$
a [Å]	10.932(2)	11.8967(17)	15.237(2)
b [Å]	11.924(2)	11.8967(17)	15.237(2)
c [Å]	12.549(3)	22.394(5)	68.672(14)
α [°]	118.03(3)	90	90
β [°]	108.44(3)	90	90
γ [°]	96.10(3)	120	120
V [Å^3]	1304.7(6)	2744.8(10)	13807(5)
Z, ρ_{calc} [g cm^{-3}]	1, 1.390	2, 1.695	6, 1.748
μ ($Mo_{K\alpha}$) [mm^{-1}]	1.431	4.045	3.816
Absorption correction type	numerical	numerical	multi-scan
2θ range [°]	4.00 to 53.60	5.36 to 52.00	4.80 to 51.40
total reflections	34245	3628	132693
unique reflections [R_{int}]	10561	3313	8698
obs. reflections [I>2σ(I)]	8825	1787	7688
parameters	548	119	489
R1 [I>2σ(I)] / *w*R2 (all data)	0.0452 / 0.1210	0.0652 / 0.1674	0.0733 / 0.1796
GooF (all data)	0.9730	0.8770	1.123
max peak/hole [e Å^3]	0.80 / –0.69	1.5500 / –0.9300	1.1800 / –1.0700
Flack parameter	**0.102(5)**	–	–

2.1. Details of the structure determination of $[K(crypt\text{-}222)]_2(Ge_2P_2)$ (1)

A numerical absorption correction has been applied based on crystal faces optimized by the XSHAPE procedure in X-AREA (Stoe 2013).

Cluster anion: The anionic cluster component is a tetrahedral $(Ge_2P_2)^{2-}$. Due to rotational disorder two germanium atoms and one phosphorous atom are equally distributed over three cluster positions leading to site occupation factors of 2/3 for Ge and 1/3 for P for these positions, while the second phosphorous atom is clearly localized. The disordered *en* molecule breaks the *P*–1 symmetry resulting in the space group *P*1, as already observed for the heavier binary tetrahedral group 14/15 Zintl anion species.

Cations: The two $[K(crypt\text{-}222)]^+$ cations are well localized. All cations were refined using geometrical restraints on the bond lengths and 1,3-distances but leaving conformational freedom (SAME option of SHELXL). This explains the large number of restraints.

Solvent: One *en* molecule was found in the unit cell, the atoms of which were refined using anisotropic displacement parameters.

Table S2. Bond lengths of the anionic cluster in **1**.

Atom numbers	Bond length
1–2	2.387(2) Å
1–3	2.388(2) Å
1–4	2.349(2) Å
2–3	2.521(1) Å
2–4	2.635(2) Å
3–4	2.598(2) Å
Average	**2.479 Å**

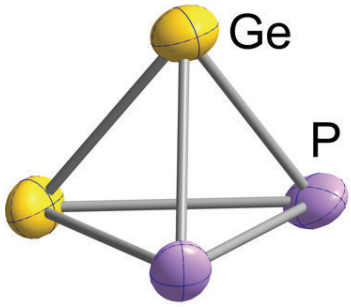

Figure S4. $(Ge_2P_2)^{2-}$ anion in **1** with one of the disorder models shown. Ellipsoids shown at 50% probability.

2.2. Details of the structure determination of $[K(crypt\text{-}222)]_2(Ge_7P_2)$ (2)

A numerical absorption correction has been applied based on crystal faces optimized by the XSHAPE procedure in XAREA (Stoe 2013).

Cluster anion: The $(Ge_7P_2)^{2-}$ anion itself has the site symmetry 32. (D_3). Around the Wyckoff position 2a, the 3-fold symmetry axis creates 24 atom positions which can be assigned to three anion orientations, in which two atoms in each anion orientation are shared with one other orientation. Ge1 and Ge2 occupy a .2. site (Wyckoff position 6f), whereas Ge3, Ge4 and P1 occupy a 12g Wyckoff position. The crystal structure is closely related to the one of $[K([crypt\text{-}222]_2(Ge_7As_2)$,[3] featuring the same crystallographic disorder.

Cations: The structure of 2 crystallizes in space group *P*–3*c*1 with the $[K(crypt\text{-}222)]^+$ cation on a 3-fold axis which runs through atoms K1, N1 and N2 with 3.. site symmetry (Wyckoff position 4d). C1-C6 as well as O1 and O2 occupy a 12g Wyckoff position. All cations were refined using enhanced rigid bond restraints (RIGU option) on the bond lengths and 1,3-distances.

Solvent: There is no solvent present.

Table S3. Selected bond lengths of the anionic cluster in **2**.

Atom numbers	Bond length
Ge1–Ge2	2.502(3) Å
Ge2–Ge4	2.630(5) Å
Ge1–Ge3	2.461(2) Å
Ge3–Ge4	2.470(5) Å
P1–Ge3	2.447(8) Å
P1–Ge4	2.578(7) Å

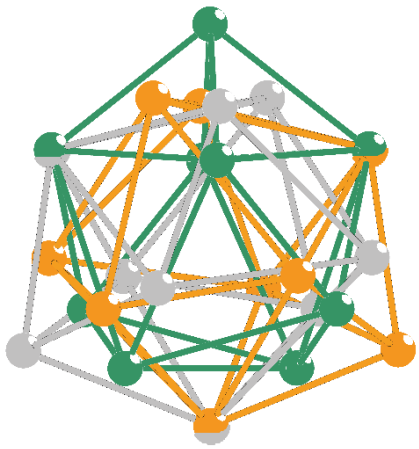

Figure S5. Three anion orientations in **2** overlaid.

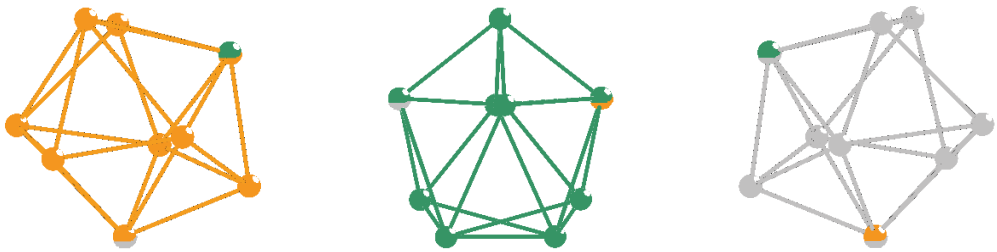

Figure S6. Separated anion orientations in **2**. Shared sites are indicated by mixed color.

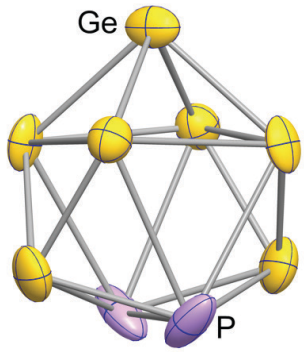

Figure S7. $(Ge_7P_2)^{2-}$ anion in **2** with only one of the disorder models shown. Ellipsoids shown at 50% probability.

2.3. Details of the structure determination of $[K(crypt\text{-}222)]_3[(Ge_3P)_3Cd_3]\cdot tol$ (3)

MULTISCAN absorption correction was applied within the APEX3 software suite (Bruker 2016). The compound crystallizes in the space group $P6_522$ with a very long *c* axis of 68.672(14) Å.

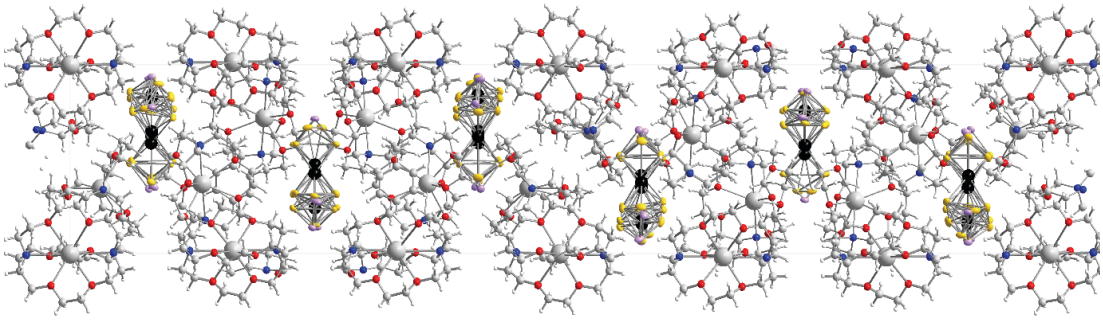

Figure S8. View of the unit cell of **3** along the *a* axis.

Cluster anion: The cluster anion consists of three $[(Ge_3P)Cd]^-$ units. The Cd atoms are coordinated and interconnected by Ge atoms of the Ge_3P unit, while the P atoms do not bind to the Cd atoms. The disk-like cluster anion has two orientations that crystallize with a 0.5:0.5 ratio on the same position. Cd1 occupies the Wyckoff position 6b with ..2 site symmetry. Cd2A and Cd2B occupy a 12c Wyckoff position with an occupancy of 0.5 each. All Ge and P atoms occupy a 12c Wyckoff position, and also possess a 0.5 occupancy.

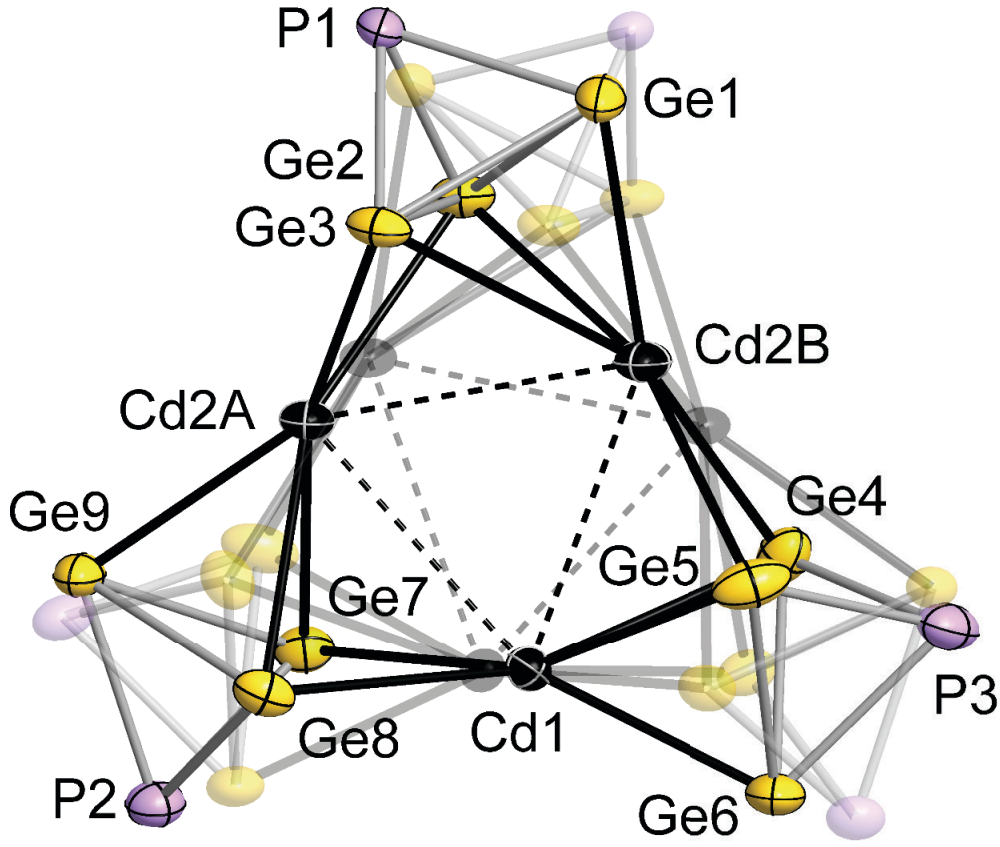

Figure S9. Overlaid image of the two anion orientations in **3**, illustrated by drawing one of them in solid mode and the other one in transparent mode. Dashed lines that connect Cd atoms do not indicate bonds but serve as a guide to the eye. Ellipsoids shown at 50% probability.

Cations: 18 $[K(crypt\text{-}222)]^+$ units are present within one unit cell. C–C distances in the cation have been fixed with DFIX at 1.49 Å or using enhanced rigid bond restraints (RIGU option) on the bond lengths and 1,3-distances.

Solvent: Six toluene molecules are present within the unit cell. To model the solvent molecule with anisotropic displacement parameters, DELU, SIMU and RIGU commands were used.

Table S4. Selected bond lengths of the anionic cluster in **3**.

Atom numbers	Bond length
Cd2A–Ge2	2.793(3) Å
Cd2A–Ge3	2.723(3) Å
Cd2B–Ge1	2.685(4) Å
Cd2B–Ge4	2.791(4) Å
Cd2B–Ge5	2.752(4) Å
P1–Ge1	2.352(7) Å
P1–Ge2	2.305(9) Å

3. Energy dispersive X-ray spectroscopy (EDX) analysis

EDX analyses were performed to support the elemental composition that was suggested based on the XRD experiments. These were carried out using an EDX-device Voyager 4.0 of Noran Instruments coupled with an electron microscope CamScan CS 4DV. Data acquisition was performed with an acceleration voltage of 20 kV and 100 s accumulation time. The radiation emitted by the atoms was analyzed: K-K, Ge-K, P-K. Results are summarized in Table S5.

Table S5. EDX analysis of **1** - **3** (K, Ge, P).

Element	k-ratio	ZAF	Atom%	Atomic ratio observed (calc)	Element wt %	wt % Err. (1-sigma)
[K(crypt-222)]$_2$(Ge_2P_2)·*en* (1)						
P-K	0.1075	1.838	30.92	1.83 (2)	19.77	+/- 0.31
K-K	0.2242	1.211	33.65	2 (2)	27.15	+/- 0.36
Ge-K	0.4798	1.106	35.43	2.11 (2)	53.08	+/- 1.93
Total			100	5.94 (6)	100	
[K(crypt-222)]$_2$(Ge_7P_2) (2)						
P-K	0.0488	2.171	19.78	2.02 (2)	10.60	+/- 0.81
K-K	0.1096	1.212	19.62	2 (2)	13.28	+/- 1.34
Ge-K	0.7222	1.054	60.60	6.12 (7)	76.12	+/- 8.67
Total			100	10.14 (11)	100	
[K(crypt-222)]$_3$($Ge_9P_3Cd_3$)·*tol* (3)						
P-K	0.0421	1.882	17.20	3.07 (3)	7.92	+/- 1.09
K-K	0.0873	1.118	16.79	3 (3)	9.76	+/- 0.72
Ge-K	0.4994	1.024	47.36	8.46 (9)	51.12	+/- 4.15
Cd-L	0.2535	1.230	18.66	3.33 (3)	31.19	+/-1.96
Total			100	17.86 (18)	100	

The results of the EDX investigations confirm the Ge:P ratios of the investigated substances within the expected accuracy. The Ge values show largest deviations from the calculated values, in accordance with the large error indicated in the rightmost column.

4. Electrospray Ionization Mass Spectrometry (ESI-MS) Investigations

ESI(–) mass spectrometry has been performed on Micromass Q-Tof *micro* or a Finnigan LTQ-FT spectrometer by Thermo Fischer Scientific in the negative ion mode: Spray voltage 3.90 kV, capillary temperature 300°C, capillary voltage –11 V, tube lens voltage –140 V, sheath gas flow rate 25 arb, sweep gas flow rate 0 arb. For the measurements, the filtered solutions were dried *in vacuo* and re-dissolved in dry DMF or *en*. Additional peaks observed in the ESI(–) spectrum are believed to belong to decomposition products and fragments formed by a dynamic re-organization of the cluster anions and their fragments in solution under ESI-MS conditions. As it is common for Zintl anions and intermetallic cluster anions, the observed fragments have been detected as oxidized, singly charged species. Despite multiple measurements with varied ionization conditions and solvents a high-resolution mass spectrum of **(1)** could not be obtained on the Finnigan LTQ-FT spectrometer, whereas it was easily obtained in low resolution on a Micromass Q-Tof *micro*. Figures S10-S14 show spectra of the observed peaks, with measured (top) and calculated (bottom) isotope patterns each.

We thank Rhonda Stoddard and Dr. Eric Janusson (University of Victoria, BC, Canada) as well as Jan Bamberger (Philipps-Universität Marburg) for their help in collecting the ESI-MS data.

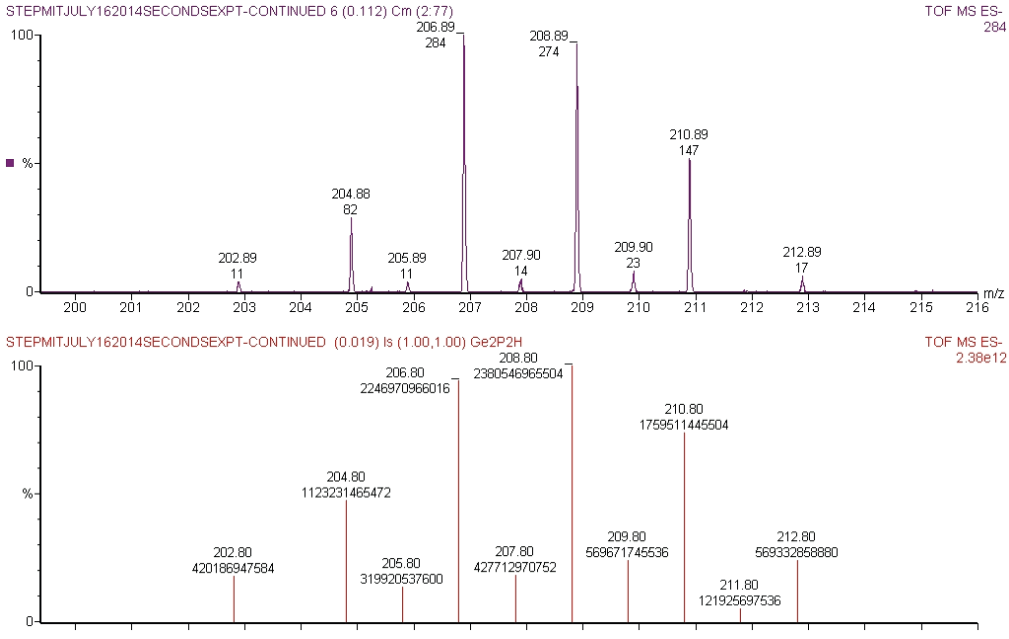

Figure S10. ESI-MS(–) spectrum of the $(Ge_2P_2H)^-$ anion.

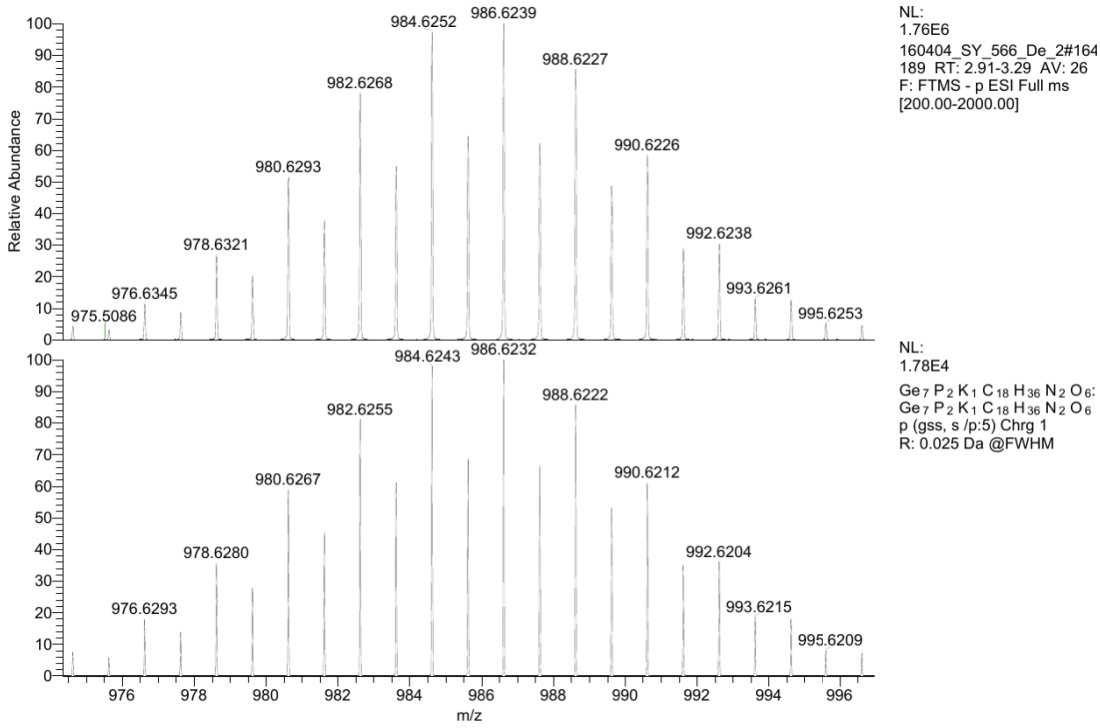

Figure S11. ESI-MS(–) spectrum of the $(Ge_7P_2K(crypt\text{-}222))^-$ anion.

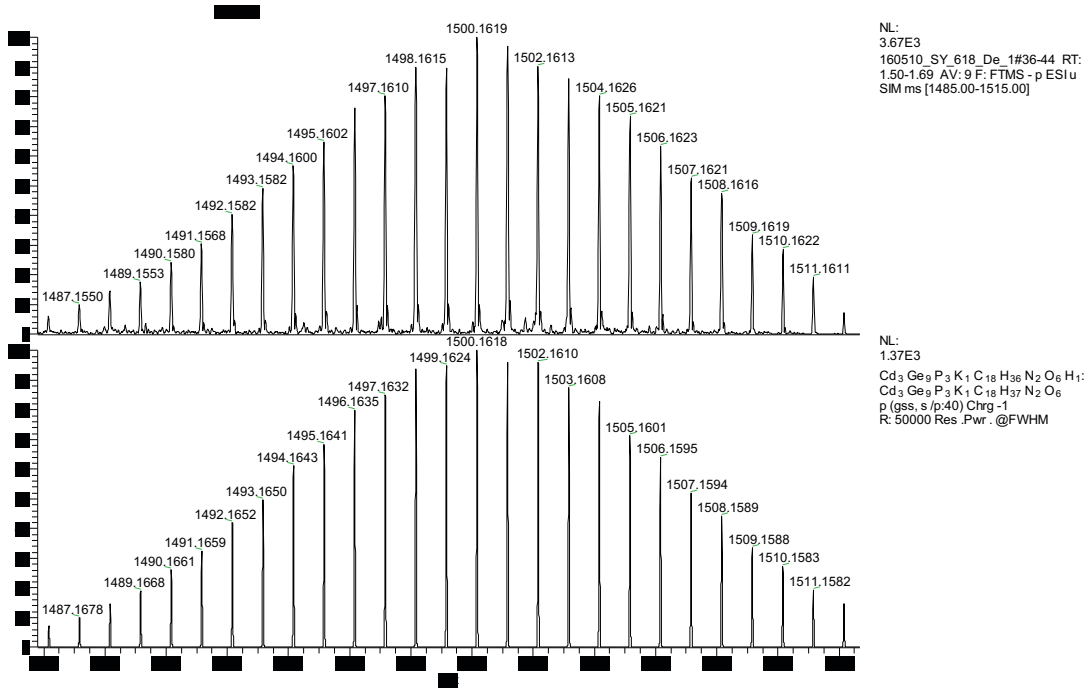

Figure S12. ESI-MS(–) spectrum of $(Cd_3Ge_9P_3K(crypt\text{-}222)H)^-$ anion.

A time-dependent ESI-MS(–) study has been performed on a suspension of "$K_2Ge_2P_2$" in *en*, utilizing pressure-sample-infusion (PSI) at 2 bar of Ar pressure. Immediately after start of the extraction the mass peak of the $(Ge_2P_2H)^-$ anion was detected. No other species have been observed within the first minutes of the extraction (see Figure S13, sum of 277 scans). This indicates the presence of the $(Ge_2P_2)^{2-}$ in the solid phase or its rapid formation upon extraction. As no evidence of the larger cluster $(Ge_7P_2)^{2-}$ was detected in the fresh extraction suspension, this study aligns with the conclusion from NMR spectroscopy, which indicates the latter to be formed in solution over time.

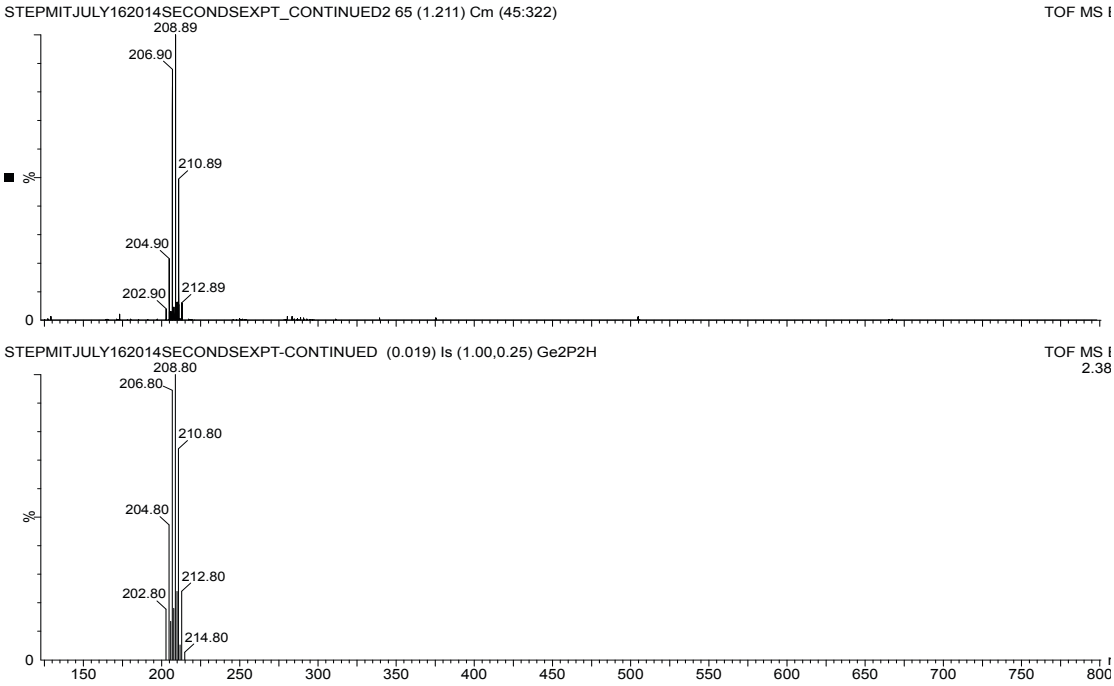

Figure S13. ESI-MS(–) spectrum of a fresh "$K_2Ge_2P_2$" suspension in *en*, showing $(Ge_2P_2H)^-$ as only peak present (sum of 277 scans, top).

In an ESI(–)-MS measurement of "$K_2Ge_2P_2$"/crypt-222 in *en* (with/without addition of pyridine), we found various peaks that can be assigned to a "GeP_3" moiety (see Figure S14). Due to the low resolution in this measurement a detailed assignment of the solvent fragments accompanying the "GeP_3" moiety a precise assignment was not possible, however, the isotopic distribution of the mass peak reveals unambiguously the presence of only one Ge atom in the isotopic pattern. This may hint at a complex reorganization process in *en* that yields "Ge_3P" moieties, as present in the crystal structure of **3**, and "GeP_3" moieties.

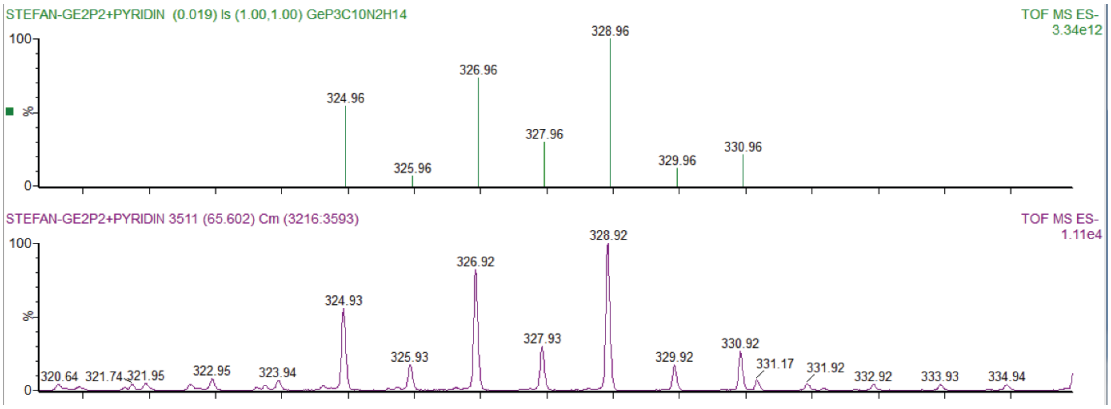

Figure S14. ESI(–)-MS spectrum of a "GeP_3" species – here $(GeP_3C_{10}N_2H_{14})^-$

5. Nuclear magnetic resonance (NMR) spectroscopy

NMR measurements of **1** and **2** have been performed a Bruker 400 MHz AV-III HD FT-NMR spectrometer equipped with H/FX Bruker SmartProbe with Automated Tuning and Matching (ATM). NMR measurements of **3** have been performed on a Bruker 500 MHz AV-III spectrometer with a Progidy cryo probe with forward observation for the broadband channel (BBO). Bruker standard single pulse sequences were used. ^{31}P-NMR and ^{113}Cd-NMR spectra were recorded at 25°C at 202.5 and 111.0 MHz, respectively.

For the ^{113}Cd-NMR experiment, in order to define the resonance signal, several spectra with a spectral width of 800 ppm were recorded to cover the whole chemical shift range (+2000 to –2000 ppm). The final spectrum was acquired with a spectral width of 200 ppm and a relaxation delay of 0.5 s with a number of 8192 scans. Chemical shift of ^{113}Cd was referenced to 1.0 M $Cd(ClO_4)_2$ in D_2O (δ = –641.0 ppm) and the spectra were processed with Bruker Topspin 3.2.

5.1. ^{31}P-NMR spectroscopy on compounds 1 and 2

Table S6 summarizes the ^{31}P-NMR data for compounds **1** and **2** observed in DMF-d_7 and *en*. respectively.

Table S6. ^{31}P-NMR chemical shift data (ppm) for the anions in **1** and **2** in different solvents.

	$[K(crypt\text{-}222)]_2(Ge_2P_2)\cdot en$ (**1**)	$[K(crypt\text{-}222)]_{22}(Ge_7P_2)$ (**2**)
DMF-d_7, 400 MHz	–432.38 (s)	–252.21 (s)
en/C_6D_6, 400 MHz	–459.75 (s)	–255.70 (s)

In a flame-sealed NMR-tube, a complete conversion from **1** into **2** was observed over the course of two weeks (see Figure S15). A red precipitate was found after complete conversion that was identified as red phosphorus by EDX measurement.

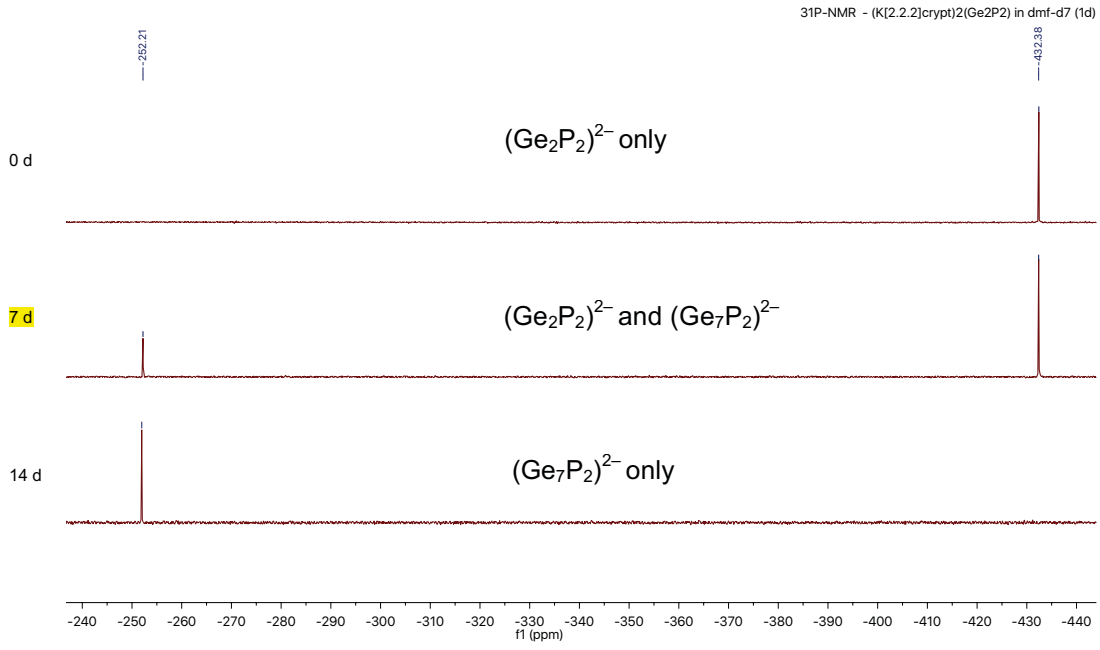

Figure S15. Time-dependent ^{31}P-NMR spectra of a solution of [K(crypt-222)]$_2$(Ge_2P_2) in DMF-d_7 (0, 7,14 days).

Upon extraction of the "$K_2Ge_2P_2$" phase and crypt-222 in *en*, a doubly protonated species was detected alongside the two anions indicated above in a proton coupled ^{31}P-NMR (see Figures S16-S17), producing a triplet at δ = –269.38 (*J* = 138.6 Hz). Upon addition of small amounts of pyridine, the triplet vanished, indicating deprotonation by the base pyridine. Notably, the signal is not present in the NMR spectrum of the extraction liquid in the aprotic solvent DMF, and it is also absent in a DMF solution of [K(crypt-222)]$_2$(Ge_2P_2) (**1**), in agreements with the assumption that *en* acts as an acid here. The chemical shift is in the range of the values known for phosphanes (PH_3: –244.3 ppm; P_2H_4: –214 ppm), yet we cannot exclude it to be $(Ge_3PH_2)^-$. The exact nature of the species is subject to an ongoing study.

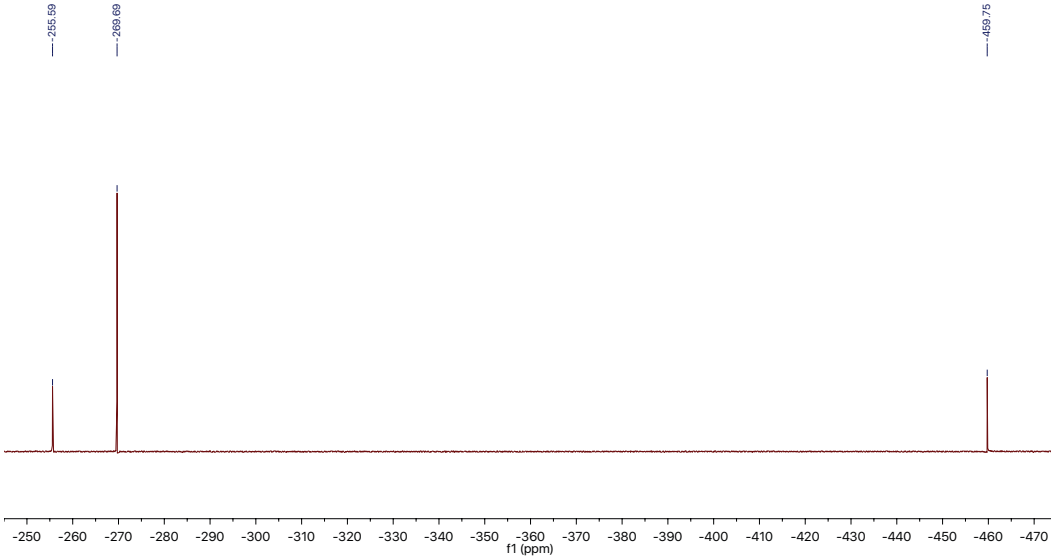

Figure S16. ^{31}P{H}-NMR spectrum of the filtered extraction liquor upon extraction of "$K_2Ge_2P_2$"/crypt-222 in *en* for 4d.

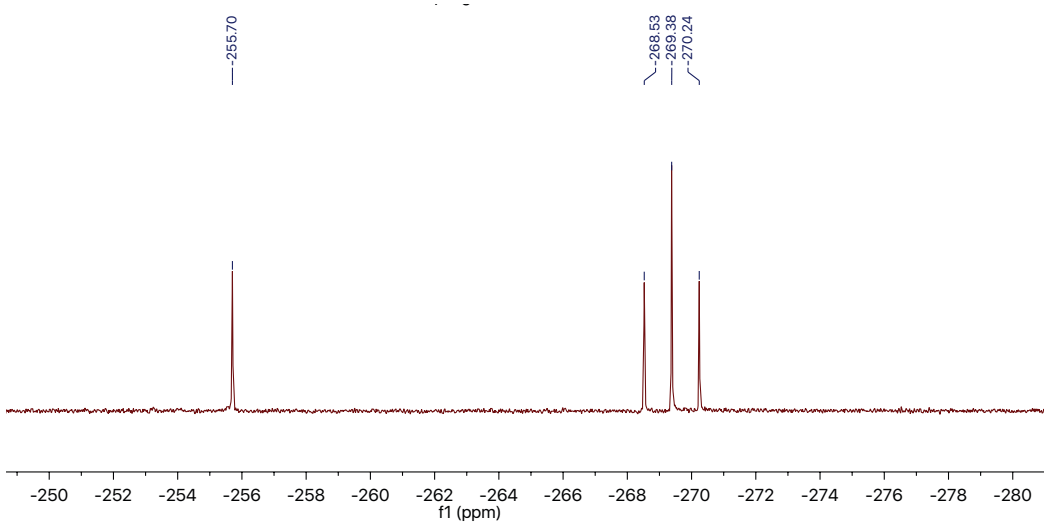

Figure S17. ^{31}P-NMR (^{1}H-coupled) spectrum of the filtered extraction liquor upon extraction of "$K_2Ge_2P_2$"/crypt-222 in *en* for 4d.

5.2. ^{113}Cd-NMR and ^{31}P-NMR spectroscopy on compound 3

In the ^{113}Cd-NMR spectrum (see Figure S18, left), a triplet was observed at 636.6 ppm, with a coupling constant of 72 Hz under the experimental condition. The observed splitting pattern of the ^{113}Cd signal is due to its coupling with the phosphorus atoms in the cluster and is in the expected range of a $^{2}J_{Cd-P}$ coupling (see below).

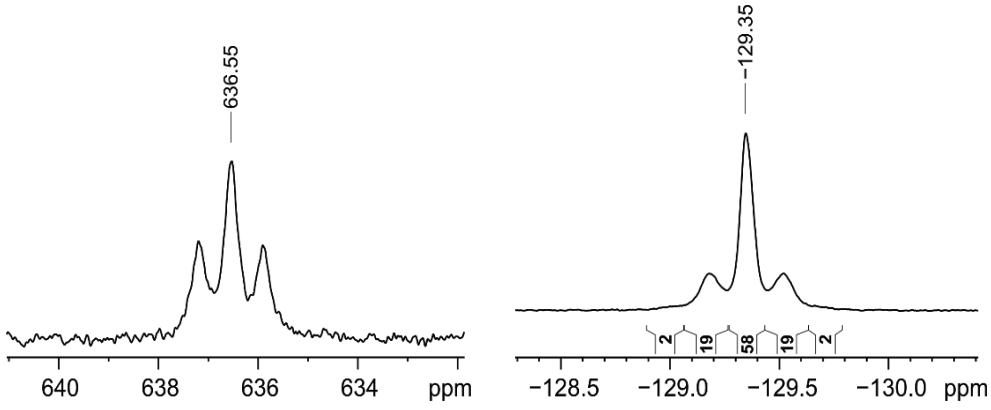

Figure S18. Detail of the ^{113}Cd (left) and the ^{31}P (right) NMR spectrum of **3** in DMF-d^7 at room temperature.

The ^{31}P-NMR spectrum consists of a central peak at –129.4 ppm, surrounded by two satellites with a separation of 72 Hz. A close inspection of the signal revealed two additional weak shoulders distributed symmetrically on either side of the central signal, with a distance of 72 Hz to the central signal. A distribution of the integral area is shown in Figure 1 (right). This complex distribution can be explained by the various isotopes of Cadmium: ^{106}Cd, ^{108}Cd, ^{110}Cd, ^{111}Cd, ^{112}Cd, ^{113}Cd, and ^{114}Cd. Among these isotopes, only ^{111}Cd and ^{113}Cd possess a non-zero spin quantum number (S = ½) and account for a natural abundance of 25%. Therefore, on the basis of the molecular structure of the anionic cluster in the crystal (see Figure S9), assuming a uniform coupling constant between all P and Cd atoms and a negligible coupling constant for all long-range couplings, a distribution for the integral area of the ^{31}P signal was calculated. After various combinations of the positioning of the different Cd isotopes within the cluster, the central peak was predicted and verified to account for 58% of the intensity. The remaining integral area is distributed over a pair of satellites with 19 % each, and two additional shoulders with 2% each.

The observed coupling constant of 72 Hz is in the range of $^2J_{Cd–P}$ couplings (e.g. 30 Hz for Cd-enriched enzyme phosphate complexes, see Ref. [4]). Literature reports values for a $^1J_{Cd–P}$ coupling to be more than one order of magnitude larger than the coupling constant observed in here (1123–2960 Hz, see Refs. [5] and [6]).

The NMR data confirms that the near C_3-symmetric structure observed in the solid state is also present in solution, as no additional ^{113}Cd signals were detected that would be expected upon opening into a chain or upon fragmentation. The presence of a $^2J_{Cd–P}$ coupling also verifies the assignment of the P atom in the crystal structure as pointing outwards instead of coordinating the Cd atoms.

6. Quantum Chemical Investigations

6.1. Methods

Quantum chemical calculations were carried out with TURBOMOLE[7] employing the B3LYP[8] functional with basis sets of type def2-TZVP[9] together with respective auxiliary basis sets[10| and an effective core potential for Cd[11] modelling the inner 28 electrons. The negative charge was compensated by the conductor-like solvation model (COSMO)[12] with default settings. Transition pathways were optimized with the method proposed by Plessow,[13] which is available in TURBOMOLE. Cartesian coordinates are provided in Tables S7-S10.

6.2. Relative stabilities of isomers of $[Cd_3(Ge_3P)_3]^{3-}$

The optimization of structure parameters was started from the X-ray structure. It yielded isomer B shown in Figure S19, center (Cartesian coordinates in Table S8), for which the original connectivity of the $(Ge_3P)^{3-}$ unit is maintained only in one of the three cases. This structure is a local minimum (with a very weak mode of 4 cm^{-1}). Enforcing C_3 symmetry during the optimization yields isomer D (for Cartesian coordinates see Table S10), which shows three imaginary modes (11,13 and 25 cm^{-1}, and is higher in energy than isomer B by 15 kJ/mol. Isomers with energies lower than that of isomer B were obtained by disturbing isomer B along the weakest vibrational mode. One ends up either in a (virtually) C_{3v} symmetric case (isomer A, see Figure S19, left hand side, and Table S7), where all P atoms are above the plane spanned by the three Cd atoms, or in a C_s symmetric case (isomer C, see Figure S19, right hand side, and Table S9), where one of the P atoms is situated below this plane. Isomers A and C are favored over B by 8 and 14 kJ/mol, respectively, and thus over the C_3-symmetric structure by 23 and 29 kJ/mol, respectively. For both isomers, A and C, the wavenumber of the weakest vibrational mode is 8 cm^{-1}. Finally, the reaction pathway A–B–C was optimized. The result is also shown in Figure S19. It is evident that the rotation of a $(Ge_3P)^{3-}$ unit is feasible with low energy (~10 kJ/mol) and not hindered by a significant barrier (< 1 kJ/mol).

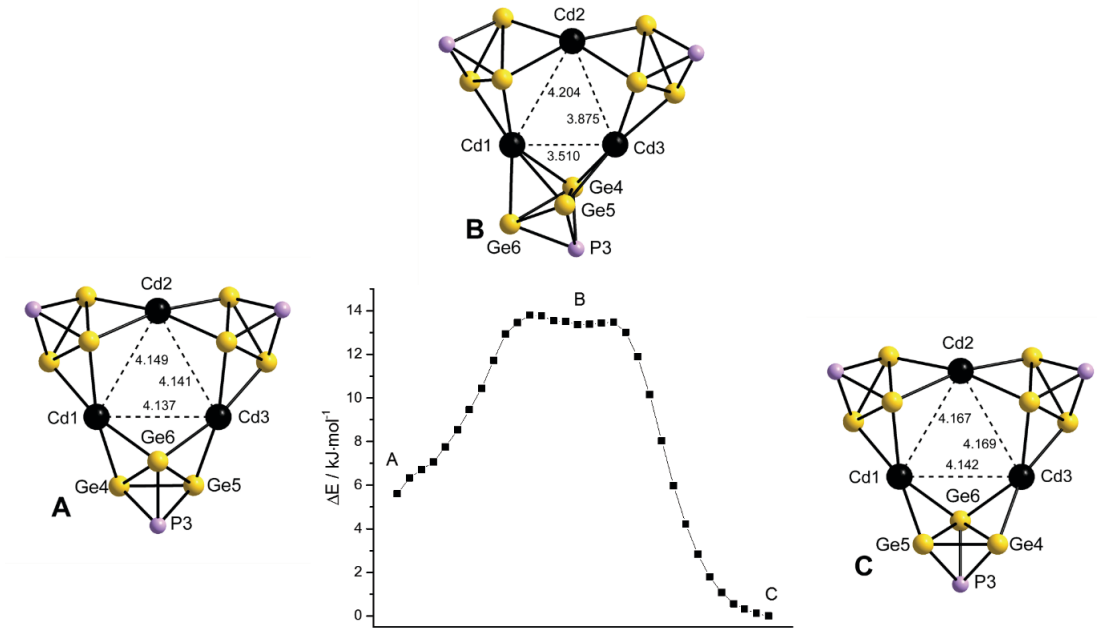

Figure S19. Relative energies of isomers of $[Cd_3(Ge_3P)_3]^{3-}$, being interlinked by two 90° rotations of one of the $(Ge_3P)^{3-}$ units about the (virtual) Cd2···P3 axis. Note that the labeling scheme of the Cd atoms is not identical to that in Figure 2 in the main document, as the calculations were done without symmetry restrictions (C_1) and do naturally not account for any disorder.

Table S7. Cartesian coordinates (in Å) for isomer A.

Cd	0.0106616	0.0064862	-0.0140049
Ge	1.6079153	-1.8717357	-1.2899844
Ge	0.2992342	-2.5278476	1.1403701
Ge	0.3714045	-4.0821403	-1.2289160
P	2.1882707	-3.6047699	0.2943055
Cd	-4.1306441	0.0047284	-0.0003718
Cd	-2.0465121	-3.5828471	0.0314239
Ge	-3.3265223	2.3370170	-1.2662270
Ge	-4.4623234	-4.0544356	-1.2455091
Ge	-2.0565838	1.5082106	1.1343302
Ge	-4.3926096	-2.5345138	1.1482672
Ge	-0.7926548	2.3469651	-1.2639035
Ge	-5.7480070	-1.8718296	-1.2511684
P	-2.0665504	3.6859118	0.2965473
P	-6.2666706	-3.6441050	0.3113954

Table S8. Cartesian coordinates (in Å) for isomer B.

Cd	0.0003216	-0.0050127	-0.0018330
Ge	1.1269667	-2.1638944	-1.4584744
Ge	1.0663767	-2.1679886	1.4966064
Ge	1.2751420	-4.4044713	-0.0005389
P	2.8842471	-2.6286966	0.0623094
Cd	-3.8747209	0.0045927	-0.0000666
Cd	-1.2550723	-3.2829845	0.0042240
Ge	-3.2207765	2.3276738	-1.3574016
Ge	-3.6007712	-3.9926690	-1.2964026
Ge	-1.9490249	1.6933798	1.1185225
Ge	-3.7106670	-2.5424147	1.1533135
Ge	-0.6812998	2.3405065	-1.3333244
Ge	-5.2528538	-2.0841802	-1.1737124
P	-1.9748441	3.7912629	0.1070931
P	-5.3774648	-3.9647628	0.3497360

Table S9. Cartesian coordinates (in Å) for isomer C.

Cd	0.0000000	0.0000000	0.0000000
Ge	0.2776194	-2.5489324	-1.1111404
Ge	1.5961034	-1.8490899	1.2907968
Ge	0.3454653	-4.0403451	1.2904645
P	2.1623603	-3.6239061	-0.2572257
Cd	-4.1691700	-0.0000000	0.0000000
Cd	-2.0597939	-3.5932058	0.0000000
Ge	-3.3619661	2.3255271	-1.2798606
Ge	-4.4648056	-4.0188959	-1.2865939
Ge	-2.0857038	1.5011568	1.1127449
Ge	-4.3936906	-2.5461853	1.1357015
Ge	-0.8375521	2.2817695	-1.3055128
Ge	-5.8038313	-1.8767937	-1.2281519
P	-2.0532271	3.6706511	0.2550860
P	-6.2493906	-3.6954227	0.3109239

Table S10. Cartesian coordinates (in Å) for isomer D.

Cd	-1.4812411	-1.2714871	0.0012022
Ge	0.6806557	-2.7814824	1.4838009
Ge	-1.1678159	-4.0247915	-0.0028197
Ge	-2.7494102	0.8064784	1.4838347
P	1.1869750	-4.5478579	0.0018016
Cd	1.8445015	-0.6489905	-0.0004363
Cd	-0.3628153	1.9240459	0.0029126
Ge	4.0689281	0.9942918	-0.0030599
Ge	-2.9039140	3.0287102	-0.0043126
Ge	2.0693479	1.9768886	1.4850814
Ge	0.6838991	-2.7831945	-1.4839497
Ge	2.0661791	1.9801936	-1.4830666
Ge	-2.7514897	0.8032603	-1.4835799
P	3.3481943	3.2953925	0.0012506
P	-4.5319944	1.2485424	0.0013407

7. References for the supplementary information

[1] 4,7,13,16,21,24-Hexaoxa-1,10-diazabicyclo[8.8.8]hexacosane / Kryptofix 222

[2] G. M. Sheldrick, *Acta Crystallogr.*, 2008, **A64,** 112–122.

[3] S. Mitzinger, L. Broeckaert, W. Massa, F. Weigend and S. Dehnen, *Nat. Commun.,* 2016, **7**, 10480.

[4] J. D. Otvos, J. R. Alger, J. E. Coleman and I. M. Armitage, *J. Biol. Chem.*, 1979, **254**, 1778–1780.

[5] B. E. Mann, *Inorg. Nucl. Chem. Lett.*, 1971, **7**, 595–597.

[6] D. Dakternieks and C. L. Roll, *Inorg. Chim. Act.*, 1985, **105**, 213–217.

[7] *TURBOMOLE* V7.1 2016, a development of University of Karlsruhe and Forschungszentrum Karlsruhe GmbH, 1989-2007, *TURBOMOLE* GmbH, since 2007.

[8] C. Lee, W. Yang and R. G. Parr, *Phys. Rev. B,* 1988, **37**, 785–789.

[9] F. Weigend and R. Ahlrichs, *Phys. Chem. Chem. Phys.,* 2005, **7,** 3297–3305.

[10] F. Weigend Phys. Chem. Chem. Phys., 2006, **8,** 1057-1065.

[11] D. Andrae, U. Häussermann, M. Dolg, H. Stoll and H. Preuss, *Theor. Chim. Acta,* 1990, **77,** 123–141.

[12] A. Klamt and G. Schüürmann, *J. Chem. Soc. Perkin Trans.*, 1993, **2,** 799–805.

[13] P. Plessow, *J. Chem. Theory Comput.,* 2013, **9**, 1305–1310.

3.4 $(SiP_6H_2)^{2-}$ and its Homologs – First Examples of Binary Notricyclane-Type Zintl Anions

This manuscript was sent Inorg. Chem. (ACS) and is awaiting peer-review.

A novel class of binary Zintl anions was revealed upon extraction of ternary solid mixtures of K, Si and P. $(SiP_6H_2)^{2-}$ and its homologs are first examples for binary nortricyclane-type structures in which one E^{15} element is replaced by an E^{14} element. Also, they represent the first binary Zintl anions of Si/P and Si/As and complement the recent endeavors to synthesize lighter Zintl anions. Quantum chemical calculations suggest the presence of protonated clusters.

S. Mitzinger conceived and performed the synthesis, performed the characterization and interpreted the analytical data. L. Guggolz performed quantum chemical calculations. W. Massa analysed and interpreted the crystallographic datasets. All authors co-wrote the manuscript.

Das Manuskript wurde zur Begutachtung bei Inorg. Chem. (ACS) eingereicht.

Im Rahmen der Synthese binarer Zintl-Anionen wurde eine nortricyclan-artige Topologie entdeckt. Die neuartigen binären Zinl-Anionen $(SiP_6H_2)^{2-}$ sowie die der schwereren Homologen der Elementkombination Ge/P und Si/As wurden beschrieben. Mit Hilfe von EDX-Spektroskopie wurde die Anwesenheit der entsprechenden Elemente in den Kristallen im erwarteten Verhältnis bestätigt. NMR-spektroskopische Untersuchungen bestätigten die Existenz von P–H Bindungen. Die Stabilität der beschriebenen Zintl-Anionen wurde zudem durch quantenchemische Rechnungen belegt und legen ebenfalls eine Protonierung nahe.

S. Mitzinger erdachte die Synthese und führte diese durch. L. Guggolz führte quantenchemische Rechnungen durch und wertete die Ergebnisse aus. W. Massa analysierte und interpretierte die kristallographischen Datensätze. Alle Autoren verfassten das Manuskript gemeinsam.

$(SiP_6H_2)^{2-}$ and its Homologs – Examples of Binary Nortricyclane-Type Zintl Anions

Stefan Mitzinger, Lukas Guggolz, Werner Massa and Stefanie Dehnen*

Philipps-Universität Marburg, Fachbereich Chemie and Wissenschaftliches Zentrum für Materialforschung, Hans-Meerwein-Str. 4, 35043 Marburg, Germany.

Supporting Information Placeholder

ABSTRACT: $(SiP_6H_2)^{2-}$ and its heavier Ge/P and Si/As homologs have been obtained upon extraction of stoichiometric ternary mixtures of the respective elements and potassium in en/crypt-222. The cluster anions are doubly protonated according to electrospray ionization mass spectrometry (ESI-MS) and nuclear magnetic resonance (NMR) spectroscopy. They represent the first binary Zintl anions of the Si/P and Si/As elemental combination and complement the recent endeavors to synthesize lighter binary Zintl anions.

The chemistry of homo-atomic Zintl anions has been pursued in the last decades in order to deepen the knowledge in (semi-)metallic cluster compounds, (semi-)metal-(semi-) metal bonding interactions and corresponding reactivity. As a result, many new cluster motifs have been discovered, and reactions were evaluated in order to achieve systematic derivatizations of Zintl anions. The most common precursor in this chemistry has been the Ge_9^{4-} anion, which can easily be accessed by extraction of the Zintl phase K_4Ge_9 in ethane-1,2-diamine (en) in the presence of the sequestering agent crypt-222.[1-3] A variety of compounds featuring organic and organometallic functionalization, including organic linkage of the cluster anions, have been reported,[4-16] as well as a large variety of intermetalloid clusters as an inorganic extension.[2,5,17-21] However, except of the relatively well-soluble E_9^{4-} anions (E = Si···Pb), most Zintl anions exhibit rather poor solubilities due to their high charges.

Our focus is to apply the pseudo-element concept to reduce the anionic charges by substituting an E^{14} atom with an E^{15} atom, hence without changing the overall electronic situation of the Zintl anion. Over the last years this approach was successfully applied to the homologs of the $E^{14}{}_4^{4-}$ unit, resulting in $(E^{14}{}_2E^{15}{}_2)^{2-}$ Zintl anions as well as larger multi-metallic clusters.[20-28] Recently, we were able to apply this method to the lighter elemental combination of Ge/P, resulting in the novel binary P_4 analogue $(Ge_2P_2)^{2-}$.[29]

Herein we present our first findings for the even lighter elemental combination of Si/P and their homologs with Ge/P and Si/As. At the same time, we also expand the chemistry of binary Zintl anions to include elements that are not metallic in nature, effectively crossing over from hetero-metallic to hetero-atomic molecules. By employing elements with a less metallic character we hope to synthesize clusters that have a higher tolerance against disproportionation reactions and the oxidation to bare metals.

In an initial attempt to determine the minimal temperature necessary to obtain $(E^{14}{}_2E^{15}{}_2)^{2-}$-type Zintl anions, novel anions comprising seven atoms were obtained by extraction of stoichiometric mixtures of the respective elements and potassium in en/crypt-222. $[K(crypt\text{-}222)]_2(SiP_6H_2)\cdot en\cdot 0.7H_2O$ (**1**) was obtained by extraction of the solid mixture "$K_2Si_1P_1$" in en (containing traces of water) in the presence of crypt-222. After filtration and layering with toluene, a few pale-yellow blocks of **1** crystallized after three weeks. Deliberate increase of the amount of water did not help to increase the yield, but rather led to the decomposition of the precursor. The compound crystallizes in the monoclinic space group *C*c with Z = 4. Figure 1 illustrates the result of the crystal structure refinement.

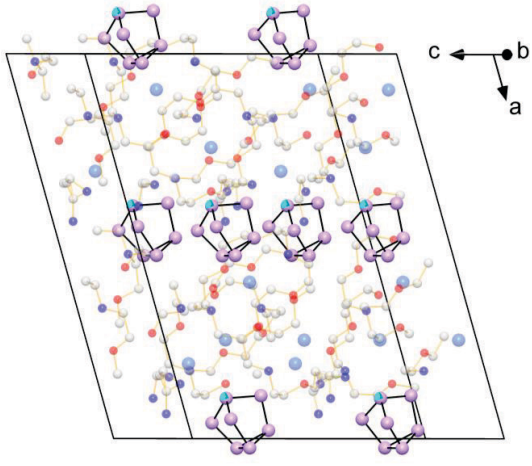

Figure 1. Fragment of the crystal structure of compound **1** in ball-stick representation (disregarding disorder). Color code: P/Si (1:6) lilac; K, light grey; C, dark grey; O, red; N, blue. The ball with turquoise inset represents the most likely Si position according to DFT calculations. Details are provided in the main text in and the Supporting Information.

One Si atom and six P atoms form a nortricyclane-type molecular anion. According to quantum chemical studies, the Si atom is preferably positioned at the top vertex that is bonded to three μ-P atoms, with other configurations being very similar in energy (see below). In the X-ray analysis, P and Si cannot be distinguished. Thus all positions were occupied with P and Si in a 6:1 ratio.

As expected, the bonds lengths within the anion of **1** are close to the ones reported for the P_7^{3-} anion (in Li_3P_7):[30] 223.2–227.0 pm for the basal P atoms in $(SiP_6H_2)^{2-}$ (223.2–226.9 pm for P_7^{3-}), 212.7–221.4 pm for the bonds connecting the basal unit to the cap (214.4–215.2 pm for P_7^{3-}) and 216.2–218.6 pm for the bonds connecting the apical atom (216.9–218.1 pm for P_7^{3-}). The only bond that is significantly elongated is the P2–P5 bond with 222.1 pm (215.2 pm for P_7^{3-}); however, at is should be noted that the position of P5 is affected by its proximity to three atoms that belong to the modelled disorder (as can be seen by the relatively large thermal ellipsoid; see the Supporting Information). Previously, Goicoechea *et al.* already reported the formation of protonated, linked P_7 species,[31] and on a separate occasion, of Tl-capped nortricyclane-type clusters of P and As,[32] but the formation of a protonated binary nortricyclane-type anion has not been reported so far.

The solid state structure of **1** indicates the presence of only two $[K(crypt\text{-}222)]^+$ cations per anion. However, according to the pseudo-element concept, the replacement of an E15 atom in the nortricyclane-type structure of P_7^{3-} or As_7^{3-}, respectively, with an E14 atom increases the total negative charge to 4– when maintaining its valence electron number (which is clearly proven by the structural features). The elemental composition of the crystal used for single crystal X-ray diffraction (SCXRD) was confirmed by energy-dispersive X-ray (EDX) spectroscopy, hence suggests the presence of exactly one Si atom among P atoms.

Clarification of this puzzling mismatch between the composition and the total charge was provided by ESI(–)-MS measurements on a solution of the homolog compound $[K(crypt\text{-}222)]_2(Ge_xP_{7-x}H_{2-x})_{1-n}(Ge_{9-y}P_yH_{2-y})_n$ (**2**), obtained upon extraction of "$K_2Ge_2P_2$", in which the anion $\{GeP_6H_3\}^-$ (m/z = 262.78) was detected (Figure 2).

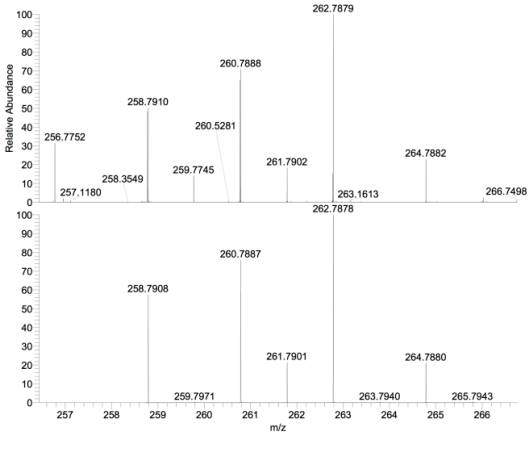

Figure 2. ESI(–) mass spectrum of $\{GeP_6H_3\}^-$ (top) in comparison with the simulated isotope pattern (bottom).

Homoatomic Zintl cluster anions are usually observed as species with reduced charge (typically, –1) under ESI(–) conditions. This can include a protonation during the ESI process, especially in the case of lighter main group elements. Since the cluster has a 2– charge, according to crystal structure refinement, only one proton may have been added. Hence, the presence of three protons in the ESI(–) mass spectrum is in agreement with a doubly protonated compound in the original material used for the analysis.

The crystal structure analysis of $[K(crypt\text{-}222)]_2(Ge_xP_{7-x}H_{2-x})_{1-n}(Ge_{9-y}P_yH_{2-y})_n$ (**2**) revealed the trigonal space group $P\bar{3}c1$ with a unit cell close to that found for $[K(crypt\text{-}222)]_2(Ge_7P_2)$,[29] $[K(crypt\text{-}222)]_2(Ge_7As_2)$[24] or $[K(crypt\text{-}222)]_2(Ge_9)$.[33] The anion is positioned on a site with the high 32 (D_3) symmetry. The observed 30 electron density maxima around this site can be interpreted by superposition of 7-atom and 9-atom clusters in different orientations, each multiplied by the 32 symmetry (Figures S7-S11) – which is not untypical for these spherical anions.[33] Consequently, a clear determination of the composition is impossible. Attempts to confirm the presence of protons at the cluster in **2** by NMR spectroscopy were unsuccessful, as the single crystals seem to undergo a rapid fragmentation in DFM solution (Figure S19-S21). A doublet in the ^{1}H NMR spectrum (Figure S21) at –10.06 ppm ($J_{P\text{-}H}$ = 3.8 Hz) would be in agreement with the existence of mono-protonated P atoms, but in the light of the large number of further signals, we do not take this as a proof. We assume that the anion is not stable in solution, and that decomposition starts immediately upon re-dissolving. The (irreversible) transformation of $(Ge_xP_y)^{q-}$ anions into larger ones was recently reported for $(Ge_2P_2)^{2-}$ anions that are obtained from the equimolar K/Ge/P mixture fused at 950°C instead of 650°C (see Supporting Information).[29]

To examine a related elemental combination, however with atoms from elements of different periods of the periodic table, the K/Si/As system was probed. As a result, $[K(crypt\text{-}222)]_2(SiAs_6H_2)\cdot en$ (**3**) was obtained upon extraction of a "$K_2Si_1As_1$" solid mixture in en/crypt-222. Upon layering with toluene, red needles of **3** crystallized with approx. 17% yield. The compound also crystallizes in the trigonal space group $P\bar{3}c1$ with Z = 2, like compound **2**. Although the cations could be well localized, we were not successful to establish a sensible disorder model for the anion, which is also located on a site of 32 (D_3) symmetry. However, EDX analysis of single crystals confirmed the presence of Si and As in a 1:6 ratio (Table S7), which lead us to the conclusion that **3** is a homolog of **2**. From the same reaction, crystals of an As_7^{3-} species were obtained in approx. 13% yield, $[K(crypt\text{-}222)]_2(KAs_7)$ (**4**). The crystal structure could be solved in space group $C2/c$ with Z = 8. The As_7^{3-} anions in **4** are interconnected by "naked" K^+ cations to form a 1-dimensional coordination polymer; the $[K(crypt\text{-}222)]^+$ cations form a honeycomb-like packing embedding the anionic chains (Figures S13-S16). **4** was found to crystallize exclusively at the bottom part of the Schlenk tube.

In order to determine the position of the E14 heteroatom within the 7-atom cages, and to rationalize the existence of doubly-protonated cages, quantum chemical calculations were performed using the program system TURBOMOLE[34] under application of density functional theory (DFT) methods.[35,36] Geometry optimizations of the isomers of the bare $(E^{14}E^{15}_6)^{4-}$ clusters (E14/E15 = Si/P, Ge/P, Si/As) indicated that the two-bonded sites (B position) always exhibit the highest

electron densities (Tables S8–S10), and that the location of E^{14} on this position is disfavored by 68 (Si/P), 78 (Ge/P), or 60 (Si/As) kJ·mol^{-1} in the three cases. In $(SiP_6)^{4-}$ and $(SiAs_6)^{4-}$, the Si atom is preferably located at the top (A position) of the cluster, whereas in $(GeP_6)^{4-}$ its preferred position is at the base of the nortricylcane-type cage (C position). However, the difference in energy between these two isomers is negligible in the context of the chosen DFT methods: 7 (Si/P), 1 (Ge/P), or 10 (Si/As) kJ·mol^{-1}, respectively.

Due to the high negative partial charge at the two-bonded E^{15} atoms, these are the only reasonable positions for protonation. Upon two-fold protonation, the preferred position of the E^{14} atom in the resulting $(E^{14}E^{15}_6H_2)^{2-}$ structures again is at the top (A) for Si/P and Si/As and in the base (C) for Ge/P (Figure 3), but the energy differences are very small, too; again, it is somewhat larger in **3** (14 kJ·mol^{-1}) as compared to the *pseudo*-homoatomic anions in **1** or **2** (4 or 8 kJ·mol^{-1}, respectively), as expected.

The results support the existence of protonated species, but also indicate the potential co-existence of different isomers in solution and, most likely, also in the solid state. Figure 3 summarizes the global minimum structures of the three doubly-protonated binary $(E^{14}E^{15}_6H_2)^{2-}$ anions.

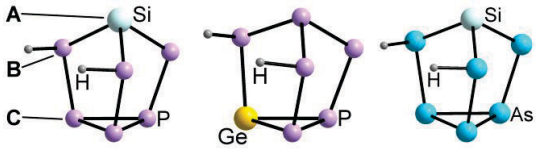

Figure 3. Minimum structures of $(SiP_6H_2)^{2-}$ (left), $(GeP_6H_2)^{2-}$ (center) and $(SiAs_6H_2)^{2-}$ (right), as optimized by means of DFT methods.

Protonated Zintl anions are rare. They have previously been reported only for $(HSn_9)^{3-}$ and its derivative $(Ni@HSn_9)^{3-}$,[37] and for several metal-carbonyl complexes, $[\eta^4\text{-}HP_7Ni(CO)]^{2-}$ [38] and $[\eta^2\text{-}HP_7M(CO)_4]^{2-}$ (M = Mo, W),[39] with protonated 7-atomic polyphosphide ligands.

In conclusion, we identified the novel anion $(SiP_6H_2)^{2-}$ and their heavier Ge/P and Si/As homologs via combinations of analytical methods and DFT calculations. Despite the difficulties in obtaining a full characterization of this series of compounds, their close relationship, combined with complementary quantum chemical calculations allowed for a first description of binary nortricyclane-type Zintl anions besides the $(Sn_3Sb_4)^{6-}$ anion in $[K_6(NH_3)_9](Sn_3Sb_4)$.[40] Their formation pathway is, as often observed for Zintl anions, not intuitive and mostly unknown. Especially for lighter heteroatomic Zintl anions, their behavior in solution proves to be even more complex than for their heterometallic relatives. Therefore, this study can only provide an initial insight into the discussed matter. More detailed studies are underway.

ASSOCIATED CONTENT

Supporting Information

Details of syntheses, SCXD, ESI-MS, EDX, NMR data and quantum chemical calculations (PDF file). The Supporting Information is available free of charge on the ACS Publications website.

AUTHOR INFORMATION

Corresponding Author

E-mail: dehnen@chemie.uni-marburg.de.

Funding Sources

No competing financial interests have been declared.

ACKNOWLEDGMENT

This work was supported by the Friedrich-Ebert Stiftung and the Deutsche Forschungsgemeinschaft (DFG).

REFERENCES

(1) Queneau, V.; Sevov, S.C. Ge_9^{4-}: a Deltahedral Zintl Ion Now Made in the Solid-State. *Angew. Chemn. Int. Ed.* **1997**, *36* (16), 1754–1756.

(2) Fässler, T.; Hoffmann, S. D. Endohedral Zintl Ions: Intermetalloid Clusters. *Angew. Chem. Int. Ed.* **2004**, *43* (46), 6242–6247.

(3) Ponou, S.; Fässler, T. Crystal Growth and Structure Refinement of K_4Ge_9. *Z. Anorg. Allg. Chem.* **2007**, *633* (3), 393–397.

(4) Denning, M. S.; Goicoechea, J. M.; Duckworth, J. C. A.; Espinoza-Quintero, G.; Hinz, A.; Jupp, A. R.; Knapp, C. M.; Krämer, T.; Large, J. S.; McGrady, J. E.; et al. $[Hg_3Ge_9)_4]^{10-}$: a Nanometric Molecular Rod Precursor to Polymeric Mercury-Linked Cluster Chains. *Dalton Trans.* **2008**, *121* (43), 5882–5885.

(5) Wang, J.-Q.; Fässler, T.; Stegmaier, S. $[Co@Ge_{10}]^{3-}$: An Intermetalloid Cluster with Archimedean Pentagonal Prismatic Structure. *Angew. Chem. Int. Ed.* **2009**, *48* (11), 1998–2002.

(6) Hull, M. W.; Sevov, S. C. Functionalization of Nine-Atom Deltahedral Zintl Ions with Organic Substituents: Detailed Studies of the Reactions. *J. Am. Chem. Soc.* **2009**, *131* (25), 9026–9037.

(7) Henke, F.; Schenk, C.; Schnepf, A. $[Si(SiMe_3)_3]_6Ge_{18}M$ (M = Zn, Cd, Hg): Neutral Metalloid Cluster Compounds of Germanium as Highly Soluble Building Blocks for Supramolecular Chemistry. *Dalton Trans.* **2009**, No. 42, 9141–9145.

(8) Li, F.; Sevov, S. C. Rational Synthesis of $[Ge_9\{Si(SiMe_3)_3\}_3]^-$ From Its Parent Zintl Ion Ge_9^{4-}. *Inorg. Chem.* **2012**, *51* (4), 2706–2708.

(9) Li, F.; Sevov, S. C.; Muñoz-Castro, A. $[Ge_9\{Si(SiMe_3)_3\}_3\{SnPh_3\}]$: A Tetrasubstituted and Neutral Deltahedral Nine-Atom Cluster. *Angew. Chem. Int. Ed.* **2012**, *51* (34), 8581–8584.

(10) Li, F.; Li, F.; Sevov, S. C. Synthesis, Structures, and Solution Dynamics of Tetrasubstituted Nine-Atom Germanium Deltahedral Clusters. *J. Am. Chem. Soc.* **2014**, *136* (34), 12056–12063.

(11) Waibel, M.; Pecher, O.; Mausolf, B.; Haarmann, F.; Fässler, T. F. $NaRb_7(Si_{4-x}Ge_x)_2$ – Soluble Zintl Phases Containing Heteroatomic Tetrahedral $[Si_{4-x}Ge_x]^{4-}$ Clusters. *Eur. J. Inorg. Chem.* **2013**, *2013* (32), 5541–5546.

(12) Bentlohner, M. M.; Klein, W.; Fard, Z. H.; Jantke, L.-A.; Fässler, T. F. Linking Deltahedral Zintl Clusters with Conjugated Organic Building Blocks: Synthesis and Characterization of the Zintl Triad $[R\text{-}Ge_9\text{-}CH{=}CH\text{-}CH{=}CH\text{-}Ge_9\text{-}R]^{4-}$. *Angew. Chem. Int. Ed.* **2015**, *54* (12), 3748–3753.

(13) Perla, L. G.; Sevov, S. C. A Stannyl-Decorated Zintl Ion $[Ge_{18}Pd_3(Sn(I)Pr_3)_6]^{2-}$: Twinned Icosahedron with a Common Pd_3-Face or 18-Vertex Hypho-Deltahedron with a Pd_3-Triangle Inside. *J. Am. Chem. Soc.* **2016**, *138* (31), 9795–9798.

(14) Geitner, F. S.; Fässler, T. F. Introducing Tetrel Zintl Ions to N-Heterocyclic Carbenes – Synthesis of Coinage Metal NHC Complexes of $[Ge_9\{Si(SiMe_3)_3\}_3]^-$. *Eur. J. Inorg. Chem.* **2016**, *17*, 2688–2691.

(15) Wang, L.; Wang, Y.; Li, Z.; Ruan, H.; Xu, L. $[Ge_9\{M(CO)_5\}_3]^{4-}$: Electrophilic Addition of $M(CO)_5$ and $[E_9]^{4-}$ Zintl Anions (M = Cr, Mo, W). *Dalton Trans.* **2017**, *46* (21), 6839–6842.

(16) Mayer, K.; Jantke, L.-A.; Schulz, S.; Fässler, T. F. Retention of the Zn-Zn Bond in $[Ge_9Zn\text{-}ZnGe_9]^{6-}$ and Formation of $[(Ge_9Zn\text{-}Ge_9)\text{-}(ZnGe_9)]^{8-}$ and Polymeric $^1_\infty[(Ge_9Zn]^{2-}$. *Angew. Chem. Int. Ed.* **2017**, *56* (9), 2350–2355.

(17) Weinert, B.; Dehnen, S. Binary and Ternary Intermetalloid Clusters. In *Structure and Bonding*; Dehnen, S., Ed.; Clusters – Contemporary Insight in Structure and Bonding; Springer International Publishing, **2017**; Vol. 174, pp 99–134.

(18) Turbervill, R. S. P.; Arnold, J.; Camp, C.; Chapman, T. A. D.; Cowley, M. J.; Denning, M. S.; Hansen, D. F.; Jackson, C. S.; Jones, C.; Jupp, A. R.; et al. Synthesis and Isolation of $[Fe@Ge_{10}]^{3-}$: A Pentagonal Prismatic Zintl Ion Cage Encapsulating an Interstitial Iron Atom. *J. Am. Chem. Soc.* **2009**, *131* (8), 2802–2803.

(19) Lips, F.; Clérac, R.; Dehnen, S. $[Eu@Sn_6Bi_8]^{4-}$: a Mini-Fullerane-Type Zintl Anion Containing a Lanthanide Ion. *Angew. Chem. Int. Ed.* **2011**, *50* (4), 960–964.

(20) Ababei, R.; Heine, J.; Hołyńska, M.; Thiele, G.; Weinert, B.; Xie, X.; Weigend, F.; Dehnen, S. Making Practical Use of the Pseudo-Element Concept: an Efficient Way to Ternary Intermetalloid Clusters by an Isoelectronic Pb^-–Bi Combination. *Chem. Commun.* **2012**, *48* (92), 11295–11297.

(21) Mitzinger, S.; Broeckaert, L.; Massa, W.; Weigend, F.; Dehnen, S. $[V@Ge_8As_4]^{3-}$ and $[Nb@Ge_8As_6]^{3-}$: Encapsulation of Electron-Poor Transition Metal Atoms. *Chem. Commun.* **2015**, *51* (18), 3866–3869.

(22) Weinert, B.; Weigend, F.; Dehnen, S. Subtle Impact of Atomic Ratio, Charge and Lewis Basicity on Structure Selection and Stability: the Zintl Anion $[(La@in_2Bi_{11})(M\text{-}Bi)_2(La@in_2Bi_{11})]^6$. *Chem. Eur. J.* **2012**, *18* (43), 13589–13595.

(23) Weinert, B.; Müller, F.; Harms, K.; Clérac, R.; Dehnen, S. Origin and Location of Electrons and Protons During the Formation of Intermetalloid Clusters $[Sm@Ga_{3-x}H_{3-2x}Bi_{10+x}]^{3-}$ (X=0, 1). *Angew. Chem. Int. Ed.* **2014**, *53* (44), 11979–11983.

(24) Mitzinger, S.; Broeckaert, L.; Massa, W.; Weigend, F.; Dehnen, S. Understanding of Multimetallic Cluster Growth. *Nat. Commun.* **2016**, *7*, 10480.

(25) Wilson, R. J.; Broeckaert, L.; Spitzer, F.; Weigend, F.; Dehnen, S. $\{[CuSn_5Sb_3]^{2-}\}_2$: a Dimer of Inhomogeneous Superatoms. *Angew. Chem. Int. Ed.* **2016**, 55 (39), 11775–11780.

(26) Wilson, R. J.; Dehnen, S. $(Ge_4Bi_{14})^{4-}$: a Case of "Element Segregation" on the Molecular Level. *Angew. Chem. Int. Ed.* **2017**, *56* (11), 3098–3102.

(27) Lichtenberger, N.; Wilson, R. J.; Eulenstein, A. R.; Massa, W.; Clérac, R.; Weigend, F.; Dehnen, S. Main Group Metal-Actinide Magnetic Coupling and Structural Response Upon U^{4+} Inclusion Into Bi, Tl/Bi, or Pb/Bi Cages. *J. Am. Chem. Soc.* **2016**, *138* (29), 9033–9036.

(28) Lichtenberger, N.; Spang, N.; Eichhöfer, A.; Dehnen, S. Between Localization and Delocalization: $Ru(Cod)^{2+}$ Units in the Zintl Clusters $[Bi_9\{Ru(Cod)\}_2]^{3-}$ and $[Tl_2Bi_6\{Ru(Cod)\}]^{2-}$. *Angew. Chem. Int. Ed.* **2017**, *56*, 778.

(29) Mitzinger, S.; Bandemehr, J.; Reiter, K.; McIndoe, J. S.; Xie, X.; Weigend, F.; Corrigan, J. F.; Dehnen, S. $(Ge_2P_2)^{2-}$: a Binary Analogue of P_4 as a Precursor to the Ternary Cluster Anion $[Cd_3(Ge_3P)_3]^{3-}$. *Chem. Commun.* **2017**, accepted manuscript, DOI: 10.1039/C7CC08348C.

(30) Manriquez, V.; Hönle, W.; Schnering, von, H. G. Trilithiumheptaphosphid Li_3P_7: Darstellung, Struktur Und Eigenschaften. *Z. Anorg. Allg. Chem.* **1986**, *539*, 95–109.

(31) Knapp, C. M.; Jackson, C. S.; Large, J. S.; Thompson, A. L.; Goicoechea, J. M. Heteroatomic Molecular Clusters Derived From Group 15 Zintl Ion Cages: Synthesis and Isolation of $[M_3(HP_7)_2]^{2-}$ (M=Ag, Au), Two Novel Cluster Anions Exhibiting Metallophilic Interactions. *Inorg. Chem.* **2011**, *50* (9), 4021–4028.

(32) Knapp, C. M.; Large, J. S.; Rees, N. H.; Goicoechea, J. M. A Versatile Salt-Metathesis Route to Heteroatomic Clusters Derived From Phosphorus and Arsenic Zintl Anions. *Dalton Trans.* **2011**, *40*, 735–745.

(33) Åkerstedt, J.; Ponou, S.; Kloo, L.; Lidin, S. *Eur. J. Inorg. Chem.* **2011**, 3999–4005.

(34) TURBOMOLE V6.6/V7.2 **2014/2017**, a development of University of Karlsruhe and Forschungszentrum Karlsruhe GmbH, 1989-2007, TURBOMOLE GmbH, since 2007; available from http://www.turbomole.com.

(35) Weigend, F.; Ahlrichs, R. Balanced Basis Sets of Split Valence, Triple Zeta Valence and Quadruple Zeta Valence Quality for H to Rn: Design and Assessment of Accuracy *Phys. Chem. Chem. Phys.* **2005**, *7*, 3297–3305.

(36) Tao, J. M.; Perdew, J. P.; Staroverov, V. N.; Scuseria, G. E. Climbing the Density Functional Ladder: Nonempirical Meta-Generalized Gradient Approximation Designed for Molecules and Solids *Phys. Rev. Lett.* **2003**, *91*, 146401.

(37) Kocak, F. S.; Downing, D. O.; Zavalij, P.; Lam, Y.-F.; Vedernikov, A. N.; Eichhorn, B. *J. Am. Chem. Soc.* **2012**, *134*, 9733–9740.

(38) Charles, S.; Fettinger, J. C.; Bott, S. G.; Eichhorn, B. W. *J. Am. Chem. Soc.* **1996**, *118*, 4713–4714.

(39) Fettinger, J. C.; Eichhorn, B. W. *Inorg. Chem.* **1996**, 35, 1540–1548.

(40) Lips, F.; Schellenberg, I.; Pöttgen, R..; Dehnen, S. *Chem. Eur. J.* 2009, 15, 12968–12973.

Supporting Information

$(SiP_6H_2)^{2-}$ and its Homologs – Examples of Binary Nortricyclane-type Zintl Anions

Stefan Mitzinger, Lukas Guggolz, Werner Massa and Stefanie Dehnen*

Fachbereich Chemie, Philipps-Universität Marburg

Hans-Meerwein-Str., 35043 Marburg, Germany

E-mail: dehnen@chemie.uni-marburg.de

Contents:

1. Synthesis details

1.1 General

All manipulations and reactions were performed under dry Ar atmosphere by using standard Schlenk or glovebox techniques. Ethane-1,2-diamine (ethylenediamine, *en*) was distilled over CaH_2 and stored over molecular sieves. Toluene was distilled over Na/K alloy and stored over molecular sieves. crypt-222[1] (Merck) was dried *in vacuo* for at least 18 h. Si, Ge and P (red) of a purity of 99.99% or higher was used.
The respective solid mixtures with were accessed by combining K, Si, Ge and P (red) in stoichiometric amounts in a niobium ampoule. The ampoule was sealed by arc-welding, and then stored in silica glass ampoule, which was sealed under vacuum, before heating in an oven at 650°C for 2 d. The resulting solid was pulverized in a mortar thoroughly prior to further use.

!!! Caution !!!

Solid mixtures of the elemental combination K/Si/P are pyrophoric and shock-sensitive. Their synthesis should be limited to small batches. The ground solid mixture can spontaneously ignite at air with a loud bang. It is strongly advised to work under proper inert conditions at all times and to dispose, even of small amounts, under inert conditions. Quenching the solid mixture with water will result in the formation of a flammable gas (phosphine - according to odour) that can ignite spontaneously at air. Because of the formation of phosphine, the disposal must be addressed in small amounts at a time under proper ventilation, due to the phosphine's toxicity. As small amounts of phosphine are released immediately from the ground solid upon contact with moisture from the surrounding air, contaminated equipment and material should be transported from the glovebox antechamber to a fume hood in a sealed plastic bag.

1.2 Syntheses

1.2.1 Synthesis of [K([crypt-222]$_2$(SiP$_6$H$_2$) · en · 0.7 H$_2$O (1)

0.20 mmol of "K_2SiP" and 0.22 mmol of crypt-222 were weighed out into a Schlenk tube. Then *en* (ethane-1,2-diamine, 6 mL) was added. The reaction mixture was allowed to stir at room temperature for 3h. The liquid was filtered through a standard glass frit (D3), yielding a pale yellow solution that was carefully layered with *tol* (toluene, 12 mL). After 21 days, clear pale yellow plates crystallized (Figure S1). As the solubility of the solid mixture in *en* was very limited, only a few crystals were obtained. The yield could not be calculated with a reasonable accuracy, but is expected to be below 5%. The crystals were found to decay rapidly once removed from the mother liquor, forming a greyish coating. Allowing more time for crystallization did not improve the yield, but resulted in the formed single crystals to dissolve again (after one month).

1.2.2 Synthesis of [K(crypt-222)]$_2$(Ge$_x$P$_{7-x}$H$_{2-x}$)$_{1-n}$(Ge$_{9-y}$P$_y$H$_{2-y}$)$_n$ (2)

0.5 mmol of "$K_2Ge_2P_2$" and 0.55 mmol of crypt-222 were weighed out into a Schlenk tube. Then *en* (ethane-1,2-diamine, 10 mL) was added. The reaction mixture was allowed to stir at room temperature for 3h. The liquid was filtered through a standard glass frit (D3), yielding an orange solution that was carefully layered with *tol* (toluene, 20 mL). After 21 days, dark yellow blocks crystallized (Figure S2). The yield of crystalline material was calculated to be approx. 18%. Note that the same treatment of a solid mixture of the same elemental combination that was obtained by fusion at 950°C affords a salt of the binary anion $(Ge_2P_2)^{2-}$.[2]

1.2.3 Co-joint synthesis of [K(crypt-222)]$_2$[(SiAs$_6$H$_2$)] (3) and [K(crypt-222)]$_2$[(As$_7$K)] (4)

0.20 mmol of "K_2SiAs" and 0.22 mmol of crypt-222 were weighed out into a Schlenk tube. Then *en* (ethane-1,2-diamine, 6 mL) was added. The reaction mixture was allowed to stir at room temperature for 3h. The liquid was filtered through a standard glass frit (D3), yielding an orange solution that was carefully layered with *tol* (toluene, 12 mL). After 10 days, red crystals of **3** were found in approx. 17%, that grew to large dark red tabular needles (Figure S3). In the bottom part of the Schlenk, which contained a red liquid phase, that did not mix with the other liquid phase, dark red polyhedra of **4** crystallized in approx. 13% (Figure S4).

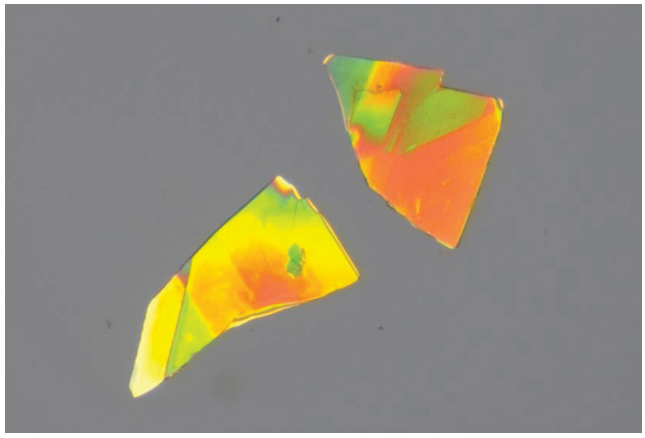

Figure S1: Light yellow plates of **1**.

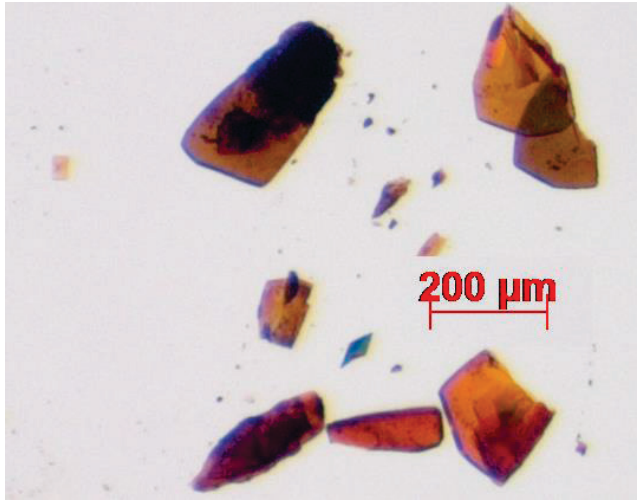

Figure S2: Dark yellow blocks of **2**.

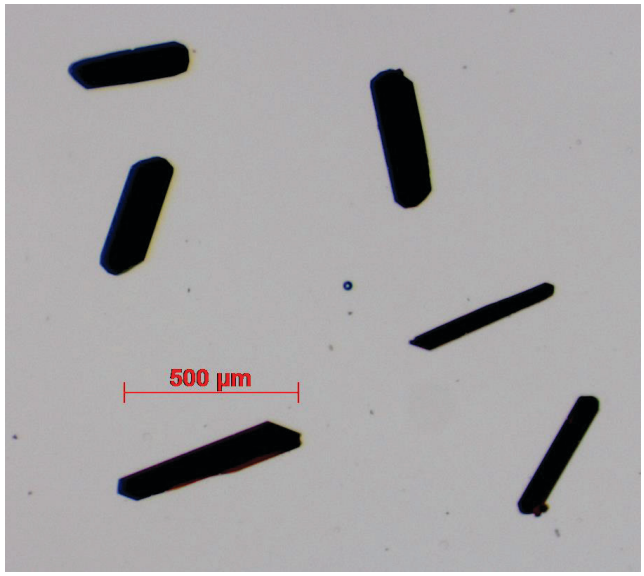

Figure S3: Dark red tabular needles of **3**.

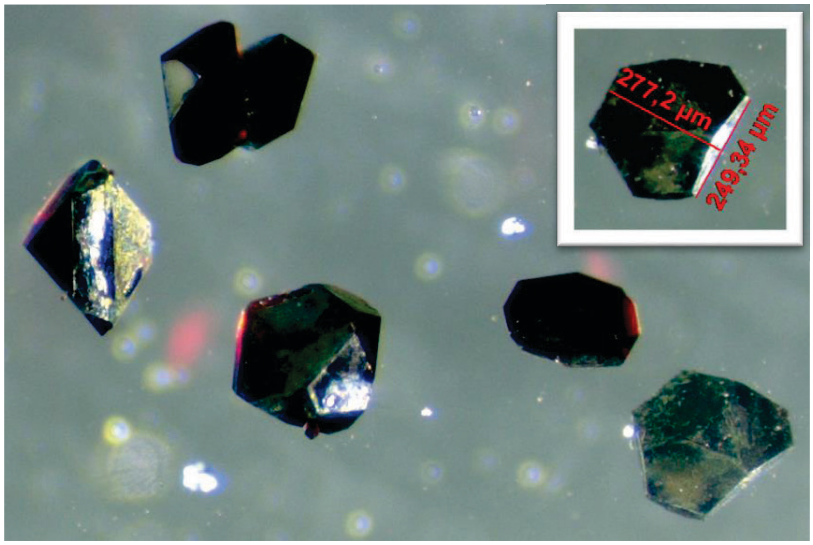

Figure S4: Dark red polyhedra of **4**.

2. Single crystal X-ray crystallography

The data for the X-ray structural analyses were collected at T = 100(2) K with Mo-K_α-radiation ($\lambda_{Mo\text{-}K\alpha}$= 0.71073 Å) on an area detector system Stoe IPDS2 (**1**) or with a CCD detector system on a Bruker QUEST diffractometer (**2**,**4**). The structures were solved by direct methods (SHELXS-97[3]), and refined by full-matrix-least-squares methods against F^2 with program SHELXL-2013.[3] Crystallographic data for the three structures reported in this paper have been deposited with the Cambridge Crystallographic Data Center as supplementary publications No. CCDC 1811887 (**1**), CCDC 1812238 (**2**), and CCDC 1811888 (**4**). The crystal data and experimental parameters of the structure determinations are collected in Tables S1 and Tables S2-S5, respectively. Supplementary Figures are provided in Figures S5–S16.

Table S1. Crystal data and details of the structure determinations of **1, 2,** and **4**.

Compound	**1**	**2**	**4**
formula	$C_{38}H_{83.4}K_2N_6O_{12.7}P_6Si$	$C_{18}H_{36}KN_2O_6Ge_{0.5}P_3$*	$C_{36}H_{72}K_3N_4O_{12}As_7$
formula weight [gmol^{-1}]	1119.93	544.83*	1394.71
crystal color, shape	Yellow block	Yellow plate	Dark red polyhedron
crystal size [mm^3]	0.26 × 0.25 × 0.13	0.10 × 0.09 × 0.08	0.13 × 0.09 × 0.09
crystal system	monoclinic	trigonal	monoclinic
space group	*Cc*	$P\bar{3}c1$	*C*2/c
a [Å]	24.107(2)	11.7150(4)	27.6394(11)
b [Å]	11.813(1)	11.7150(4)	14.9919(6)
c [Å]	20.400(2)	22.2324(9)	26.6512(11)(9)
α [°]	90	90	90
β [°]	107.033(7)	90	103.261(2)
γ [°]	90	120	90
V [Å^3]	5554.6(9)	2642.4(2)	10748.8(8)
Z, ρ_{calc} [g cm^{-3}]	4, 1.339	4, 1.369*	8, 1.724
μ ($Mo_{K\alpha}$) [mm^{-1}]	0.424	0.974*	4.586
Absorption correction type	multi-scan	multi-scan	multi-scan
2θ range [°]	3.66 to 49.88	3.664 to 49.884	4.166 to 50.698
total reflections	72123	39355	162737
unique reflections [R_{int}]	9740	1557	9812
obs. reflections [I>2σ(I)]	8769	1009	8910
parameters	685	134	627
R1 [I>2σ(I)] / *w*R2 (all data)	0.0363 / 0.0862	0.0499 / 0.1115	0.0305 / 0.0489
GooF (all data)	1.058	1.096	3.301
max peak/hole [e Å^3]	0.598 / –0.414	0.303 / –0.327	0.353 / –0.332
Compound	**1**	**2**	**4**

* The real formula and the derived parameters may be different

2.1. Details of the structure determination of $[K(crypt\text{-}222)]_2(SiP_6H_2)$)·en·0.7 H_2O (1)

A multi-scan absorption correction was applied with T(min) = 0.6912 and T(max) = 0.7457.

Cluster anion: The anionic cluster component is a nortricyclane-type cluster with an overall charge of –2 according to the number of counter ions. It proved to be disordered over two orientations (Figure S5). Due to the neighboring position of P and Si in the periodic table, the atoms could not be distinguished from each other. Therefore, the anionic component was first refined with P on all positions. Then, based on the refined ratio for the disordered components of 82.35 to 17.65%, all atom sites were occupied by Si and P in a 1:6 ratio. Of course, the two H-atoms of the $[SiP_6H_2]^{2-}$ anion could not be localized.

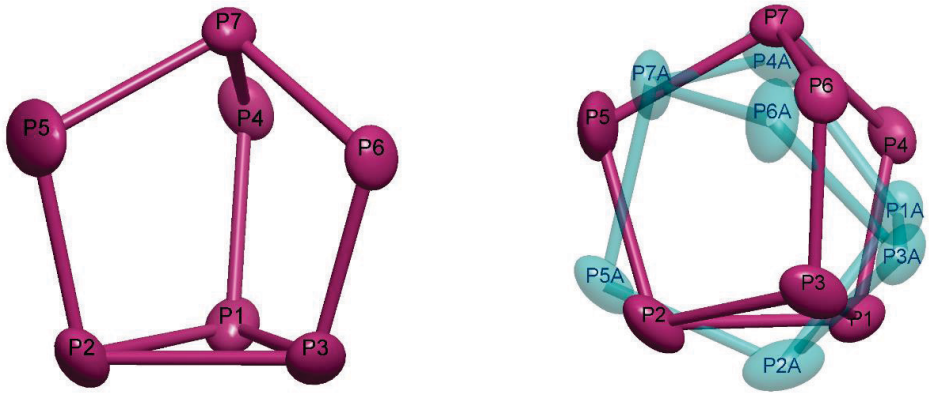

Figure S5. a) Structure of the main component of the $[SiP_6H_2]^{2-}$ anion in **2**; **b)** Disorder model with orientation I (82.35%, violet) and II (17.65%, green). Displacement ellipsoids shown at 50% probability

Cations: The two $[K(crypt\text{-}222)]^+$ cations are well localized and could be refined using anisotropic displacement parameters (Figure S6). All H-atoms were included riding on calculated positions with isotropic displacement parameters taken as 1.2 U_{eq} of their bonding partners.

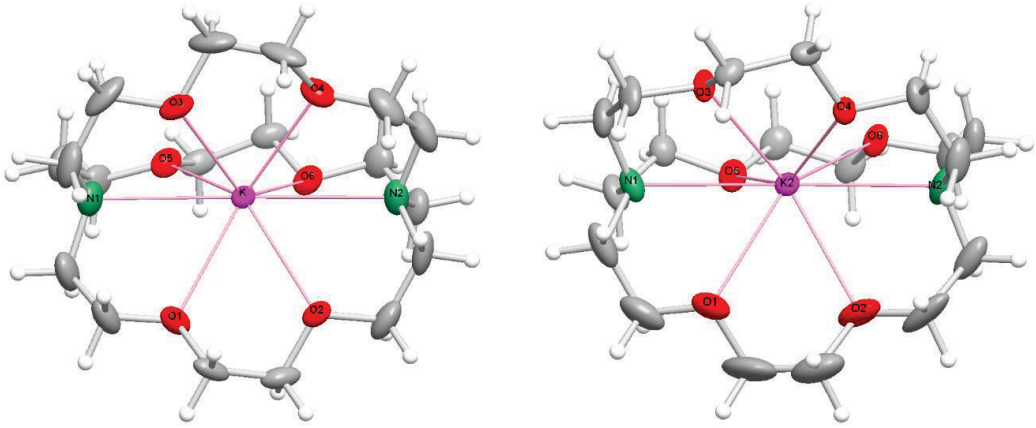

Figure S6. a) [K[2.2.2]crypt] cation No. 1; **b)** No. 2. Displacement ellipsoids shown at 50% probability

Solvent: One *en* molecule was found in the unit cell, which could be refined assuming disorder over two positions occupied by 65.7 and 34.3%. In addition residual electron density in the surrounding of one of the cations was refined as O of a H_2O molecule introduced possibly by not completely dry *en*. Its occupation refined to 70.0%.

Table S2. Bond lengths of the anionic cluster (main component) in **2**.

Si/P Atom numbers	Bond length / Å
P1–P2	2.268(3)
P1–P3	2.231(2)
P1–P4	2.130(3)
P2–P3	2.258(2)
P2–P5	2.213(3)
P3–P6	2.136(3)
P4–P7	2.166(2)
P5–P7	2.186(2)
P6–P7	2.161(2)
Average	**2.194 Å**

2.2. Details of the structure determination of $[K(crypt\text{-}222)]_2(Ge_xP_{7-x}H_{2-x})_{1-n}(Ge_{9-y}P_yH_{2-y})_n$ (2)

A multi-scan absorption correction was applied with T(min)= 0.823 and T(max)= 0.906.

Cluster anion: The anion shows severe disorder on a site with 32-symmetry (D_{3h}). Thus, it was not possible to decide which type of cluster (according to the results of mass spectroscopy, NMR, and DFT calculations, possibly $[GeP_6H_2]^{2-}$ and $[Ge_7P_2]^{2-}$) is present and in which ratio. To describe approximately the electron density distribution, six atom sites were refined as P atoms, five of them with free occupancies. Thus, the stoichiometry of the model does not reflect the true composition of the crystal. Even several crystallization methods and trials did not produce crystals with lower degree of disorder. Possible interpretations of the disorder model are shown below in Figures S7-S11.

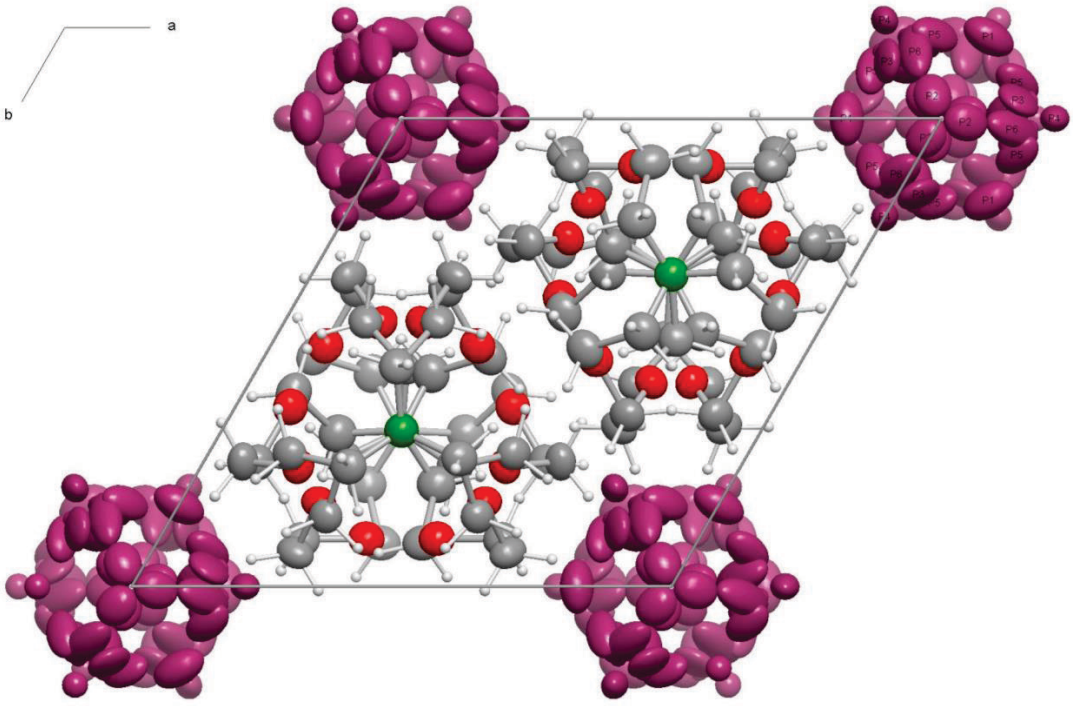

Figure S7. View of the unit cell of **2** along the *c*-axis.

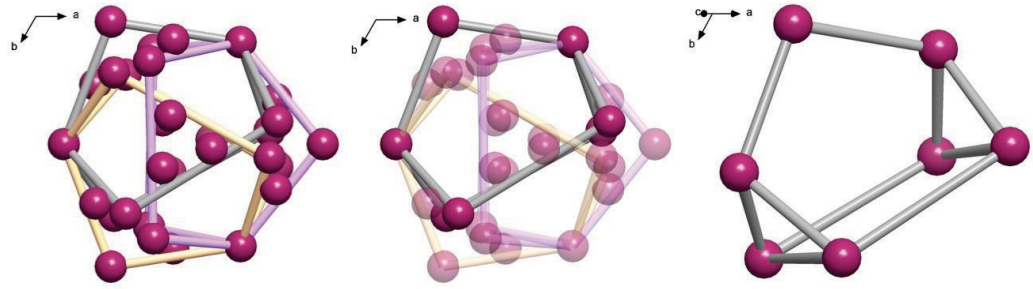

Figure S8. Possible disorder models for a 7-vertex clusters enabled by symmetry. Overlay (left), one orientation highlighted (mid), single orientation (right).

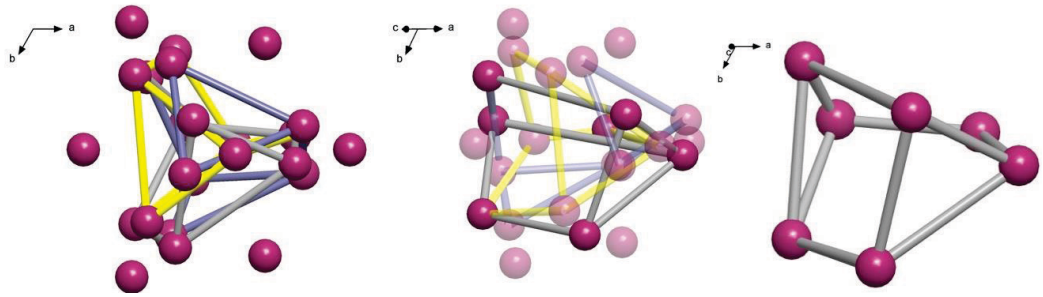

Figure S9. A possible disorder model for 7-vertex cluster. Overlay (left), one orientation highlighted (mid), single orientation (right).

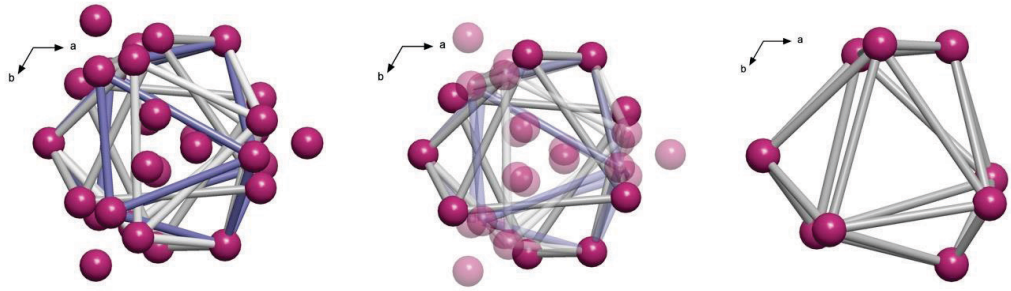

Figure S10. A possible disorder model for 9-vertex cluster as distorted capped prisms. Overlay (left), one orientation highlighted (mid), single orientation (right).

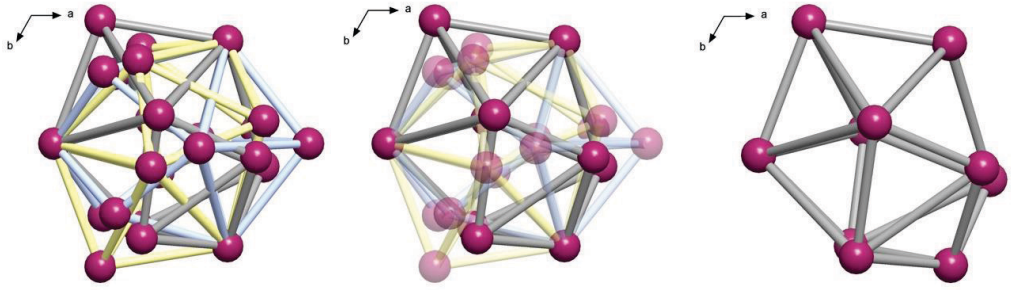

Figure S11. A possible disorder model for 10-vertex cluster. Overlay (left), one orientation highlighted (mid), single orientation (right).

Cations: The $[K(crypt\text{-}222)]^+$ cations are well localized on a 3-fold axis and could be refined using anisotropic displacement parameters (Figure S12). All H-atoms were included riding on calculated positions with isotropic displacement parameters taken as 1.2 U_{eq} of their bonding partners.

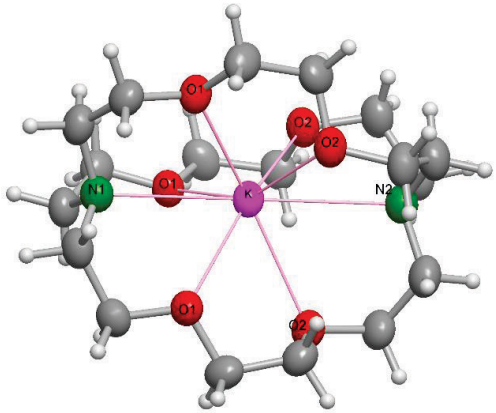

Figure S12. [K[2.2.2]crypt] cation in **2**. Displacement ellipsoids shown at 50% probability

Solvent: There is no solvent present.

The unit cell found for **2** varies only slightly (approx. 1.5 %) from a previously obtained compound containing the 9-atom cluster $(Ge_7P_2)^{2-}$ as anionic component (see also CCDC 1579584[2] and Table S3).

Table S3. Unit cell data comparison

	Compound **2**	$[K(crypt\text{-}222)]_2(Ge_7P_2)$
a [Å]	11.7150(4)	11.8967(17)
b [Å]	11.7150(4)	11.8967(17)
c [Å]	22.2324(9)	22.3940(5)
Space group	$P\bar{3}c1$	$P\bar{3}c1$

This only marginal difference in unit cell size clearly enables the formation of mixed anionic sites within the crystal lattice, resulting in the observed complex disorder on this position. Obviously, the channels along the *c*-axis, formed by the honeycomb-like packing of the cations (like in **1**), may be filled by different anions of suitable size.

2.3. Details of the structure determination of $[K(crypt\text{-}222)]_2(SiAs_6H_2)$ (3)

Crystals of **3** grew to a large dimension (0.5 mm – see Figure S3). The compound crystallizes in the space group $P\bar{3}c1$ (like **2)** and has a very similar unit cell: *a, b* = 11.6921(12), *c* = 22.238(3), V = 2632.7(5). Though several data sets of apparently high quality were recorded, and the substructure of the [K(crypt-222)] cations could be well refined, we were not successful to establish a sensible disorder model for the region of the anion cluster which is located on a site of 32 (D_3) symmetry. The reason may be that the data are affected by merohedral twinning that distorts the results of direct methods and Fourier summations. In addition, overlay of many alternative orientations of a low-symmetric anion on a site of high symmetry may generate misplaced electron density maxima preventing to recognize the true geometry of the components. Thus, this trigonal structure **3** will not be further discussed here.

Table S4. Crystal data for structure **3**.

empirical formula	$C_{38}H_{72}K_2N_6O_{12}As_7$
formula weight [gmol^{-1}]	1407.66
crystal color, shape	Red tabular prism
crystal size [mm^3]	0.046 × 0.061 × 0.062
crystal system	trigonal
space group	$P\bar{3}c1$
a [Å]	11.692 (2)
b [Å]	11.692(2)
c [Å]	22.238(3)
α [°]	90
β [°]	90
γ [°]	120
V [Å^3]	2632.7 (5)
Z, ρ_{calc} [g cm^{-3}]	2, 1.663
μ ($Mo_{K\alpha}$) [mm^{-1}]	4.890

2.4. Details of the structure determination of $[K(crypt\text{-}222)]_2(KAs_7)$ (4)

Cluster anion: The cluster anion is a nortricyclane-type cluster of As_7 with a charge of 3–. The cluster anions are interconnected by K^+ cations and form a chain in direction of the *c*-axis. The As_7^{3-} cage is disordered over two orientations (occupancy 0.50) in which the apical atoms (As1) point into opposite directions (Figure S13). K3 (on a 2-fold axis) is six-coordinated and connects the As_7 groups in both orientations (K···As 3.40 – 3.88 Å). As-As bond lengths are collected in Table S4. K4 itself is disordered by a close inversion center over two positions which can be attributed to the both orientations of the anion. Thus, their occupancy ratio must be 1:1. The coordination of K4 is 8 (3.19 – 3.84 Å). Figure S13 shows a part of the $[KAs_7]^{2-}$ chain in one of the alternative configurations.

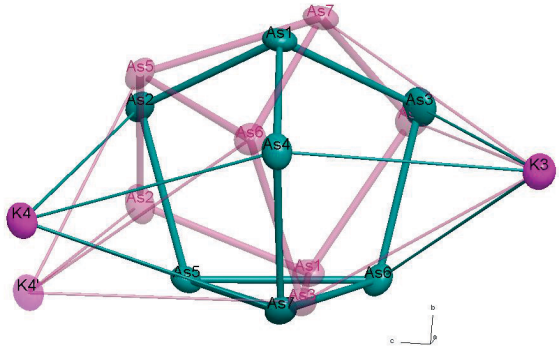

Figure S13. The two orientations of the disordered As_7 group in **4** and the connecting K^+ ions.

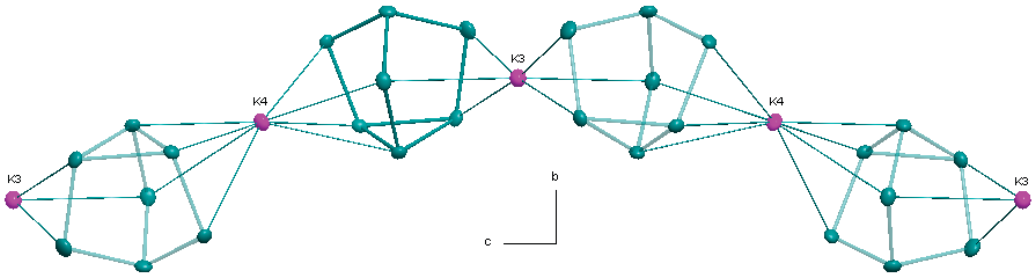

Figure S14. Part of the $[KAs_7]^{2-}$ chain with 2-fold axis through K3 along the *b* direction. One of the two alternative configurations.

Table S5. Bond lengths within the As_7^{3-} cluster anion of 4.

Atom numbers	orientation I	orientation II
As1 – As2	2.4115(9)	2.4213(8)
As1 – As3	2.392(7)	2.406(4)
As1 – As4	2.424(3)	2.416(6)
As2 – As5	2.3417(7)	2.3473(7)
As3 – As6	2.331(6)	2.360(5)
As4 – As7	2.362(5)	2.350(6)
As5 – As6	2.5103(8)	2.537(2)
As5 – As7	2.532(3)	2.4864(9)
As6 – As7	2.503(5)	2.522(3)
Average	**2.423 Å**	**2.427 Å**

Cations: The two $[K(crypt\text{-}222)]^+$ cations are well localized and could be refined using anisotropic displacement parameters (Figure S15). All H-atoms were included riding on calculated positions with isotropic displacement parameters taken as 1.2 U_{eq} of their bonding partners.

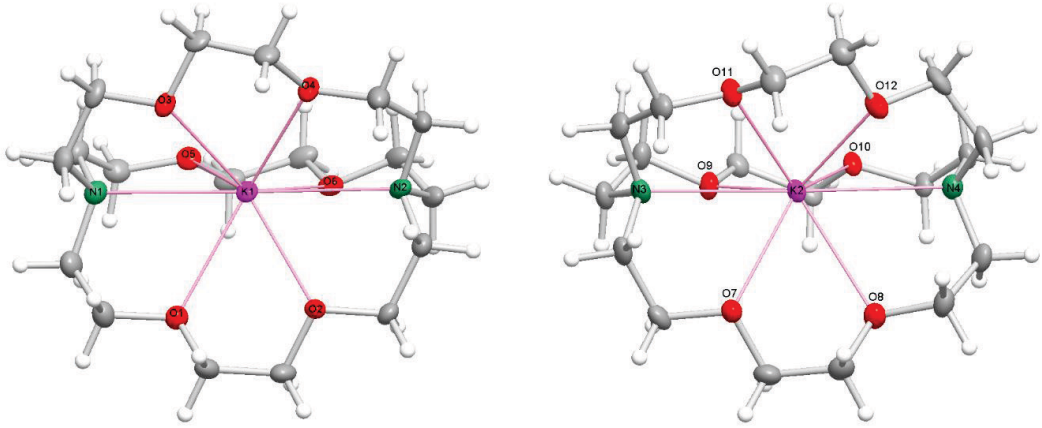

Figure S15. The two $[K(crypt\text{-}222)]^+$ cations in **4**. Displacement ellipsoids shown at 50% probability

The $[K(crypt\text{-}222)]^+$ cations form a honeycomb-like packing, in the channels of which the anionic chains are positioned (Figure S16).

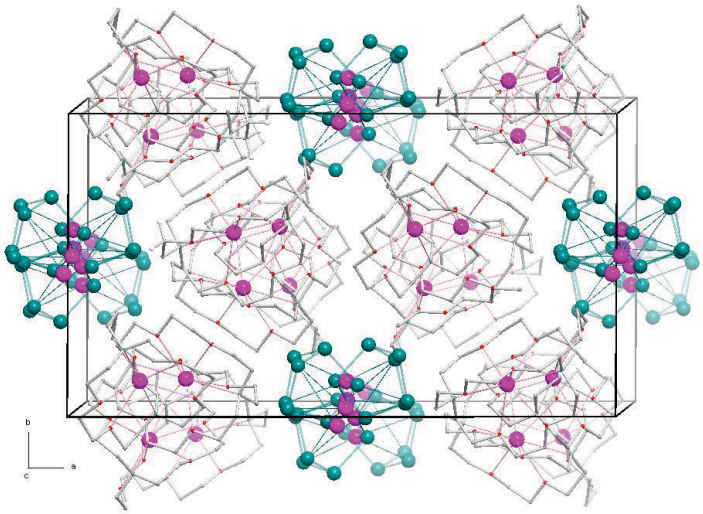

Figure S16. Unit cell of **4** projected approximately along the chain direction *c*. As green, K violet, wire model for the cryptand ligands.

3. Energy dispersive X-ray spectroscopy (EDX) analysis

EDX analyses were performed to support the elemental composition that was suggested based on the XRD experiments. These were carried out using an EDX-device Voyager 4.0 of Noran Instruments coupled with an electron microscope CamScan CS 4DV. Data acquisition was performed with an acceleration voltage of 20 kV and 100 s accumulation time. The radiation emitted by the atoms was analyzed. Results are summarized in Tables S6-S7.

Table S6. EDX analysis of **1** - **2** (K, Si, Ge, P)

Element	k-ratio	ZAF	Atom%	Atomic ratio observed (calc)	Element wt %	wt % Err. (1-sigma)
$[K(crypt\text{-}222)]_2(SiP_6H_2)\cdot en \cdot 0.7\,H_2O$ (1)						
K-K	0.3055	1.299	34.00	3.53 (2)	39.68	+/- 1.36
Si-K	0.0639	1.089	57.70	6 (6)	6.96	+/- 0.90
P-K	0.4526	1.179	8.31	0.86 (1)	53.35	+/- 1.35
Total			100	12.09 (9)	100	
$[K(crypt\text{-}222)]_2(Ge_xP_{7-x}H_{2-x})_{1-n}(Ge_{9-y}P_yH_{2-y})_n$ (2)						
K-K	0.1478	1.658	24.02	2.28 (K)	24.51	+/- 0.28
P-K	0.2780	1.833	63.04	6 (6)	50.96	+/- 0.33
Ge-K	0.2115	1.159	12.94	1.23 (1)	24.53	+/- 0.66
Total			100	9.51 (9)	100	

The results of the EDX investigations confirm the Si:P and Ge:P ratios of the investigated substances within the expected accuracy. The K or Ge values, respectively, show largest deviations from the calculated values, in accordance with the large error indicated in the rightmost column.

Table S7. EDX analysis of **3** - **4** (K, Si, As)

Element	k-ratio	ZAF	Atom%	Atomic ratio observed (calc)	Element wt %	wt % Err. (1-sigma)
$[K(crypt\text{-}222)]_2(SiAs_6H_2)$ (3)						
K-K	0.1497	1.214	27.89	2.64 (2)	18.18	+/- 0.58
Si-K	0.0164	3.014	10.54	1 (1)	4.93	+/- 0.80
As-K	0.7290	1.055	61.57	5.84 (6)	76.89	+/- 3.87
Total			100	9.48 (9)	100	
$[K(crypt\text{-}222)]_2(KAs_7)$ (4)						
K-K	0.1583	1.200	31.01	3 (3)	19.00	+/- 0.67
As-K	0.7773	1.042	68.99	6.67 (7)	81.00	+/- 4.48
Total			100	9.67 (10)	100	

The results of the EDX investigations confirm the Si:As and K:As ratios of the investigated substances within the expected accuracy. The As values show the largest deviations from the calculated values, in accordance with the large error indicated in the rightmost column.

4. Electrospray Ionization mass spectrometry (ESI-MS) investigations

ESI(–) mass spectrometry has been performed on Micromass Q-Tof *micro* or a Finnigan LTQ-FT spectrometer by Thermo Fischer Scientific in the negative ion mode: Spray voltage 3.90 kV, capillary temperature 300°C, capillary voltage –11 V, tube lens voltage –140 V, sheath gas flow rate 25 arb, sweep gas flow rate 0 arb. For the measurements, the filtered solutions were dried *in vacuo* and re-dissolved in dry DMF or *en*. Additional peaks observed in the ESI(–) spectrum are believed to belong to decomposition products and fragments formed by a dynamic re-organization of the cluster anions and their fragments in solution under ESI-MS conditions. As it is common for Zintl anions and intermetallic cluster anions, the observed fragments have been detected as oxidized, singly charged species. Figures S17-S18 shows the isotopic pattern of the respective anions, with measured (top) and calculated (bottom) isotope patterns each.

We thank Rhonda Stoddard and Dr. Eric Janusson (University of Victoria, BC, Canada), as well as Jan Bamberger (Philipps-Universität Marburg) for their help in collecting the ESI-MS data.

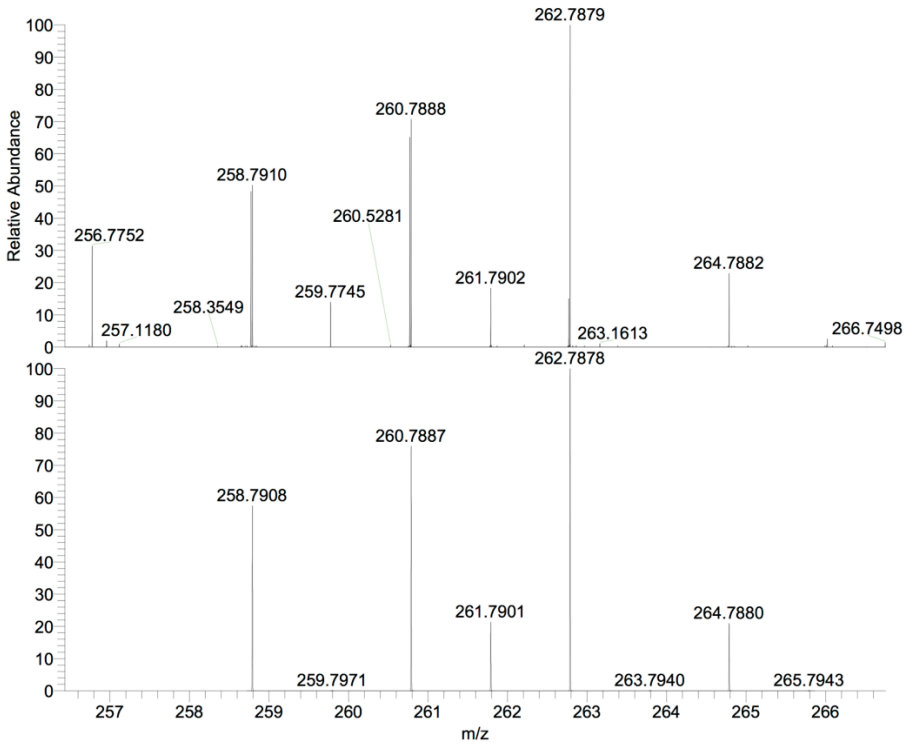

Figure S17. ESI-MS(–) spectrum of the $(GeP_6H_3)^-$ anion.

5. Nuclear magnetic resonance (NMR) spectroscopy

NMR measurements of **1** and **2** were performed a Bruker 400 MHz AV-III HD FT-NMR spectrometer equipped with H/FX Bruker ATM. ^{31}P-NMR spectroscopy was performed on freshly dissolved single crystals of **1** and **2** in DMF-d_7. Due to the small yield of **1** no useful spectrum was obtained, even with a large number of scans. The ^{31}P-NMR spectrum of **2** indicates the presence of various polyphosphide compounds that are believed to be decomposition products, nevertheless they show significant evidence of proton coupling. The results are presented in Figures S19-S21.

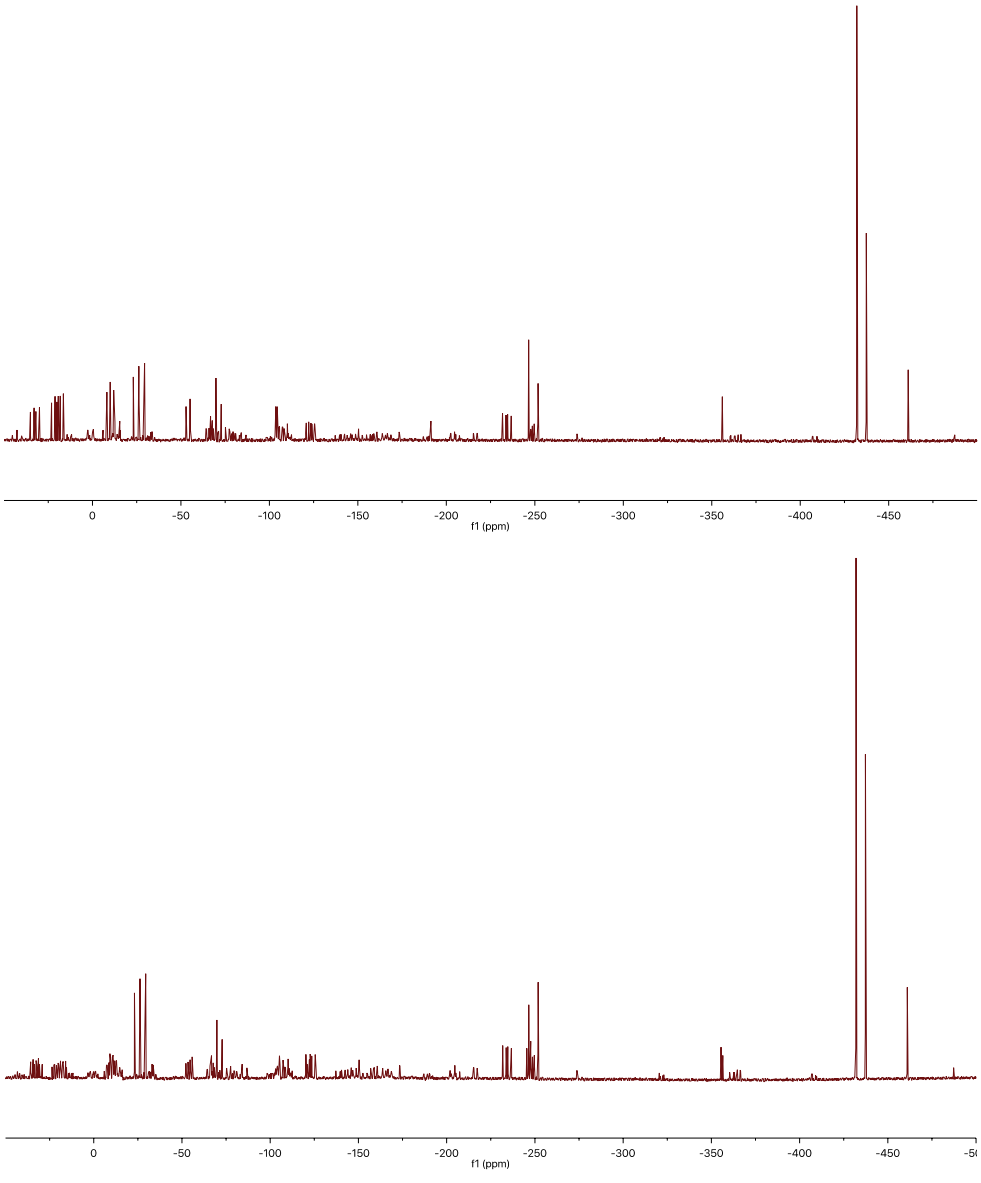

Figure S19. Top: ^{31}P-NMR spectrum of **2**. Bottom: proton-coupled ^{31}P-NMR spectrum. A zoom into the 50 to –190 ppm range is given in Figure S20.

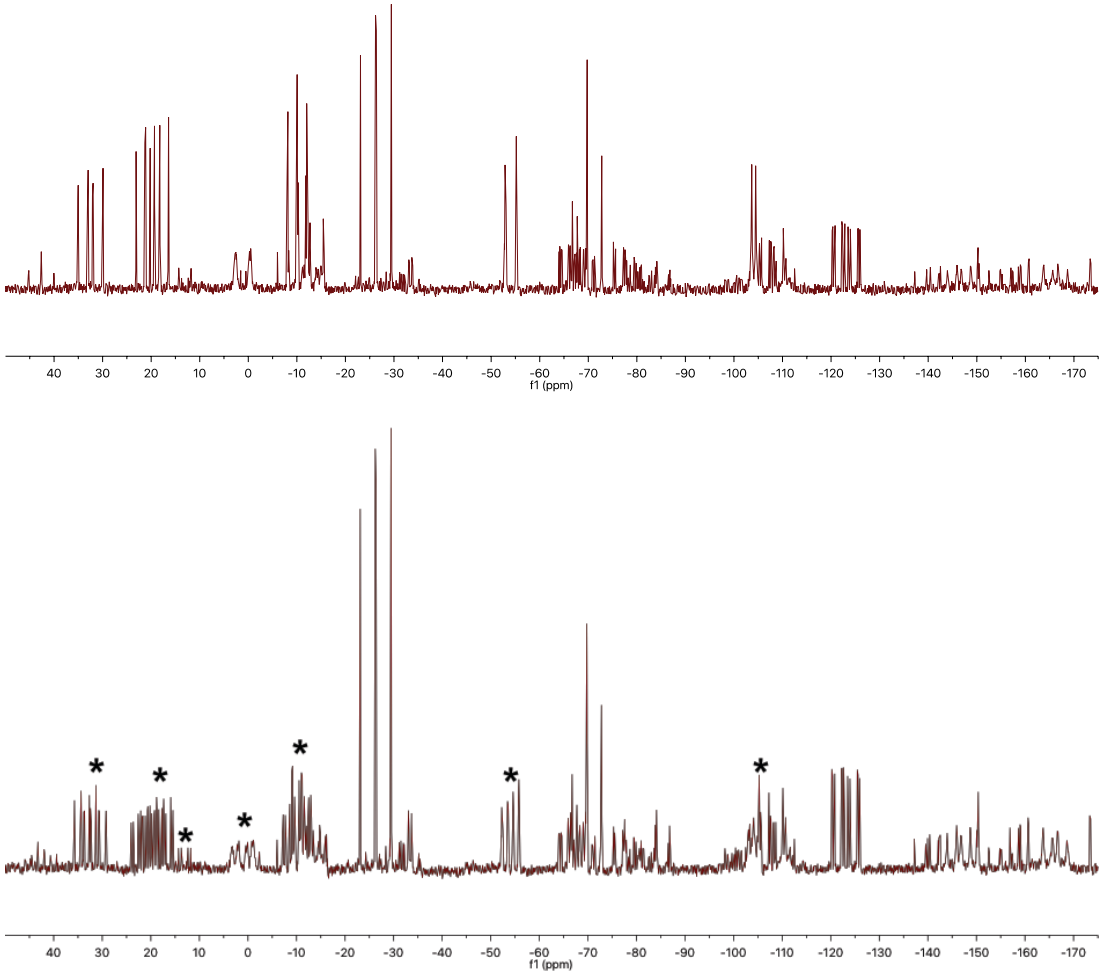

Figure S20. Top: ^{31}P-NMR spectrum of **2** (detail). Bottom: proton coupled ^{31}P-NMR spectrum of **2** (detail). Signal sets that exhibit proton coupling are marked by an asterisk.

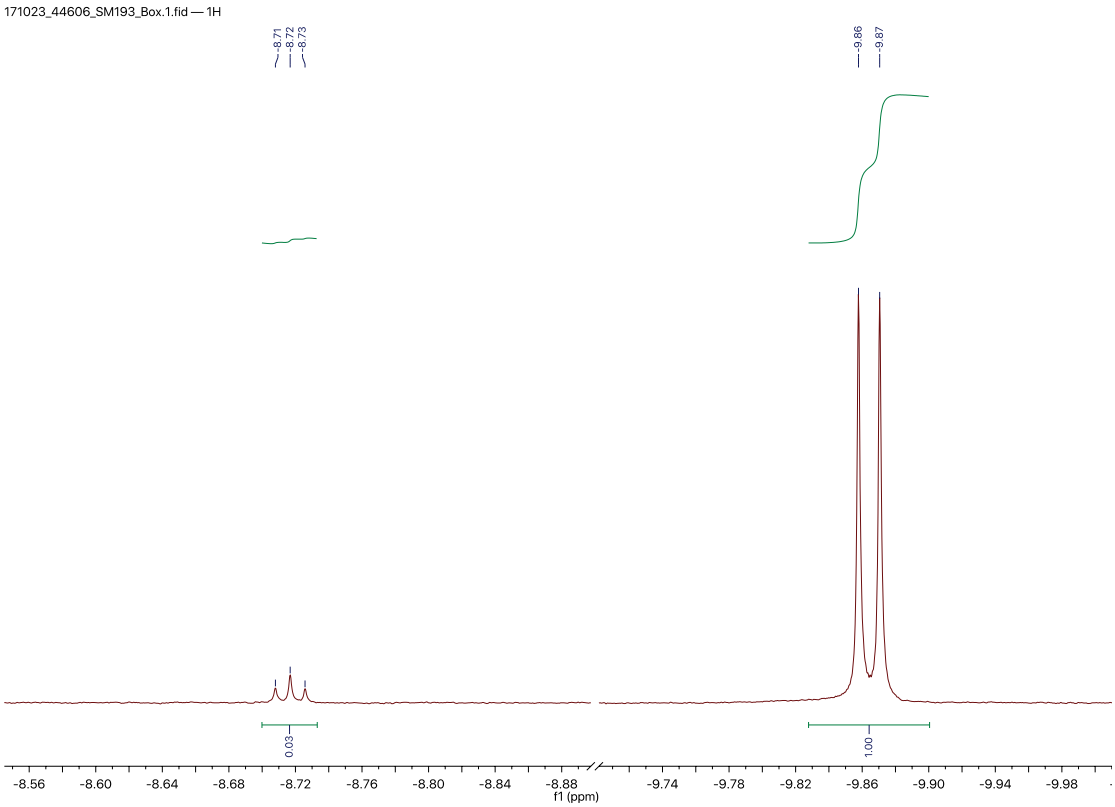

Figure S21. Detail of the ^{1}H-NMR spectrum of compound **2**.

In the ^{1}H-NMR spectrum, a doublet at –9.86 ppm was found as evidence of the presence of P–H bonds. A triplet at –8.72 with low intensity was identified in addition to the doublet (integral value doublet vs. triplet found to be 1:0.03).

It is obvious that several P-rich species that exhibit proton couplings are present in solution, excluding a clear assignment to the proposed nortricyclane-type species, that has been identified in the high resolution ESI(–)-MS.

^{29}Si- and ^{75}As-NMR studies on dissolved crystals of **3** did not produce a satisfying dataset, even from very concentrated solutions with >100.000 scans. This is due to the low content of Si in the anion combined with the complex coupling to ^{75}As, which also possesses a broad signal width by nature.

6. Quantum Chemical Investigations

6.1. Methods

Quantum chemical calculations were carried out with TURBOMOLE[4] employing the TPSS[5] functional with basis sets of type def2-TZVP[6] together with respective auxiliary basis sets[7]. The negative charge was compensated by the conductor-like solvation model (COSMO)[8] with default settings. The electronic structures were investigated by means of natural population analysis (NPA).[9] The geometry optimizations were performed without any symmetry restrictions.

6.2 Calculations of the unprotonated clusters

6.2.1 Geometry optimizations of isomeric 7-atom cages

Figure S22. Optimized structures of the three isomers of the bare anions $(SiP_6)^{4-}$, $(GeP_6)^{4-}$, and $(SiA_6)^{4-}$, along with the energy differences ΔE (kJ/mol) with respect to the global minimum structure.

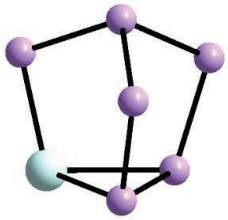	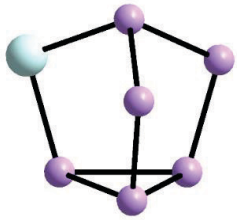	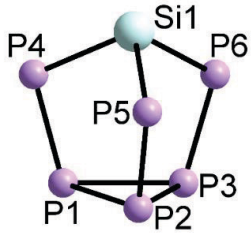
+7	+68	0
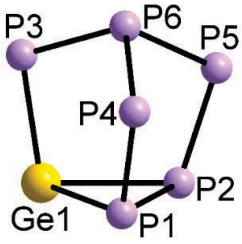	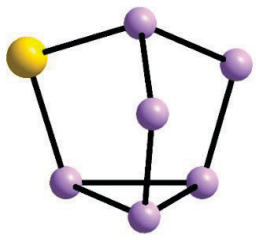	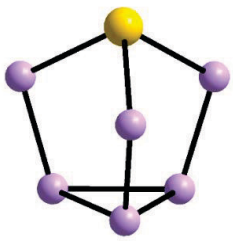
0	+78	+1
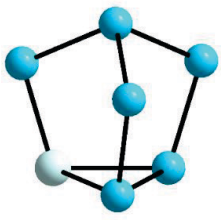	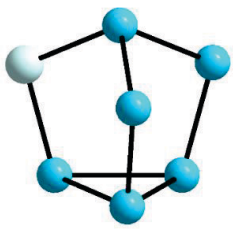	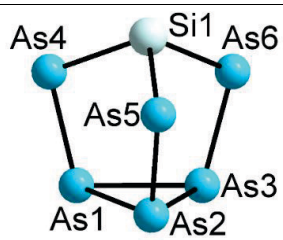
+10	+60	0

6.2.2 Natural population analyses of the unprotonated clusters

Tables S8, S9 and S10 show the results of the NPA for the unprotonated compounds **1**, **2** and **3**. The two-bonded P atoms (P4, P5, and P6 in compound **1** and **3,** and P3, P4, and P5 in compound **2**) have the highest negative partial charge. Protonation at these sites is hence energetically favored.

Table S8. Calculated natural charges for each atom in a hypothetically unprotonated compound **1** according to NPA.

Atom	Natural charge
P1	−0.33921
P2	−0.33921
P3	−0.33921
P4	−0.89573
P5	−0.89573
P6	−0.89573
Si1	−0.29590

Table S9. Calculated natural charges for each atom in a hypothetically unprotonated compound **2** according to NPA.

Atom	Natural charge
Ge1	−0.17905
P1	−0.51625
P2	−0.51655
P3	−0.97932
P4	−0.77946
P5	−0.77946
P6	−0.24988

Table S10. Calculated natural charges for each atom in a hypothetically unprotonated compound **3** according to NPA.

Atom	Natural charge
As1	−0.33999
As2	−0.33976
As3	−0.33962
As4	−0.85761
As5	−0.85727
As6	−0.85765
Si1	−0.40810

6.3 Computational results for the anion in compound 1

Figure S23 shows the computationally optimized structure of the anion in compound **1**. Here the group 14 atom is most likely located at the cluster's top. The results are again in good agreement with the experimental data. Since we have no disorder in the calculated structure, it seems to be less symmetrical than the experimental structure (see Table S11).

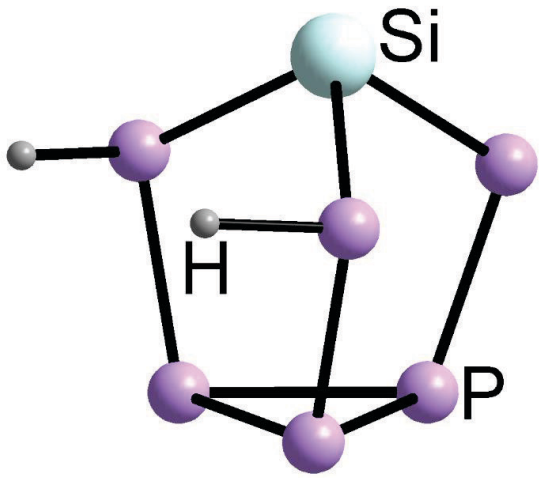

Figure S23. Computationally optimized structure of the anion in compound **1**.

Table S11. Comparison of experimentally and computationally obtained bond lengths in the anion in compound **1**.

	Experiment	Calculation
P1–P2	2.255	2.257 Å
P1–P3	2.233	2.264 Å
P2–P3	2.248	2.258 Å
P1–P4	2.132	2.222 Å
P2–P5	2.221	2.222 Å
P3–P6	2.137	2.186 Å
P4–Si1	2.166	2.302 Å
P5–Si1	2.194	2.302 Å
P6–Si1	2.161	2.255 Å
P4–H1	–	1.437 Å
P5–H2	–	1.437 Å

Figure S24 shows a comparison of the three most stable isomers for the Si/P cluster. The close values again indicate that an equilibrium in solution, and also in the solid state, is most likely.

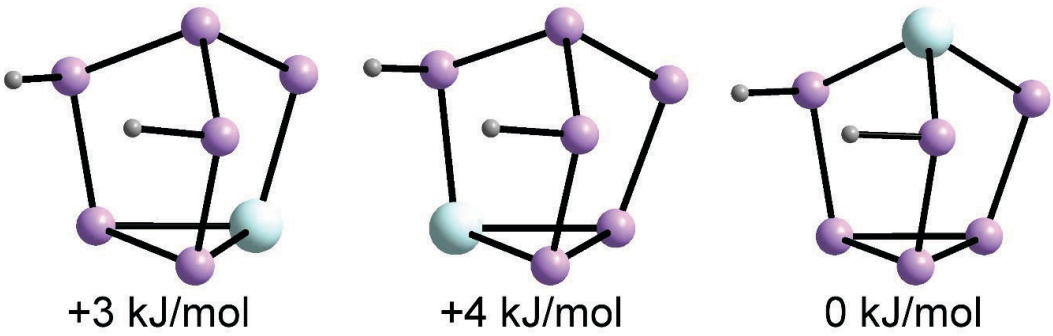

Figure S24. Comparison of the three most stable $(SiP_6H_2)^{2-}$ cluster isomers.

6.4 Computational results for the anion in compound 2

Figure S25 shows the computationally optimized structure of the anion in compound **2**. The isomer with the group 14 atom in the trigonal cluster base is the most favorable. The results are given in Table S12.

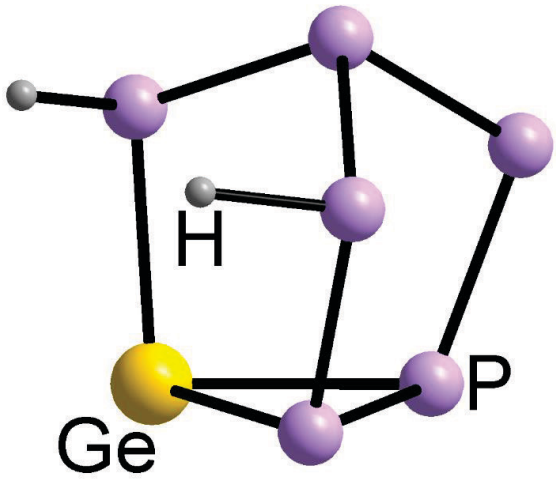

Figure S25. Computationally optimized structure of the anion in compound **2**.

Table S12. Computationally obtained bond lengths in the anion in compound **2**.

	Calculation
Ge1–P1	2.443 Å
Ge1–P2	2.425 Å
P1–P2	2.261 Å
Ge1–P3	2.408 Å
P1–P4	2.219 Å
P2–P5	2.213 Å
P3–P6	2.216 Å
P4–P6	2.229 Å
P5–P6	2.165 Å
P3–H1	1.437 Å
P4–H2	1.439 Å

Figure S26 shows a comparison of the three most stable isomers for the Ge/P cluster. The close values indicate that an equilibrium in solution is well possible, thus that all isomers might also be included in the solid state structure.

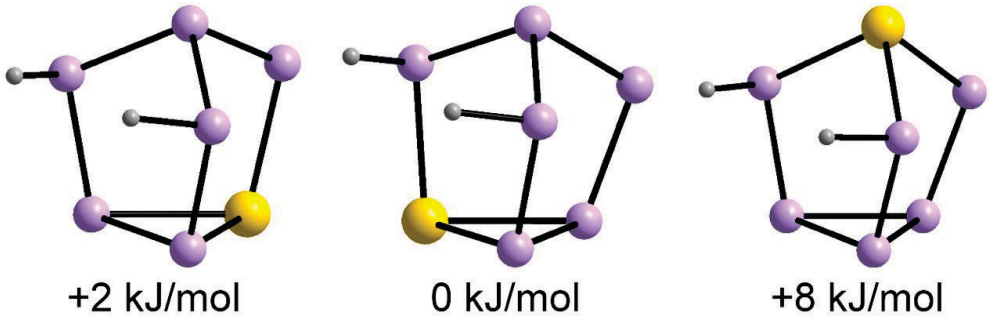

Figure S26. Comparison of the three most stable $(GeP_6H_2)^{2-}$ cluster isomers.

6.5 Computational results for the anion in compound 3

Figure S27 shows the computationally optimized structure of the anion in compound **1**. The isomer with the group 14 atom in the trigonal cluster base is the most favorable. The results are given in Table S13).

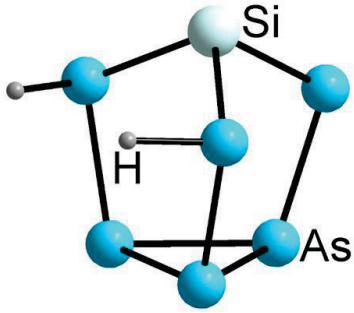

Figure S27. Computationally optimized structure of the anion in compound **3**.

Table S13. Computationally obtained bond lengths in the anion in compound **3**.

	Calculation
As1–As2	2.474 Å
As1–As3	2.473 Å
As2–As3	2.475 Å
As1–As4	2.461 Å
As2–As5	2.460 Å
As3–As6	2.422 Å
As4–Si1	2.395 Å
As5–Si1	2.396 Å
As6–Si1	2.337 Å
As4–H1	1.539 Å
As5–H2	1.539 Åh

Figure S28 shows a comparison of the three most stable isomers for the Ge/P cluster. The close values indicate that an equilibrium in solution might at least be possible.

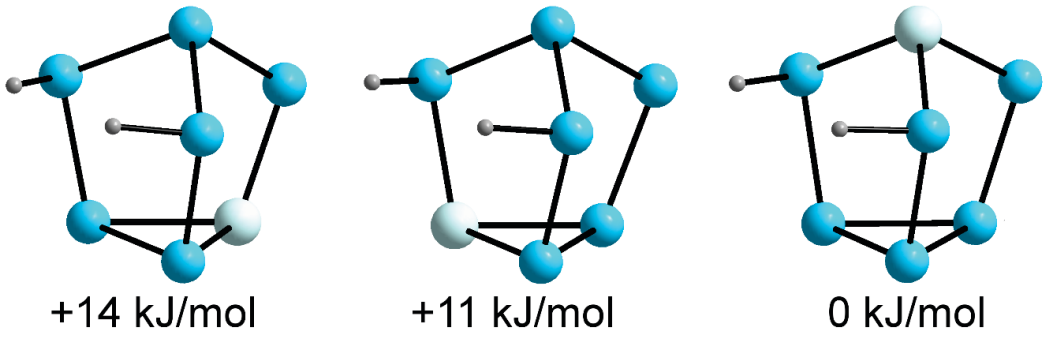

Figure S28. Comparison of the three most stable $(SiAs_6H_2)^{2-}$ cluster isomers.

7. References for the Supplementary Information

[1] 4,7,13,16,21,24-Hexaoxa-1,10-diazabicyclo[8.8.8]hexacosane / Kryptofix 222

[2] Mitzinger, S.; Bandemehr, J.; Reiter, K.; McIndoe, J. S.; Xie, X.; Weigend, F.; Corrigan, J. F.; Dehnen, S. $(Ge_2P_2)^{2-}$: a Binary Analogue of P4 as a Precursor to the Ternary Cluster Anion $[Cd_3(Ge_3P)_3]^{3-}$. *Chem. Commun.* **2017**, accepted manuscript, DOI: 10.1039/C7CC08348C.

[3] Sheldrick, G. M. A short history of SHELX. *Acta Crystallogr*., 2008, **A64,** 112 – 122.

[4] TURBOMOLE V6.6 2016, a development of University of Karlsruhe and Forschungszentrum Karlsruhe GmbH, 1989-2007, TURBOMOLE GmbH, since 2007; available from http://www.turbomole.com.

[5] Tao, J. M.; Perdew, J. P.; Staroverov, V. N.; Scuseria, G. E. Climbing the Density Functional Ladder: Nonempirical Meta–Generalized Gradient Approximation Designed for Molecules and Solids. *Phys. Rev. Lett.* **2003**, *91*, 146401.

[6] Weigend, F.; Ahlrichs, R. Balanced basis sets of split valence, triple zeta valence and quadruple zeta valence quality for H to Rn: Design and assessment of accuracy. *Phys. Chem. Chem. Phys.* **2005**, *7*, 3297–3305.

[7] Weigend, F. Accurate Coulomb-fitting basis sets for H to Rn. *Phys. Chem. Chem. Phys.* **2006**, *8*, 1057–1065.

[8] Klamt, A.; Schüürmann, G. COSMO: a new approach to dielectric screening in solvents with explicit expressions for the screening energy and its gradient. *J. Chem. Soc., Perkin Trans. 2* **1993**, 799–805.

[9] Reed, A. E. ; Weinstock, R. B.; Weinhold, F. Natural population analysis. *J. Chem. Phys.* 1985, **83**, 735–746.

4 Conclusion and Outlook

Novel Zintl-anions of the elemental combinations Ge/P, Ge/As, Si/P and Si/As have been successfully synthesised. For Ge/P and Ge/As anions their capability to undergo derivatisation reactions was demonstrated, for example with $CdPh_2$, to yield unprecedented cluster topologies, like the disc-shaped trimeric cluster anion $[Cd_3(Ge_3P)_3]^{3-}$. In combination with E^5-elements, the formation of 12- and 14-atom cluster shells with an endohedral centre was demonstrated. For the E^5-element Ta a comprehensive pathway for multi-metallic cluster growth could be conceived by combining quantum-mechanical studies with analytical data received from the stepwise crystallisation of intermediary products formed during the cluster growth process. This pathway also sheds light towards the isomerisation process from deltahedral to non-deltahedral cluster topologies. The results presented in this thesis form a basis towards understanding cluster growth processes for Zintl-Anions and enable further studies towards the reactivity of binary cluster anion species. Especially for the Ge/P system the found Zintl anion species will help to facilitate a deeper understanding of cluster formation. $(Ge_2P_2)^{2-}$ and $(Ge_7P_2)^{2-}$ can be seen as a hybrid between the metallic Germanium polyanions and the non-metallic P_4 tetrahedron present in white phosphorus. By utilising ^{31}P-NMR spectroscopy as a probe, cluster formation processes may be observed *in situ* in the future and referenced to the known reactivity of P_4, especially in terms of the differences towards P–P bond activation and the formation of poly-phosphides. Therefore detailed studies upon the formation of tetrahedral species and their reactivity in the solid mixture and the early extraction process are necessary next steps. In learning the influence of an increasing metallic character onto cluster formation, the black box of multi-metallic cluster formation may one day be replaced by a comprehensive understanding of the behavior of inorganic fragments and clusters in solid state, flux and in solution. Thereby finally replacing a trial-and-error influenced approach by rational design to synthesise clusters and cluster frameworks for specific purposes and tasks.

5 Abstract (in German)

Im Rahmen dieser Arbeit wurden neuartige Zintl-Anionen der Elementkombination E^{14}/E^{15} hergestellt. Besonderen Fokus wurde auf die leichteren Homologen der binären tetraedrischen Anionen gelegt. So konnten $(Ge_2As_2)^{2-}$ und $(Ge_2P_2)^{2-}$, welche isovalenzelektronisch zu weißem Phosphor sind, zum ersten mal dargestellt werden. Von diesen leichten tetraedrischen Zintl-Anionen ausgehend, wurde die Synthese multi-metallischer sowie hetero-atomarer Cluster untersucht. Ergebnis dieses Prozesses sind die neuartigen Clusteranionen $[V@Ge_8As_4]^{3-}$, $[Nb@Ge_8As_6]^{3-}$, $[Ta@Ge_6As_4]^{3-}$, $[Ta@Ge_8As_4]^{3-}$, $[Ta@(Ge_8As_6)]^{3-}$ sowie $[Cd_3(Ge_3P)_3]^{3-}$.
Darüber hinaus wurden die größeren Zintl-Anionen $(Ge_7P_2)^{2-}$, $(Ge_7As_2)^{2-}$, $(SiP_6H_2)^{2-}$ und dessen Homologe erfolgreich dargestellt.
Die $[K(crypt\text{-}222)]^+$-Salze der Clusteranionen $[V@Ge_8As_4]^{3-}$ und $[Nb@Ge_8As_6]^{3-}$ wurden durch die Extraktion einer quaternären festen Mischung aus $K/Ge/As/E^5$ erhalten (E = V, Nb). Das $[V@Ge_8As_4]^{3-}$ Clusteranion ist die erste Zintl-Spezies, die ein formal fünffach positiv geladenes V-Kation enthält. Damit ist es das kleinste jemals in Hauptgruppen-Metallcluster eingeführte Kation. Zudem ist diese Verbindung erst die zweite, welche eine neuartige 12-Vertex Cluster-Topologie aufweist. Die Bindungssituation wurde mit Hilfe quantenchemischer Methoden untersucht und erlaubte die definitive Zuordnung von Ge- und As-Atomen auf Positionen im Cluster-Gerüst, welche durch Methoden der Röntgenbeugung nicht voneinander unterschieden werden können. Für ein System aus Ta-, Ge- und As-haltigen Metallclustern konnte zum ersten Mal durch die geschickte Kombination von modernsten quantenchemischen Rechnungen und anorganischer Synthese die Bildung von Metallclustern ausgehend von $(Ge_2As_2)^{2-}$ hin zu $[Ta@(Ge_8As_6)]^{3-}$ beleuchtet werden. Das Spektrum der vorgefundenen Cluster reicht dabei vom kleinen tetraedrischen $(Ge_2As_2)^{2-}$, über einen 9-Atom-Käfig der Zusammensetzung $(Ge_7As_2)^{2-}$, hin zu den endohedralen Clustern $[Ta@Ge_8As_4]^{3-}$ und [Ta@Ge8As6]$^{3-}$. Jedoch ermöglichte es erst der Fund einer Zwischenstufe, nämlich des Clusters $[Ta@Ge_6As_4]^{3-}$, den Reaktionspfad der Clusterbildung nachzuvollziehen. Mit Hilfe einer

kürzlich entwickelten quantenchemischen Methode zur Berechnung der günstigsten Energie von Isomeren multimetallischer Systeme (GA-RP) sowie der erstmaligen Modellierung ihrer Reaktionspfade, gelang schließlich der Schluss des Kreises und die Einordnung der Cluster in eine Reaktionskaskade zur intermetalloiden Clusterbildung: Von den tetraedrischen Anionen ausgehend wird zunächst ein 9-Atom-Käfig gebildet. Dieser Schritt ist multimetallischen und homoatomaren Clustern, die Tetrelatome enthalten, gemein. Von hier ausgehend findet unter Aufnahme und des Übergangsmetallatoms eine partielle Fragmentierung und Reorganisation des Clusters statt. Das Übergangsmetall bindet in diesem Moment an eine Clusterhalbschale und ist in der Lage mit einem $(Ge_2As_2)^{2-}$ Anion zu reagieren. Hierbei bildet sich das Clusteranion $[Ta@Ge_6As_4]^{3-}$, in dem das Ta-Atom bereits im Clusterinneren eingeschlossen ist. Dieses Molekül muss nun einen Umorganisationsschritt durchlaufen, bevor es von einem weiteren Äquivalent des tetraedrischen Edukts angegriffen werden kann und das fertige endohedrale Produkt bildet. Die genauere Betrachtung von Isomeren der auskristallisierten Zwischenstufe $[Ta@(Ge_6As_4)]^{3-}$ lieferte weitere Hinweise auf einen gemeinsamen Reaktionspfad, dem alle nicht-deltaedrischen, intermetalloiden Cluster, die Tetrelatome enthalten, folgen. Mit nur wenig Energie lassen sich aus der „Schlüssel"-Spezies $[Ta@(Ge_6As_4)]^{3-}$ Isomere erzeugen, welche exakte Ausschnitte aus bekannten Strukturen der nicht-deltaedrischen, intermetalloiden Cluster darstellen. Dieser Fund erlaubt die Einordnung der vorgefundenen Zwischenstufe als einen „gemeinsamen Vorfahren" der bisher bekannten endohedralen homo- und multi-metallischen Tetrelcluster aus 10, 12, 13 und 14 Atomen in der Clusterhülle. Darüber hinaus lieferte die Studie erstmals eine quantenchemisch fundierten Vorschlag für die Reorganisation von deltaedrischen zu nicht-deltaedrischen Clustern. Das neue binäre Zintl-Anion $(Ge_2P_2)^{2-}$, welches aus der festen Mischung KGeP extrahiert wurde und isovalenzelektronisch zu P_4 ist, hat sich als geeignetes Edukt zur Synthese multimetallischer Cluster erwiesen. Es konnte durch NMR-spektroskopische Untersuchungen und Einkristallröntgendiffraktometrie gezeigt werden, dass sich $(Ge_2P_2)^{2-}$ über die Zeit in $(Ge_7P_2)^{2-}$ umwandelt. Die Reaktion von $(Ge_2P_2)^{2-}$ mit $CdPh_2$ ergab $[K(crypt\text{-}222)]_3[Cd_3(Ge_3P)_3]$, ein trimeres, multi-metallisches Clusteranion, welches eine bisher unbekannte Cd_3-Dreieckseinheit besitzt.

Im Rahmen der Synthese binarer Zintl-Anionen wurde eine nortricyclan-artige Topologie entdeckt. Die neuartigen binären Zinl-Anionen $(SiP_6H_2)^{2-}$ sowie die der schwereren Homologen der Elementkombination Ge/P und Si/As wurden beschrieben. Mit Hilfe von EDX-Spektroskopie wurde die Anwesenheit der entsprechenden Elemente in den Kristallen im erwarteten Verhältnis bestätigt. NMR-spektroskopische Untersuchungen bestätigten die Existenz von P–H Bindungen. Die Stabilität der beschriebenen Zintl-Anionen wurde zudem durch quantenchemische Rechnungen belegt und legen ebenfalls eine Protonierung nahe.

Die in dieser Dissertation vorgestellten Arbeiten erweitern damit die Grundlagenforschungen zu binären Clusteranionen des Zintl-Typs um die Elementkombinationen Ge/P, Ge/As, Si/P

und Si/As und die Klasse der multi-metallischen Clusteranionen um die Einbettung von E^5-Elementen (V, Nb und Ta) als endohedrales Zentrum. Die Nutzung der neuen tetraedrischen Zintl-Anionen $(Ge_2P_2)^{2-}$ und $(Ge_2As_2)^{2-}$ zur Derivatisierung konnte anhand der Reaktion mit Diphenylcadmium demonstriert werden und legen den Grundstein für weitere Arbeiten mit diesen gut synthetisierbaren Zintl-Anionen.

Stichwörter:
Zintl · Germanium · Phosphor · Arsen · Clusteranionen · Cluster · multimetallisch · heteroatomar · Hauptgruppenchemie · Polyanionen der Hauptgruppenelemente · Funktionalisierung · Derivatisierung

List of Abbreviations

18-c-6	1,4,7,10,13,16-hexaoxacyclooctadecane
2c2e	two center two electron bonds
bcc	body centered cubic
crypt-222	4,7,13,16,21,24-hexaoxa-1,10-diazabicyclo[8.8.8]hexacosane
Cp	cyclopentadienyl
dppe	ethane-1,2-diylbis(diphenylphosphane)
en	ethylene diamine
ESI	electron-spray-ionisation
EXAFS	extended X-ray absorption fine structure
hcp	hexagonal close packing
MS	mass spectrometry
NMR	nuclear magnetic resonance
VEC	valence electron concentration

List of Publications

peer-reviewed journals

W. J. Humenny, S. Mitzinger, C. B. Khadka, B. K. Najafabadi, I. Vieira, J. F. Corrigan *N-heterocyclic carbene stabilized copper- and silver-phenylchalcogenolate ring complexes*, Dalton Trans. 2012, **41**, 4413–4422.

S. Mitzinger, L. Broekaert, W. Massa, F. Weigend, S. Dehnen, *$[V@Ge_8As_4]^{3-}$ and $[Nb@Ge_8As_6]^{3-}$: Unprecedented Encapsulation of Electron-Poor Transition Metal Atoms* Chem. Commun. 2015, **51**, 3866-3869.

S. Mitzinger, L. Broekaert, W. Massa, F. Weigend, S. Dehnen *Understanding of Multimetallic Cluster Growth*, Nat. Commun. 2016,**7**:10480.

S. Mitzinger, J. Bandemehr, K. Reiter, S. J. McIndoe, X. Xie, F. Weigend, J. F. Corrigan, S. Dehnen *$(Ge_2P_2)^{2-}$: A Binary Analogue of P_4 as a Precursor to the Ternary Cluster Anion $[Cd_3(Ge_3P)_3]^{3-}$* Chem. Commun. *accepted manuscript.*

S. Mitzinger, L. Guggolz, W. Massa, S. Dehnen *$(SiP_6H_2)^{2-}$ and its Homologs – First Examples of Binary Notricyclane-Type Zintl Anions* Inorg. Chem. (ACS), *submitted.*

B. Weinert, S. Mitzinger, S. Dehnen *Review: (Multi-)Metallic Cluster Growth* Chem. Eur. J., *in print.*

non peer-reviewed journals

S. Mitzinger, S. Dehnen *Wie Metallcluster wachsen (in German)* GIT-Labor: Portal für Anwender in Wissenschaft und Industrie, 08/2016.

Bibliography

[1] M.-C. Daniel and D. Astruc, *Chem. Rev.*, 2004, **104**, 293–346.

[2] Z.-A. Qiao, P. Zhang, S.-H. Chai, M. Chi, G. M. Veith, N. C. Gallego, M. Kidder and S. Dai, *J. Am. Chem. Soc.*, 2014, **136**, 11260–11263.

[3] X. Wang, B. He, Z. Hu, Z. Zeng and S. Han, *Sci. Technol. Adv. Mater.*, 2014, **15**, 043502.

[4] M. B. Gawande, A. Goswami, T. Asefa, H. Guo, A. V. Biradar, D.-L. Peng, R. Zboril and R. S. Varma, *Chem. Soc. Rev.*, 2015, **44**, 7540–7590.

[5] T. F. Fässler, *Zintl Ions*, Springer, Berlin, Heidelberg, 2011.

[6] T. Fässler, S. Scharfe, F. Kraus, S. Stegmaier and A. Schier, *Angew. Chem. Int. Ed.*, 2011, **50**, 3630–3670.

[7] F. Li, A. Muñoz-Castro and S. C. Sevov, *Angew. Chem. Int. Ed.*, 2016, **55**, 8630–8633.

[8] F. Li, F. Li and S. C. Sevov, *J. Am. Chem. Soc.*, 2014, **136**, 12056–12063.

[9] M. W. Hull and S. C. Sevov, *J. Organomet. Chem.*, 2012, **721-722**, 85–91.

[10] M. M. Bentlohner, W. Klein, Z. H. Fard, L.-A. Jantke and T. F. Fässler, *Angew. Chem. Int. Ed.*, 2015, **54**, 3748–3753.

[11] J.-Q. Wang, S. Stegmaier and T. Fässler, 2009, **121**, 2032–2036.

[12] F. S. Geitner and T. F. Fässler, *Eur. J. Inorg. Chem.*, 2016, **17**, 2688–2691.

[13] N. Wiberg, A. F. Holleman and E. Wiberg, *Lehrbuch der Anorganischen Chemie*, De Gruyter, Berlin, Boston, 103rd edn, 2016.

[14] J. M. Goicoechea, *Clusters – Contemporary Insight in Structure and Bonding*, Springer International Publishing, Cham, 2016, vol. 174, ch. Homoatomic Polyanions of the Early p-Block Elements, pp. 63–97.

[15] Z. C. Dong and J. D. Corbett, *Inorg. Chem.*, 1996, **35**, 2301–2306.

[16] Z. C. Dong and J. D. Corbett, *Inorg. Chem.*, 1996, **35**, 3107–3112.

[17] M. L. Fornasini and M. Pani, *JALCOM*, 1994, **205**, 179–181.

[18] Z. C. Dong and J. D. Corbett, *Angew. Chem. Int. Ed.*, 1996, **35**, 1006–1009.

[19] J. T. Zhao and J. D. Corbett, *Inorg. Chem.*, 1995, **34**, 378–383.

[20] K. Frank and K. Schubert, *J. Less Common Met.*, 1970, **20**, 215–221.

[21] R. Nesper, J. Curda and H. G. von Schnering, *J. Solid St. Chem.*, 1986, **62**, 199–206.

[22] F. Zurcher and R. Nesper, *Z. Kristallogr. NCS*, 2001, **216**, 505–506.

[23] I. Todorov and S. C. Sevov, *Inorg. Chem.*, 2005, **44**, 5361–5369.

[24] I. Todorov and S. C. Sevov, *Inorg. Chem.*, 2004, **43**, 6490–6494.

[25] S. Wengert and R. Nesper, *Z. Anorg. Allg. Chem.*, 1998, **624**, 1801–1806.

[26] A. Palenzona, P. Manfrinetti and M. L. Fornasini, *JALCOM*, 2002, **345**, 144–147.

[27] A. Palenzona, P. Manfrinetti and M. L. Fornasini, *JALCOM*, 2000, **312**, 165–171.

[28] W. Müller, *Z. Naturforsch. B*, 1974, **29**, 304–307.

[29] S. Bobev and S. C. Sevov, *Angew. Chem. Int. Ed.*, 2000, **39**, 4108–4110.

[30] S. Wengert and R. Nesper, *Z. Anorg. Allg. Chem.*, 1998, **624**, 1801–1806.

[31] S. Scharfe and T. F. Fässler, *Z. Anorg. Allg. Chem.*, 2011, **637**, 901–906.

[32] A. Ugrinov and S. C. Sevov, *J. Am. Chem. Soc.*, 2002, **124**, 10990–10991.

[33] A. Ugrinov and S. C. Sevov, *Inorg. Chem.*, 2003, **42**, 5789–5791.

[34] C. Downie, Z. Tang and A. Guloy, *Angew. Chem. Int. Ed.*, 2000, **39**, 337–340.

[35] F. Gascoin and S. C. Sevov, *J. Am. Chem. Soc.*, 2000, **122**, 10251–10252.

[36] L. Xu, S. Bobev, J. El-Bahraoui and S. C. Sevov, *J. Am. Chem. Soc.*, 2000, **122**, 1838–1839.

[37] A. Cisar and J. D. Corbett, *Inorg. Chem.*, 1977, **16**, 2482–2487.

[38] F. Kraus, J. C. Aschenbrenner and N. Korber, *Angew. Chem. Int. Ed.*, 2003, **42**, 4030–4033.

[39] C. B. Benda and T. F. Fässler, *Z. Anorg. Allg. Chem.*, 2014, **640**, 40–45.

[40] W. Hönle, H. G. von Schnering, A. Schmidpeter and G. Burget, *Angew. Chem. Int. Ed.*, 1984, **23**, 817–818.

[41] O. Kühl, *Phosphorus-31 NMR Spectroscopy*, Springer, Berlin, Heidelberg, 2008.

[42] T. Sen, R. Poupko, U. Fleischer, H. Zimmermann and Z. Luz, *J. Am. Chem. Soc.*, 2000, **122**, 889–896.

[43] M. Reil and N. Korber, *ChemInform*, 2007, **38**, 1599.

[44] D. Knettel, M. Reil and N. Korber, *Z. Naturforsch. B*, 2001, **56**, 965–969.

[45] T. Hanauer and N. Korber, *Z. Anorg. Allg. Chem.*, 2006, **632**, 1135–1140.

[46] B. Weinert, A. R. Eulenstein, R. Ababei and S. Dehnen, *Angew. Chem. Int. Ed.*, 2014, **53**, 4704–4708.

[47] U. Müller, *Anorganische Strukturchemie*, Vieweg+Teubner, Wiesbaden, 6th edn, 2008.

[48] E. Zintl, J. Goubeau and W. Dullenkopf, *Z. Phys. Chem. A*, 1931, **154**, 1–46.

[49] E. Zintl and A. Harder, *Z. Phys. Chem. A*, 1931, **154**, 47–91.

[50] M. Joannis, *C. R. Hebd. Seances Acad. Sci.*, 1891, **113**, 795.

[51] F. Heusler, *Verhandl. Deuts. Phys. Ges.*, 1903, **5**, 219.

[52] R. Alsfasser, C. Janiak, T. M. Klapötke and H. Meyer, *Moderne Anorganische Chemie*, De Gruyter, Berlin, New York, 2007.

[53] *RÖMPP Lexikon Chemie*, Georg Thieme Verlag, Stuttgart, 10th edn, 2014.

[54] R. Nesper, *Prog. Solid St. Chem.*, 1990, **20**, 1–45.

[55] E. Zintl and W. Dullenkopf, *Z. Phys. Chem. B*, 1932, **16**, 183–194.

[56] E. Zintl and H. Kaiser, *Z. Anorg. Allg. Chem.*, 1933, **211**, 113–131.

[57] W. Klemm, *Proc. Chem. Soc.*, 1958, **12**, 329–341.

[58] W. Klemm, *Festkörperprobleme*, Springer, Berlin, Heidelberg, 1964, vol. 3, pp. 233–251.

[59] W. Klemm, *Z. Anorg. Allg. Chem.*, 1941, **247**, 1.

[60] R. Hoffmann, *Angew. Chem. Int. Ed.*, 1987, **26**, 846–878.

[61] D. Santamaría Pérez and A. Vegas, *Acta Crystallogr. B*, 2003, **59**, 305–323.

[62] E. Busmann, *Naturwissenschaften*, 1960, **47**, 82–82.

[63] R. Blachnik and U. Wickel, *Z. Naturforsch. B*, 1982, **37**, 1507–1513.

[64] V. Manriquez, W. Hönle and H. G. von Schnering, *Z. Anorg. Allg. Chem.*, 1986, **539**, 95–109.

[65] E. Zintl, *Angew. Chem.*, 1939, **52**, 1.

[66] F. Wang and G. J. Miller, *Inorg. Chem.*, 2011, **50**, 7625–7636.

[67] H. G. von Schnering, M. Baitinger, U. Bolle, W. Carrillo Cabrera, J. Curda, Y. Grin, F. Heinemann, J. Llanos, K. Peters and A. Schmeding, *Z. Anorg. Allg. Chem.*, 1997, **623**, 1037–1039.

[68] V. Queneau and S. C. Sevov, *Angew. Chem. Int. Ed.*, 1997, **36**, 1754–1756.

[69] F. Lips, I. Schellenberg, R. Pöttgen and S. Dehnen, *Chem. Eur. J.*, 2009, **15**, 12968–12973.

[70] U. Friedrich, M. Neumeier, C. Koch and N. Korber, *Chem. Commun.*, 2012, **48**, 10544–10546.

[71] J. D. Corbett and S. C. Critchlow, *Inorg. Chem.*, 1982, **21**, 3286–3290.

[72] L. Diehl, K. Khodadadeh, D. Kummer and J. Strähle, *Chem. Ber.*, 1976, **109**, 3404–3418.

[73] R. W. Rudolph, W. L. Wilson, F. Parker, R. C. Taylor and D. C. Young, *J. Am. Chem. Soc.*, 1978, **100**, 4629.

[74] B. W. Eichhorn and S. Kocak, *Clusters – Contemporary Insight in Structure and Bonding*, Springer, Berlin, Heidelberg, 2010, vol. 140, ch. Dynamic Properties of the Group 14 Zintl Ions and Their Derivatives, pp. 59–89.

[75] L. J. Guggenberger and E. L. Mutterties, *J. Am. Chem. Soc.*, 1976, **98**, 7221–7225.

[76] F. Teixidor, M. L. Luetkens and R. W. Rudolph, *J. Am. Chem. Soc.*, 1983, **105**, 149–150.

[77] M. Bown, T. Jelínek, B. Štíbr, S. Heřmánek, X. L. R. Fontaine, N. N. Greenwood, J. D. Kennedy and M. Thornton-Pett, *J. Chem. Soc., Chem. Commun.*, 1988, **0**, 974–975.

[78] T. Birchall, R. C. Burns, L. A. Devereux and G. J. Schrobilgen, *Inorg. Chem.*, 2002, **24**, 890–894.

[79] J. Rosdahl, T. F. Fässler and L. Kloo, *Eur. J. Inorg. Chem.*, 2005, **14**, 2888–2894.

[80] S. Mitzinger, L. Broeckaert, W. Massa, F. Weigend and S. Dehnen, *Nat. Commun.*, 2016, **7**, 10480.

[81] S. Gärtner and N. Korber, *Comprehensive Inorganic Chemistry II*, Elsevier, Amsterdam, 2013, ch. Zintl Anions, pp. 251–267.

[82] D. Y. Zubarev, A. I. Boldyrev, Xi Li, L.-F. Cui and L.-S. Wang, *J. Phys. Chem. A*, 2005, **109**, 11385–11394.

[83] J. D. Corbett, *Structural and Electronic Paradigms in Cluster Chemistry*, Springer, Berlin, Heidelberg, 1997, pp. 157–193.

[84] M. M. Bentlohner, C. Fischer and T. F. Fässler, *Chem. Commun.*, 2016, **52**, 9841–9843.

[85] T. Damhus, R. M. Hartshorn and A. T. Hutton, *Nomenclature of inorganic chemistry: IUPAC recommendations*, RSC Publishing, Cambridge, 2005.

[86] J. B. Casey, W. J. Evans and W. H. Powell, *Inorg. Chem.*, 1983, **22**, 2228–2235.

[87] J. B. Casey, W. J. Evans and W. H. Powell, *Inorg. Chem.*, 1983, **22**, 2236–2245.

[88] J. B. Casey, W. J. Evans and W. H. Powell, *Inorg. Chem.*, 1984, **23**, 4132–4143.

[89] K. Wade, *Adv. Inorg. Chem. Radiochem.*, 1976, **18**, 1–66.

[90] D. M. P. Mingos, *Nat. Phys. Sci.*, 1972, **236**, 99–102.

[91] S. Joseph, C. Suchentrunk, F. Kraus and N. Korber, *Chem. Ber.*, 2009, **31**, 4641–4647.

[92] D. M. P. Mingos, *Pure Appl. Chem.*, 1991, **63**, 807–812.

[93] M. A. Fox and K. Wade, *Pure Appl. Chem.*, 2003, **75**, 1315–1323.

[94] S. Scharfe, F. Kraus, S. Stegmaier, A. Schier and T. F. Fässler, *Angew. Chem. Int. Ed.*, 2011, **50**, 3630–3670.

[95] J.-Q. Wang, T. Fässler and S. Stegmaier, *Angew. Chem. Int. Ed.*, 2009, **48**, 1998–2002.

[96] G. Espinoza-Quintero, J. C. A. Duckworth, W. K. Myers, J. E. McGrady and J. M. Goicoechea, *J. Am. Chem. Soc.*, 2014, **136**, 1210–1213.

[97] F. Lips, M. Hołyńska, R. Clérac, U. Linne, I. Schellenberg, R. Pöttgen, F. Weigend and S. Dehnen, *J. Am. Chem. Soc.*, 2012, **134**, 1181–1191.

[98] F. Lips, R. Clérac and S. Dehnen, *Angew. Chem. Int. Ed.*, 2011, **50**, 960–964.

[99] R. B. King, I. Silaghi-Dumitrescu and A. Lupan, *Inorg. Chem.*, 2005, **44**, 3579–3588.

[100] R. B. King, I. Silaghi-Dumitrescu and A. Lupan, *Inorg. Chem.*, 2005, **44**, 7819–7824.

[101] R. B. King, *Clusters – Contemporary Insight in Structure and Bonding*, Springer, Berlin, Heidelberg, 2011, vol. 140, ch. Structure and Bonding in Zintl Ions and Related Main Group Element Clusters, pp. 1–24.

[102] R B King, I. Silaghi-Dumitrescu, and M. M. Uţă, *J. Chem. Theory Comput.*, 2007, **4**, 209–215.

[103] R. B. King and I. Silaghi-Dumitrescu, *Dalton Trans.*., 2008, **13**, 6083–6088.

[104] G. S. Armatas and M. G. Kanatzidis, *Nature*, 2006, **441**, 1122–1125.

[105] D. Sun, A. E. Riley, A. J. Cadby, E. K. Richman, S. D. Korlann and S. H. Tolbert, *Nature*, 2006, **441**, 1126–1130.

[106] T. F. Fässler, *Angew. Chem. Int. Ed.*, 2007, **46**, 2572–2575.

[107] J. M. Goicoechea and S. C. Sevov, *J. Am. Chem. Soc.*, 2004, **126**, 6860–6861.

[108] J. M. Goicoechea and S. C. Sevov, *Inorg. Chem.*, 2005, **44**, 2654–2658.

[109] S. Joseph, C. Suchentrunk and N. Korber, *Z. Naturforsch. B*, 2010, **65**, 1059–1065.

[110] G. J. Schrobilgen and J. Campbell, *Inorg. Chem.*, 1997, **36**, 4078–4081.

[111] C. Suchentrunk and N. Korber, *New J. Chem.*, 2006, **30**, 1737–1739.

[112] C. Belin, J. D. Corbett and A. Cisar, *J. Am. Chem. Soc.*, 1977, **99**, 7163–7169.

[113] M. M. Bentlohner, C. Fischer and T. F. Fässler, *Chem. Commun.*, 2016, **52**, 9841–9843.

[114] P. A. Edwards and J. D. Corbett, *Inorg. Chem.*, 1977, **16**, 903–907.

[115] S. C. Critchlow and J. D. Corbett, *J. Am. Chem. Soc.*, 1983, **105**, 5715–5716.

[116] T. F. Fässler and M. Hunziker, *Inorg. Chem.*, 1994, **33**, 5380–5381.

[117] A. Spiekermann, S. D. Hoffmann and T. F. Fässler, *Angew. Chem. Int. Ed.*, 2006, **45**, 3459–3462.

[118] B. Zhou, M. S. Denning, D. L. Kays and J. M. Goicoechea, *J. Am. Chem. Soc.*, 2009, **131**, 2802–2803.

[119] N. Lichtenberger, R. J. Wilson, A. R. Eulenstein, W. Massa, R. Clérac, F. Weigend and S. Dehnen, *J. Am. Chem. Soc.*, 2016, **138**, 9033–9036.

[120] E. N. Esenturk, J. Fettinger and B. Eichhorn, *Polyhedron*, 2006, **25**, 521–529.

[121] F. Lips, R. Clérac and S. Dehnen, *J. Am. Chem. Soc.*, 2011, **133**, 14168–14171.

[122] S. Mitzinger, L. Broeckaert, W. Massa, F. Weigend and S. Dehnen, *Chem. Commun.*, 2015, **51**, 3866–3869.

[123] L. G. Perla and S. C. Sevov, *J. Am. Chem. Soc.*, 2016, **138**, 9795–9798.

[124] J. M. Goicoechea and S. C. Sevov, *J. Am. Chem. Soc.*, 2005, **127**, 7676–7677.

[125] C. B. Benda, M. Waibel and T. F. Fässler, *Angew. Chem. Int. Ed.*, 2015, **127**, 532–536.

[126] S. Scharfe and T. Fässler, *Eur. J. Inorg. Chem.*, 2010, **8**, 1207–1213.

[127] L. J. Schiegerl, F. S. Geitner, C. Fischer, W. Klein and T. F. Fässler, *Z. Anorg. Allg. Chem.*, 2016, **642**, 1419–1426.

[128] A. Spiekermann, S. D. Hoffmann, F. Kraus and T. F. Fässler, *Angew. Chem. Int. Ed.*, 2007, **46**, 1638–1640.

[129] F. S. Geitner, M. A. Giebel, A. Pöthig and T. F. Fässler, *Molecules*, 2017, **22**, 1204.

[130] K. Mayer, L. J. Schiegerl and T. F. F ssler, *Chem. Eur. J.*, 2016, **22**, 18794–18800.

[131] T. Fässler, *Angew. Chem. Int. Ed.*, 2001, **40**, 4161.

[132] A. Nienhaus, R. Hauptmann and T. F. Fässler, *Angew. Chem. Int. Ed.*, 2002, **41**, 3213–3215.

[133] K. Mayer, L.-A. Jantke, S. Schulz and T. F. Fässler, *Angew. Chem. Int. Ed.*, 2017, **56**, 2350–2355.

[134] M. M. Bentlohner, W. Klein, Z. H. Fard, L.-A. Jantke and T. F. Fässler, *Angew. Chem. Int. Ed.*, 2015, **54**, 3748–3753.

[135] S. C. Critchlow and J. D. Corbett, *Inorg. Chem.*, 1985, **24**, 979–981.

[136] R. Ababei, J. Heine, M. Hołyńska, G. Thiele, B. Weinert, X. Xie, F. Weigend and S. Dehnen, *Chem. Commun.*, 2012, **48**, 11295–11297.

[137] B. Eisenmann and J. Klein, *J. Less Common Met.*, 1991, **175**, 109–117.